

DISS. ETH NO. 17100

# CATALYTIC HYDROTHERMAL GASIFICATION OF BIOMASS FOR THE PRODUCTION OF SYNTHETIC NATURAL GAS

A dissertation submitted to

ETH ZURICH

for the degree of  
DOCTOR OF SCIENCES

presented by

Maurice Henri Waldner  
Dipl. Chem.-Ing. ETH  
born 21.03.1977

citizen of  
Basel and Oberdorf (BL), Switzerland

accepted on the recommendation of  
Prof. Dr. A. Wokaun, examiner  
Prof. Dr. P. Rudolf von Rohr, co-examiner  
Dr. F. Vogel, co-examiner

Zurich 2007



# Acknowledgment

I thank my referee Prof. Dr. A. Wokaun for giving me the opportunity to work in this interesting field of energy technology, Prof. Dr. P. Rudolf von Rohr for the co-examination of my work, and Dr. F. Vofsi for his mentoring and guidance throughout the PhD studies.

I thank the following people for their contribution to this work: C. Aguzard (exp. support), P. Binkert<sup>†</sup> (construction), R. Brützel (SEM, EDXS), E. De Boni (construction, LabView interface), A. Frei (XRD), E. Gálvez (BET), F. Geiger (BET), P. Hottiger (LabView interface), F. Krumeich (TEM), F. Loviat (XPS), T. Marti (construction), V. Monney (exp. support), S. Rabe (exp. support), J. Schneebeli (lab support), M. Schneider (elemental analysis), M. Schubert (Acemiasorption, exp. support), A. Schuler (ICP), M. Topic<sup>†</sup> (Ru/TiO<sub>2</sub> mesh), T.-B. Truong (analytics), and P. Witschi (exp. support).

I express my gratitude to the following people working in industry for their support of this project: C.V. Cavagnoli (Engelhard, catalysts and carbon supports), R.-L. Meisel (H.C. Starck, skeletal Ni samples), S. Schmidt and K. Van Gorp (Grace Davison, tailored skeletal Ni samples), and M. Zürcher (Timcal, graphite supports).

I also thank my project partners: H. Brogli (Romaco Fryma Koruma), U. Baier (FH Wädenswil), B. Guggisberg (BEE, funding, project No. 100131/150163), J.-L. Hessew (Ingenieurbüro Hessew), R. Herzog (Romaco Fryma Koruma), P. Kuoer (Innoplana Um-

welttechnik AG), and U. Meier (Meritec GmbH).

A special thank you goes to K. Dürbe (Docu+Design Dürbe) for his generous Adobe FrameMaker support.

I shall not forget my parents and my sister Annette, who have always been not just family, but also friends:  
Thanks for everything!

Joachim Wötter

# Table of Contents

<b>Chapter 0: Preamble</b> . . . . .	<b>i</b>
Acknowledgment . . . . .	i
Table of Contents . . . . .	iii
Zusammenfassung . . . . .	ix
Abstract . . . . .	xiii
Notation . . . . .	xvii
Greek Symbols . . . . .	xvii
Roman Symbols . . . . .	xviii
Abbreviations . . . . .	xx
<b>Chapter 1: Introduction</b> . . . . .	<b>1</b>
1.1 Motivation – Positioning of the Hydrothermal Gasification . . . . .	1
1.1.1 Biomass Potentials and Swiss Energy Consumption . . . . .	1
1.1.2 Established Biomass Processing Technologies . . . . .	2
1.1.3 High Temperature Gasification . . . . .	3
1.1.4 Anaerobic Digestion . . . . .	3
1.1.5 Hydrothermal Gasification . . . . .	4
1.1.6 Comparison of the Technologies . . . . .	5
1.2 Process Idea of Hydrothermal Gasification . . . . .	8
1.3 Synthetic Natural Gas (SNG) – a Viable Option . . . . .	9
1.4 Aim of the project . . . . .	10
1.5 Possible Feedstocks for SCWG . . . . .	11
1.6 Process Challenges . . . . .	13
1.7 Properties of Water at Elevated Pressures and Temperatures . . . . .	15
1.7.1 Critical Point and Supercritical Phase Behavior . . . . .	15
1.7.2 Ion Product and Dielectric Constant $\epsilon_r$ . . . . .	15
1.7.3 Density . . . . .	17
1.7.4 Enthalpy and Heat Capacity at Constant Pressure $c_p$ . . . . .	18
<b>Chapter 2: Literature Review and Wood Reaction Network</b> . . . . .	<b>21</b>
2.1 Present Status of Research on Hydrothermal Gasification of Biomass . . . . .	21

---

2.2	Chemical Fundamentals . . . . .	27
2.2.1	Effect of temperature and feed concentration . . . . .	27
2.2.2	Effect of pressure . . . . .	28
2.2.3	Biomass Decomposition to Smaller Molecules (Liquefaction) . . . . .	30
2.2.4	CO Hydrogenation (CO Methanation) . . . . .	32
2.2.5	CO <sub>2</sub> Hydrogenation (CO <sub>2</sub> Methanation) . . . . .	33
2.2.6	Water Gas Shift Reaction (WGSR) . . . . .	34
2.2.7	Decomposition Pathways of Formic Acid . . . . .	36
2.3	Catalysis in the Hydrothermal Environment . . . . .	37
2.3.1	Potential Active Metals for SCWG . . . . .	38
2.3.2	Potential Supports for SCWG . . . . .	40
2.4	Proposed Reaction Network of Wood Gasification . . . . .	43
2.4.1	Introduction . . . . .	43
2.4.2	Reaction Network . . . . .	45
2.4.3	Avoidance of the Tar Problem of Conventional Gasification . . . . .	46
<b>Chapter 3:</b>	<b>Experimental Setup. . . . .</b>	<b>49</b>
3.1	General . . . . .	49
3.2	Batch Reactor . . . . .	50
3.2.1	Setup . . . . .	50
3.2.2	Feed Preparation and Experimental Procedure . . . . .	52
3.2.3	Analysis . . . . .	53
3.3	Continuously Operating Catalyst Test Rig . . . . .	56
3.3.1	Setup . . . . .	56
3.3.2	Experimental Procedure . . . . .	60
3.3.3	Analysis . . . . .	61
3.4	Heating System for Quartz Capillaries . . . . .	62
3.4.1	Reactor Setup . . . . .	62
3.4.2	Quartz Capillaries . . . . .	63
3.4.3	Experimental . . . . .	65
<b>Chapter 4:</b>	<b>Analytical Tools . . . . .</b>	<b>67</b>
4.1	Gas Chromatography / Mass Spectrometry . . . . .	67
4.2	High Pressure Liquid Chromatography / High Pressure Ion Exchange Chromatography . . . . .	69
4.3	Soxhlet Extraction . . . . .	71
4.4	Karl Fischer Titration . . . . .	71
4.5	Dohrmann-Rosemount DC-190 . . . . .	72
4.6	Inductively Coupled Plasma – Optical Emission Spectrometry (ICP-OES) . . . . .	73
4.7	Brunauer-Emmett-Teller Surface Area (BET) . . . . .	74

---

4.8	Temperature Programmed Oxidation/Reduction with a TG–FTIR . . . . .	75
4.8.1	TPO/TPR for the Detection of Carbonaceous Deposits. . . . .	75
4.8.2	Oxygen Chemisorption Dispersion Measurement. . . . .	75
4.9	X-Ray Diffraction (XRD). . . . .	77
4.10	X-Ray Photoelectron Spectroscopy (XPS) . . . . .	78
4.11	Scanning Electron Microscopy (SEM) . . . . .	79
4.12	Scanning Transmission Electron Microscopy (STEM) . . . . .	79
<b>Chapter 5: Analysis of Feedstocks . . . . .</b>		<b>81</b>
5.1	Spruce and Fir – Woody Biomass . . . . .	81
5.2	Synthetic Liquefied Wood . . . . .	83
5.3	Swine Manure . . . . .	86
5.3.1	General. . . . .	86
5.3.2	Dry Matter Content and Elemental Analysis . . . . .	87
5.3.3	Incineration Residue. . . . .	87
5.3.4	Thermal vs. Chemical Viewpoint. . . . .	88
5.3.5	Washing Procedure and Soxhlet Extraction . . . . .	89
5.3.6	Analysis of Ions Contained In Swine Manure . . . . .	90
5.3.7	Analysis of Metal Oxides Contained in Swine Manure. . . . .	92
5.3.8	Summary of Analytical Results . . . . .	93
5.4	Palm Oil Pyrolysis Condensate. . . . .	94
<b>Chapter 6: Selection of Catalysts . . . . .</b>		<b>99</b>
6.1	Experiments for the Attainment of the Chemical Equilibrium Composition with a Skeletal Ni Catalyst . . . . .	99
6.1.1	Starting Point and Aim of The Experiments. . . . .	99
6.1.2	Experimental Details and Overview. . . . .	99
6.1.3	Results of Wood Gasification with Raney 2800 Ni (Aldrich) . . . . .	101
6.1.4	Comparison Between Catalytic Liquefaction (300 °C, small $\tau$ ) and Catalytic Gasification (400 °C, large $\tau$ ) . . . . .	104
6.1.5	Catalytic Gasification at 400 °C . . . . .	107
6.1.6	Catalyst Analysis with XPS, BET and TPO . . . . .	109
6.1.7	Differential Pressure Analysis . . . . .	113
6.1.8	Conclusions from the Experiments with Raney Ni 2800 (Aldrich). . . . .	118
6.2	Gasification Experiments of Manure using a Skeletal Nickel Catalyst . . . . .	119
6.2.1	Aim of The Experiments . . . . .	119
6.2.2	Experimental Details and Overview. . . . .	120
6.2.3	Results of the Manure Gasification Experiments. . . . .	121
6.2.4	Product Gas Composition. . . . .	123
6.2.5	Gasification Efficiency and Dissolved Carbon Conversion $X_C$ . . . . .	125
6.2.6	Volume of Gas Produced and Methane Yield $Y_{CH_4}$ . . . . .	127
6.2.7	Solid Residue and Tarry Compounds After Gasification . . . . .	128

---

6.2.8	Carbon Distribution to Gas, Liquid, Residue, and Tars . . . . .	130
6.2.9	Conclusions of the Manure Gasification Experiments. . . . .	130
6.3	Batch Reactor Catalyst Screening using Wood as Feedstock . . . . .	132
6.3.1	Skeletal Nickel Catalysts. . . . .	132
6.3.2	Supported Ruthenium Catalysts . . . . .	136
6.3.3	Stability Experiments with Supported Ruthenium Catalysts and Carbon Supports in the Batch Reactor . . . . .	147
6.4	Experiments using Gas Mixtures as Reactants Instead of Biomass .	150
6.4.1	Overview of the Experiments . . . . .	150
6.4.2	CO/CO <sub>2</sub> , (H <sub>2</sub> ), Ru/C (or support) . . . . .	151
6.4.3	Mixing Problem of the Batch Reactor . . . . .	152
6.4.4	Formic Acid, H <sub>2</sub> O, Ru/C . . . . .	153
6.4.5	Conclusions of the Experiments Using Gas Mixtures as Reactants . . . . .	154
6.5	Comparison of the Reactivity of Wood to Synthetic Liquefied Wood. . . . .	155
6.5.1	Possibilities to Take Samples During Reaction . . . . .	156
6.5.2	Comparison of Spruce Slurries to Synthetic Liquefied Wood . . . . .	158
6.5.3	Conclusions of the Comparison Experiments . . . . .	161
6.6	Batch Gasification of Palm Oil Pyrolysis Condensate with Ru/C. .	162
6.7	Experiments using Quartz-Capillaries as Micro-Reactors. . . . .	163
6.7.1	Capillary Gasification Experiment with Wood Slurry and Raney 2800 Nickel . . . . .	163
6.7.2	Capillary Experiment with Pure Water . . . . .	165
6.7.3	Capillary Experiment with 5 wt % NaCl in Water . . . . .	166
6.7.4	Conclusions of the Capillary Experiments . . . . .	168
<b>Chapter 7: Catalyst Testing and Characterization . . . . .</b>		<b>171</b>
7.1	Towards a Hydrothermally Stable Catalyst . . . . .	171
7.1.1	Starting Point and Aim of The Experiments. . . . .	171
7.1.2	Gasification of Synthetic Liquefied Wood over Raney 2800 Ni . . . . .	172
7.1.3	Gasification of Synthetic Liquefied Wood over Raney 2800 Ni/Ru . . . . .	175
7.1.4	Gasification of Ethanol over 1 wt % Ru/TiO <sub>2</sub> . . . . .	178
7.1.5	Gasification of Synthetic Liquefied Wood over 2 wt % Ru/C . . . . .	182
7.1.6	Blank Test Gasification of Synthetic Liquefied Wood over $\alpha$ -Al <sub>2</sub> O <sub>3</sub> . . . . .	192
7.1.7	Conclusions of the Long-Term Stability and Activity Experiments with Various Catalysts . . . . .	195
7.2	Methodology for Testing the Sodium Sulfate Tolerance of the 2 wt % Ru/C Catalyst	196
7.2.1	Gasification of Synthetic Liquefied Wood with Increasing Sodium Sulfate Con- tent	197
7.2.2	Possible Catalyst Deactivation Mechanisms . . . . .	200
7.2.3	Identification of the Governing Deactivation Mechanism – Hypothesis of Deactivation due to Ru Leaching (i) . . . . .	201
7.2.4	Hypothesis of Deactivation due to Loss of Active Metal Surface Area (ii) .	202



---

7.2.5 Hypothesis of Deactivation due to Physical Blockage by Precipitated Sodium Sulfate (iii) . . . . .	202
7.2.6 Hypothesis of Deactivation due to Chemical Interaction of Ru with a Sulfur Species (iv), i.e. $\text{SO}_4^{2-}$ or $\text{S}^{2-}$ . . . . .	208
7.2.7 Catalyst Regeneration with Hydrogen Peroxide Solution . . . . .	212
7.2.8 Catalyst Characterization after Sulfate Deactivation and $\text{H}_2\text{O}_2$ Regeneration. . . . .	213
7.2.9 Conclusions . . . . .	223

## **Chapter 8: Process Demonstration Unit (PDU) . . . . . 225**

8.1 Introduction . . . . .	225
8.2 Experiments to Identify Suitable Conditions for the Non-Catalytic Liquefaction of Wood (Batch Reactor) . . . . .	228
8.2.1 Starting Point and Aim of The Experiments. . . . .	228
8.2.2 Experimental Details and General Observations . . . . .	229
8.2.3 Successful Liquefaction with Subsequent Gasification . . . . .	234
8.2.4 Basic Dimensioning of a Preheater for the Liquefaction in the PDU . . . . .	235
8.2.5 Conclusions of the Wood Liquefaction Experiments . . . . .	236
8.3 Feed Conditioning (Milling) . . . . .	237
8.4 Suitable Pump Systems for the PDU. . . . .	239
8.4.1 Gear Pumps . . . . .	239
8.4.2 Twin-Screw Extruders . . . . .	240
8.4.3 Eccentric Screw Pumps . . . . .	240
8.4.4 Piston Diaphragm Pumps. . . . .	240
8.4.5 Piston / Plunger Pumps. . . . .	241
8.4.6 Evaluation Process towards a Suitable Pump for the PDU . . . . .	241
8.5 Novados N-P31 Plunger Pump Testing . . . . .	243
8.5.1 Alternatives to the Novados N-P31 . . . . .	245
8.5.2 Final Solution . . . . .	247
8.6 Setup and Process Flow Sheet . . . . .	248
8.6.1 Storage and Conveying. . . . .	252
8.6.2 Preheater . . . . .	253
8.6.3 Salt Separator . . . . .	254
8.6.4 Reactor. . . . .	256
8.6.5 Cooling and Pressure Control and Letdown . . . . .	256
8.6.6 Product Phase Separation (G/L Separator) . . . . .	257
8.6.7 Product Gas Analysis and Treatment . . . . .	258
8.6.8 Safety Considerations. . . . .	259
8.7 Preliminary Gasification Experiments . . . . .	260
8.8 Preliminary Salt Separation Experiments . . . . .	264
8.8.1 Operating Conditions. . . . .	264
8.8.2 Results . . . . .	265
8.9 Problems, Conclusions and Outlook . . . . .	266

<b>Chapter 9: Summary, Conclusions and Recommendations . . . . .</b>	<b>269</b>
9.1 Summary and Conclusions . . . . .	269
9.2 Recommendations for Further Research. . . . .	271
<b>References . . . . .</b>	<b>273</b>
<b>Appendix A: Ru/C Catalyst Preparation and Analysis . . . . .</b>	<b>297</b>
A.1 Impregnation of the Support with Ruthenate. . . . .	297
A.2 Reduction of Ru(III) to Ru(0) with Hydrogen . . . . .	298
A.3 Catalyst Analysis . . . . .	299
<b>Appendix B: Publications and CV</b>	
List of Publications . . . . .	303
Patents . . . . .	303
Peer-Reviewed Articles. . . . .	303
Articles. . . . .	304
Conference Proceedings (Posters and Talks) . . . . .	304
Curriculum Vitae . . . . .	307

---

# Zusammenfassung

Energie aus Biomasse ist eine CO<sub>2</sub>-neutrale, nachhaltige Energieform. Durch Vergärung kann heute aus Biomasse Biogas gewonnen werden, das neben CO<sub>2</sub> und zahlreichen Verunreinigungen rund 60 % Methan enthält. Die meisten Biomassesortimente enthalten nicht vergärbare Bestandteile; bei holzartiger Biomasse ist dieser besonders hoch. Daher eignen sich konventionelle Vergärungsverfahren nicht zur Biogasproduktion aus holzartiger Biomasse. Während Holz bereits durch konventionelle thermische Verfahren energetisch genutzt wird (Vergasung mit nachgeschalteter Methanierung), stellen insbesondere Hofdünger, Gülle, und Klärschlamm ein nahezu ungenutztes Energiepotenzial dar (Schweizer Güllenutzung derzeit: 0.4 %). Hier jedoch liefern aufgrund des hohen Wassergehalts konventionelle Gasphasenverfahren einen zu tiefen Wirkungsgrad (Feuchtigkeit wird verdampft, energetisch aufwändig). Als Alternative bietet sich die hydrothermale Vergasung an: der Wassergehalt der Biomasse dient als Reaktionsmedium, welches unter hohem Druck um 30 MPa als überkritisches Fluid vorliegt und apolare Eigenschaften besitzt; Teer-Vorläufersubstanzen, die bei der konventionellen Vergasung zu Problemen führen, können so gelöst und vergast werden. Aufgrund der fehlenden Verdampfungswärme sind hohe thermische Wirkungsgrade möglich (65 – 70 %). Die in der Biomasse enthaltenen Nährsalze (Gülle: ca. 20 gew % der Trockenmasse, TM) können aufgrund der stark reduzierten Löslichkeit in überkritischem Wasser abgeschieden und für Düngezwecke weiterverwendet werden. Mit der energetischen Nutzung geht also eine stoffliche einher.

Ziel des Projekts am PSI war es, ein katalytisches Verfahren zu entwickeln, das die Vergasung nasser Biomasse zu synthetischem Naturgas

(SNG) in einer kontinuierlichen Anlage im Labormassstab demonstriert (Biomassedurchsatz 1 kg/h, liefert bei 40 gew % ca. 200 L<sub>SNG</sub>/h, was einer thermischen Brennleistung von 1 kW<sub>th</sub> entspricht). Die Anlage sollte idealerweise Feststoffsuspensionen fördern können. Verschiedene Katalysatoren wurden ausgewählt (z.T. selbst synthetisiert) und auf ihre Stabilität im hydrothermalen Medium und auf ihre Salzverträglichkeit (am Beispiel Sulfat) getestet und charakterisiert (mittels TG/FTIR, TPO/TPR, TOC, BET, XRD, XPS, ICP, TEM, HAADF-STEM und SEM-EDXS). Die Biomasse wurde auf ihre Bestandteile untersucht (Soxhlet-Extraktion, ICP, HPIEC), um eine zuverlässige Abschätzung des Energieinhalts zu erhalten, was den Grundstein für Wirtschaftlichkeitsrechnungen bildet. Der untere Heizwert der aufkonzentrierten Schweinegülle wurde zu 16.3 MJ/kg<sub>Trockenmasse</sub> bestimmt.

Skelettartige Nickelkatalysatoren, aufgrund ihres attraktiven Preises in der Industrie häufig eingesetzt, vermochten Holz suspensionen (Konz. 10 – 30 gew %) in einem Batchreaktor hydrothermal vollständig zu synthetischem Naturgas zu vergasen, mit einer Methanausbeute von 0.33 g<sub>CH<sub>4</sub></sub>/g<sub>Holz</sub>, was der thermodynamisch maximalen Ausbeute entsprach. Güllesuspensionen wurden ebenfalls hydrothermal vergast. Die höchste Ausbeute war jedoch nur 0.21 g<sub>CH<sub>4</sub></sub>/g<sub>TM</sub>, was bei 80 % des thermodynamisch Möglichen lag. Grund dafür waren in der Gülle enthaltene Salze, die vor den Versuchen nicht abgetrennt worden waren und den Katalysator deaktivierten. Dies verdeutlichte die Wichtigkeit einer integrierten Salzausschleusung bei einer Demonstrationsanlage.

In einer kontinuierlich arbeitenden Laborapparatur, mit der nur Flüssigkeiten gefördert werden können, wurden die vielversprechendsten Katalysatorsysteme (Nickel, Ruthenium) auf ihre Langzeit-Aktivität und -Stabilität in hydrothermaleml Milieu geprüft. Als Biomasse diente ein Gemisch aus fünf organischen Substanzen (Ameisen- und Essigsäure, Ethanol, Phenol und Anisol), das hydrolysiertem Holz chemisch ähnlich ist. Die Nickel-Skelettkatalysatoren erwiesen sich als aktiv aber nicht stabil, und deaktivierten innert weniger Stunden. Eine Stabilisierung durch

---

Zudotieren weiterer Metalle (Ru, Mo, Cu) war nicht erfolgreich. Ru/TiO<sub>2</sub> war zuwenig aktiv, aber Ru/C vergaste das Gemisch bei hohen Katalysatorbelastungen vollständig während über 200 h, wobei das Produktgas Gleichgewichtszusammensetzung aufwies.

Dieser Katalysator wurde auf seine Sulfatverträglichkeit hin untersucht, welche sich als schlecht herausstellte: die Zufuhr weniger ppm deaktivierte den Katalysator innert weniger Stunden. Der Deaktivierungsmechanismus wurde als chemische Vergiftung identifiziert; die im hydrothermalen Umfeld vorliegende Spezies (Sulfat oder Sulfid) ist unklar. Die Beobachtungen können mit beiden Thesen erklärt werden.

Ein Heizsystem für Quarzkapillaren erlaubte die optische Untersuchung von hydrothermalen Vorgängen. Die geringen Mengen an verwendetem Material (wenige hundert Milligramm) und häufige Kapillarexplosionen führten jedoch dazu, dass das System nicht weiter genutzt wurde.

Die Förderung von Feststoffsuspensionen erwies sich im Labormassstab als ein nicht zu lösendes Problem. Entsprechend können mit der neu aufgestellten Anlage nur Flüssigbiomassen gefördert werden. Als geeignet erschien Palmöl-Pyrolysekondensat, ein in Indonesien problematischer Abfallstrom mit hohem Organikagehalt (über 40 gew %). Erste Vergasungsversuche mit Ethanol und Salzausschleusungsversuche mit Natriumsulfat in dieser Anlage waren erfolgreich.



---

# Abstract

Energy from biomass is a CO<sub>2</sub> neutral, sustainable form of energy. Anaerobic digestion is an established technology for converting biomass to biogas, which contains around 60 % methane, besides CO<sub>2</sub> and various contaminants. Most types of biomass contain material that cannot be digested; in woody biomass, this portion is particularly high. Therefore, conventional anaerobic digestion is not suited for the production of biogas from woody biomass.

While wood is already being converted to energy by conventional thermal methods (gasification with subsequent methanation), dung, manure, and sewage sludge represent types of biomass whose energy potential remains largely untapped (present energetic use of manure in Switzerland: 0.4 %). Conventional gas phase processes suffer from a low efficiency due to the high water content of the feed (enthalpy of vaporization). An alternative technology is the hydrothermal gasification: the water contained within the biomass serves as reaction medium, which at high pressures of around 30 MPa turns into a supercritical fluid that exhibits apolar properties. Under these conditions, tar precursors, which cause significant problems in conventional gasification, can be solubilized and gasified. The need to dry the biomass prior to gasification is obsolete, and as a consequence high thermal process efficiencies (65 – 70 %) are possible. Due to their low solubility in supercritical water, the inorganics that are present in the biomass (up to 20 wt % of the dry matter of manure) can be separated and further used as fertilizer. The biomass is thus not only converted into an energy carrier, but it allows valuable substances contained in the biomass to be extracted and re-used. Furthermore, the process can be used for aqueous waste stream destruction.

---

The aim of this project at PSI was to develop a catalytic process that demonstrates the gasification of wet biomass to synthetic natural gas (SNG) in a continuously operating plant on a laboratory scale (throughput 1 kg/hr, which yields about 200 L<sub>SNG</sub>/hr with a thermal heating power of 1 kW<sub>th</sub> for a feed concentration of 40 wt %). Ideally, the pilot plant should be capable of conveying solid containing slurries.

Various catalysts were selected (some of them were synthesized in-house) and tested for their stability under hydrothermal conditions and for their tolerance towards inorganic salts (sulfate was chosen as model substance for these tests). The catalysts were characterized by numerous techniques (such as TG/FTIR, TPO/TPR, TOC, BET, XRD, XPS, ICP, TEM, HAADF-STEM, and SEM-EDXS). The biomass was analyzed for its constituents in order to get a reliable estimate of its energy content, which is essential for the calculation of the process economics. The lower heating value of concentrated swine manure was found to be 16.3 MJ/kg<sub>dry matter</sub>. Skeletal nickel catalysts, which are widely used in the industry due to their attractive price, gasified wood suspensions (conc. 10 – 30 wt %) in a batch reactor completely to SNG. The methane yield was 0.33 g<sub>CH<sub>4</sub></sub>/g<sub>wood, dry</sub>, which corresponds to the maximum yield governed by thermodynamics. Manure suspensions were also gasified in the hydrothermal environment. The highest methane yield achieved was only 0.21 g<sub>CH<sub>4</sub></sub>/g<sub>dry matter</sub>, which is 80 % of the maximum yield by thermodynamics. The reason for this were the salts present in the manure, which had not been separated before the experiments and caused the deactivation of the catalyst. Thus, the importance of an integrated salt separator in a demonstration plant cannot be emphasized enough.

The most promising catalyst systems (nickel, ruthenium) were tested for their activity and stability in the hydrothermal environment in a continuously operating test rig, where due to the applied pump only liquids could be fed. A mixture of five organic substances (formic and acetic acid, ethanol, phenol, and anisole) that approximates hydrolyzed wood served as feed. The skeletal nickel catalysts turned out to be active but not stable,



as they deactivated within a few hours. The attempt to stabilize them by co-doping of other metals (Ru, Mo, Cu) was not successful. Ru/TiO<sub>2</sub> was not active enough, but Ru/C completely gasified the mixture at high space velocities over a period of more than 200 hours; the product gas composition corresponded at all times to the the thermodynamic equilibrium composition. This catalyst was tested for its tolerance towards sulfate, which turned out to be low: the addition of a few ppm to the feed led to a deactivation within hours. The deactivation mechanism was identified as chemical poisoning. The poisoning species which is present *in-situ* in the hydrothermal environment (sulfate vs. sulfide) is not clear. The experimental evidence can be explained by both hypotheses.

A heating system for quartz capillaries rendered the visual examination of hydrothermal processes possible. Due to the required low amounts of feed material (a few hundred milligrams) and frequent capillary explosions, the usage of the system was discontinued.

The conveying of solid containing slurries on the laboratory scale turned out to remained to be an unsolved problem. Thus, only liquid type biomass can be fed with the process demonstration unit that was built. A suitable feedstock was found with palm oil pyrolysis condensate, a problematic waste stream very common in Indonesia, that has a high organic content (exceeding 40 wt %). Preliminary gasification experiments with ethanol and salt separation experiments with sodium sulfate were successful.



# Notation

## Greek Symbols

symbol	meaning	units
$\alpha_i$	slope of the linear regression of molar density vs. pressure of substance $i$ , as used in (3.2) on page 53	mol/(m <sup>3</sup> Pa)
$\beta_i$	intercept of the linear regression of molar density vs. pressure of substance $i$ , as used in (3.2) on page 53	mol/m <sup>3</sup>
$\Delta 2\theta$	peak width of X-Ray diffractogram	rad
$\Delta H_{\text{vap.}}$	enthalpy of vaporization	kJ/mol, kJ/kg
$\Delta_r H^\circ$	standard enthalpy of reaction	kJ/mol
$\varepsilon$	void fraction	[-]
$\varepsilon_r$	dielectric constant (relative dielectric permittivity)	[-]
$\eta$	dynamic viscosity	Pa s
$\eta_{\text{th.}}$	thermal process efficiency	[-]
$\theta$	half-angle of incidence of X-Ray	rad
$\lambda$	wave-length	nm
$\lambda_i$	thermal conductivity of substance $i$	W/(m K)
$\rho$	density	kg/m <sup>3</sup>
$\tau$	residence time	min.
$\chi$	electrical conductivity	$\mu\text{S/cm}$

## Roman Symbols

symbol	meaning	units
$a$	thermal diffusivity	$\text{m}^2/\text{s}$
$A_s$	specific surface area of active metal M, $A_s = w_M \cdot S$	$\text{m}^2/\text{g}_{\text{cat.}, \text{dry}}$
$B$	crystallite size determined by XRD	nm
CE	carbon equivalents	$\text{mg}_C/\text{L}$
$c_p$	heat capacity at constant pressure	$\text{kJ}/\text{mol}$ , $\text{kJ}/\text{kg}$
$D$	dispersion of metal M, $D = n_{M, \text{surface}}/n_{M, \text{tot.}}$	[-]
$d_i$	inner diameter	m
DOC	Dissolved Organic Carbon	$\text{mg}/\text{L}$
$\text{DOC}_{\text{aq.}}$	Dissolved Organic Carbon in the residual aqueous phase, $\text{DOC}_{\text{aq.}} = m_{C, \text{org.}}/m_{\text{solution}}$	$\text{mg}/\text{kg}$
GE	carbon gasification efficiency, $\text{GE} = n_{C, \text{gas}}/n_{C, \text{feed}}$	[-]
$\text{GE}_{100}$	carbon gasification efficiency scaled to 100 % carbon balance closure, $\text{GE}_{100} = \text{GE}/C_{\text{balance}}$	[-]
ha	hectares ( $= 10'000 \text{ m}^2$ )	
HHV	Higher Heating Value	$\text{MJ}/\text{kg}$
IC	Inorganic Carbon	$\text{mg}/\text{L}$
$\text{IC}_{\text{aq.}}$	Inorganic Carbon in the residual aqueous phase, $\text{IC}_{\text{aq.}} = m_{C, \text{inorg.}}/m_{\text{solution}}$	$\text{mg}/\text{kg}$
IL	Incineration Loss	%
IR	Incineration Residue	%
$k$	adsorption frequency factor (by BET)	[-]
$K_H^0$	Henry's law constant	$\text{mol}/(\text{Pa m}^3)$

---

symbol	meaning	units
$l$	crystallite size determined by oxygen chemisorption	nm
$L$	length of the preheater, as defined by (8.2) on page 235	m
LE	carbon liquefaction efficiency, $LE = (n_{C, H_2O} + n_{C, tars})/n_{C, feed}$	[-]
LHSV	liquid hourly space velocity $LHSV = V_{feed}/(V_{reactor} \text{ hr})$	$\text{hr}^{-1}$ , short for $L_{feed}/(L_{reactor} \text{ hr})$
LHV	Lower Heating Value	MJ/kg
$M_{Ru}$	molar mass of ruthenium (101.07 g/mol)	g/mol
$N_A$	Avogadro's number ( $= 6.022 \times 10^{23}/\text{mol}$ )	1/mol
$p_c$	critical pressure (22.1 MPa for water)	MPa
ppm	parts per million; if used for concentrations of inorganic salts, ppm is defined as $\text{mg}_{\text{salt}}/\text{kg}_{\text{mixture}}$ , e.g. $\text{mg}_{\text{Na}_2\text{SO}_4}/\text{kg}_{\text{mixture}}$ .	$(\text{mg}_{\text{salt}}/\text{kg}_{\text{mixture}})$
$R$	universal gas constant ( $= 8.314 \text{ Pa m}^3/(\text{K mol})$ )	$\text{Pa m}^3/(\text{K mol})$
$S$	active metal surface area	$\text{m}^2/\text{g}_{\text{active metal}}$
$S_{\text{BET}}$	BET surface area	$\text{m}^2/\text{g}_{\text{cat.}, \text{ dry}}$
$S_m$	occupation surface of one ads. molecule	$\text{m}^2$
$t$	time	s, min., hr
$T_c$	critical temperature (374 °C for water)	°C
TC	Total Carbon Content	mg/L
$TC_{\text{res.}}$	total carbon content in the residue by DC-190 (boat module), $TC_{\text{res.}} = m_C/m_{\text{res.}}$	mg/g <sub>res.</sub>
TOC	Total Organic Carbon	mg/L
$v$	velocity	m/s

---

symbol	meaning	units
$V_m$	volume of a monolayer of adsorbed $N_2$	$m^3$
$w$	weight fraction	[-]
WHSV <sup>a</sup>	weight hourly space velocity, $WHSV = m_{\text{biomass}} / (m_{\text{cat.,dry}} \text{ hr})$	$\text{hr}^{-1}$ , short for $\text{g}_{\text{biomass}} / (\text{g}_{\text{cat.,dry}} \text{ hr})$
$X_C$	dissolved carbon conversion, $X_C = 1 - (n_{C, H_2O} / n_{C, \text{feed}})$	[-]
$Y_{CH_4}$	methane yield $Y_{CH_4} = m_{CH_4} / m_{\text{biomass}}$	$\text{g}_{CH_4} / \text{g}_{\text{biomass}}$
$Y_{\text{gas}}$	gas yield at normal atmospheric conditions (1 atm, 0 °C) $Y_{\text{gas}} = V_{\text{gas}} / m_{\text{biomass}}$	$L / \text{g}_{\text{biomass}}$
$z_i$	compressibility factor of gas $i$	[-]

a. The WHSV is defined with respect to the flow rate of biomass, i.e. hydrocarbons, rather than with respect to the total flow rate. The feed concentration is thus incorporated.

## Abbreviations

abbreviation	meaning
5-HMF	5-hydroxymethylfurfural
BPR	Backpressure Regulator
CSTR	Continuous Stirred Tank Reactor
daf	dry ash free
DM	Dry Matter
EA	Elemental Analysis
EDXS	Energy Dispersive X-Ray Spectroscopy
EJ	exajoule ( $10^{18}$ J)

---

abbreviation	meaning
EPFL	Ecole Polytechnique Fédérale de Lausanne
ETH	Eidgenössische Technische Hochschule
EXAFS	Extended X-Ray Absorption Fine Structure
FID	Flame Ionization Detector
GC	Gas Chromatography
HAADF	High-Angular Annular Dark Field
HOPG	Highly Oriented Pyrolytic Graphite
HPIEC	High Pressure Ion Exchange Chromatography
HPLC	High Pressure Liquid Chromatography
KF	Karl Fischer
MIT	Massachusetts Institute of Technology
MS	Mass Spectrometry
PDU	Process Demonstration Unit
PJ	petajoule ( $10^{15}$ J)
PSA	Pressure Swing Adsorption
PSI	Paul Scherrer Institut
SCW	Supercritical Water
SCWG	Supercritical Water Gasification
SCWO	Supercritical Water Oxidation
SEM	Scanning Electron Microscopy
SLW	Synthetic Liquefied Wood (acetic acid, formic acid, ethanol, phenol, anisole)
SNG	Synthetic Natural Gas
(S)TEM	(Scanning) Transmission Electron Microscopy
TCD	Thermal Conductivity Detector
TG–FTIR	Thermogravimetry–Fourier Transform Infrared Spectroscopy
TM	Trockenmasse

---

---

abbreviation	meaning
TOX	Total Oxidation
TPO	Temperature Programmed Oxidation
TPR	Temperature Programmed Reduction
WGS(R)	Water Gas Shift (Reaction)
XPS	X-Ray Photoelectron Spectroscopy
XRD	X-Ray Diffraction

---



---

# Chapter 1: Introduction

## 1.1 Motivation – Positioning of the Hydrothermal Gasification

### 1.1.1 Biomass Potentials and Swiss Energy Consumption

Worldwide, biomass is the fourth largest energy resource after coal, oil, and natural gas [1], providing about 14 % of the world's energy needs [2]. The potential of biomass in the European Union (EU15) adds up to 6.75 EJ/yr (corresponding to 9 % of the EU energy consumption, 72 EJ/yr), out of which roughly half stems from wood, and 11 % or 750 PJ/yr from manure (remainder: straw and other crop residues) [3]. The amount of residual biomass in the European Union only is reported to exceed 200 Mt/yr [4], which equals to some 3000 PJ/yr.

In Switzerland, the ecological annual energy potential of biomass is around 122 PJ, out of which 45 PJ arise from wood (2003 used: 9 PJ). Manure has a substantial potential of 23 PJ which is largely untapped, as only 0.1 PJ or 0.4 % are used to produce energy today (mostly by anaerobic digestion). Also, industrial and household waste streams (27 PJ) could be used more extensively for energy production (2003 used: 19 PJ) [5]. Clearly, agricultural waste has the largest incremental potential of all types of biomass.

Opposed to these 122 PJ that could be used for the production of energy from biomass, the annual site energy<sup>1</sup> demand in Switzerland in 2003 was 875 PJ (200 PJ electricity, 400 PJ heating fuels, 275 PJ transportation fuels) [5]. Thus, if all manure were processed to fuels (at 65 % net effi-

---

1. site energy corresponds to the secondary energy, where losses due to transportation to the final user are deducted.

ciency), more than 5 % of all fuels used for transportation in Switzerland could be replaced. This figure seems small, but corresponds to savings of 460 million liters of gasoline<sup>2</sup> per year. In addition, emissions from the manure to the soil and the air can be avoided, waste biomass can be destroyed, and valuable nutrients recovered at the same time (see section 1.1.5).

### 1.1.2 Established Biomass Processing Technologies

Biomass is a generic term for a variety of different feedstocks. Hence, different technologies exhibit better or poorer performance when processing these different types of biomass. They can be classified into two main groups: thermal and biological conversion technologies [3].

Typical thermal conversion processes are:

- pyrolysis (where charcoal, bio-oil, or fuel gas are the target products)
- gasification (where fuel gas is the target product, which can be further processed to liquid fuels by Fischer–Tropsch synthesis, or to synthetic natural gas by methanation)
- combustion (where the generation of heat is the main product)

Typical biological conversion technologies are:

- fermentation (where ethanol and carbon dioxide are produced with yeast)
- anaerobic, bacterial digestion (where biogas is the main product).

For the production of fuel gas as a secondary energy carrier, high temperature gasification and anaerobic digestion are the main established technologies.

---

2. average energy content of gasoline: 32 MJ/L [6].

### 1.1.3 High Temperature Gasification

High temperature gasification is an option for dry feedstocks such as coal, straw, or wood. At the temperatures used (800 – 1000 °C), synthesis gas (H<sub>2</sub> and CO) is the main product. A methanation unit can be added if synthetic natural gas (SNG) is the target product rather than synthesis gas [7], or a Fischer–Tropsch unit for the production of liquids (synthetic diesel) [8]. For more information about SNG, refer to section 1.3. The efficiency of biomass to SNG is good (around 54 – 58 % for absolutely dry wood [9]), but the feedstock should be as dry as possible (max. 10 – 15 wt % water [10]). SNG production costs from dry wood by gasification are 9 – 10 €/GJ<sub>SNG</sub><sup>3</sup> for a 100 MW<sub>th</sub> plant [10], no calculations for smaller plants could be found. However, for wet biomass, the efficiency drops drastically due to the heat of evaporation (2.4 MJ/kg at atmospheric conditions).

### 1.1.4 Anaerobic Digestion

For wet types of biomass, anaerobic digestion is a proven technology. A drawback is the very long residence time (typically 10 to 30 days) of the feedstock to yield a reasonable gas production. Thus, it is limited to small-scale, decentralized applications. To process the manure on large cattle farms, huge digesters would be necessary. A farm with 10'000 cattle (typical farm size in Canada and the US [11]) produces 260 tons of manure in just one day (average cattle mass 450 kg, producing manure at 58 kg/1000 kg cattle) [12]. Over a typical 20 days anaerobic digestion cycle, this sums to more than 5000 m<sup>3</sup>, illustrating the required size of a digester.

In addition, only 30 – 60 % of the solid input is typically converted to biogas, while the rest transforms into a solid residue, which needs to be disposed of. In order to obtain a gas that meets the requirements for

---

3. Mozzafarian et al. originally reported 8 – 9 €/GJ<sub>SNG</sub> for a process efficiency of 65 % for wood to SNG. Duret and co-workers presented a more realistic calculation and reported an efficiency of 54 – 58 % [9]. Thus, the costs reported by Mozzafarian et al. were corrected from 65 % to 58 %.

injection into the gas grid, the biogas (around 55 – 75 vol %  $\text{CH}_4$ , 25 – 45 vol %  $\text{CO}_2$ , with traces of  $\text{H}_2\text{S}$ ,  $\text{NH}_3$ , and other, often odorous substances) needs to be cleaned and upgraded.

### 1.1.5 Hydrothermal Gasification

The hydrothermal gasification is a promising new route for most kinds of wet biomass streams such as manure, sewage sludge, and wet forestry residues. Unlike anaerobic digestion, it fully converts all organic feedstock leaving no residue. Thus, not only can the feedstock be converted to gas, but the waste problem is simultaneously solved as well.

The hydrothermal gasification concept developed at the Paul Scherrer Institut (PSI) targets a more holistic usage of the wet biomass' contents, shown in Figure 1.1. The organic part is fully decomposed to synthetic natural gas (used for heating purposes, generation of electricity, or as fuel), the inorganic nutrients (N, P, K, Mg, Ca) are recovered in a rather pure and concentrated brine (to be used as fertilizer) and possible toxic or bioactive substances such as prions, hormones, or antibiotics are fully destroyed. The water content is leaving the plant as an aqueous stream virtually free of dissolved organics. It can be fed to the municipal waste water treatment plant without any further purification step.

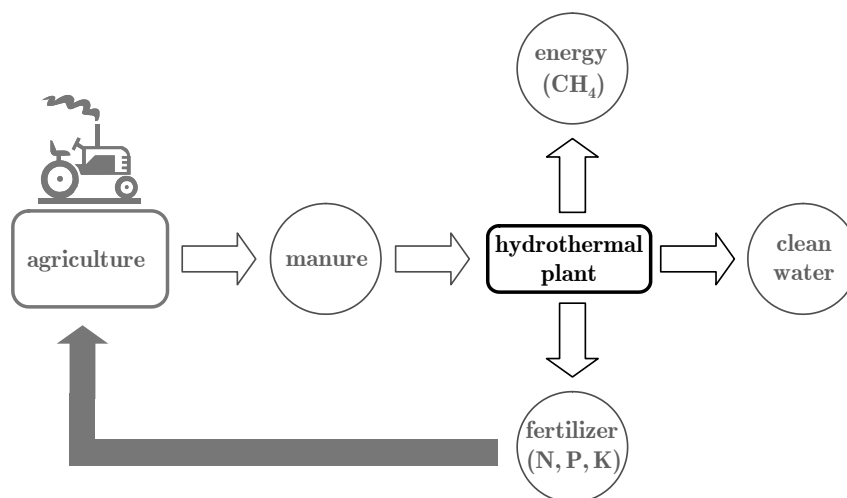


Figure 1.1: The concept proposes a holistic usage of the biomass, here in the case of manure.

Within the process, the nutrient salts can be fully recovered and used for fertilization. In contrast, if manure is directly distributed onto the fields as fertilizer, only about 1/3 of the total nitrogen contained is transferred to the plants as a fertilizing agent, while more than 2/3 are lost to the air or to the soil [13], as is depicted in Figure 1.2.

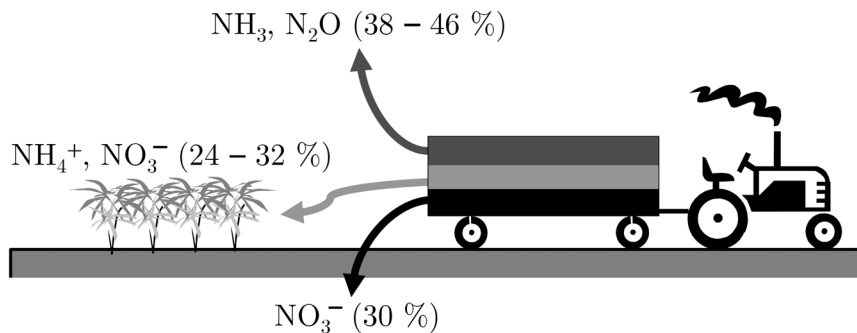


Figure 1.2: Distribution of the nitrogen containing compounds to air, plants, and soil. Only 1/3 is delivered as nutrient to plants.

The technologies are compared in the following subsection, while a more technical description of the process idea of the hydrothermal gasification is described in section 1.2.

### 1.1.6 Comparison of the Technologies

Yoshida and co-workers have carried out a comparison of several biomass processing technologies [14]. They conclude that from an energetic point of view, supercritical water gasification (SCWG, or hydrothermal gasification), is the technology of choice for all wet types of biomass. However, this new technology is still at a stage of development.

The efficiencies of the three technologies (high temperature gasification, anaerobic digestion and hydrothermal gasification) for the generation of electricity and the generation of heat are depicted in Figure 1.3. The total efficiency is defined as the energy content of the product divided by the energy content of all inputs, including the feedstock and the electricity for the biomass production. It can be clearly seen that for biomass with a moisture content exceeding 40 wt %, supercritical water gasification is superior to any of the other technologies.

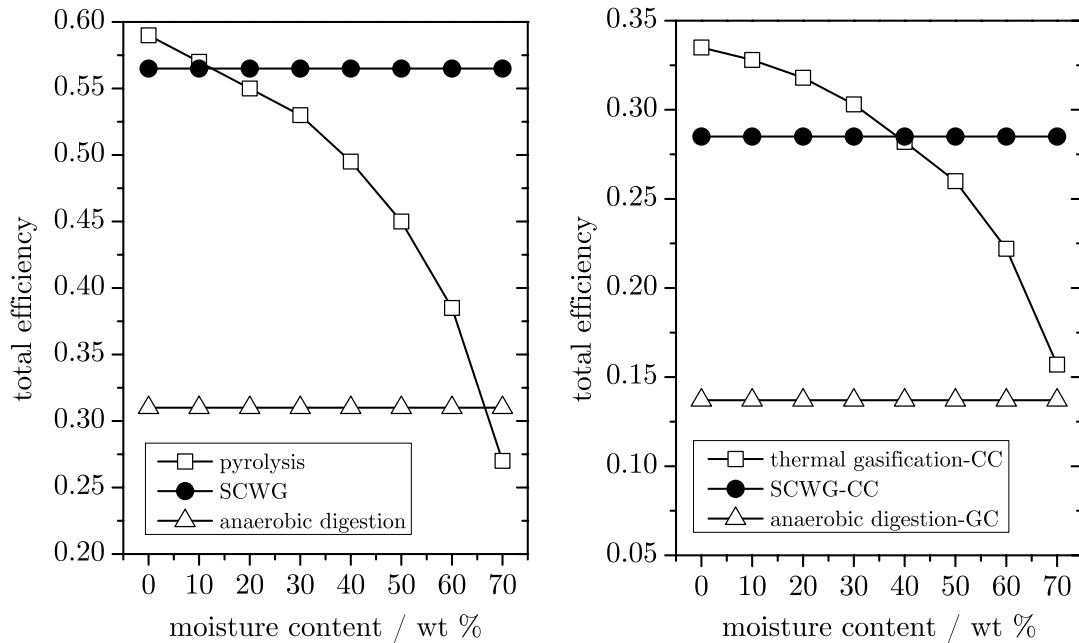


Figure 1.3: Comparison of the efficiency of thermal processing, supercritical water gasification and anaerobic digestion for variable feed stock moisture content. Left: total efficiency of heat utilization process. Right: total efficiency of a combined cycle (thermal and supercritical water gasification + steam turbine, anaerobic digestion + gas combustion). Data from Yoshida et al. [14]

Thermal process efficiencies  $\eta_{\text{th}}$  as high as 70 % for wood-to-methane can be expected for a hydrothermal gasification plant (size: 20 MW<sub>th</sub>), yielding an SNG price of around 10 USD/GJ<sub>SNG</sub> [15-17]. Matsumura calculated the thermal efficiency of producing natural gas from water hyacinths and presented similar figures ( $\eta_{\text{th}} = 65$  %). He also compared it to biomethanation (anaerobic digestion,  $\eta_{\text{th}} = 49$  %<sup>4</sup>), for which huge fermenters and long residence times ( $\tau$  around 20 days) are required, leaving solid residues that need to be disposed of [18].

A further comparison of the three technologies can be found in Table 1.1. If the hydrothermal process can be developed to reach a commercial

4. Matsumura assumed that the product gas consisted of 100 vol % CH<sub>4</sub>. A concentration of 60 vol % is more realistic. Then, gas cleaning is an extra step, additionally lowering the thermal efficiency to 25 – 30 %, which is in better agreement with data from other researchers, such as from Yoshida et al. [14].

stage, a significant contribution to the use of wet biomass for the production of a secondary energy carrier can be made. However, a few challenges need yet to be solved (outlined in section 1.6).

Table 1.1: Qualitative comparison of high temperature gasification, anaerobic digestion, and hydrothermal gasification.

critierion	gasification (plus methanation)	anaerobic digestion	hydrothermal gasification
typical feeds	wood, straw ( $w_{\text{water}} < 15$ wt %)	manure, household residues, sewage sludge	most wet types ( $w_{\text{water}} > 60$ wt %)
process efficiency to SNG	54 – 58 % <sup>a</sup>	25 – 35 % ( $\leq 8$ wt % DM) [14]	65 – 70 % [15-17]
typical residence times	< 1 min.	20 days [14]	< 1 min.
establishment / readiness	good <sup>b</sup>	very good	not yet, PDU (1 MW <sub>th.</sub> ) expected for 2010.
SNG cost	9 – 10 €/GJ <sub>SNG</sub> <sup>c</sup>	N/A	10 USD/GJ <sub>SNG</sub> <sup>d</sup>
pro	high efficiency for dry biomass	established, commercialized	full conversion, high efficiency, no residues
contra	low efficiency for wet biomass	residues, residence time, plant size, efficiency	technical barriers yet to be solved

a. Based on absolutely dry wood [9].

b. PDU built in Güssing, AT; plant size ca. 2 MW<sub>SNG</sub>.

c. Based on process efficiency 58 %, 2.3€/GJ<sub>wood</sub>, and 100 MW<sub>th.</sub> plant size [10].

d. Calculated 2002 based on 70 wt % efficiency, a wood price of 3.5 USD/GJ, and 20 MW<sub>th.</sub> plant size, as outlined in [15-17]; corresponded to ~9.5 €/GJ<sub>SNG</sub>.

## 1.2 Process Idea of Hydrothermal Gasification

"Hydrothermal" refers to an aqueous system at elevated pressures and temperatures, especially near the critical point of water (374 °C, 22.1 MPa) or above it. Near-critical and supercritical water provides an interesting environment to carry out chemical reactions (see section 1.7). In particular, hydrolytic and reforming reactions involving water both as reactant and as solvent look promising for converting biomass into liquid and gaseous fuels. The energy requirement for bringing water to supercritical conditions is less than for evaporating and superheating water to the same temperature at subcritical pressures.

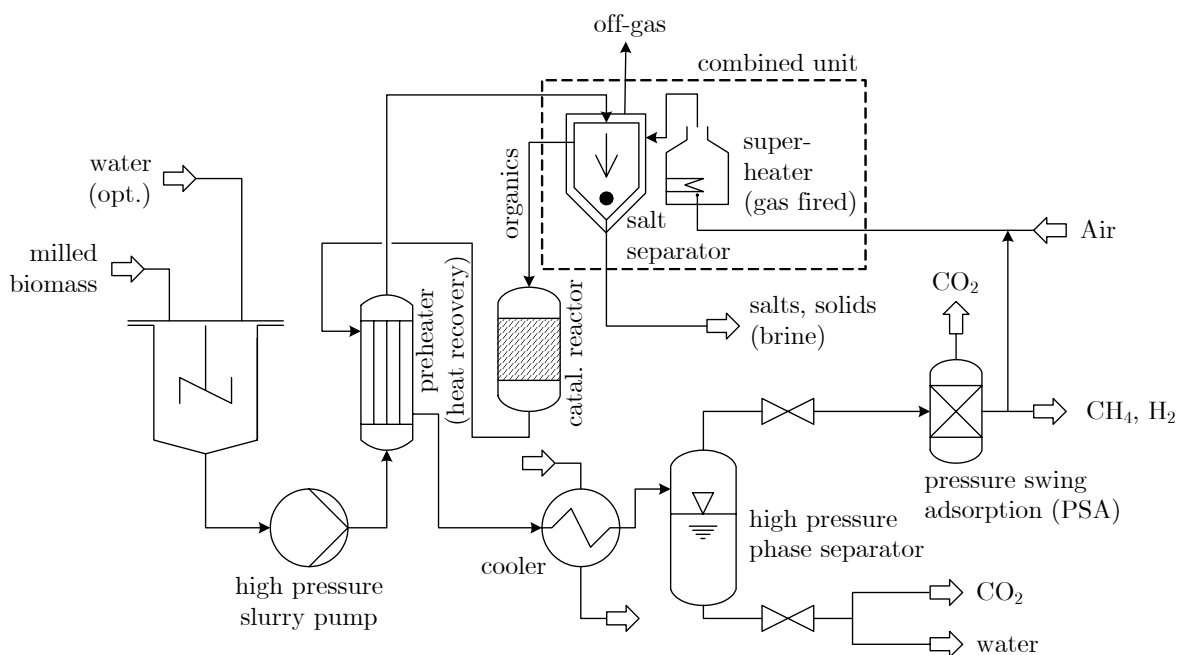


Figure 1.4: Simplified process scheme of a hydrothermal gasification plant.

In contrast to the conventional gasification route with subsequent gas cleaning (tar removal) and methanation, the hydrothermal process – having emerged over the last two decades and having been initiated by the pioneering work of Modell at MIT [19] – makes the necessity to dry the feedstock (energetically intensive) prior to thermal conversion obsolete, allowing for the high thermal process efficiencies described in section 1.1.6. In the hydrothermal process, the wet biomass is milled,



pumped and fed into a preheater, where it is hydrolyzed at temperatures around 350 °C. The inorganic constituents are separated in a salt separator, the organic feed stream is superheated and then gasified in a catalytic reactor. The endothermic gasification step and the exothermic methanation step are carried out in one reactor, leading to a slightly exothermic overall reaction. After the catalytic reactor, the fluid product phase is cooled, separated into a liquid and a gaseous phase and expanded. The process is depicted in Figure 1.4.

### 1.3 Synthetic Natural Gas (SNG) – a Viable Option

Biomass has a great potential as a renewable feedstock for producing energy carriers such as fuels or electricity. For the former, synthetic natural gas (SNG, consisting mainly of methane) is an interesting option, as natural gas is an established energy carrier and thus the infrastructure for its use exists already today. For the latter, SNG can be used in gas engines or gas turbines for power generation. Upon its rather clean combustion, it releases few atmospheric pollutants and significantly less carbon dioxide per unit mass than fossil fuels. If generated from renewable biomass, it is even carbon dioxide neutral. Used as a transportation fuel – the technology is available today with compressed natural gas vehicles – a significant contribution to the fossil CO<sub>2</sub> reduction target can be achieved (Kyoto protocol: compared to 1990, –10 % CO<sub>2</sub> emissions in 2010 from fossil fuels in Switzerland [20]). The superior environmental performance of SNG was published in a comprehensive comparison of different biofuel options [21]. Yoshida and co-workers concluded that a supercritical water gasification combined cycle would be the most efficient for high moisture content biomass [14]. The use of SNG would also allow countries to become less dependent on imported fossil fuels.

SNG from a hydrothermal gasification plant is produced at high pressures, together with the side-product CO<sub>2</sub>. If the gas and the liquid product phases are separated under pressure (typically around 30 MPa),

most of the carbon dioxide is dissolved in the liquid phase (according to the solubility) and leaves the system with that stream. The gas phase is enriched in methane, and the residual CO<sub>2</sub> can be separated in a pressure swing adsorption column (PSA). The CH<sub>4</sub>/CO<sub>2</sub> separation under pressure is an advantage over the state of the art, solvent intensive gas sweetening processes (amine wash) used to separate the two gases in natural gas mixtures [22]. Additionally, the resulting SNG is available at pressures around 15 MPa, and can be fed into the existing gas grid without the use of compressors; it can even be expanded to ~7 MPa before injection into the high pressure grid.

It has to be noted that methane losses can occur during the production and storage of SNG, mainly during the purification by pressure swing adsorption (around 3 %) [23]. The figure could be reduced to around 0.1 % by using low pressure membrane technology, which, however, is not yet fully developed and expensive. The loss from pipelines is small, 0.016 % per 1000 km [23]. However, methane is a stronger greenhouse gas than carbon dioxide, and the losses should be considered for the economic and ecological evaluation of SNG. A life-cycle assessment carried out at PSI concluded that SNG still has the best ecological performance among several types of fuels if the consumption of fossil resources is strongly weighted [24].

## 1.4 Aim of the project

The aim of the project was to demonstrate the technical feasibility of a continuously operating hydrothermal gasification unit. This goal was subdivided into several objectives:

- Screening and synthesis of catalysts capable of gasifying biomass at high feed concentrations and methanating the gaseous products (chapter 6), and their analysis and characterization with adequate methods (chapter 4).

- 
- Choice of the most promising method to separate the inorganics (on stream) from the organics.
  - Identification of the manure's constituents for a reliable estimation of its heating value (section 5.3). Most analyses described in the literature only referred to incineration residue that do not allow such an estimation.
  - Identification of reaction intermediates and choice of a liquid biomass model mixture that adequately represents hydrolyzed real woody biomass as it is expected to enter the catalytic reactor downstream of the superheater (see section 5.2).
  - Testing and characterization of promising catalysts in view of long-term stability and tolerance towards salts during continuous operation in the hydrothermal environment (chapter 7).
  - Design and build-up of a process demonstration unit (PDU) with incorporated salt separation and feeder for real biomass (in contrast to using model compounds), outlined in chapter 8.
  - Identification of operating parameters ensuring good liquefaction of biomass to design the preheater in the PDU (section 8.2).

The approach to and the results of each objective are given in the corresponding chapters. The most important results are concluded and listed in chapter 9, where also recommendations for future research are given.

## 1.5 Possible Feedstocks for SCWG

A wide range of feedstocks are suitable for hydrothermal gasification. Wet biomass ( $w_{\text{water}} > 60$  wt %) is particularly appropriate, as it cannot be efficiently processed with conventional techniques, and its water content is the actual reaction media. The methane production depends on the carbon-to-hydrogen-to-oxygen ratio: A lower (O/C) and a higher (H/C)

will increase the  $\text{CH}_4/\text{CO}_2$  product gas ratio [25].

Feedstocks with a high content of inorganics will yield less gas per unit mass of feedstock, i.e. the thermal efficiency of the process will be lower. However, if the inorganics can be separated and collected in a concentrated form, and potentially be used for other applications, then the benefit of processing such a feedstream in a hydrothermal plant cannot only be seen in terms of efficiency, but the overall benefit of the plant (energy generation by solving a waste problem) should be considered.

Typical feedstocks could include (depending on biomass waste streams produced in a specific country):

- wet forestry residues
- manure
- sewage sludge
- pyrolysis condensates - a waste stream very common in Indonesia (see section 5.4)

There exists also the possibility to specifically grow certain types of wet biomass instead of using waste streams. Water hyacinth (*Eichhornia crassipes*) for instance could be produced at over 150 tons/(ha yr) of dry organic matter, or cattails (*Typha* sp.) with almost 100 tons/ha in 7 months [26].

The reasonable size of a hydrothermal plant processing biomass waste streams is largely affected by the transportation cost of the feedstock. In the case of manure, it might not be feasible to carry it over wide distances (in Switzerland, more than 10 kms are not feasible<sup>5</sup> [13]), as the water content of raw manure is too high (typically > 95 wt % prior to concentration over a curved screen). Thus, for this type of feed, smaller ( $P \sim 2 \text{ MW}_{\text{th}}$ ) and decentralized plants are to be considered. However, in

---

5. Fines are imposed by Swiss law if manure is transported over more than 10 kms (CHF 500 per DGVE (Dünergrossvieheinheit); 1 DGVE corresponding to the nutrients contained in dung and manure annually produced on average by a cow that weighs 600 kg; i.e. 105 kg N and 15 kg P) [27].

other countries, the situation might be different. Examples are Dodge City (KA, USA) where about 5 million cattle are confined in a small area, or Lethbridge (Alberta, Canada, about 1 million cattle), leading to a substantial waste problem. In the latter region, manure pipelines originating from huge cattle farms are projected [12]. There, larger SCWG plants could be realized and conveniently used to render the farms self sufficient in terms of their energy demand. Also in the case of sewage sludge, larger plants are possible (up to 20 MW<sub>th.</sub>), e.g. to process waste streams originating from a chemical plant, other industrial zones, or municipal sewage from big urban agglomerations.

## 1.6 Process Challenges

As promising as the catalytic hydrothermal gasification is – a few problems need to be tackled and solved in order to commercialize the technology:

High pressures are necessary for a hydrothermal application. Whereas commercial products are available to pump slurries with solid concentrations of up to 40 wt % reliably to pressures exceeding 30 MPa (throughput 50 – 100 kg/hr and more), it was a major challenge to find a slurry pump operating on the laboratory scale, with throughputs around 1 kg/hr (refer to section 8.4).

Due to the corrosive nature of inorganics contained in certain types of biomass, e.g. chloride in manure, the plant's material must be corrosion resistant (stainless steel with special coatings, titanium, Hastelloy or Inconel), especially for operations below the critical temperature. Hastelloy and Inconel are less suited as the Ni is readily leached out in supercritical water in presence of Cl<sup>-</sup> ions under oxidizing conditions (i.e. in SCWO applications) [28]. For SCWG, a general prediction is difficult. These specialty materials increase the investment costs (and therefore increases the minimum size of a plant in order to operate economically).

The parts which are most prone to corrosion are the heat exchanger, where the biomass is liquefied (operated in the subcritical regime), and the salt separating vessel. Downstream of this apparatus, most inorganics are separated (based on their solubility), and the focus should be more on hydrogen embrittlement.

Whereas for the heat exchanger the main problem is corrosion (which can be solved with state-of-the-art engineering [29]), the same problem arises for the salt separator, but there its design is an additional challenge, and further research is needed to obtain good separation and a reliable operation. Currently, at the Paul Scherrer Institut and the Massachusetts Institute of Technology, this problem is the subject of several studies [30].

The heart of a catalytic hydrothermal gasification plant is the catalyst. It needs to be stable in the hydrothermal environment (the support as well as the active metal), exhibit a reasonable activity, and be selective towards methane generation, if SNG is the desired product. The price of the catalyst influences the investment cost of the plant. However, if regeneratable, this figure can be significantly lowered, and in comparison with the cost for the rest of the plant, the investment for the catalyst might not be a dominating factor, not even for a precious metal catalyst. A corresponding assessment is currently carried out at PSI and EPFL.

Catalysis and salt separation are thus the two main challenges yet to be solved before a commercialization of the technology can be accomplished. This work can be understood as a contribution to find a suitable catalyst for the hydrothermal SNG process.

## 1.7 Properties of Water at Elevated Pressures and Temperatures

### 1.7.1 Critical Point and Supercritical Phase Behavior

The phase behavior of pure water is displayed in Figure 1.5. The end of the liquid/vapor phase boundary is reached at the critical point at  $T_c = 374\text{ }^\circ\text{C}$  and  $p_c = 22.1\text{ MPa}$ .

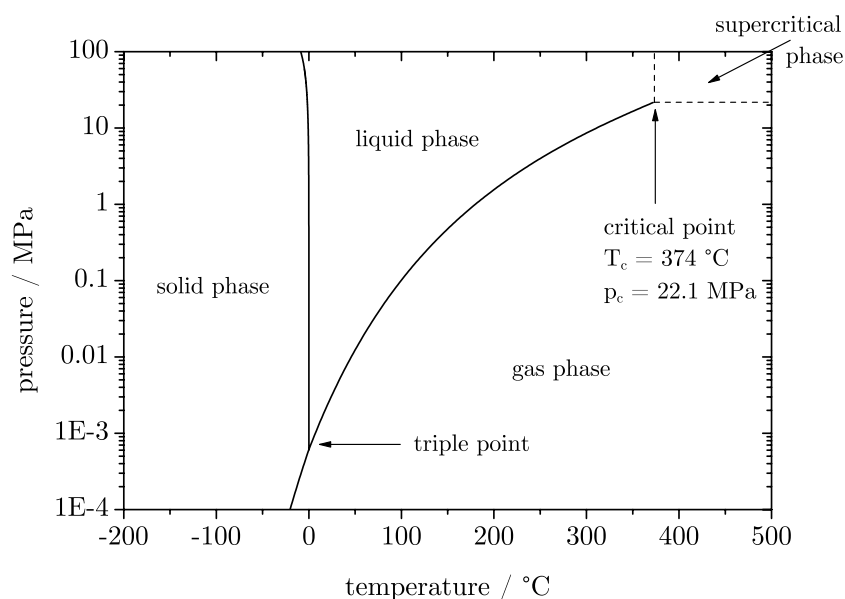


Figure 1.5: Pressure vs. temperature phase diagram of pure water. Note the logarithmic pressure scale. Above  $374\text{ }^\circ\text{C}$  and  $22.1\text{ MPa}$ , there is only the supercritical phase.

Above the critical point, water exists as a homogeneous fluid phase, with drastically changed physical properties, as will be described later in this section. The absence of a phase boundary can significantly reduce mass-transfer limitations in heterogeneous catalysis [31].

### 1.7.2 Ion Product and Dielectric Constant $\epsilon_r$

While water at ambient conditions exhibits its well-known behavior such as dissolving salts and being immiscible with apolar solvents due to its high polarity, its properties change drastically from the sub-critical to the

supercritical state. The ion product is reduced from  $10^{-14}$  (mol/kg)<sup>2</sup> at ambient conditions to below  $10^{-20}$  (mol/kg)<sup>2</sup> in supercritical water [32]. The dielectric constant (relative permittivity)  $\epsilon_r$  decreases with increasing temperature, and drops around the (pseudo-)critical point due to the diminishing hydrogen bonds, as depicted in Figure 1.6 [33]. In the window of catalytic hydrothermal gasification temperatures, 300 °C to 500 °C,  $\epsilon_r$  decreases from  $\sim 20$  (acetone at ambient conditions) to below 3, having similar solvation properties as the highly apolar n-hexane.

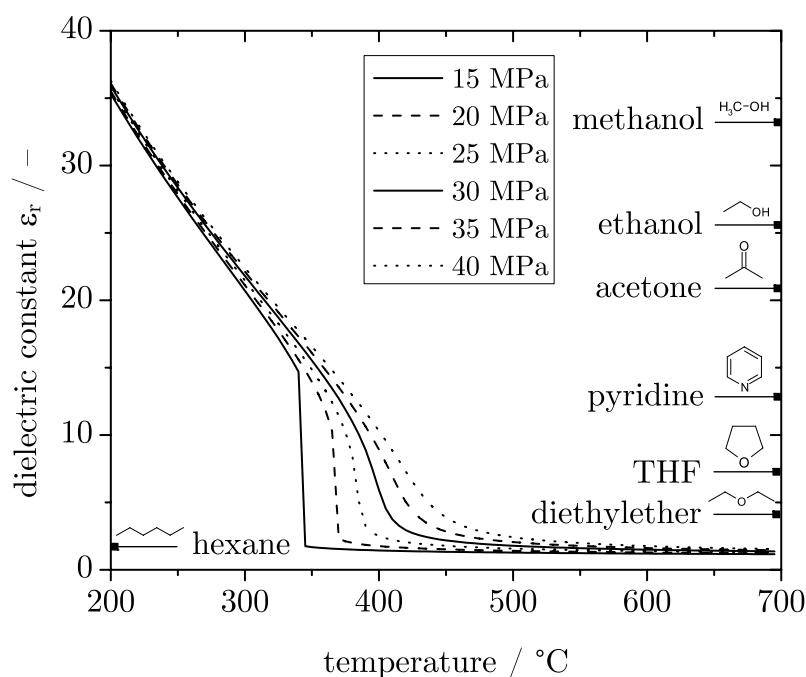


Figure 1.6: Dielectric constant of water at various pressures (15 to 40 MPa) and temperatures (200 to 700 °C). As a reference, the dielectric constant of well-known solvents at standard conditions are included [34]. THF = tetrahydrofuran.

Supercritical water is more like an organic solvent, with high miscibility with apolar substances and low salt solubility. This unique feature is the basis for two advantages of the hydrothermal process:

- Salt separation by increasing the temperature prior to gasification (implemented in the process demonstration unit presented in chapter 8).



- Tar-free gasification, as apolar tar-precursors are dissolved in supercritical water and gasified on the catalyst (see section 2.4).

### 1.7.3 Density

The water density at various pressures as a function of temperature is depicted in Figure 1.7 [35]. In the two phase region, where  $T < T_c$  and  $p < p_c$ , the density drops discontinuously at the boiling point, i.e. at a pressure of 15 MPa, evaporation takes place at a temperature of 340 °C, and the density drops from 600 kg/m<sup>3</sup> (liquid) to 100 kg/m<sup>3</sup> (vapor). Above the critical point ( $T > T_c$ , and  $p > p_c$ ), the transition from liquid to fluidic is continuous, as  $\Delta H_{\text{vap.}} = 0$ .

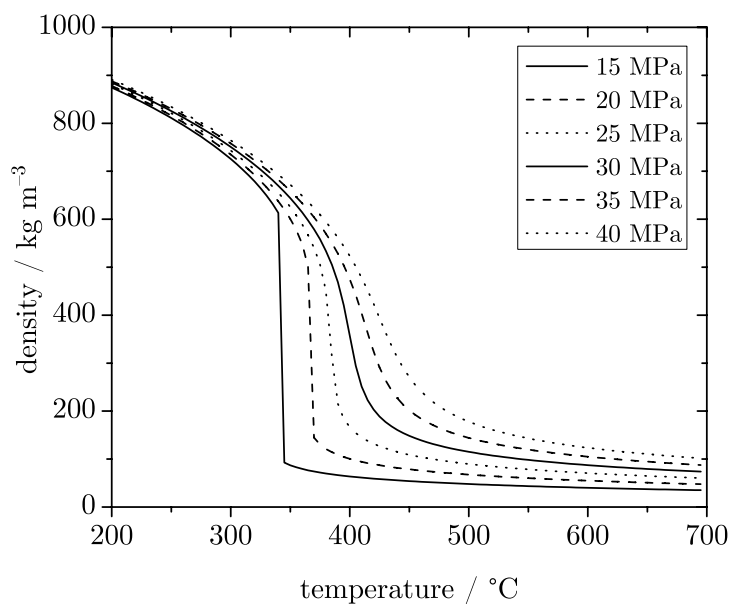


Figure 1.7: Density of water at various temperatures and pressures from 15 to 40 MPa. Below 22.1 MPa, there is a discontinuity due to the liquid/vapor phase boundary (evaporation – condensation).

The dissolving power of a fluid is exponentially dependent on its density [36]. The density of supercritical water can be tuned by a change in pressure or temperature; the effect is largest in the vicinity of the critical point. While the dissolving power of supercritical water is generally lower than the one of liquid water, it is the combination with the high gas miscibility that makes it such an excellent reaction medium.

### 1.7.4 Enthalpy and Heat Capacity at Constant Pressure $c_p$

As described in section 1.7.3 on page 17, there is no evaporation–condensation beyond the critical point. Thus, the enthalpy is continuous as well, see Figure 1.8. The transition at higher pressures is energetically less demanding. The heat capacity  $c_p$  has a significant peak around the critical point as a result of the enthalpy discontinuity, generally from 20 to 30 MPa.

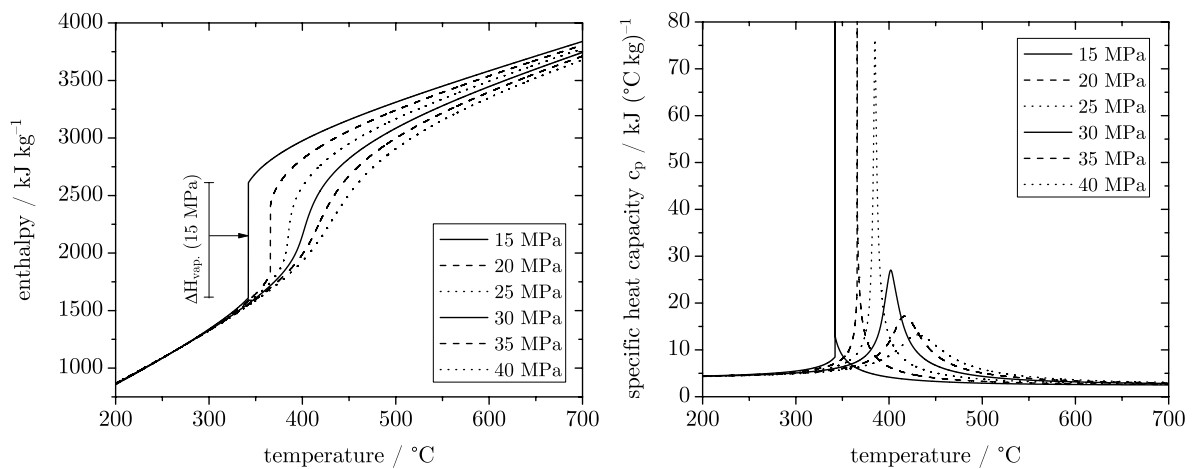


Figure 1.8: Left: Enthalpy of water at various temperatures and pressures from 15 to 40 MPa. Below 22.1 MPa there is a discontinuity due to the liquid/vapor phase boundary ( $\Delta H_{\text{vap.}}$ ). Right: Heat capacity  $c_p$  of water at various temperatures and pressures ( $c_p \rightarrow \infty$  at  $T_{\text{vap.}}$  for  $p < p_c$ ).

The combination of these properties of supercritical water has led to its various applications, of which a good overview was presented by Kritzer [37] (see Table 1.2):

Table 1.2: Applications of supercritical water.

---

application	properties exploited	refs.
chemical reactions	high solvency for organics, tunable conc. of $H^+$ and $OH^-$	[31, 38-41]
hydrothermal syntheses	solubilities	[42, 43]
waste oxidation	high solvency for organics and oxygen	[44, 45]
radioactive waste reduction	high solvency for organics and oxygen; solubilities	[46-48]
biomass conversion	high solvency for organics	[4, 17, 49-54]
synthesis of nanoparticles	low solubility of salts	[55-57]

---



# Chapter 2: Literature Review and Wood Reaction Network

## 2.1 Present Status of Research on Hydrothermal Gasification of Biomass

Pioneering work in the field of catalytic hydrothermal biomass gasification has been carried out at the Pacific Northwest National Laboratory (by Elliott, Sealock Jr., and co-workers) and resulted in the TEES process (Thermochemical Environmental Energy System) [58, 59]. Typical TEES conditions are in the subcritical region (350 °C, 20 MPa) with complex chemistry, including pyrolysis, steam reforming, hydrogenation, methanation and water-gas-shift (refer to section 2.2 and 2.4 for details of these reactions).

Many researchers carried out experiments in hydrothermal water (sub- or supercritical) with glucose or other simple compounds rather than taking real biomass as feed. On the one hand they used model compounds to overcome the feeding problem, as these substances are solutions, on the other hand to investigate the decomposition pathways of single molecules. These results are outlined in section 2.2 – 2.4. Therefore, experimental data with real biomass are less available than data from model compounds. Nonetheless, some works on hydrothermal gasification with real biomass as feed shall be presented here (a summary is given in Table 2.1). Sealock Jr. et al. also carried out experiments at supercritical conditions (not only at subcritical TEES conditions), and attained a maximum methane yield of 0.22 g CH<sub>4</sub>/g wood (with 33 vol % CH<sub>4</sub> in the product gas) using a stirred batch autoclave with a stainless steel liner, operated at 450 °C and 34 MPa for 150 min., with Harshaw-Ni as catalyst [59].

Yoshida et al. gasified wood of unspecified origin in a stainless steel batch

Table 2.1: Overview of gasification experiments reported in the literature with real biomass as feedstock (sorted acc. to publishing date; own experiments and publications are excluded).

feed	reactor	T °C	p MPa	ref.
wood flour	stirred autoclave	450	34	[59]
starch + sewage sludge, starch + poplar wood dust	flow type	650	28	[60]
potato starch, wood sawdust	flow type	685	28	[61]
straw, wood, sewage sludge	tumbling autoclave	450 – 500	31.5 – 35	[4]
wood	continuous	650	N/A	[62]
baby food	stirred autoclave / CSTR	330 – 410	30 – 50	[63]
wood	batch reactor	400	25	[64]
dairy manure, distillers' dried grains and solubles (DDG&S)	flow type (fixed bed)	350	21	[65]
waste water	flow type	360	20	[66-69]
phyto- and zoomass	stirred autoclave / CSTR	500	30	[70]
wood sawdust	batch autoclave	500	27	[71]
pine sawdust and wastepaper	batch autoclave	225	N/A	[72]
corn and clover grass	flow type	625 – 700	25	[73, 74]

reactor at supercritical conditions (400 °C, 25 MPa, residence time 25 min.) and attained a methane yield of 0.112 g CH<sub>4</sub> per gram of wood, with a methane volume fraction of 0.28 in the product gas [64].

Schmieder et al. reported on the results using a tumbling batch autoclave, lined with Inconel 625, operated at 450 – 500 °C and 31.5 – 35 MPa, reaction time 120 min., with three feedstocks: wood, straw, and manure, at very dilute concentrations (i.e. wood at 4900 ppm C, corresponding to about 1 wt % wood; sewage sludge even at 2300 ppm C) [4]. They report acceptable gas yields (80 – 90 %), but had low concentrations of CH<sub>4</sub> (less than 20 vol %) in the product gas.

Hong and Spritzer used a continuously operated reactor made of stainless steel to study the partial oxidation of wood at a concentration of 9 wt % in supercritical water [62]. Two modes of operation, autothermal (where ethanol and air were added in order to produce heat by partial oxidation) and allothermal, were tested. The allothermal mode yielded higher methane concentrations in the product gas, around 34 vol % at 650 °C, and is thus according to Hong favored for the production of SNG.

Antal Jr. and co-workers studied the gasification of several types of biomass in a tubular flow reactor at 685 °C catalyst bed temperature and 28 MPa [61]. A gel-like mixture of sawdust (11 wt %) and cornstarch (4 wt %) yielded 17 % CH<sub>4</sub>, while 43 % hydrogen were formed. Slower heating rates favored the formation of refractory compounds, resulting in more methane production.

Similarly, Xu and Antal Jr. fed mixtures of starch and sewage sludge (conc. 7.7 wt %), and mixtures of starch and poplar wood dust (conc. 11.5 wt %) to a flow reactor (packed with coconut shell activated carbon) by means of a cement pump. They gasified the biomass at 650 °C and 28 MPa at 98 – 99 % conversion and received a gas rich in hydrogen (42 – 57 vol %) and carbon dioxide (33 – 39 vol %), with some methane (6 – 17 vol %) and traces of carbon monoxide (1 – 4 vol %).

Kruse and Gawlik gasified baby food (conc. 10.8 wt %, mainly carrots and potatoes, representing wastes from the food industry) non-catalytically in a stirred batch reactor (Ni base alloy Nimonic 90, preheated with water and biomass fed cold with a screw press) at Forschungszentrum Karlsruhe and received high amounts of CO<sub>2</sub> (1.05 mol/kg<sub>biomass</sub>) and H<sub>2</sub> (0.5 mol/kg<sub>biomass</sub>), and few CH<sub>4</sub> (0.04 mol/kg<sub>biomass</sub>) at 410 °C and 30 MPa. The gas yield at 40 and 50 MPa was lower [63].

Kruse and other researchers also gasified phyto- and zoomass (conc. 5 wt %, some exp. with the addition 0.5 wt % K<sub>2</sub>CO<sub>3</sub>) in a continuous stirred tank reactor made of Inconel 625 at 500 °C and 30 MPa [70]. They reported that the gas yield from zoomass was significantly lower than from phytomass, but could not yet state a scientific explanation for this observation (further experiments were planned). After the runs with zoomass, the reactor showed signs of corrosion. They suspected that the sul-

fur-containing amino acids within the zoomass were responsible for this corrosion, and that the sulfur species were reduced to  $\text{H}_2\text{S}$  in the hydrothermal environment.

At the same institute, D'Jesús and co-workers carried out gasification experiments in supercritical water with corn and clover grass (conc. 5 wt %), in an continuous plug<sup>1</sup> flow reactor made of Inconel 625 (the feed was pressed out of a pressure tank) at 625 – 700 °C and 25 MPa ( $\text{KHCO}_3$  added) [74]. The gasification yield was 82 % (92 % with 500 ppm  $\text{KHCO}_3$ ) for corn starch at 700 °C, but only 40 % at 625 °C, illustrating the strong effect of temperature. Clover grass could be gasified at a yield of 88 % (700 °C), and corn silage nearly completely at sufficiently large space times (9 min., calculated under ambient input-output conditions). In an earlier paper, they had reported the gasification yield of corn silage as a function of concentration: the yield decreased from 100 % at a concentration of 5 wt % to 84 % at a concentration of 10 wt %, and to 82 % at a concentration of 20 wt %, accompanied by an increase of the carbon content in the aqueous product phase (from 1000 to 4500 ppm) [75]. D'Jesús and colleagues also determined the rate of corn silage gasification (at a fixed concentration of 5 wt %) in their plug flow reactor to follow approximatively kinetics of order zero, thus the corn silage gasification yield increased linearly with residence time, up to a certain maximum value (which was dependent on temperature) [73]. This maximum value, however, could not be predicted by the model, and thus it can only be used to describe the initial rate of gasification.

Elliott et al. have carried out gasification experiments in a fixed bed tubular bench-scale and microscale reactor ( $V_{\text{reactor}} = 0.9 \text{ L}$  and 40 mL, respectively; catalyst: Ru/C, no manufacturer or metal loading reported) with manure (dissolved org. carbon conc. 4.7 wt %) and distiller's dried grains and residues (dissolved org. carbon conc. 6.5 – 12.6 wt %), with particle sizes smaller than 250  $\mu\text{m}$ , using a reciprocating plunger pump for feeding (for the bench-scale unit; the microscaled unit used filtrated

---

1.  $L/d$  of the reactor was  $> 100$ , thus the axial dispersion coefficient  $D$  tends to go to zero, indicating plug flow [74].



manure extract) [65]. They received a product gas rich in methane (52 – 61 vol %) at high carbon conversions (95 – 99.9 %), but applied a low space velocity (LHSV 1.4 – 2.6 hr<sup>-1</sup>, corresponding to a WHSV<sup>2</sup> of around 0.3 hr<sup>-1</sup>). The longest accumulated time on stream with the same catalyst loading was 29 hrs in the bench-scale unit, after which the carbon conversion had decreased from 99.9 % to 95.1 %. Despite the good results with this setup, experiments under similar conditions in a larger unit led to a decrease of the carbon gasification efficiency from 100 % to 8 % over a period of 16 hrs, accompanied by a shift in product gas composition from methane-rich towards hydrogen-rich, due to catalyst deactivation. The catalyst was covered with a shell of magnesium and phosphorus. The ruthenium was still well-dispersed, but sulfur was highly associated with it. They further reproduced the deactivation in their microscale reactor unit. Very similar findings were received in own catalyst deactivation experiments with sulfate, refer to section 7.2.

Hao et al. carried out catalytic gasification experiments in a 316L stainless steel batch reactor with cellulose as feedstock at pressures from 13 to 27 MPa, temperatures from 250 to 500 °C, and residence times from 10 to 60 min. [71]. Besides these experiments with the model substance cellulose, they also gasified a mixture of wood sawdust and carboxymethylcellulose (CMC, to enhance the mixing with water) with a 5 wt % Ru/C catalyst at 500 °C (residence time 20 min.) and 27 MPa, at a wood concentration of 8.8 wt %, a CMC-concentration of 3.5 wt %, and a wood-to-catalyst-ratio of 5. They attained a carbon gasification efficiency of 77.2 % (in contrast to 93.7 when using cellulose as feed), with a product gas composition of 26.6 vol % CH<sub>4</sub>, 30.1 vol % H<sub>2</sub>, 40.2 vol % CO<sub>2</sub>, and 3.1 vol % CO.

Valenzuela and colleagues performed aqueous phase reforming of woody biomass (pine sawdust) and wastepaper at a concentration of about 10 wt % in a 100 mL batch reactor at 225 °C with the use of a 0.5 wt % Pt/Al<sub>2</sub>O<sub>3</sub> catalyst during 3 hours (biomass-to-catalyst-ratio of 9) [72].

---

2. based on a catalyst loading density of 415 g<sub>cat.,dry</sub>/L<sub>reactor</sub> as measured in own experiments with Ru/C in a tubular reactor.

They additionally added 5 % (based on the biomass feed) of 2 M  $\text{H}_2\text{SO}_4$  to enhance hydrolysis. The cellulose and hemicellulose in the biomass were well decomposed, but 87.4 % of the lignin remained unconverted. The total carbon conversion was thus low, 36.7 %. The product gas composition of the catalytic wood gasification experiments was 32.1 vol %  $\text{H}_2$ , 58.5 vol %  $\text{CO}_2$ , and 9.8 vol %  $\text{CO}$ , with no methane, while the composition of wastepaper gasification was 13.8 vol %  $\text{H}_2$ , 77.4 vol %  $\text{CO}_2$ , 8.3 vol %  $\text{CO}$ , and 0.5 vol %  $\text{CH}_4$ . Interestingly, they found no chemisorption activity of the spent catalyst after wood gasification experiments. They stated that the most likely cause was poisoning with sulfur (from the sulfuric acid and/or sulfur from the biomass), and found a molar S/Pt ratio of 24.3 by elemental analysis. The sulfur poisoning of another catalyst is described in this thesis in section 7.2.

Researchers in the Netherlands are targeting a hydrothermal fluidized reactor concept, but only experiments in microreactors have been carried out so far [76, 77] (see also chapter 3.4).

Other projects aim at the gasification of waste streams with very low organic content (below 2 wt %) [66-69].

Osada and colleagues recently published a short review paper on the gasification of real biomass in the hydrothermal environment [78]. However, they provide a less complete overview (all of the comprised data was also presented here).

Due to the manifold hurdles associated with supercritical water gasification (stability of catalysts, pumping of real biomass, plugging due to precipitation of ash and sticky salts, etc.), no full demonstration of the whole process from feed tank to gas has been realized yet [79].

## 2.2 Chemical Fundamentals

Among several other important parameters, the effect of temperature and pressure on the biomass conversion shall be briefly outlined in the following sections, where individual steps from biomass to SNG are examined. The findings give rise to a network of individual pathways, as presented in section 2.4.

### 2.2.1 Effect of temperature and feed concentration

Methane is preferentially formed at lower temperatures, whereas at higher temperatures, hydrogen is the main product, besides  $\text{CO}_2$ . This is also true in a hydrothermal environment. The behavior is less pronounced for high feed concentrations, see Figure 2.1.

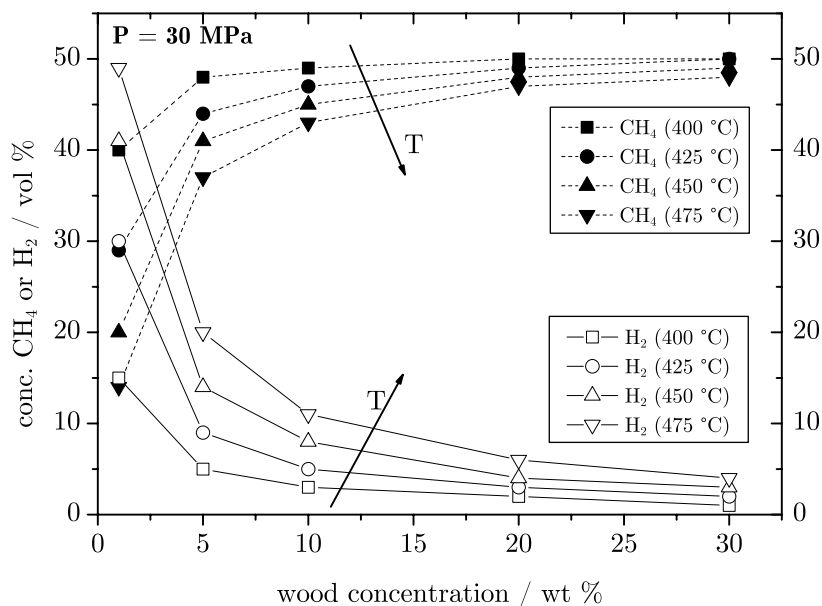
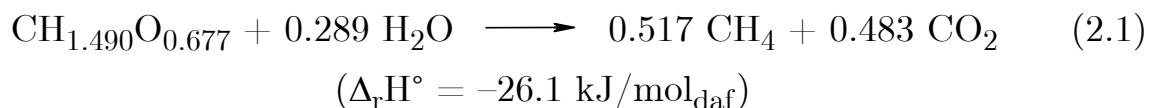


Figure 2.1: Calculated equilibrium methane and hydrogen concentrations in the product gas as a function of wood feed concentration and reaction temperature (total pressure 30 MPa; Peng-Robinson equation of state used).

As pointed out before, many researchers have conducted experiments at very dilute conditions (biomass concentrations in the range of 0.1 –

2 wt %). Depicted in Figure 2.1, the product gas composition expected from thermodynamics varies greatly at small concentrations, especially at high temperatures. Care should thus be taken when comparing experimental results from individual researchers operating at different temperatures, pressures, and concentrations.

The theoretical maximum methane yield  $Y_{\text{CH}_4}$  of  $0.34 \text{ g}_{\text{CH}_4}/\text{g}_{\text{wood}}$  (dry ash free, daf, chemical formula  $\text{CH}_{1.490}\text{O}_{0.677}$ , see chapter 5.1 on page 82) is obtained when no hydrogen is formed, according to:



For high feed concentrations, methane yields close to the theoretical maximum yield can be expected in the range of  $400 - 475 \text{ }^\circ\text{C}$  (compare Figure 2.1), e.g. at  $400 \text{ }^\circ\text{C}$ , it is  $0.33 \text{ g}_{\text{CH}_4}/\text{g}_{\text{wood}}$  for wood concentrations larger than 10 wt %). However, at these temperatures, a catalyst must be used to overcome the slow gasification rates: gasification of corn and clover grass for instance did not occur without a catalyst at temperatures below  $500 \text{ }^\circ\text{C}$  [74]. Additionally, higher temperatures favor free-radical reactions, which are an important pathway for the gas production from biomass in SCW [80]. However, free-radical reactions also take place at temperatures much lower than the critical temperature  $T_{\text{c}}$ , but to a smaller extent.

### 2.2.2 Effect of pressure

Lu and co-workers have published a parametric study on the supercritical water gasification of biomass to hydrogen [81]. Their findings of the pressure dependence are summarized as follows:

- A higher pressure favors the water gas shift reaction (WGSR, compare with the decomposition pathways of formic acid, section 2.2.7). They state that  $\text{CH}_4$  production is favored by lower pressures, which is contradictory to the findings of others [4, 82] and the general

understanding that pressure promotes the methanation due to a reduction in the number of molecules. Henrikson and Savage found that it is the concentration of water rather than pressure alone that affects the rate (there: for phenol oxidation in SCWO) [83]. Thus, for constant pressure (e.g. in a plant), the water concentration decreases with an increased amount of product gas, and thereby the density decreases, whose influence is displayed next. A higher pressure also lowers the enthalpy change during heat-up (compare section 1.7.4 on page 18 and the corresponding Figure 1.8), allowing for smaller heat-exchangers of a gasification plant. While the pressure can affect the product gas composition, the effect of pressure on the driving force ( $-\Delta G$ , Gibbs' free energy) for the gasification itself is according to Feng negligible [84].

- Density, static dielectric constant and ion product increase with pressure, thus ion-reaction rates are increased (corrosion increases, even in supercritical water which is less corrosive than subcritical water). Free-radical reactions are somewhat restrained, and gas formation, likely a free-radical reaction, may be less pronounced at higher pressures [63]. No reports were found whether this behavior is also true in presence of a heterogeneous catalyst. Sato and co-workers have identified a water density of  $200 \text{ kg/m}^3$  as optimum for the gasification of lignin over Ni/MgO [85]. This density corresponds to a water partial pressure of  $p_{\text{H}_2\text{O}} = 26.4 \text{ MPa}$  (thus at 20 wt %:  $p_{\text{tot}} = 33 \text{ MPa}$ ).
- Hydrolysis increases with increasing pressure, as it requires  $\text{H}^+$  or  $\text{OH}^-$ , whose concentration depends on the ion product and the density, which increase with pressure [81].
- Water is an effective energy transfer agent (more important at gas-like densities [86]), as it participates as collision partner in intermolecular energy transfer steps. Increasing the water density (by increasing pressure) should thus accelerate the overall gasification rate. This is balanced by the adverse effect of hindered free-radical reactions, the main pathway of the decomposition of the hydrolysis

products of biomass, especially of aromatic rings (radical ring opening) [81].

- Water as a solvent can act as a cage around molecules (more important at liquid-like densities [86]). Depending on their stabilization, either products or reactants can be favored (e.g. if the products are caged, they are more likely to recombine and regenerate the reactants; fission-type reactions as decomposition are hindered). The solvent cage thus promotes solute-solvent reactions (e.g. hydrolysis), but prevents solute-solute reactions [81].

To conclude, several (partially counterbalancing) effects make a straightforward prediction of an optimum pressure for the gasification of a specific biomass type complicated, although it is believed to exist. However, the main driving force for gasification is clearly temperature, and not pressure [87].

A closer look shall be taken at some reactions, since they play a major role in the hydrothermal gasification to SNG: biomass liquefaction to smaller molecules and their reforming to the primary gases CO and CO<sub>2</sub>, the methanation thereof, the water gas shift reaction and reaction pathways of formic acid (as an important intermediate of the WGSR and the CO<sub>2</sub> methanation reaction).

### **2.2.3 Biomass Decomposition to Smaller Molecules (Liquefaction)**

In non-catalytic pyrolysis and reforming, a long residence time of biomass at high temperatures can lead to the production of char, even in supercritical water. Thus, there exists an optimum residence time which depends on many factors such as temperature, pressure, composition and particle size of the biomass, etc. High heating rates should be applied [88, 89]. Saisu et al. carried out non-catalytic conversion experiments in SCW with lignin-phenol mixtures at 400 °C [90]. They found that by increasing the water density from zero to 500 kg/m<sup>3</sup> ( $p_{\text{H}_2\text{O}} = 37.2 \text{ MPa}$ ), the lignin

conversion was highly promoted, but led to different products (more high molecular weight compounds in the THF insoluble fraction, possibly due to polymerization (char), and more low molecular weight compounds in the THF soluble fraction).

Alkali salts can enhance the liquefaction process as they support the splitting of C–C-bonds [63] as well as they catalyze the water gas shift reaction. Karagöz and co-workers ranked the order of activity of alkali and earth alkali for wood liquefaction (conc. = 14.3 wt %) in a batch autoclave (280 °C,  $\tau = 15$  min.,  $\text{conc.}_{\text{alkali}} \sim 1$  mol/kg) as follows:  $\text{K}_2\text{CO}_3 > \text{KOH} > \text{Na}_2\text{CO}_3 > \text{NaOH}$  [91]. Unfortunately, KOH and NaOH are extremely corrosive to Ni-based alloys in supercritical water under oxidizing conditions [45]. Without the addition of alkali salts, 42 % of the wood remained as solid residue, while only 4 % remained when alkali were added to the feed. The liquid products shifted from mostly methylphenols to methoxyphenols. Yilgin and Pehlivan proposed to add formic acid (conc. 0.4 wt %) instead of alkali to enhance the liquefaction process, as it was more effective [92]. As a side-effect, however, much more gas was formed (up to 37 %, mostly  $\text{CO}_2$ ), which is not desired in a plant where the liquefaction is carried out non-catalytically in one vessel, and subsequent catalytic gasification in another apparatus. Yilgin did not find an influence of the size of the wood particles on the liquefaction process, presumably because they were very small already (90 to 150  $\mu\text{m}$ ). In contrast, Lu et al. reported that smaller particles are hydrolyzed more easily [81]. However, more intensive grinding requires more energy, and thus a compromise should be made. They do not recommend an optimum size, as it is certainly dependent on the actual liquefaction process.

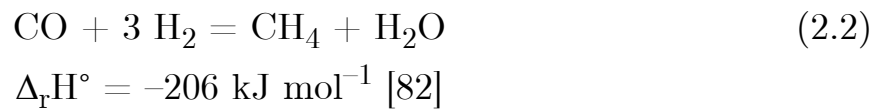
A near-commercial liquefaction process is the hydrothermal upgrading (HTU), which focuses on the non-catalytic production of liquid fuels from biomass [93]. It is operated in the subcritical region at 300 – 350 °C, and pressures around 18 MPa. The main products are a mixture of liquids and solids, so called biocrude with molecular weights ranging from 260 – 760  $\text{g mol}^{-1}$ , and  $\text{CO}_2$  (25 wt % of the initial biomass). For the production of SNG in a hydrothermal plant, these parameters do not seem ideal: due to economical factors, only one pump should be used. By doing so, the pres-

sure is fixed and therefore equal for every unit operation, i.e. liquefaction, salt separation, and gasification. Pressures in the supercritical zone are generally favorable to take advantage of the unique properties of SCW. Hence, no optimum process parameters could be directly retrieved from the literature and adapted to this project, and liquefaction experiments had to be carried out in-house with our own biomass and reactors to identify reasonable process parameters for a demonstration unit (as described in section 8.2).

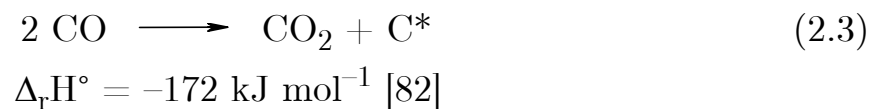
The non-catalytic reforming of methane back to CO or CO<sub>2</sub> did not occur in supercritical water up to 700 °C [53]; it is not favored by thermodynamics either.

#### 2.2.4 CO Hydrogenation (CO Methanation)

The overall stoichiometry of the carbon monoxide hydrogenation to methane is usually expressed as:



Jackson et al. have proposed that methane is a by-product of the carbon and CO<sub>2</sub> formation from carbon monoxide on the surface of a heterogeneous catalyst without the generation of water [94], which is the Boudouard-reaction:



where the residual carbon C\* readily reacts with 4 adsorbed hydrogen atoms in several consecutive steps, of which the hydrogenation of already partially hydrogenated carbon is assumed to be rate-determining. The CO<sub>2</sub> can then be methanated with additional hydrogen under generation of water (refer to section 2.2.5), thus the stoichiometry yields

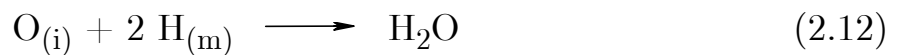
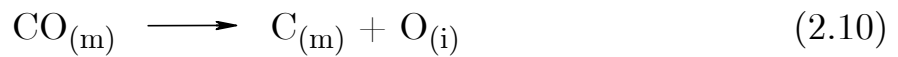


which can be reduced to the previously presented equation (2.2).



### 2.2.5 CO<sub>2</sub> Hydrogenation (CO<sub>2</sub> Methanation)

Prairie and co-workers have carried out gas-phase CO<sub>2</sub> methanation experiments with supported ruthenium catalysts (Ru/TiO<sub>2</sub> and Ru/Al<sub>2</sub>O<sub>3</sub>) [95]. Although their proposed mechanism was not verified in supercritical water, Aki and Abraham reported that the mechanistic behavior on heterogeneous catalysts in SCW is similar to the behavior in the gas-phase, and thus gas-phase data have the potential to be extrapolated to supercritical conditions [96]. Prairie et al. identified the following mechanism:



$$\Delta_{\text{r}}H^\circ = -232 \text{ kJ mol}^{-1}, \Delta G^\circ = -139 \text{ kJ mol}^{-1} [97]$$

with (b) referring to the bulk phase, and (m), (s), and (i) to metal, support and interfacial adsorption sites.

CO<sub>2</sub> reacts with adsorbed hydrogen atoms on the ruthenium sites (one H per Ru [98]) to form the intermediate formic acid (2.7), which decomposes to either H<sup>+</sup> and HCOO<sup>-</sup> on the support ((2.8), less likely in SCW), or via reverse WGS to CO<sub>(m)</sub> and water (2.9). CO<sub>(m)</sub> and 4 H<sub>(m)</sub> then form

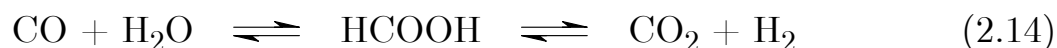
methane via several steps ((2.10) and (2.11)), which are rate-determining [94]. The oxygen recombines with 2 H<sub>(m)</sub> to water (2.12). These last steps require adsorbed hydrogen atoms (following the adsorption equilibrium between the SCW phase and the catalyst surface). The proposed mechanism yields the well known overall equation (2.13).

Prairie et al. reported the reaction rate to be independent of the concentration of CO on the surface ( $\theta_{\text{CO}}$ ), and thus independent of the CO<sub>2</sub> concentration, but to be dependent on the concentration of H<sub>2</sub> (~1.5 order). While the methanation over Ru/TiO<sub>2</sub> and Ru/Al<sub>2</sub>O<sub>3</sub> exhibited the same activation energy, and both catalysts had similar metal surface area, Ru/TiO<sub>2</sub> was 15 times more active due to smaller metal particle sizes (1 – 1.5 nm vs. 2.5 – 3 nm). According to the mechanism, for the reaction to take place, the reaction's participants are required on neighboring sites, and smaller particles therefore increase the reaction rate by increasing the active site density. Thus, small metal clusters are a key factor to activity among other parameters.

Scirè et al. have outlined that the electronic interaction between Ru and its support is essential. The induction of a higher positive polarization of the metal from the support is beneficial for the CO<sub>2</sub> methanation: The Ru-CO bond is weakened, thereby the H<sub>2</sub> concentration increases, and consequently the transformation of the intermediate CO to CH<sub>4</sub> is favored [99].

### 2.2.6 Water Gas Shift Reaction (WGSR)

The water gas shift reaction (2.14) is an important step in the hydrothermal gasification of biomass [100].

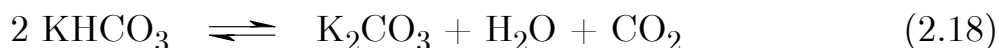
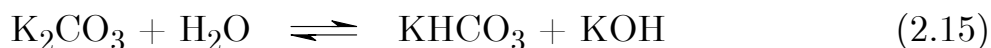


Besides, it is widely used in industry to produce hydrogen [101]. High water densities are favorable for the water gas shift reaction [88], but Sato et al. stated that for water partial pressures below 30 MPa, the kinetics are not a function of density (and thus of pressure) [102], and hence proposed a rate law which was first order in the concentration of CO only

(see below, (2.19)).

The water gas shift reaction is accelerated by increasing the temperature, or by the addition of alkali salts [4, 103] (due to the formation of an alkali-formate-complex), or by metal catalysts. Generally, compounds that generate  $\text{CO}_3^{2-}$ ,  $\text{HCO}_3^-$ , or  $\text{OH}^-$  act as catalysts for the water gas shift reaction [104]. “Non-catalytic” experimental data gathered with experiments in an Inconel reactor (an alloy with a high Ni content) such as by D’Jesús and co-workers are disguised by catalytic wall effects and alkali metals contained in the biomass [74]. They found that in the temperature range of 500 – 700 °C, the gasification rate of corn and clover grass yielded more  $\text{H}_2$  at increased temperatures, but not more CO, due to the fast WGSR. Although they did not deliberately add any catalyst, the reactor walls and potassium that was present in the biomass led to the high rate of the shift reaction. Nonetheless, they reported that for concentrations of K exceeding 500 ppm (based on experiments with variable potassium content in the feed), no further acceleration of the WGSR could be observed. Schmieder et al. similarly reported that the CO concentration in the product gas of biomass gasification was lowered by a factor of 20 with the use of KOH or  $\text{K}_2\text{CO}_3$  (no metal catalyst was added) [4].

The rate increase by the addition of alkali or earth alkali compounds can be understood as follows (catalytic cycle outlined with  $\text{K}_2\text{CO}_3$ ):



where the CO stems from biomass [105]. The order of influence on the WGSR was reported to be [106]: alkali > transition metals > earth alkali, similar to the findings of Karagöz for biomass liquefaction (see

section 2.2.3). Although alkali compounds promote the water gas shift reaction (whose products can potentially methanate) the methanation itself is reported to be suppressed by alkali [82].

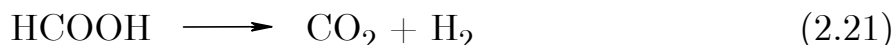
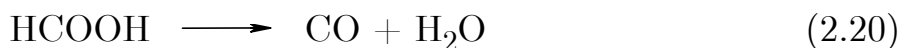
Sato et al. have estimated the reaction rate of the WGSR in supercritical water (at  $\text{CO}/\text{H}_2\text{O} = 0.03$ , hence  $p_{\text{CO}} = 0.9$  MPa at 30 MPa) and proposed 1<sup>st</sup> order kinetics for  $T < 520$  °C [102]:

$$-\text{d}[\text{CO}]/\text{dt} = k [\text{CO}] \quad (2.19)$$

They state that without a catalyst, the shift is very slow ( $k = 1.1 \times 10^{-4}$  mol (L sec)<sup>-1</sup>), yielding 7 % conversion at 400 °C (19 % at 440 °C) after 300 sec. With a metal catalyst, however ( $\text{Fe}_2\text{O}_3\text{-Cr}_2\text{O}_3$  was used), the rate was ~60'000 times faster ( $k = 6.7 \times 10^3$  mol (L sec)<sup>-1</sup>) [107].

### 2.2.7 Decomposition Pathways of Formic Acid

Formic acid can decompose to carbon monoxide and water via the dehydration/decarbonylation pathway (2.20), or to carbon dioxide and hydrogen via the decarboxylation pathway (2.21):



Yagasaki and co-workers carried out quantum mechanical calculations of formic acid and water clusters, combined with molecular dynamics and Monte Carlo simulations, and showed that the decomposition is water catalyzed [108]. The dehydration (2.20) occurs from the *trans*-formic acid, while the decarboxylation (2.21) takes place with *cis*-formic acid, see Figure 2.2.

The hydration of the *trans*-isomer is much weaker in supercritical than in subcritical water, while the same amount of water molecules are coordinated around the *cis*-isomer both in sub- and supercritical water. Thus, in supercritical water, the decarboxylation is the dominating pathway, and  $\text{CO}_2$  and  $\text{H}_2$  are the main products. Yu and Savage proposed the same behavior based on experimental results. They stated that other

reaction types such as a free-radical mechanism (experiments with radical scavengers), or an ionic reaction pathway are unlikely in supercritical water (except on surfaces) [109]. Hence, increasing pressure (leading to a higher water density) will increase cage effects and thus accelerate the water gas shift reaction by promoting the intermediate complex depicted in Figure 2.2.

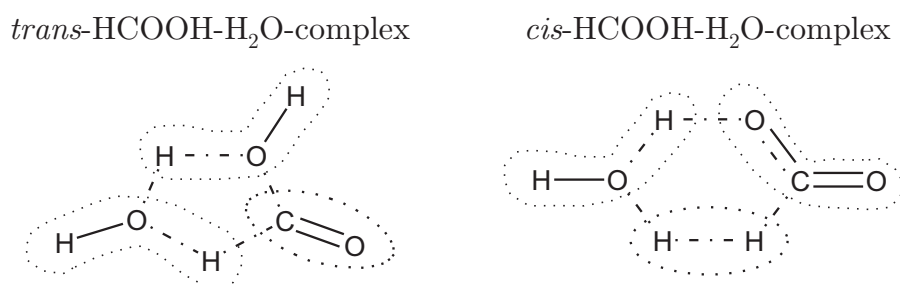


Figure 2.2: Coordination of water with *trans*- and *cis*-formic acid in the intermediate complex, leading to the decomposition products H<sub>2</sub>O and CO (left, *trans*), or H<sub>2</sub>O, CO<sub>2</sub> and H<sub>2</sub> (right, *cis*).

### 2.3 Catalysis in the Hydrothermal Environment

There is evidence that homogeneous catalysis works for the gasification of biomass in supercritical water [25, 110], but heterogeneous catalysts usually exhibit better activity [111, 112]. Mass transfer limitations, commonly present in heterogeneous catalysis (often, the transfer of gases to the solid surface of the catalyst is limited and thus rate-determining), are virtually inexistent in supercritical water due to the low kinematic viscosity and high diffusivity of the fluid [113]. The Thiele Modulus  $\phi$ , a measure for the importance of pore diffusion limitation, is  $\sim 0.03$ , thus much smaller than unity for typical catalysts in supercritical water (here calc. at 450 °C and  $\sim 28$  MPa [114]). As a consequence, there is no pore diffusion limitation on heterogeneous catalysts in supercritical water. The Brownian diffusion is about 40 times faster than in water at ambient conditions [115].

A catalyst for the hydrothermal gasification of complex mixtures of macromolecules such as wood or manure must be able to decompose the compounds to smaller molecules, reform them, and hydrogenate the resulting primary gases CO and CO<sub>2</sub> to CH<sub>4</sub>.

For the production of SNG, the catalyst should additionally be selective towards the generation of methane, rather than of hydrogen. The third criterion is stability, which is the most crucial issue in a hydrothermal environment. In the following sections, suitable active metals and their supports are compared.

### 2.3.1 Potential Active Metals for SCWG

Steam reforming and methanation is generally catalyzed by transition metals from group VIII in the periodic table, which are known as good hydrogenation catalysts.

Nickel is often used in a skeletal form, invented in 1925 by Raney [116] (except for steam reforming). These skeletal catalysts, also known as Raney catalysts, are manufactured by starting with a nickel-aluminum-alloy, from which the aluminum is partly leached out, which results in a sponge-like structure. The higher the residual Al content is, the higher is the surface area of the catalyst. Often, a third metal is added to increase the stability as well as to promote reactions by electronic interaction with the d-bands of nickel (induction of a decrease of saturation magnetization of Ni) [117]. Advantages of skeletal nickel are the good dispersion, a high surface area, robustness and good thermal conductivity due to its fully metallic nature. It was reported to exhibit a high activity for the hydrothermal gasification [58]. Skeletal catalysts exist also made of copper and aluminum, or iron and aluminum.

Kudo and Komatsu reduced carbon dioxide, dissolved in water, to methane with skeletal catalysts [97, 118]. The aluminum of the catalyst was thereby oxidized to Al(OH)<sub>3</sub>. They concluded that for the production of hydrogen, a skeletal copper catalyst was best, while for the production of methane, a skeletal iron catalyst, mixed with Ru/C, was best. The

$\text{CH}_4/\text{H}_2$  ratio was maximized at 380 °C. Apparently, Ru/C efficiently catalyzed the formation of formate, leading to methane, and skeletal Fe was much more active than skeletal Ni. No stability assessment of the catalyst was presented; however, Hoffer and co-workers report that iron leaches severely in supercritical water [119], and experiments with skeletal nickel catalysts in this thesis revealed sintering (see section 6.3.1). The Hoffer group outlined that the co-doping with Mo, Cr, or Fe on skeletal nickel catalysts had a positive effect on the hydrogenation rate of D-glucose. Increased hydrogenation rates are also favorable for the production of SNG as well.

In contrast, the co-doping with Cu (generally with a group IB metal on a group VIII metal) suppresses the hydrogenation (and methanation) [120]. Cu is usually surface-enriched, so that even small weight fractions can shift the selectivity substantially [111]. Co-doping with Cu is therefore recommended if hydrogen is the target compound. Copper is, however, oxidized to  $\text{Cu}_2\text{O}$  and  $\text{CuO}$  in SCW [121], and stability tests would be inevitable.

The order of the group VIII metal's activities for steam reforming (of methane to carbon dioxide) is reported to be: Ru, Rh > Ir > Ni, Pt, Pd [122].

Thirty years ago, Vannice ordered these metals in view of their gas-phase-methanation activity from  $\text{H}_2/\text{CO}$  mixtures as follows: Ru > Fe > Ni > Co > Rh > Pd > Pt > Ir, while he reported the selectivity towards methane (rather than towards higher hydrocarbons such as ethane) to be Pd > Pt > Ir > Ni > Rh > Co > Fe > Ru [123]. Consequently, the latter three (Co, Fe, and Ru) are typical Fischer-Tropsch catalysts.

These findings do not agree well with knowledge gained from experiments in supercritical water, just recently published by Osada et al. [124]. This information was only available at a late stage of this project (published in May 2006). According to Osada's group, the sequence of activity in supercritical water is: Ru > Rh > Pt > Pd (reasonably matching Vannice's order). In view of the metal's selectivity to methane, the order was as follows: Ru > Rh > Pt > Pd > Ni (not matching Vannice's order).

Other researchers identified only Ni, Ru, and Rh as active metals in the hydrothermal environment, while other group VIII, VIB, IB, or IIB metals were inactive [58]. Co, Fe, Cr, Mo, W, and Zn are known to be easily oxidized.

In light of these findings, from a chemical point of view, ruthenium is clearly the active metal of choice, despite its higher initial cost because it is a precious metal (EUR 12'500/kg in December 2006). However, the costs can be substantially reduced by regenerating the spent catalyst. Usually, more than 96 % of the ruthenium can be recovered (by oxidation to volatile  $\text{RuO}_4$ ) [125]. Compared to nickel catalysts, the final overall costs are about the same (derived from a study of the hydrogenation for the production of sorbitol, a process industrially carried out both over skeletal nickel and Ru/C catalysts) [126]. Nonetheless, Ni catalysts should be considered as well due to their low price and abundant supply, preferably in the form of skeletal, or immobilized on carbon.

### 2.3.2 Potential Supports for SCWG

As the properties of water are strong functions of p and T, so does catalyst stability vary with the individual process parameters, and findings described in the literature are not 1:1 transferrable to this project. Nonetheless, the general trend is unaffected and outlined here.

Many metal oxide supports are reported to be unstable in SCW, mostly due to hydrolysis leading to migration of the active sites [127].

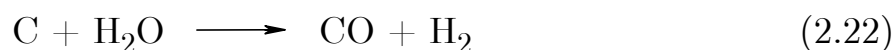
$\text{MnO}_2/\gamma\text{-Al}_2\text{O}_3$  was unstable due to agglomeration of  $\gamma\text{-Al}_2\text{O}_3$  at 370 °C.  $\text{Pt}/\gamma\text{-Al}_2\text{O}_3$ , however, seemed to be stable, possibly thanks to platinum's ability to redistribute on the support during oxidation [96].

A comprehensive stability study in subcritical water at 350 °C and 20 MPa (TEES conditions) is available from Elliott and co-workers [58] (stability in supercritical water is expected to be higher than in subcritical water [112]). Stable were only:  $\alpha\text{-Al}_2\text{O}_3$ ,  $\text{ZrO}_2$ , rutile- $\text{TiO}_2$ , and C. Unstable were:  $\text{SiO}_2$  (hydrolysis and mashing), anatase- $\text{TiO}_2$  (transformation to rutile), Ca/aluminate, kieselguhr,  $\gamma$ -,  $\delta$ -, and  $\eta\text{-Al}_2\text{O}_3$  (hydrolyzed



to AlOOH, böhmite). The stable phase of zirconia ( $\text{ZrO}_2$ ) is only the monoclinic phase [128].

Gallezot et al. reported that carbon is more stable in acidic conditions than metal oxides [129]. Unfortunately, at temperatures from 680 – 800 °C, carbon gasification according to the water-gas-reaction (2.22) can take place [130]:



possibly followed by methanation. Matsumura and co-workers presented a rate expression for the carbon gasification [131] (made from coconut shell, one of the most stable carbons to exist [125]), which was dependent on the partial pressure of water and hydrogen. However, at temperatures below 560 °C, the rate approaches zero (nearly independently of the pressure for  $p > p_c$ ), and thus, carbon supports made of coconut shell are not susceptible to gasification during the production of SNG (where thermodynamically lower temperatures around 400 – 500 °C are feasible). While this is true for the support alone, metal catalysts on coconut shell carbon can exhibit a different behavior due to the catalytic activity of the metal clusters.

Sugiyama et al. conducted carbon stability tests at SCWO conditions (30 MPa, 400 – 450 °C, 3.6 wt %  $\text{O}_2$ ,  $\tau = 300$  sec) [132]. They used three types of carbon: activated (unspecified origin, possibly not stemming from coconut), synthetic graphite, and highly oriented pyrolytic graphite (HOPG). During the treatment, the activated carbon was dissolved, and the less crystalline structure of the synthetic graphite was selectively oxidized (measured with Raman spectroscopy). The HOPG, however, was stable because it consisted of highly crystalline graphite which is difficult to oxidize. Thus, also HOPG could be considered as a support for heterogeneous catalysts.

The stability of carbon supported metal catalysts (and not only their support alone) towards self-methanation was recognized as a fundamental parameter. It can be enhanced by proper thermal treatment of the carbon

before impregnation with the active metal; Rossetti et al. recommended to use high temperatures in vacuo [133]. Unfortunately, this may lead to a decrease in surface area, thus to a trade-off between activity and stability. Co-doping of promoters such as Ba to the active metal can greatly suppress the (self-)methanation. A suppressed methanation activity is not feasible for the production of SNG, but could be favorable if hydrogen were the desired product gas. Kowalczyk and co-workers showed that the addition of K as promoter increased the methanation rate eightfold compared to the unpromoted Ru/C catalyst, not only leading to enhanced activity, but possibly to increased self-methanation as well [98]. The loading of the active metal itself (there: Ru) had no effect on the degree of self-methanation.

A novel Ni/C catalyst was invented by Japanese researchers, based on a synthetic carbon (metacrylic acid type anion exchange resin) as support. It was used to gasify lignin and phenol solutions at 360 °C and 20 MPa [66-69]. They report only mild sintering and near-complete conversion (98 %). However, despite their LHSV of 50 hr<sup>-1</sup>, the WHSV was very low, 0.13 hr<sup>-1</sup>, due to the highly diluted feed (TOC 0.2 – 2 wt %). Incomplete conversion under these conditions must be judged as a hint for low activity.

The support does not only have a passive role, it can also influence the reaction pathways, e.g. due to its acidity or basicity. Formaldehyde for example can decompose to CO and H<sub>2</sub> on a TiO<sub>2</sub> support (acidic), while it can decompose to methanol and formic acid following a Cannizzarro reaction on CeO<sub>2</sub> or ZrO<sub>2</sub>, which are more basic supports (the basicity or acidity depends on the electronegativity of the metal ion; the larger the more acidic) [134].

## 2.4 Proposed Reaction Network of Wood Gasification

### 2.4.1 Introduction

As outlined in the earlier sections, wood must be decomposed into its main constituents, i.e. cellulose, hemicelluloses and lignin, before it can be gasified (in our case: over a heterogeneous catalyst). These must be broken down to smaller molecules (liquefaction, presented in section 2.2.3), as only small molecules can access the active sites of a heterogeneous catalyst. Near-critical and supercritical water are excellent media for breaking down the wood because many chemical bonds can be cleaved by hydrolysis (i.e. the reaction with water).

The analysis of wood liquefaction experiments in presence of a skeletal nickel catalyst, conducted within the frame of this thesis, revealed which reaction intermediates were gasified in supercritical water, and which ones remained in the liquid phase after reaction (for details refer to section 6.1.5 and Table 6.3 on page 106). This knowledge was used to judge the ease with which certain molecules are gasified:

D-glucose, formic acid, levulinic acid, methanol, ethanol and 5-hydroxymethyl furfural (5-HMF) were the main constituents of liquefied wood that were degraded to other molecules during hydrothermal gasification (i.e. gasification is “easy”). In contrast, oxalic acid, acetic acid, acetaldehyde and phenol were rather stable degradation products, staying in the liquid phase after reaction at the conditions studied (i.e. gasification is difficult). Acetic acid is significantly stabilized in supercritical water [128], and even in supercritical water oxidation processes, the decomposition of acetic acid is considered a critical, rate-limiting step [112].

Based upon wood degradation knowledge available from the literature [135] and the above results from experiments carried out within the framework of this thesis, a simplified wood-to-SNG reaction network could be drawn, depicted in Figure 2.3. Similar findings were published by Kruse and Gawlik [63].

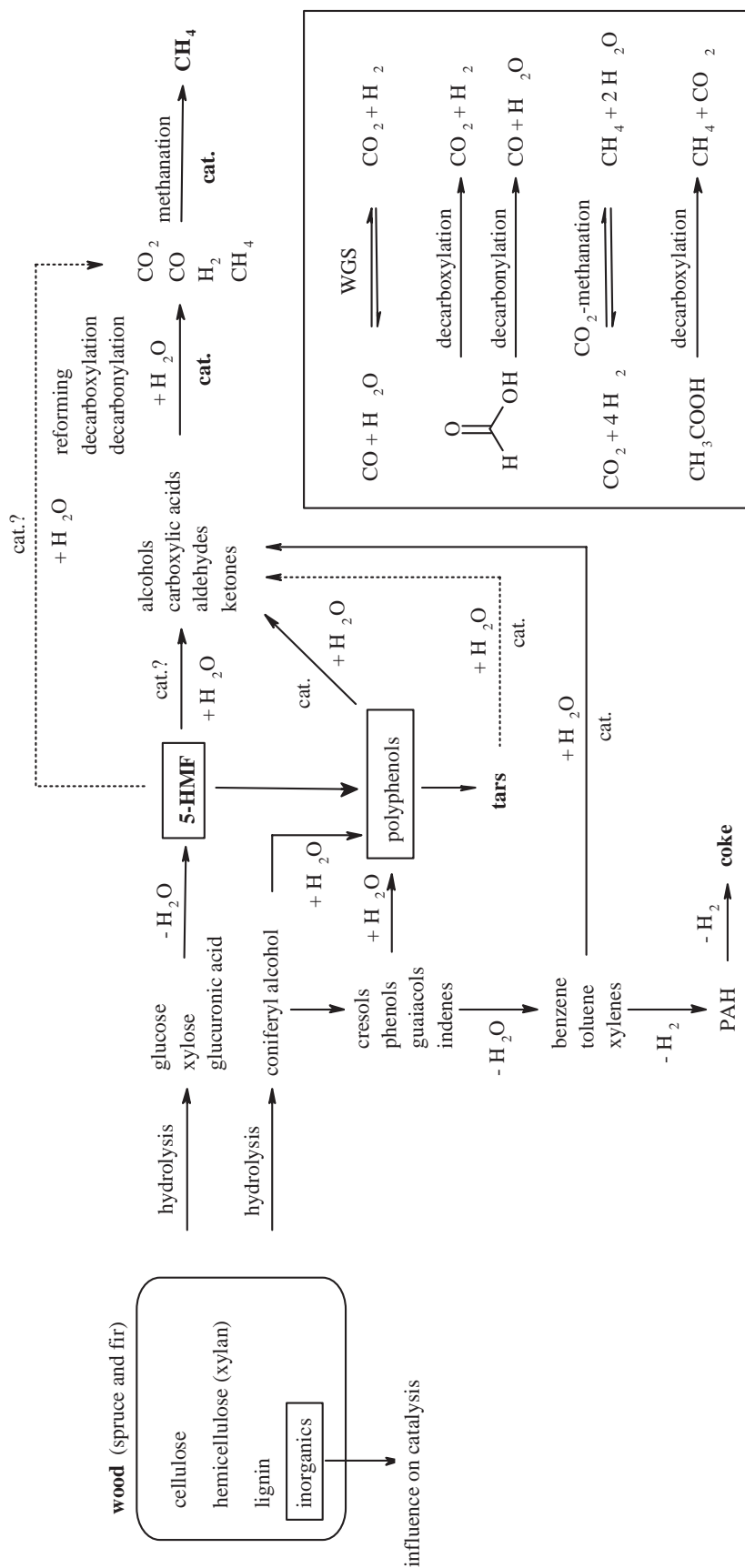
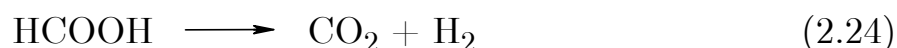


Figure 2.3: Proposed simplified reaction network of wood degradation to SNG.

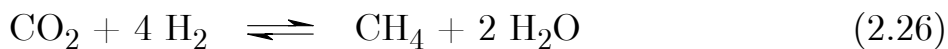
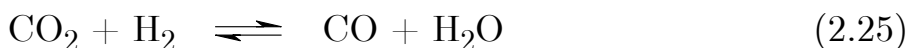
### 2.4.2 Reaction Network

Cellulose is hydrolyzed to glucose, the hemicelluloses to xylose and gluconic acid, and the lignin to phenolics and aldehydes by hydrolysis of the ether and ester bonds [90, 136]. Coniferyl alcohol is a typical representative of the building blocks of spruce lignin (see chapter 5.2). 5-HMF is formed by dehydration of glucose. An extensive study of the decomposition of glucose in sub- and supercritical water was presented by Kabyemela et al. [137, 138]. Dehydration of the phenolics leads to aromatics (benzene, toluene, xylenes), which in turn may pyrolyze to coke. Hydroxylation of the phenols yields polyphenols (e.g. di- or trihydroxybenzenes). Polyphenols can condense to form oligomeric, tar-like substances. Interestingly, also 5-HMF can form the polyphenol 1,2,4-trihydroxybenzene [139]. This important reaction links the non-phenolic wood building block cellulose to the phenolic lignin.

According to Minowa and Fang [140], the polyphenols and 5-HMF are decomposed at suitable reaction conditions to low molecular-weight carboxylic acids (acetic, formic, levulinic), aldehydes (acetaldehyde, furfural, formaldehyde), alcohols (ethanol, methanol), and ketones (acetone). The product distribution and the exact pathways are a function of the temperature, pressure, residence time, catalyst, and the composition of the biomass itself [141]. These small molecules can be reformed efficiently on a nickel or ruthenium catalyst to  $\text{CO}_2$ ,  $\text{CO}$ ,  $\text{H}_2$ , and  $\text{CH}_4$ . Dealkylation of alkyl groups on alkylphenol structures stemming from lignin can form  $\text{CH}_4$  directly [142]. Acetic and formic acid can decarboxylate to form  $\text{CH}_4$ ,  $\text{CO}_2$ , and  $\text{H}_2$ , [109, 128]:



The gaseous products  $\text{CO}_2$ ,  $\text{CO}$ ,  $\text{CH}_4$ , and  $\text{H}_2$  may equilibrate with water according to the following reactions (reverse WGSR (2.25) as outlined in section 2.2.6,  $\text{CO}_2$  methanation (2.26) as outlined in section 2.2.5,  $\text{CO}$  methanation (2.27) as outlined in section 2.2.4):



At high  $\text{CO}_2$  and  $\text{H}_2$  partial pressures, CO may be formed via the reverse water gas shift reaction. CO may also be formed as a primary product of decarbonylation of aldehydes [143].

As outlined earlier by the findings of many researchers, the attainment of the water gas shift (2.25) and the methanation equilibria (2.26) and (2.27) are catalytically accelerated. Also Minowa and Fang, who used a nickel catalyst, depicted this acceleration [140]. Accordingly, in all short term experiments carried out in the batch reactor in presence of such a catalyst (see section 6.1), the concentration of carbon monoxide in the product gas was below 0.1 vol %.

### 2.4.3 Avoidance of the Tar Problem of Conventional Gasification

Tar formation can be avoided by rapidly converting 5-HMF and the polyphenols to low molecular weight compounds. Modell first observed that wood could be gasified in supercritical water without the formation of tars and char [144]. The conversion of tars and char is a big advantage of the hydrothermal gasification over the conventional gasification technology, where tar formation is a major problem (the general definition of “tar” in thermal process engineering is quite loose: “organic contaminant with a molecular mass larger than the one of benzene” [145]). These tarry substances may represent a significant portion of the heating value of the wood and thus lower the gasification efficiency, if not used thermally. Tars must be removed from the fuel gas before entering other downstream equipment in conventional gasification [146]. Bridgwater actually stressed that the tar problem still represents the most significant technical barrier in conventional gasification [8].

The excellent solvation properties of supercritical water are probably enhancing the reforming of the polyphenols. Polyphenols tend to form

dark and oily oligomeric compounds when heated and/or exposed to oxygen. Since these oligomers are not volatile, they stick to the surface of reactors and catalysts and form tarry deposits. Supercritical water solubilizes the polyphenolic precursors and allows for their efficient gasification when a suitable catalyst is present. In a low pressure vapor phase, these compounds would not be solubilized and would thus be difficult to gasify. This behavior is depicted in Figure 2.4. When operating a hydrothermal gasification plant, care should therefore be taken not to enter the vapor region to avoid tar formation.

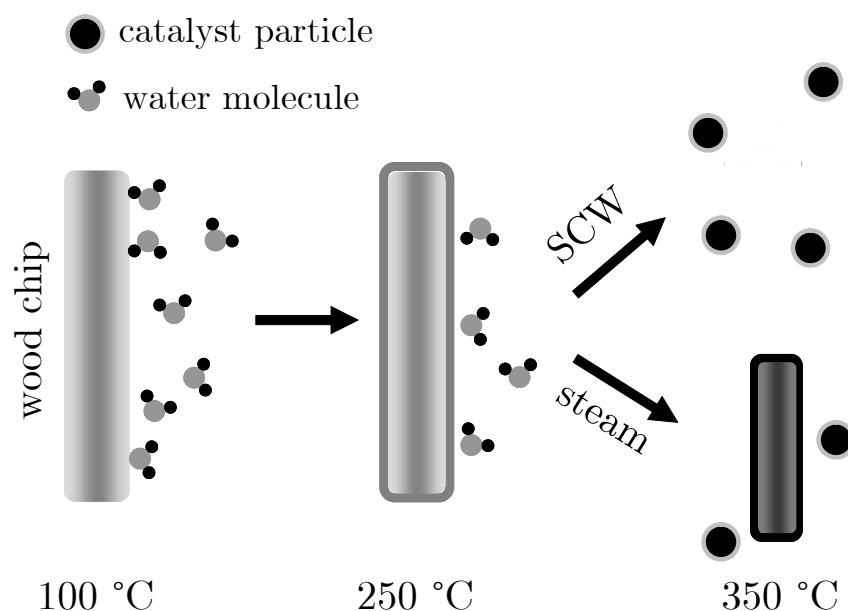


Figure 2.4: Tar-free gasification in supercritical water (SCW). Left: wood is attacked by water molecules which hydrolyze the lignin and celluloses. Middle: Hydrolysis products (e.g. sugars, phenolics) form a liquid film around the particle. Water must diffuse through this film to access the wood particle. Right: While in SCW, the oily film is quickly dissolved and removed, and water can penetrate into the wood particle, in steam gasification the sugars and phenolics polymerize to tars, the particles are covered with an unpenetratable oily film, and the particles eventually pyrolyze to coke and gas.





# Chapter 3: Experimental Setup

## 3.1 General

Several reaction systems were used to carry out gasification and liquefaction experiments, long-term catalyst tests, catalyst screenings and validations of the comparability of model substances to real biomass feeds. An overview is given in Table 3.1.

Table 3.1: Different reactor systems used.

system	pro	contra
batch reactor	<ul style="list-style-type: none"> <li>– real biomass slurries can be used up to high conc.</li> <li>– simple and robust</li> </ul>	<ul style="list-style-type: none"> <li>– small amounts</li> <li>– no long-term exp. (with the setup used for this thesis)</li> <li>– <math>p = f(m_{\text{biomass}}, T, \text{cat.}, X_C, \text{etc.})</math></li> <li>– off-line analysis (in this case, not generally)</li> <li>– mixing by convection (could be improved)</li> </ul>
continuously operating test rig	<ul style="list-style-type: none"> <li>– long-term testing</li> <li>– p, T control</li> <li>– on-line gas analysis</li> <li>– flow system</li> </ul>	<ul style="list-style-type: none"> <li>– laborious</li> <li>– large pressure drop for fine catalyst powders</li> <li>– feed must be liquid</li> </ul>
quartz capillaries	<ul style="list-style-type: none"> <li>– no catalytic wall effects</li> <li>– optically accessible</li> </ul>	<ul style="list-style-type: none"> <li>– difficult (welding etc.)</li> <li>– very small samples</li> <li>– analysis difficult</li> <li>– potentially harmful (capillary explosion)</li> </ul>

As each setup had its advantages and disadvantages, all three were used in a complementary way. The setups are presented in more detail in the following sections.

## 3.2 Batch Reactor

### 3.2.1 Setup

Most experiments with real biomass feeds (wood slurries, oil shale, reed, peat, manure, etc.) were carried out in a small batch reactor system developed at PSI. High feed concentrations could be used, but relatively low amounts of biomass feed (0.5 – 1.0 g) were required to keep the pressure within safety limits. A sketch of the reactor system is shown in Figure 3.1, and a picture of the hot parts is given in Figure 3.2.

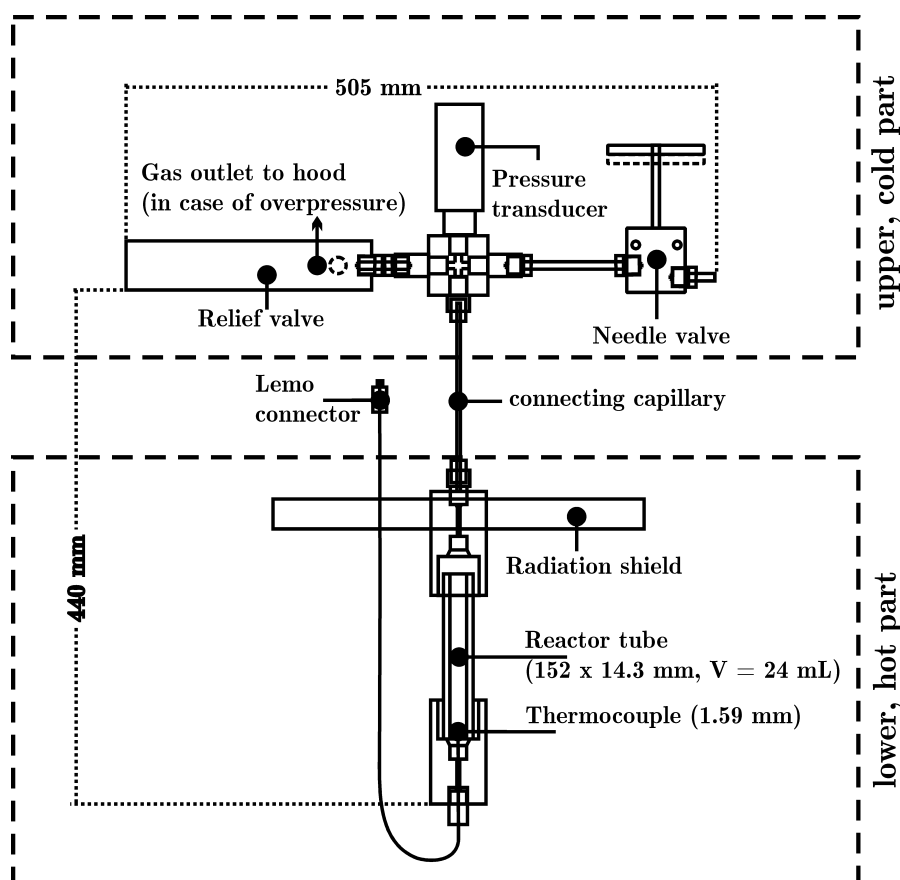


Figure 3.1: Sketch of the batch reactor used.

The high-pressure section of the apparatus was constructed with standard parts from HiP (High Pressure Equipment Company, USA). The reactor consisted of a high-pressure 316 stainless steel tube (25.4 mm o.d.  $\times$  14.3 mm i.d., length 152.4 mm, internal volume  $\sim$ 24 mL). A sheathed 1.6 mm type K thermocouple was fitted to the bottom of the reactor in contact with the reaction medium. For experiments with biomass containing corrosive salts, a titanium liner was inserted into the reactor tube, decreasing the effective volume to  $\sim$ 18 mL.

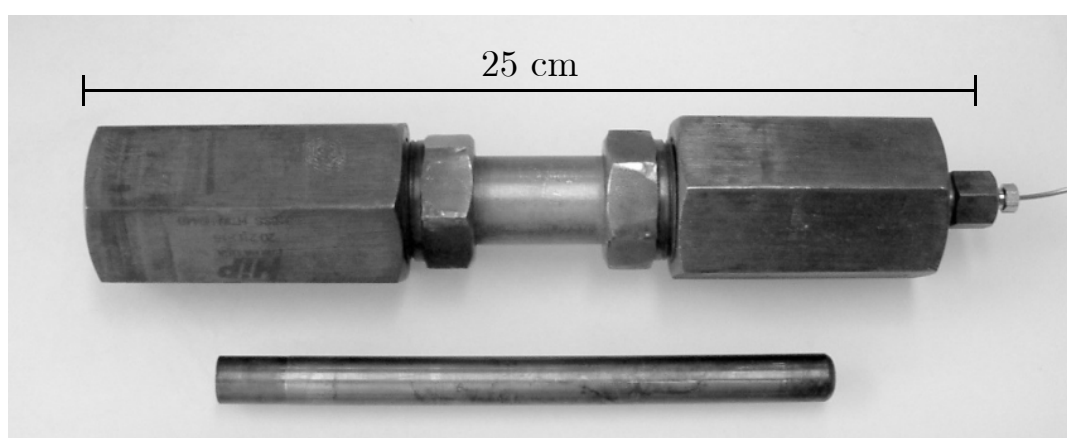


Figure 3.2: Hot parts of the high pressure batch reactor, including the titanium liner.

A 316 stainless steel capillary tube (length 223 mm, 3.2 mm o.d.  $\times$  1.6 mm i.d.) was connected to the reactor tube by a high-pressure union. A type K thermocouple was attached to the outside of the upper part of the reactor in order to identify possible temperature gradients. After reaction, the gases were held within the reactor (at about 4 MPa after cool down). As an alternative, they could be transferred into a pre-evacuated 1 L stainless steel bomb (Whitey), or at a later stage of the project to a gas sampling bag (volume 1 L, SKC). Gas samples could then be taken with a gas-tight syringe (SGE) through the needle valve (HiP) of the reactor, or through the septum port of the stainless steel bomb or the gas sampling bag, respectively. The gas was analyzed off-line by gas chromatography.

For later experiments, in order to gain more insight into the general time-scale of gas production by hydrothermal gasification in the batch system, a second high-pressure valve was connected to the existing one by a small stainless-steel tube (length 4 mm, 1/4" i.d.). This addition made gas sampling during experiments possible. By opening the first valve, a certain amount of the reactor content was driven into the transfer line. Care had to be taken not to open the valve too quickly or too widely in order to avoid sucking the hot aqueous phase into the line. After closing the first valve, a gas-sampling bag could be attached to the second valve, and the gas transferred into the bag by opening the valve. More details on this setup and a sketch are presented in section 6.5.1 (and Figure 6.22 on page 157), together with the corresponding experimental results.

### 3.2.2 Feed Preparation and Experimental Procedure

A premeasured amount of biomass was mixed with water and catalyst in a beaker to yield the desired feed concentration (10 – 30 wt %; the weight percentages are calculated for the mixture of dry biomass and water, only). In a typical experiment, a biomass-to-catalyst ratio of 2 was used. The slurry was then loaded into the reactor tube with the help of a spatula. The reactor tube was screwed tightly to the high-pressure union attached to the capillary tube using a torque wrench. Air was removed by evacuating the apparatus with the help of a water-driven ejector pump for about 30 seconds. For liquid, volatile biomass model compounds (such as synthetic liquefied wood, presented in section 5.2), the reactor was not evacuated but flushed two times with argon. To avoid water evaporation and dry out of the slurry during heat-up, the reactor was pressurized with 1.9 – 2.2 MPa of argon, serving also as a leak test.

The reaction was initiated by immersion of the reactor assembly into a preheated fluidized sand bath (Techne SBL-2D). Maximum initial heat-up rates of 1 – 1.3 °C/s (up to 350 °C) were achieved, but could be varied down to 0.1 °C/s by immersion of the reactor into the sand bath at 70 °C and simultaneously heating both the bath and the reactor. A radiation

shield avoided excessive heat-up of the non-immersed reactor parts. Before each experiment, an approximate calculation of the expected maximum pressure was carried out. In case the calculated pressure exceeded the preset pressure of the relief valve, the amount of feed slurry and/or the operating conditions were adapted. For most of the experiments, no samples were taken during the gasification process. To stop the reaction after a predetermined time, the reactor was lifted out of the fluidized sand bath and quenched in a cold water bath. The pressure inside the reactor and the temperatures were measured at intervals of 1 s using a LabView™-based data acquisition system.

### 3.2.3 Analysis

Gas samples were analyzed off-line for CH<sub>4</sub>, C<sub>2</sub>H<sub>6</sub>, CO<sub>2</sub>, CO, H<sub>2</sub> and Ar on an Agilent 6890 GC using a TCD and a two-column switching system with helium as the carrier gas. When the product gas was not transferred into an SKC sampling bag, the total moles of gas were calculated as follows:

$$n_{\text{tot}} = \sum_i \frac{y_i \cdot p_{\text{end}} \cdot V_{\text{gas}}}{R \cdot T} \cdot \frac{1}{z_i} + n_{\text{CO}_2, \text{diss.}} \quad (3.1)$$

with  $y_i$  being the volume fraction of gas  $i$  in the gas-phase analyzed by GC,  $p_{\text{end}}$  the resulting reactor pressure at 25 °C after quenching,  $T$  being the absolute temperature of the gas,  $R$  being the universal gas constant and  $V_{\text{gas}}$  being the volume available for the gas inside the system ( $V_{\text{reactor}} - V_{\text{liquid}}$ ). For all gases, compressibility factors  $z_i$  (calculated through regression of the molar density vs. pressure, data from NIST [147]) accounted for non-ideal behavior at elevated pressures:

$$z_i = \frac{p_{\text{end}}}{R \cdot T \cdot (\alpha_i \cdot p_{\text{end}} + \beta_i)} \quad (3.2)$$

The slopes  $\alpha_i$  and the intercepts  $\beta_i$  of the linear regressions used are summarized in Table 3.2.

Table 3.2: Compressibility factors  $z_i$  of the gases detected by GC.

gas $i$	$\alpha_i$ mol/(m <sup>3</sup> Pa)	$\beta_i$ mol/m <sup>3</sup>
CH <sub>4</sub>	$4.11 \times 10^{-7}$	-21
C <sub>2</sub> H <sub>6</sub>	$4.41 \times 10^{-7}$	-84
H <sub>2</sub>	$4.01 \times 10^{-7}$	6
CO <sub>2</sub>	$4.27 \times 10^{-7}$	-52
CO	$4.05 \times 10^{-7}$	-3

Where applicable, the gas was transferred into the evacuated gas bomb, which lowered the total pressure to less than 0.2 MPa, where ideal behavior can be assumed, or transferred into an evacuated gas sampling bag. There, the volume was determined by evacuation with a 60 mL plastic syringe, and the total moles were calculated with the ideal gas law. The amount of dissolved CO<sub>2</sub> in the water phase after cool down,  $n_{\text{CO}_2, \text{diss.}}$ , lost during the depressurization and opening of the reactor, was calculated using Henry's law [148]:

$$n_{\text{CO}_2, \text{diss.}} = K_{\text{H}, \text{CO}_2}^0 \cdot y_{\text{CO}_2} \cdot p_{\text{end}} \cdot V_{\text{liquid}} \quad (3.3)$$

and

$$\ln\left(K_{\text{H}, \text{CO}_2}^0(T)\right) = A + \frac{B}{T} + \frac{C}{T^2} \quad (3.4)$$

with  $T$  being the absolute temperature and  $A$ ,  $B$ , and  $C$  constants, see Table 3.3. The solubility of the other gases in water was calculated in an analogous way. However, their solubility is much lower than the one of CO<sub>2</sub>, and thus, their contribution was neglected. A good compilation of solubility data for hydrocarbons and CO<sub>2</sub> mixtures in water was published by Dhima [149].

Table 3.3: Parameters for calculating the Henry's law constant  $K_{\text{H}}^0$ .

gas	$A / -$	$B / \text{K}$	$C / \text{K}^2$
carbon dioxide	$-6.027 \times 10^{-1}$	$5.857 \times 10^3$	$-1.239 \times 10^6$
methane	$-2.172$	$7.886 \times 10^3$	$-1.420 \times 10^6$
ethane	$-5.056$	$1.023 \times 10^4$	$-1.887 \times 10^6$

After cool down, the reactor was depressurized, opened and emptied. The remaining slurry was filtered by vacuum filtration with a membrane filter (regenerated cellulose, 0.45  $\mu\text{m}$  pore size, Schleicher & Schuell). The reactor was rinsed with methanol to remove any water-insoluble deposits. The methanol washings were filtered over the same filter that was used for the aqueous phase. This procedure yielded two liquid phases (one aqueous, one methanolic) and a wet solid residue, consisting mainly of the recovered catalyst. The solid residue was dried in a vacuum oven at 105  $^{\circ}\text{C}$  over night and analyzed for its carbon content (Dohrmann boat module and DC-190, see section 4.5 on page 72). The aqueous phase was analyzed for dissolved organic carbon (DOC, Dohrmann DC-190 catalytic combustion at 800  $^{\circ}\text{C}$ ). Low molecular carboxylic acids, aldehydes, alcohols, ketones and phenols were determined high pressure by ion exchange chromatography. The methanolic solution was analyzed for its water content by Karl-Fischer titration to account for the water that could not be recovered from the reactor (mainly sorbed on the catalyst) in the first step. The methanolic solution was evaporated (45  $^{\circ}\text{C}$ , 200 hPa) and the tar-like residue was analyzed for its carbon content (Dohrmann boat module and DC-190). For most experiments, total mass balances and elemental balances (CHO and Ar) were calculated. The experimental procedure and analysis is summarized in Figure 3.3.

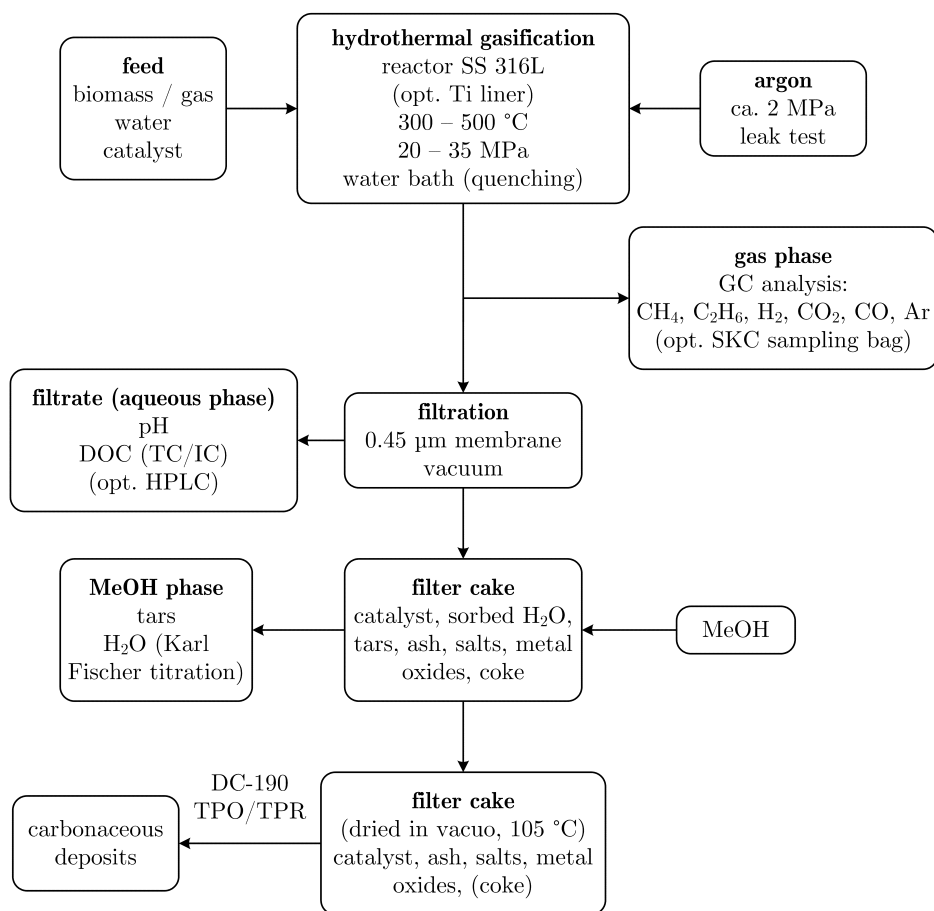


Figure 3.3: Procedure of a typical batch reactor experiment.

### 3.3 Continuously Operating Catalyst Test Rig

While catalyst screening was mostly carried out in the batch reactor, no information about catalyst stability could be gained beyond the time-scale of a typical batch reactor experiment (~1 hr). A different reactor system was thus needed. The system of choice was a continuously operating packed bed flow-through system.

#### 3.3.1 Setup

The continuously operating test rig was made of 316L stainless steel. The process flow sheet is depicted in Figure 3.4, and a photograph is shown in Figure 3.5.



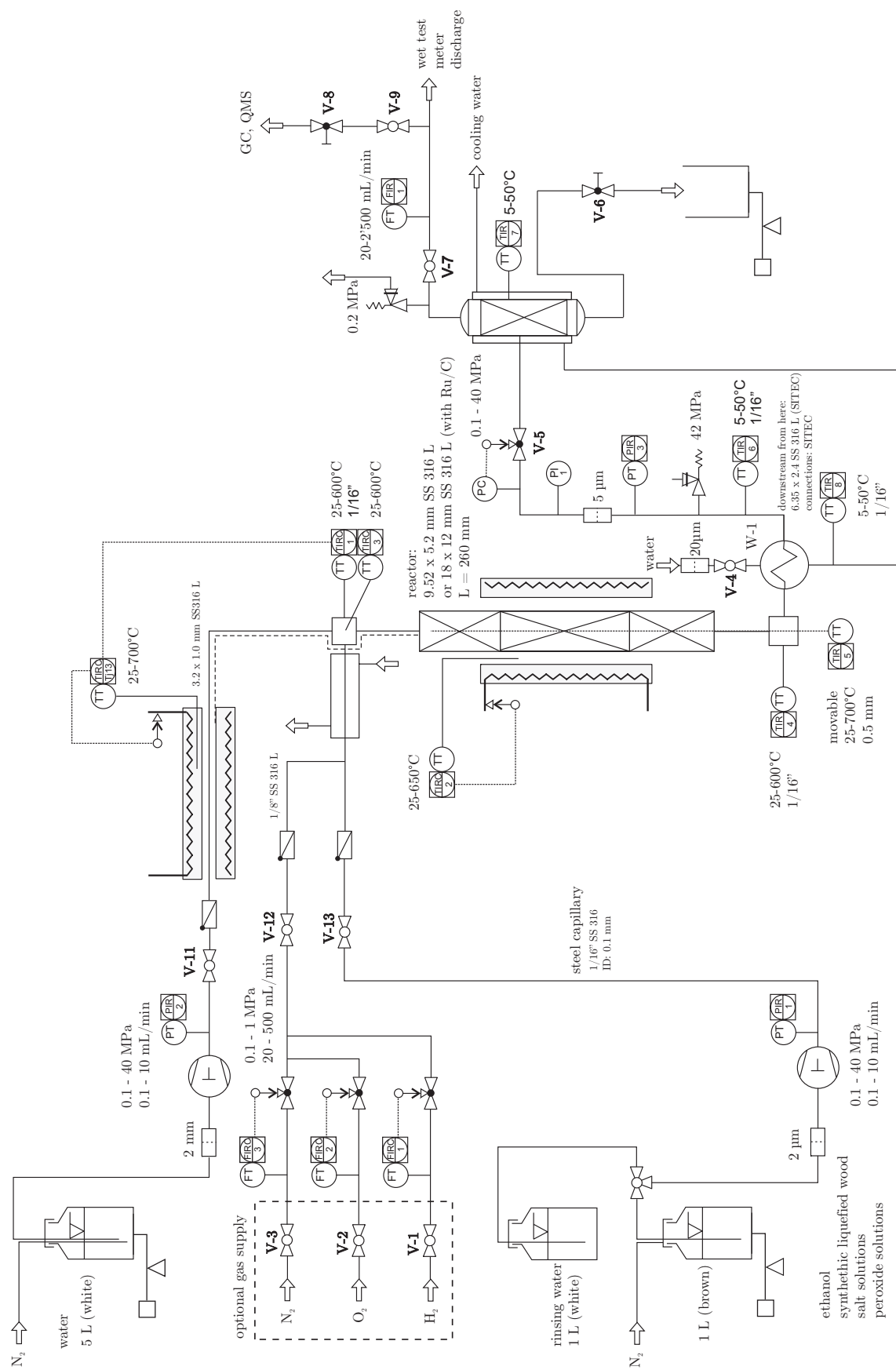


Figure 3.4: Process flow sheet of the continuously operating reactor.

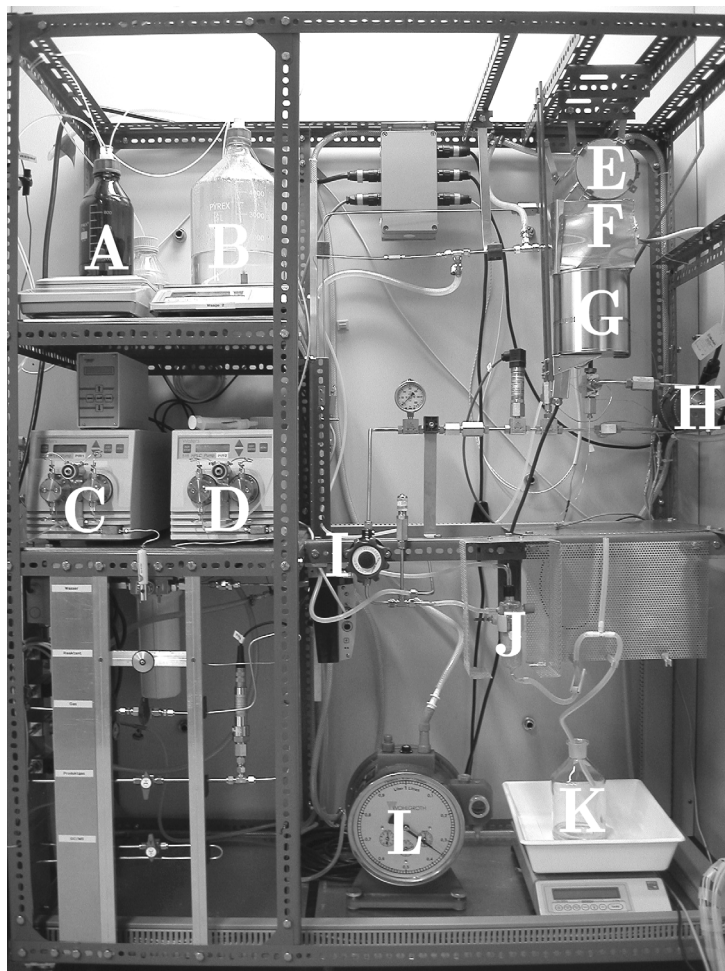


Figure 3.5: Photograph of the continuously operating catalyst test rig. A: Liquid model mixture feed flask. B: Water feed flask. C: Model mixture feed pump. D: Water feed pump. E: Superheater (only water phase). F: Mixing cross (heated, insulated). G: Tubular fixed-bed reactor (heated, insulated). H: Cooler. I: Back pressure regulator. J: Glass phase separator. K: Liquid product phase. L: Wet test meter.

All hot high pressure parts were purchased from SITEC, Switzerland. Swagelok fittings were used to connect most cold parts. Two HPLC pumps (Waters 515) were used to feed the organic mixture and the water, stored in glass containers (degassed off-line by immersion into an ultrasonic bath and on-line by purging nitrogen to remove dissolved oxygen) at a pressure of 30 MPa. Two balances monitored the mass flow rates.

The setup with two feed lines allowed to change concentrations and individual flow rates during an experiment. The water was preheated and brought to the supercritical state in a heater before being mixed in a

cross with the cold organic stream prior to entering the tubular fixed bed reactor. For most experiments, the hot water entered the cross vertically from the top, and the cold biomass model mixture entered it horizontally from the side (up to exp. no. 8 of the deactivation campaign outlined in section 7.2). Later, the hot water entered the cross horizontally, while the cold biomass entered vertically from the top. This arrangement had just been reported at that time to ensure best mixing of the fluids [150]. However, no difference in the resulting thermal profiles along the reactor could be measured for this test rig. A heatable U-type jacket insulated the cross and held it at a desired temperature. For experiments with Raney nickel or 1 wt % Ru/TiO<sub>2</sub>, the reactor tube was 5.2 mm i.d., length 250 mm, and for experiments with 2 wt % Ru/C, the tube was 12 mm i.d., length 250 mm. Type K thermocouples were used at several positions in order to measure the temperature inside the reactor. The vertically mounted reactor tube (inlet at top, outlet at bottom) was surrounded by an oven operated with heating cartridges, which resulted in a rather uniform temperature profile along the reactor. This was measured with a sheathed thermowell (1/16 " o.d., 1/32 " i.d.) that protruded coaxially from the effluent side of the reactor. Due to technical reasons, the thermowell for the wider tube used for the Ru/C experiments was 30 mm shorter, thus no temperature information was available from the first 3 mm of the reactor length.

Below and above the catalyst packing was a bed of  $\alpha$ -Al<sub>2</sub>O<sub>3</sub> beads (particle size 1 mm for Ru/C, 110  $\mu$ m for other catalysts). Downstream of the reactor, a cooler was used to cool the outlet to 40 °C. A 5  $\mu$ m filter (SITEC) prevented possibly entrained particles of the bed from disrupting the manually regulated backpressure regulator (Tescom, model 54-2000, valve seat made of polyetheretherketone, PEEK), BPR, over which the fluid was expanded to atmospheric pressure. Initially, the valve seat was made of polytetrafluoroethylene, PTFE, and later Kalrez<sup>®</sup> (a perfluoroelastomer from DuPont), which is said to be more stable against chemicals (i.e. against unreacted feed). However, the seat had to be changed frequently, after 50 – 70 hrs of operation, until PEEK was used, with which the best results were achieved.

The liquid phase was separated in a glass tube from the gas phase, which was routed to a wet test meter to measure the accumulated volume of the gas. A gas pump (KNF Laboport, model 1393-86) continuously withdrew 12 mL/min. of product gas, and fed it over a cryo trap to the gas chromatograph. Most data was registered on-line with a Labview™-based computer program (Figure 3.6). The accumulated gas volume and the temperature profile along the reactor had to be recorded manually.

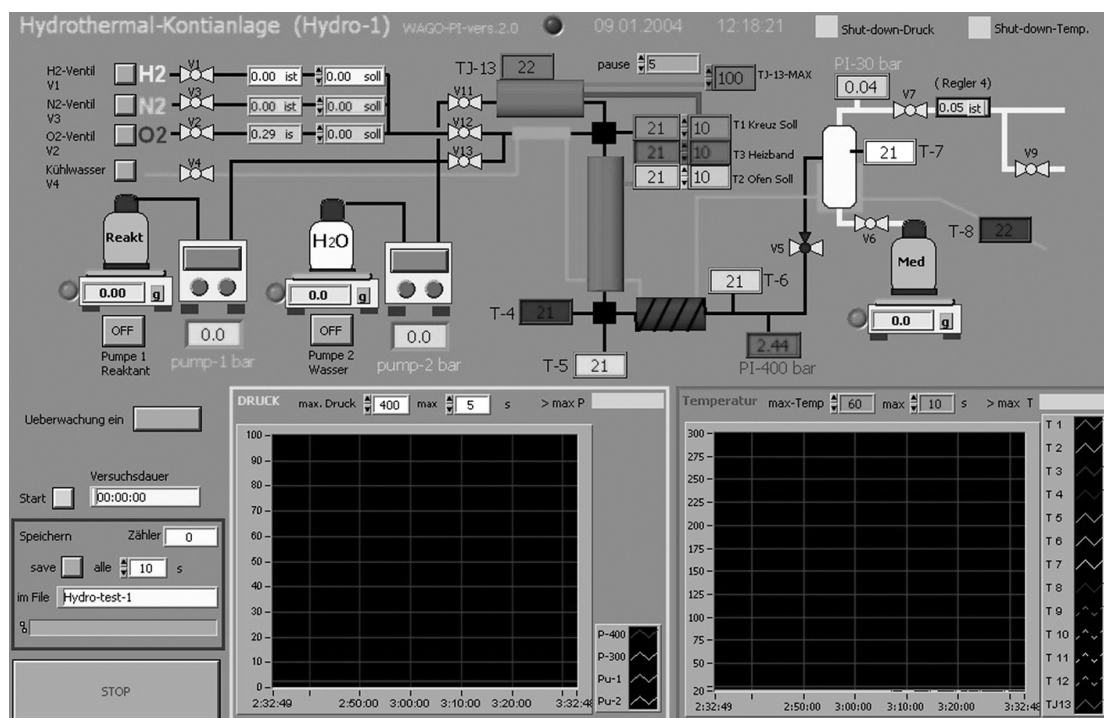


Figure 3.6: LabView™-based data acquisition and monitoring program.

### 3.3.2 Experimental Procedure

During start-up, the plant was heated up by feeding pure water through both pumps at the same flowrates used later in the gasification experiment. Once stable temperatures were reached in the superheater and the reactor, the feed line was switched to feeding biomass. While a change in the weight hourly space velocity,  $WHSV^1$  had an immediate effect, a change in concentration was affected by a short time lag until the new mixture was flown from the mixing cross over the reactor.

1. units:  $g_{organics}/(g_{cat.,dry} \text{ hr})$ .

At the end of an experimental campaign, the organics feed pump was switched to water, and the heating was only switched off after there was no further gas production registered. If the catalyst had to be exchanged, the reactor was depressurized at the preceding temperature (e.g. 400 °C) in order to evaporate the water and empty all feed lines. This greatly facilitated the discharge of the catalyst. Skeletal nickel catalysts however were discharged in a wet condition due to their pyrophoric nature.

### 3.3.3 Analysis

The gas phase was measured on-line with a gas chromatograph (Agilent 6890) with helium as the carrier gas using a Thermal Conductivity Detector (TCD) and a two column switching system (HP-Plot Q and HP-Plot Molecular Sieve) for carbon dioxide, carbon monoxide and hydrogen. An Alltech Heliflex<sup>®</sup> column and a Flame Ionization Detector (FID) were used for the separation and detection of hydrocarbons (methane, ethane, propane and higher HC). It was coupled to a mass spectrometer (HP 5972). However, the MS was only used for qualitative analyses. For a complete description of the method, refer to section 4.1.

Samples of the liquid product phase were taken manually on a regular basis. Their organic and inorganic carbon content was measured off-line with a Dohrmann DC-190 device, allowing for calculating the carbon conversion  $X_C$  as follows:

$$X_C = 1 - \frac{\text{DOC}_{\text{sample}}}{\text{DOC}_{\text{feed}}} \quad (3.5)$$

with DOC being the content of dissolved organic carbon. For all monophasic samples, high pressure ion exchange chromatography yielded the concentration of low-molecular carboxylic acids, aldehydes, alcohols, ketones and phenols. Refer to section 4.2 on page 69 for a description of the applied analytical method.

## 3.4 Heating System for Quartz Capillaries

Most reaction systems described in the literature were made of stainless steel, titanium, Hastelloy, or Inconel. Important data on the catalytic hydrothermal gasification of wet biomass could be gathered [103, 151, 152], but these reactors can themselves exhibit catalytic wall effects [152, 153]; thus, even experiments with no catalysts used were not necessarily non-catalytic. The batch reactor and the continuously operating catalyst test rig presented in this thesis are no exceptions, as they are made of stainless steel. It must be noted however, that the mixing cross and in an early stage also the reactor tube of the continuously operating catalyst test rig were gold coated (gold is reported to be inert also in SCW [121]), but no significant influence of the wall on the macroscopic variables monitored (gas concentration, carbon conversion) was identified.

The University of Twente in the Netherlands was the first to present the idea of using quartz capillaries as micro reactors for hydrothermal experiments [77]. Quartz as reactor material has – besides having no catalytic effect – the additional advantage of being transparent. That the reaction process can be monitored on-line led to the construction of a similar setup here at the Paul Scherrer Institut.

### 3.4.1 Reactor Setup

The capillary reactor system consisted of a bottom plate (145×175 mm, thickness 10 mm) and an upper part with milled notches to place the capillaries. Both parts were made of brass. Six heating cartridges (6.5 mm o.d., length 160 mm, 175 W power) were inserted between the bottom plate and the upper part, adding up to a heating power of ~1 kW. The two sections were held together with 16 screws, attached from the lower part. A scheme of the reactor is displayed in Figure 3.7.

On top of the capillaries and the block, a quartz disk (thickness: 5 mm) was used as a protective media. Additionally, a macrolon window (thickness: 10 mm) secured the microscope (Leica Wild M3Z) and the camera (Leica DFC 320) used to survey the process from glass splinters in case of

capillary explosion. Between the quartz disk and the macrolon window, air was blown to cool the plexiglass. Without this measure, the air above the reactor became too hot and the macrolon started to melt. This caused air bubbles to be incorporated into the plastic matrix which disturbed the view on the capillaries.

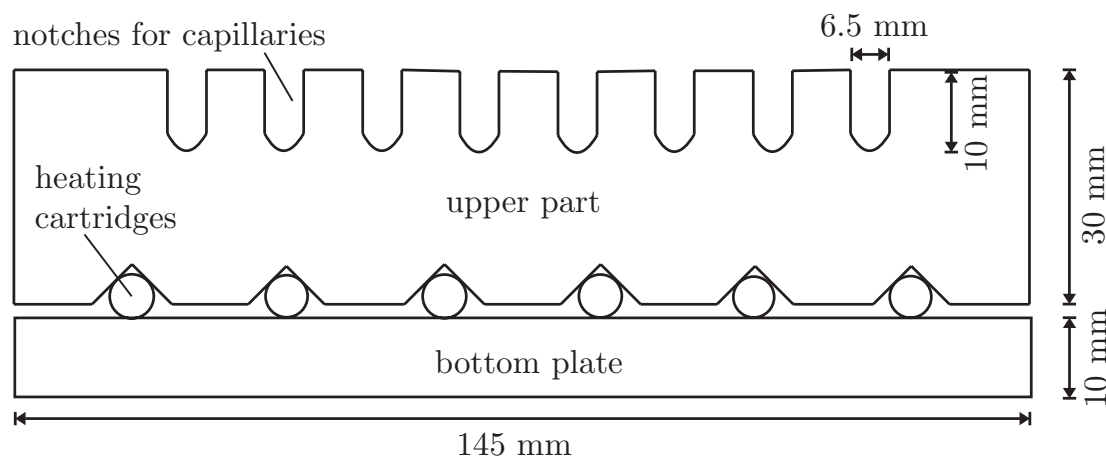


Figure 3.7: Sketch of the side-view of the quartz capillary heating block, made of brass. Between the bottom plate and the upper part with notches, six heating cartridges ensured proper heat input.

The heating block was insulated on its sides and bottom with mineral wool, and the whole apparatus was put into a steel box. A drawback of this setup was the absence of a cooling means, so typical cooling times after reaction were 1 – 2 hours. Two photographs of the apparatus can be seen in Figure 3.8.

### 3.4.2 Quartz Capillaries

Quartz tubes (2 – 3 mm i.d., 5 – 6 mm o.d.) were used as starting material for the capillaries. A wall thickness of 1 – 1.5 mm proved to be sufficient to withstand internal pressures up to 40 – 50 MPa<sup>2</sup>. The tubes were sawed into pieces of 155 mm length. To decrease the tensile stress of the material, the capillaries were heated to 110 °C in vacuo at a rate of

2. Many capillaries were still destroyed during heat-up, possibly due to pressure surges and high tensile stress within the glass. The heating in vacuo prior to reaction served as a remedy.

2 °C/min. and kept at this temperature for three hours. Then, they were slowly cooled down to room temperature within five hours.

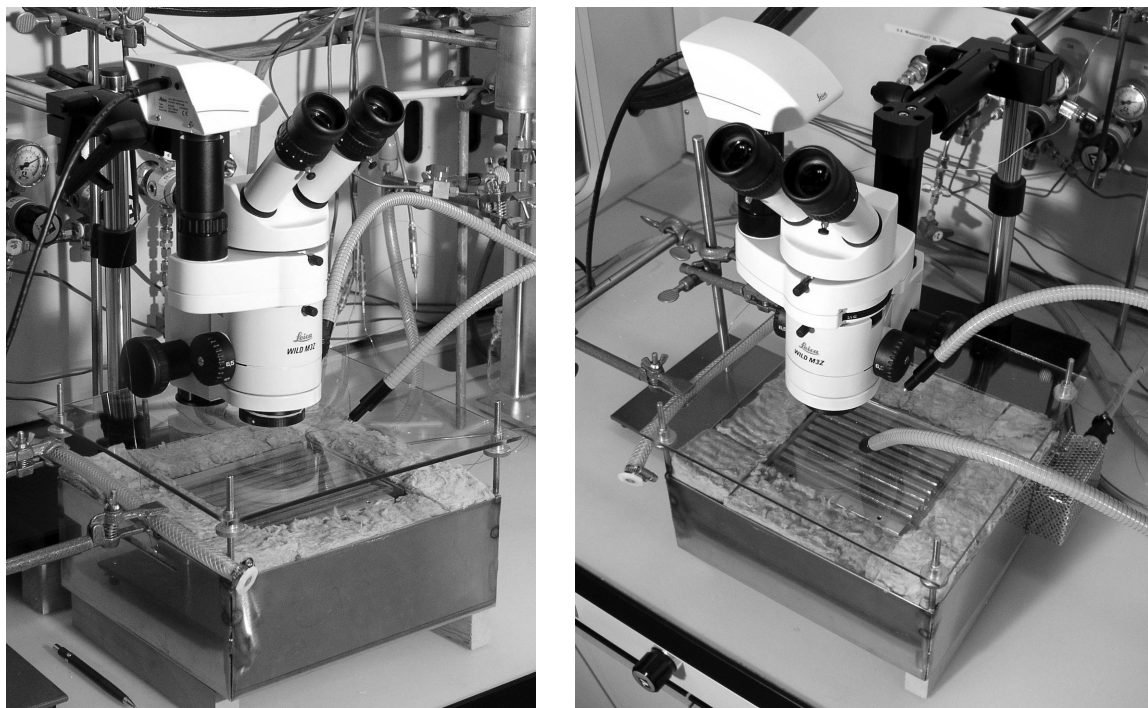


Figure 3.8: Photographs of the setup used for capillary experiments.

After cool-down, the capillaries were sealed on one side by welding with an oxyacetylene torch. Considerable practice was required to close the capillaries nicely: it was important to turn the tube during the procedure, and not to cool it down too fast, i.e. still in the welding flame, but in a cooler section. Additionally, the thickness of the tube at the tip had not to be increased by more than  $\sim 0.3$  mm (the end can easily get the form of a bulb); otherwise, the capillary would not fit into the heating block's notches anymore. On the other hand, the wall thickness of the capillary in the tip should not be reduced either, because a significant thinner tube could easily explode under pressure. An illustration of a capillary after reaction is given in Figure 3.9, together with a magnification of the tips. Once the capillaries were closed on one side by welding, they could be filled with a previously prepared mixture, e.g. wood sawdust slurry and catalyst. The amount to be loaded was calculated in view of the pressure that would result from the temperature planned for the experiment. The



slurry was then transferred into the capillary with a Pasteur pipette. Typical feed amounts were as little as 70 mg.

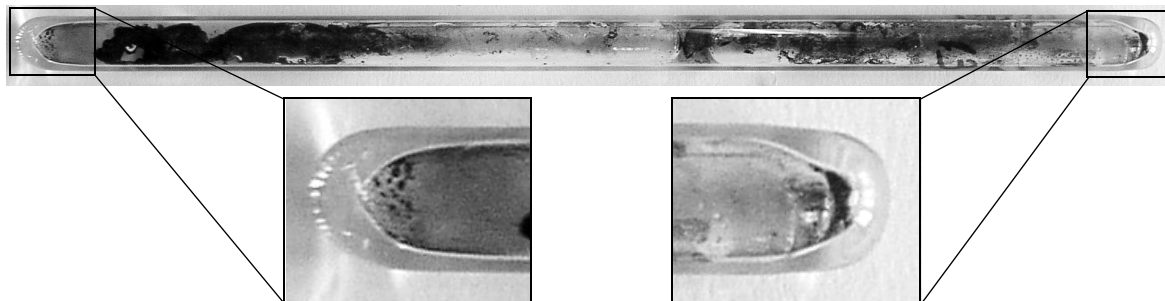


Figure 3.9: Exemplary capillary after reaction, with magnified tips (experiment: S. Rabe, PSI).

Frequently, the amount of water in the slurry was increased by  $\sim 20$  mg due to likely evaporation during the welding closure of the capillary. While one had enough time to seal the first tip of the empty capillary, the welding of the second tip had to be carried out within  $\sim 30$  seconds. To avoid excessive loss of water due to evaporation, the already closed end of the capillary was immersed into liquid nitrogen for  $\sim 20$  seconds until the biomass slurry was frozen. Then it was quickly removed and the open end of the glass tube was sealed with the welding torch. If there were biomass particles close to the torch flame, the particles or the catalyst (especially skeletal nickel) would catch fire. In this case, the capillary had to be disposed of.

### 3.4.3 Experimental

After the capillaries had been sealed, the amount of water lost by evaporation was determined by mass difference. Up to eight capillaries could be put into the heating block at a time, but it was wise not to load more than two simultaneously. In case of explosion, the pressure wave destroyed the quartz disk above the notches, and thereby the intact capillary was destroyed as well.

The capillaries were put into the notches, the final temperature of the block and the heating ramp set, and the process was made visible with

the microscope. Air was made to flow over the block at a rate of 10 L/min. to keep the temperature of the plexiglass window reasonably low. At the end of the experiment, the heating cartridges were switched off which allowed the setup to cool down.

Although originally designed as a quick screening technique, a significant amount of time had to be spent for each experiment, as the welding and loading of the quartz tubes turned out to be difficult. In addition, the analysis of the end-products was very challenging, last but not least due to their enclosure within the glass and the very small feed amounts that were required to keep the pressure within safety limits. For these reasons, the capillaries were mostly used to visualize processes (e.g. the transition into the supercritical state) rather than for extensive catalyst testing.

# Chapter 4: Analytical Tools

## 4.1 Gas Chromatography / Mass Spectrometry

The gas samples of the various experiments were analyzed with the help of a gas chromatograph (Agilent 6890). Helium was used as the carrier gas at a flow rate of 20 mL/min. The device was equipped with a Thermal Conductivity Detector (TCD) heated to 250 °C and a two column switching system (HP-Plot Q, 30 m × 0.53 mm × 40 μm film thickness, and HP-Plot Molecular Sieve 5A, 30 m × 0.53 mm × 50 μm film thickness). The sample loop (volume 1 mL) was injected at  $t = 0.5$  min., with the valve switching between columns at  $t = 2.4$  min. and  $t = 6.0$  min. A split ratio of 1:1 was used.

All off-line gas analyses had to be made with this setup, as the front injector (ready for manual injections, heated to 250 °C) was physically connected to these two columns. Carbon dioxide, carbon monoxide, argon, hydrogen, and lower hydrocarbons (methane, ethane, propane) were detected. The relative scatter in the data was generally low, around 3 %, except for hydrogen, where at low concentrations a scatter in the data of up to 10 – 15 % was registered. The lower detection limit was 1 – 2 vol %, due to the rather small difference in thermal conductivity of hydrogen and the carrier gas helium (0.07 W/(m K) for hydrogen, > 0.16 W/(m K) for all other gases), see Figure 4.1. When nitrogen was used as the carrier gas instead, hydrogen was well detected, but all other gases much worse than with helium, and carbon monoxide was not registered at all, even at high concentrations (> 5 vol %), because its thermal conductivity is overlapping with the one of nitrogen.

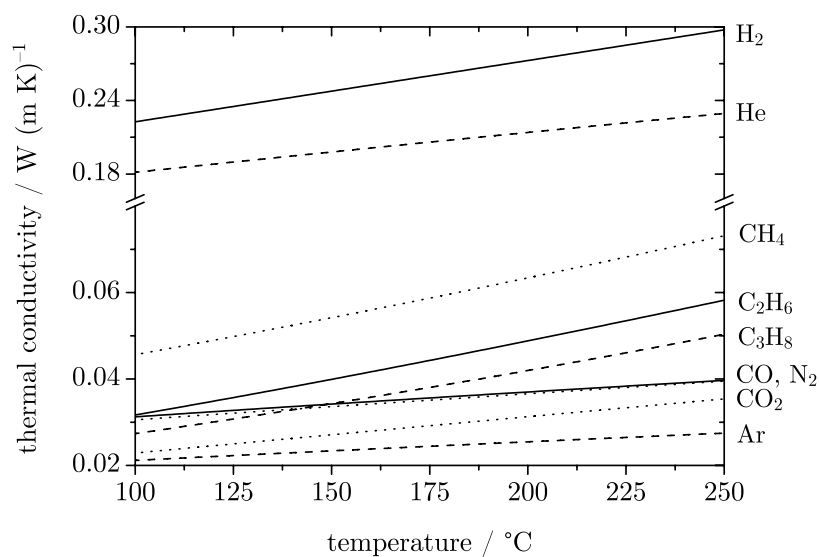


Figure 4.1: Thermal conductivity of the calibrated gases at 1 atm (data from NIST [35]). The conductivity of hydrogen above 126 °C was extrapolated due to the lack of reference data.

Table 4.1: Gas mixtures used for GC calibration.

component	mixture 1 vol %	mixture 2 vol %	mixture 3 vol %	retention time TCD / min.	retention time FID / min.
CH <sub>4</sub>	10	60	92	8.0	4.2
C <sub>2</sub> H <sub>6</sub>	–	0.5	7	4.0	4.4
C <sub>3</sub> H <sub>8</sub>	–	–	1	5.8	4.7
CO <sub>2</sub>	10	33	–	3.1	–
CO	5	0.5	–	8.5	–
H <sub>2</sub>	10	1	–	7.2	–
Ar	65	–	–	7.4	–
N <sub>2</sub>	–	5	–	7.6	–

For the on-line measurements carried out at the continuously operating catalyst test rig, an Alltech Heliflex<sup>®</sup> AT-5 column (30 m × 0.53 mm × 5 µm film thickness, split ratio 5:1, split flow 146 mL/min.) and a Flame Ionization Detector (FID, operating at 250 °C, H<sub>2</sub> flow 35 mL/min., air flow 350 mL/min.) were additionally used to detect the hydrocarbons

(methane, ethane, propane and higher HC), coupled to a mass spectrometer (HP 5972). However, the MS was only used for qualitative analyses.

The temperature profile used for the gas analysis was as follows: hold at 50 °C until  $t = 2.7$  min., heat-up to 150 °C at 50 °C/min. and hold until  $t = 7.2$  min., cool-down to 100 °C at -50 °C/min. and hold until  $t = 9.2$  min. Total duration of the analysis was 9.2 min.

Calibration was carried out with three different gas mixtures and pure CO<sub>2</sub> over a wide concentration range, see Table 4.1, to ensure that the quantification of all reaction gas compositions was properly accomplished.

## 4.2 High Pressure Liquid Chromatography / High Pressure Ion Exchange Chromatography

For the identification and quantification of reaction intermediates such as aldehydes, carboxylic acids, alcohols, and phenols, high pressure liquid chromatography (HPLC, ion exclusion) was used (Dionex P680 pump, Dionex UVD340U UV detector (200 - 600 nm), amperometry by Dionex ED-50 electrochemical detector with Pt-electrode). The eluents and flow rates as well as the specific column types used are tabulated in Table 4.2.

The analysis of cations and anions, e.g. in manure or hydrothermally liquefied wood solutions, was performed with high pressure ion exchange chromatography (HPIEC, Dionex ED-50 electrochemical detector (conductivity mode) with Dionex DS3-1 detector stabilizer). A sketch of the analytical setup is depicted in Figure 4.2.

Table 4.2: Details of the high pressure liquid chromatography setup used.

	alcohols, aldehydes, carboxylic acids	phenols	cations	anions
guard column	–	integrated	Dionex CG12A 4 mm	Dionex GA 1 4 mm
separation column	Dionex ICE AS1 (9 × 250 mm)	MN Nucleodur C8 Gravity (4 × 250 mm)	Dionex CS12A (4 × 250 mm)	Dionex AS11-HC (4 × 250 mm)
self-regenerating suppressor	–	–	Dionex CSRS Ultra II (4 mm)	Dionex ASRS Ultra II (4 mm)
eluent A	H <sub>2</sub> O ( $\chi < 0.07 \mu\text{S/cm}$ )	KH <sub>2</sub> PO <sub>4</sub> (20 mmol/L)	H <sub>2</sub> O ( $\chi < 0.07 \mu\text{S/cm}$ )	H <sub>2</sub> O ( $\chi < 0.07 \mu\text{S/cm}$ )
eluent B	H <sub>2</sub> SO <sub>4</sub> (10 mmol/L)	acetonitrile CH <sub>3</sub> CN	H <sub>2</sub> SO <sub>4</sub> (50 mmol/L)	NaOH (100 mmol/L)
ratio A:B	5 : 95	40 : 60	78 : 22	40 : 60
total flow rate	0.8 mL/min.	0.8 mL/min.	1.0 mL/min.	1.0 mL/min.

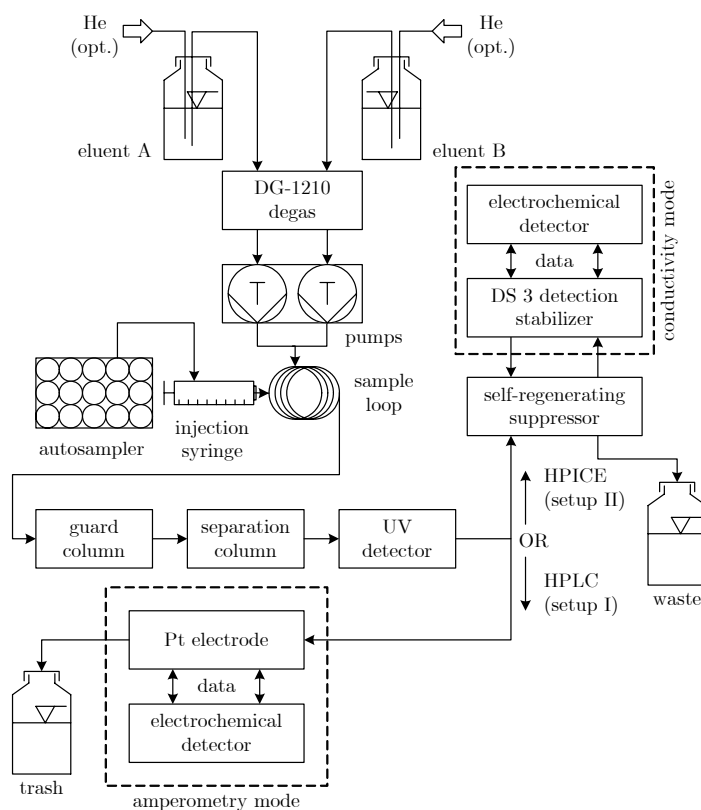


Figure 4.2: Sketch of the high pressure liquid chromatography setup used.

### 4.3 Soxhlet Extraction

Soxhlet extraction was carried out to analyze the biomass and/or the catalysts for their content in inorganics, organics and volatile substances. The procedure was as follows: ~10 g of sample were loaded into a soxhlet jacket and placed into a 250 mL soxhlet apparatus. Water (~200 g, double distilled,  $\chi < 0.07 \mu\text{S}/\text{cm}$ ) in a 500 mL round-bottomed flask was used as extracting agent under reflux at 100 °C for 4 – 5 hours.

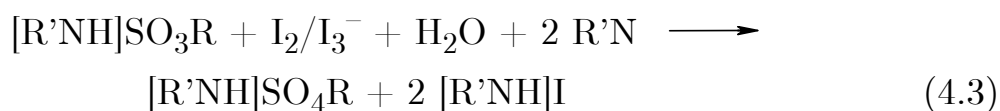
### 4.4 Karl Fischer Titration

The Karl Fischer (KF) method for determining the water content in solutions is well established and has been applied for decades.

The starting point for the development of the method was the Bunsen reaction, where sulfur dioxide is oxidized by iodine in the presence of water, according to (4.1) [154]:



In modern KF titration, an alcohol ROH (typically methanol) reacts with sulfur dioxide and a base R'N (earlier: pyridine, nowadays mostly imidazole) to form an intermediate alkylsulfite salt (4.2), which is then oxidized by iodine to an alkylsulfate salt by consumption of water (4.3):



In this reaction, iodine and water are consumed stoichiometrically 1:1. The iodine is generated electrochemically *in-situ* during the titration. The total amount of water consumed is calculated on the basis of total charge Q passed ( $Q = I \cdot t$ , with 1 mg H<sub>2</sub>O corresponding to a charge of 10.72 C).

Once all water is consumed, iodine is present in excess and detected voltametrically by the titrator's indicator electrode (double Pt electrode), signaling the end-point of the titration. In earlier titration devices, diaphragm cells were used to separate the anode from the cathode in order to prevent the iodine generated at the anode from being reduced to iodide at the cathode instead of reacting with water. Newer devices incorporate a diaphragm free design, where the migration of iodine to the cathode is hindered through a smart combination of factors.

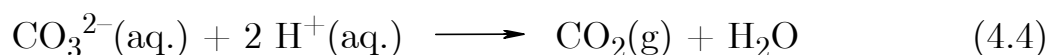
The analysis of water in solutions was carried out on a Metrohm KF-coulometer 737. Typical injection volumes were on the order of 20 – 100 mg, depending on the sample's water content.

## 4.5 Dohrmann-Rosemount DC-190

A Dohrmann-Rosemount DC-190 TOC analyzer was used to measure the total carbon (TC) and inorganic carbon (IC), both in aqueous solutions as well as in solids with the help of a boat module.

For the total carbon measurement, 50  $\mu\text{L}$  of solution were injected with a syringe into an oven at 800  $^{\circ}\text{C}$ . There, the sample was evaporated and oxidized over a Pt catalyst under oxygen flow (250 mL/min.) to  $\text{CO}_2$ , which was detected by a non-dispersive infrared (NDIR) detector. The lower detection limit was 50 – 100 ppm C. Solutions with more than 5000 ppm C had to be diluted first. As long as the samples were homogeneous, the scatter in data was 3 – 5 %. Inhomogeneous samples had to be diluted until they formed a singular phase.

In order to measure the content of inorganic carbon, samples of 50  $\mu\text{L}$  were injected into a phosphoric acid bath (conc. 20 wt %), where the following reaction took place:





The CO<sub>2</sub> was stripped out of the phosphoric acid by oxygen and detected by NDIR. The detection limit was in the same range of ~50 – 100 ppm C. The total organic carbon content of the samples (or dissolved organic carbon content, DOC) was calculated by subtracting the inorganic from the total carbon measured.

A boat module was connected via a Teflon tube with the DC-190. The boat module consisted of a hatch where ceramic boats, filled with the solid sample, could be loaded into a glass tube. The boats were placed onto a wire (length ~40 cm) with a magnet at the opposite end. With the help of the magnet, the boat could be moved through the glass tube into a tubular oven, heated to 1200 °C, where the sample was burnt under flowing oxygen. The combustion gas flowed then via a Co oxide catalyst (to oxidize any potential residual carbon monoxide) and a Cu catalyst (in case of HCl in the gas) over the NDIR detector.

Calibration of the total carbon was achieved with solid samples or liquid solutions of potassiumhydrogenphthalate (C<sub>8</sub>H<sub>5</sub>KO<sub>4</sub>, puriss. p.a., Fluka) which burns in oxygen without residue. The inorganic carbon was calibrated with solutions of sodium carbonate (water free, 99.9 %, p.a., Merck).

## 4.6 Inductively Coupled Plasma - Optical Emission Spectrometry (ICP-OES)

For inductively coupled plasma (ICP) analyses, the samples were chemically decomposed if necessary (solid samples) in a digester (Anton Paar Microwave 3000, max. temperature 200 °C, max. pressure 6.0 MPa) and brought into solution, typically with a mixture of solutions of HNO<sub>3</sub>, HF, and H<sub>3</sub>BO<sub>3</sub>.

This solution was nebulized and sprayed into the argon plasma flame (temperature 6000 – 8000 °C) of the analysis device (Varian Liberty 110), which decomposed the compounds of the solution into atoms and ions. The plasma flame brought the atoms and ions into an excited state;

during the transition back to the unexcited state, the elements emit light. This light was resolved in a spectrometer, and the elements were detected on a photocell multiplier by means of the element specific wavelength of the emitted light. Quantitative analysis was realized by measuring the corresponding intensities.

## 4.7 Brunauer-Emmett-Teller Surface Area (BET)

Full Brunauer, Emmett, and Teller (BET) isotherm measurements (on Micromeritics ASAP 2010 and Micromeritics TriStar 3000) were carried out to identify BET surface area, external surface area, average pore diameter, and total pore volume of the catalysts or supports. Nitrogen at  $-195.8\text{ }^{\circ}\text{C}$  was used as adsorptive.

For the isotherm measurements, a known amount  $V_{\text{ads}}$  of adsorptive is given to the pre-evacuated sample, and the resulting pressure  $p$  is measured. Some of the nitrogen will adsorb on the surface or on already adsorbed nitrogen molecules (multilayer adsorption is accounted for in BET, in contrast to the Langmuir isotherms).

The following formula (4.5) can be applied to calculate the volume of a monolayer  $V_{\text{m}}$  as well as the frequency factor  $k$  (the ratio of the residence time for adsorption on uncovered surfaces to the residence time for adsorption to already adsorbed molecules):

$$\frac{p}{V_{\text{ads}} \cdot (p_0 - p)} = \frac{1}{V_{\text{m}} k} + \frac{k-1}{V_{\text{m}} k} \cdot \frac{p}{p_0} \quad (4.5)$$

with  $p_0$  being the pressure at which condensation occurs. Plotting  $p/V_{\text{ads}}(p_0 - p)$  versus  $p/p_0$  yields a straight line with slope  $(k-1)/V_{\text{m}}k$  and intercept  $1/V_{\text{m}}k$ . The BET surface area  $S_{\text{BET}}$  is then calculated by taking the ratio of the volume of a monolayer  $V_{\text{m}}$  to the molar volume of the gas at standard conditions, multiplied by the area  $S_{\text{m}}$  that one molecule occupies ( $16.2\text{ \AA}^2$  for  $\text{N}_2$  at  $-195.8\text{ }^{\circ}\text{C}$ ) times Avogadro's number  $N_{\text{A}}$ :

$$S_{\text{BET}} = \frac{V_{\text{m}}}{22.414 \text{ L/mol}} \cdot N_{\text{A}} \cdot S_{\text{m}} \quad (4.6)$$

These calculations are automatically carried out by the software of the measurement device.

## 4.8 Temperature Programmed Oxidation / Reduction with a TG–FTIR

### 4.8.1 TPO/TPR for the Detection of Carbonaceous Deposits

Temperature programmed reduction (TPR) and oxidation (TPO) of some samples were carried out in a TG–FTIR instrument (thermogravimetry with Fourier transform infrared spectroscopy; TG: Netzsch STA 449C Jupiter; FTIR: Bruker TGA–IR Tensor 27).

Possible carbonaceous deposits on catalysts after their use could be identified by heating the sample under airflow or under inert atmosphere and measuring both the weight change and the evolution of CO<sub>2</sub> at temperature T by IR spectroscopy. For these experiments, ~20 mg of catalyst were put into an Al<sub>2</sub>O<sub>3</sub> crucible prior to analysis and purged with nitrogen. The samples were then dried at 110 °C for 30 min. under inert nitrogen atmosphere before being heated up to 800 °C with a heating rate of 11 °C/min. For TPO, synthetic air was used instead of nitrogen during heat-up.

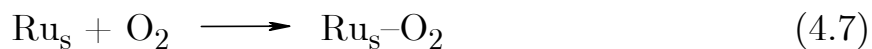
### 4.8.2 Oxygen Chemisorption Dispersion Measurement

To determine the dispersion and average cluster size of heterogeneous metal (particularly ruthenium) catalysts, an oxygen chemisorption method was developed. For these analyses, ~200 mg of granular catalyst was put into a metal basket made of Pt, and purged with helium (quality 6.0; O<sub>2</sub>, N<sub>2</sub>, H<sub>2</sub>O, H<sub>2</sub>, Ne < 0.5 ppm, C<sub>n</sub>H<sub>m</sub>, CO, CO<sub>2</sub> < 0.1 ppm). The analysis was divided in two steps: reduction followed by oxidation.

Reduction: The samples were heated to 300 °C at a rate of 10 °C/min. under an inert helium atmosphere (purified with a Supelco Supelpure™-O oxygen trap, coupled to a Supelco OMI™-1 Indicating Purifier) and held until weight constancy was reached. Hydrogen was then passed over the sample at 300 °C to reduce the dispersed metal. Upon completion (no further decrease in weight), the sample was cooled to room temperature under helium.

Oxidation: At room temperature, oxygen was fed over the catalyst until weight constancy was reached, after which helium was used again. This procedure was repeated to ensure full oxidation of the surface metal. Care had to be taken to be at low temperatures (< 40 °C) in order to avoid oxidation of the metal in the bulk. Masthan and co-workers suggested to carry out the oxygen chemisorption even at -78 °C [155], which was unfortunately not possible with our device.

The surface ruthenium oxidation was assumed to take place according to (4.7) [155-157]:



where multiple adsorption of oxygen is proposed. This stoichiometry holds for particles smaller than  $4 \pm 1$  nm. However, for larger crystallites [158] or ruthenium weight fractions below 0.5 wt % [155], an average of 0.5 O<sub>2</sub> per ruthenium site has been reported. By measuring the weight increase from the fully reduced to the surface oxidized catalyst, the dispersion  $D$  [158] can be calculated as follows:

$$D \equiv \frac{n_{\text{Ru},s}}{n_{\text{Ru}}} = \text{O}_2/\text{Ru} = \frac{n_{\text{O}_2, \text{ deposited}}}{n_{\text{Ru}}} = \frac{\Delta m / (2 \cdot M_{\text{O}})}{m_{\text{Ru}} / M_{\text{Ru}}} \quad (4.8)$$

with

$$m_{\text{Ru}} = w_{\text{Ru}} \cdot m_{\text{cat.,reduced}} \quad (4.9)$$

where  $\Delta m$  refers to the weight increase measured due to oxidation,  $w_{\text{Ru}}$  to

the ruthenium loading of the catalyst,  $m_{\text{cat.,reduced}}$  to the mass of the dry, reduced catalyst sample, and  $M_{\text{O}}$  and  $M_{\text{Ru}}$  refer to the molar mass of oxygen and ruthenium, respectively.

The average crystallite size  $l$  assuming cubic shape derives from [159]:

$$l = \frac{6}{S \cdot \rho_{\text{Ru}}} \quad (4.10)$$

with

$$S = \frac{D \cdot (m_{\text{Ru}}/M_{\text{Ru}}) \cdot N_{\text{A}} \cdot A_{\text{Ru}}}{m_{\text{Ru}}} = \frac{D \cdot N_{\text{A}} \cdot A_{\text{Ru}}}{M_{\text{Ru}}} \quad (4.11)$$

where  $S$  refers to the surface area per gram of metal,  $\rho_{\text{Ru}}$  to the ruthenium density (1237 kg/m<sup>3</sup>),  $N_{\text{A}}$  to Avogadro's number, and  $A_{\text{Ru}}$  to the average surface that one ruthenium atom occupies ( $9.03 \times 10^{-20}$  m<sup>2</sup> [160]). The specific active metal surface per gram of catalyst  $A_s$  is then:

$$A_s = S \cdot w_{\text{Ru}} \quad (4.12)$$

As most catalysts after use contained some metal corrosion products on the surface which would interfere with the dispersion measurement (they are commonly less noble and are thus oxidized first), this procedure was only used to measure the dispersion of fresh catalysts.

## 4.9 X-Ray Diffraction (XRD)

X-ray diffraction (XRD) on a Philips X'Pert device using Fe K $\alpha$  radiation (wave-length 0.1936 nm) yielded the crystal size and by comparison with reference spectra in certain cases also the oxidation states of the catalysts (e.g. NiO). Due to the device's sensitivity,  $\geq 5$  wt % of the metal had to be present in order to be identified, and crystallite sizes of  $\geq 5$  nm were needed. The crystallite size  $B$  was calculated using the modified Scherrer equation (4.13) [161]:

$$B = \frac{0.89 \cdot \lambda}{\Delta 2\theta \cdot \cos \theta} \quad (4.13)$$

with 0.89 a constant referring to measuring the peak width at half intensity,  $\lambda$  being the wave-length of the X-ray used,  $\Delta 2\theta$  the peak width and  $\theta$  the half angle of incidence of the X-ray beam ( $5 - 55^\circ$  used) at which the peak arose. It must be noted that the calculated particle size is the lower limit, as the smallest particles determine the spectral linewidth.

The X-rays interfere with the atoms of the crystallites, which as a result emit spherical waves of the same wavelength that overlap and eventually cancel out if they are not in phase, i.e. the waves must fulfill the Bragg condition (4.14) to be reflected.

$$\Delta = 2d \cdot \sin \theta = n \cdot \lambda \quad (4.14)$$

with  $d$  being the lattice layer distance,  $\theta$  the half angle of incidence of the X-ray,  $n$  the diffraction order and  $\lambda$  the wave length of the X-ray. Reflections at a slightly different angle,  $\theta + d\theta$ , will extinguish each other for sufficiently large crystals, as there will always be another lattice layer  $n$  so that the emitted wave has a phase difference of  $\pi$  with the wave of the first layer. For small crystallites, however, the number of lattice layers is limited, and not all waves are thus canceling each other out. As a result, there is a peak in the spectrum. The angles of incidence at which the reflections take place are characteristic for each different element.

## 4.10 X-Ray Photoelectron Spectroscopy (XPS)

X-ray photoelectron spectroscopy (XPS) was carried out on the catalyst samples to analyze the surface in terms of the oxidation state of the metal and potential deposits. As the samples were usually dried in air, most metals were oxidized. Twin-anode Mg  $K\alpha$  radiation was used as the X-ray source in a VG Escalab 220i XL apparatus.

## 4.11 Scanning Electron Microscopy (SEM)

The morphology of catalyst samples was visualized with scanning electron microscopy (SEM) on a Zeiss DSM 962 (thermionic electron gun at 30 kV). It was coupled to energy dispersive X-ray spectroscopy (EDXS, Noran System SIX, Pioneer Si(Li) detector, Norvar window) which allowed for the quantification of the metal content near the surface, possible corrosion product depositions on aged catalysts, and presumably bound sulfur (on the Ru/C catalyst). The samples were made conductive with a carbon spray, thus carbon was not accounted for in the analysis. Point-and-shoot analysis served to identify corrosion product deposits, while mappings with full EDXS analysis of the spectra over representative surface areas were used for global quantifications.

## 4.12 Scanning Transmission Electron Microscopy (STEM)

To visualize the crystal size and its distribution on the carrier, scanning transmission electron microscopy (STEM) was used. For this, the material was ground, dispersed in ethanol and some droplets were deposited onto a perforated carbon foil, supported on a copper grid. The investigations were performed at ETH Zurich on a Tecnai F30 microscope (FEI (Eindhoven); field emission cathode, operated at 300 kV). STEM images, obtained with a high-angle annular dark field (HAADF) detector, revealed the metal particles with bright contrast (Z contrast). Energy dispersive X-ray spectroscopy (EDXS) was carried out using an EDAX system which was attached to the Tecnai F30 microscope. For a good overview of the technique used for the characterization of heterogeneous catalysts, see the recent publication of Liu [162].





# Chapter 5: Analysis of Feedstocks

## 5.1 Spruce and Fir – Woody Biomass

For experiments with woody biomass, a mixture of spruce and fir chips (bark-free, purchased from Hans Schwere, Sägewerk u. Holzhandel AG, Leuggern, Switzerland) was dried and milled to small particles with a knife mill ( $x_{50} \sim 300 \mu\text{m}$ ).

The wood's ash content was determined by incineration in a ceramic pot at 550 °C according to the DIN standard 38414-S3 to be 0.31 wt % of the dry matter.

The wood was analyzed at ETH Zurich (Laboratory for Organic Chemistry) for its elemental composition, i.e. C, H, O, N, and S. The results are tabulated in Table 5.1.

Table 5.1: Elemental composition of the spruce and fir mixture (bark-free) used.

element	wt %	ash-free wt % <sup>a</sup>	ash-free mol %
C	49.34	49.30	31.6
H	6.13	6.12	47.0
O	44.53	44.49	21.4
N	0.08	0.07	$4.11 \times 10^{-2}$
S	0.02	0.02	$4.8 \times 10^{-3}$
ash	0.31	–	–

a. normalized to 100 %.

To simplify matters, the nitrogen and sulfur was accounted for in volatile substances not ending up in the ash. This simplification is valid as the

content in N and S is very low. For manure, a more sophisticated approach had to be used.

The empirical formula for the wood used in this work was thus  $\text{CH}_{1.490}\text{O}_{0.677}$ , neglecting the nitrogen and sulfur.

The higher heating value (comprising the heat release due to condensation of the product water generated upon combustion) of the dry ash-free wood,  $\text{HHV}_{\text{daf}}$ , was calculated by using an empirical formula [163] to 19.8 MJ/kg, while the lower heating value,  $\text{LHV}_{\text{daf}}$ , was calculated (acc. to an empirical formula [164]) to 18.2 MJ/kg.

The content of lignin, cellulose and hemicellulose was not determined experimentally. As a reference, data was taken from the literature [165]. For spruce, the lignin content was reported to be 28 wt % (acid insoluble lignin), while the hemicellulose content was 20.9 wt %, and the cellulose content was 41.1 wt %.

An HPIEC analysis of the soxhlet extractive of bark-free spruce and fir yielded the composition in and content of inorganic ions contained in the wood, see Table 5.2.

Table 5.2: Ions detected in the soxhlet extractive of bark-free spruce and fir.

cation	conc. mg/kg <sup>a</sup>	conc. mmol/kg <sup>a</sup>	anion	conc. mg/kg <sup>a</sup>	conc. mmol/kg <sup>a</sup>
sodium	573	24.9	acetate	6524	144.9
ammonium	153	8.5	propanoate	2	0.03
potassium	467	11.9	chloride	481	13.6
magnesium	107	4.4	nitrate	2584	41.7
calcium	499	12.5	sulfate	1080	11.2
			oxalate	197	2.2
			phosphate	54	0.6
			thiosulfate	1	0.01

a. based on the dry matter of the wood.

Acetate, propanoate and oxalate are likely to exist in their acidic form in woody biomass slurries as acetic, propanoic and oxalic acid. The nitrate content was surprisingly high, whereas the content of chloride was rather low. Therefore, the stainless steel batch apparatus was suitable for performing hydrothermal gasification experiments; there was no titanium liner needed to prevent corrosion.

In a typical gasification experiment using the batch reactor,  $\sim 0.7$  g wood were gasified in  $\sim 7$  g water. Thus, inside the reactor the concentration of chloride and sulfate was typically  $\sim 50$  ppm and  $\sim 110$  ppm<sup>1</sup>, respectively. Mild corrosion can occur at these low concentrations around the critical point of water [166], but for short batch experiments (usually 1 – 2 hrs), no countermeasures had to be taken. In contrast to near-critical water, much higher chloride contents (of the order of  $10^4$  ppm) are needed for stainless steel to corrode at ambient conditions (in acidic media, pH = 2) [167].

## 5.2 Synthetic Liquefied Wood

While wood slurries are an excellent feedstock for initial catalyst screenings in the batch reactor, their deficiency is that they cannot be pumped reliably on a laboratory scale. A liquid feed with chemical behavior akin to wood was thus needed.

As described in section 5.1, spruce is made up of 28 wt % of lignin. Lignin is a large biopolymer consisting of linked (mostly ether and ester bonds) p-coumaryl, coniferyl, and sinapyl alcohol monomers (depicted in Figure 5.1). For simplicity, only coniferyl alcohol was chosen to represent

---

1. Sulfate was later determined to deactivate ruthenium based catalysts (and possibly also nickel based catalysts). For the stable 2 wt % Ru/C (Engelhard) catalyst, 110 ppm  $\text{SO}_4^{2-}$  corresponded to a molar sulfate-to-ruthenium ratio of 0.056 (for a wood-to-catalyst ratio of 1), and 0.113 (for a wood-to-catalyst ratio of 2). However, a deactivating effect of sulfate in continuous experiments became only apparent for sulfate-to-ruthenium ratios exceeding 0.7, compare with section 7.2 and Figure 7.17 on page 207. The amount fed with wood was thus insufficient to poison the catalyst.

the lignin fraction of the wood, as it has one methoxy group (in contrast to none for p-coumaryl, or two for sinapyl alcohol).

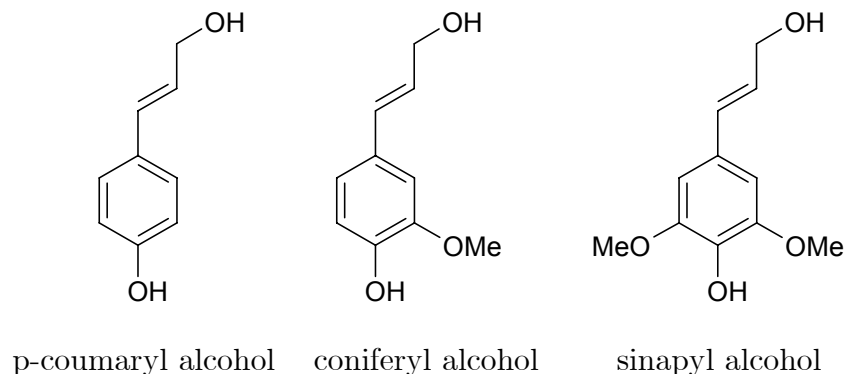


Figure 5.1: Lignin monomers.

Accordingly, 72 wt % of spruce are made up of cellulose and hemicellulose. Cellulose is a straight chain polymer (unlike starch) made of glucose monomers, linked through  $\beta$ -1,4 glycosidic bonds (opposed to  $\alpha$ -1,4 linkages for starch yielding in a weaker polymer [168]), as displayed in Figure 5.2. Thus, glucose was chosen to represent the cellulose and hemicellulose fraction of wood.

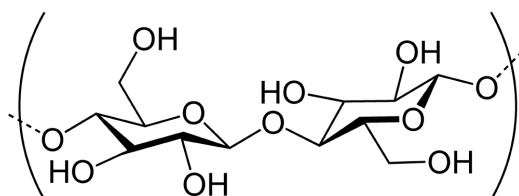


Figure 5.2: Cellulose, a straight chain polymer of glucose monomers.

The two building blocks of spruce are summarized in Table 5.3. Both monomers have a molecular mass of 180.2 g/mol, and therefore their mass proportion is equal to their molar proportion. The simplified empirical formula of hydrolyzed wood is  $\text{CH}_{1.69}\text{O}_{0.72}$ , thus consisting of 47.60 wt % C, 6.75 wt % H, and 45.65 wt % O.

As glucose and coniferyl alcohol are hydrothermally decomposed prior to being gasified, a mixture of organic substances representing these two

Table 5.3: Hydrolyzed wood and its building blocks glucose and coniferyl alcohol.

	C	H	O	$M_i$ g/mol	$w_i$	$x_i$
glucose	6	12	6	180.2	0.72	0.72
coniferyl alcohol	10	12	3	180.2	0.28	0.28
hydrolyzed wood	1	1.69	0.72	25.3		

building blocks should be chosen to simulate the mixture entering the catalytic reactor, downstream of the preheater where the liquefaction is carried out. To define such a mixture, wood liquefaction experiments were carried out in the batch reactor, see section 6.1.5 and Figure 6.5 on page 105. The resulting liquid phase containing hydrolyzed spruce was analyzed for its constituents by HPLC. Among the many substances detected, the following five were chosen to represent hydrolyzed wood (see also Figure 5.3 and Table 5.4): formic acid, acetic acid, ethanol, phenol, and anisole (methoxybenzene).

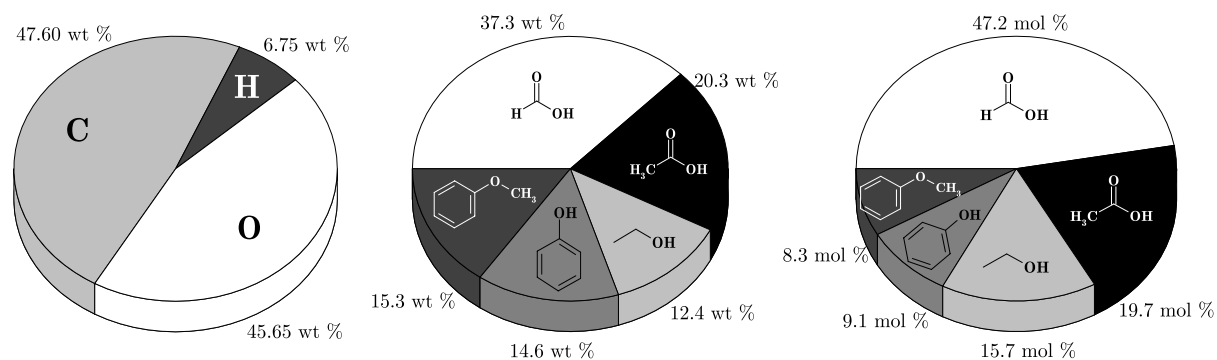


Figure 5.3: Left: C, H, O composition of hydrolyzed wood (and SLW). Middle: weight fractions of formic acid, acetic acid, ethanol, phenol, and anisole in SLW. Right: Mole fractions.

Some of the components are easily degraded, while others might be persistent even after successful gasification experiments, as was investigated with the batch reactor (details are presented in section 6.1.5). The synthetic liquefied wood has the same carbon to hydrogen to oxygen ratio as the bark-free hydrolyzed spruce (1 : 1.69 : 0.72), and the same content in

Table 5.4: Constituents of synthetic liquefied wood.  $w_{C,i}$  = carbon mass fraction in substance  $i$ ,  $w_i/x_i$  = mass/molar fraction of substance  $i$ ,  $C_{C,i}$  = percentage of carbon in feed by substance  $i$  ( $w_{C,i} \cdot w_i$ ),  $X_{C,i}$  = contribution to total carbon gasification if substance  $i$  is converted completely ( $C_{C,i}/\sum C_{C,i}$ ).

substance $i$	C	H	O	$w_{C,i}$	$w_i$	$x_i$	$C_{C,i}$ wt %	$X_{C,i}$ %	gasification
formic acid	1	2	2	0.26	0.373	0.472	9.6	20.0	easy
acetic acid	2	4	2	0.40	0.203	0.197	8.0	16.7	hard
ethanol	2	6	1	0.52	0.124	0.157	6.5	13.6	medium
phenol	6	6	1	0.77	0.146	0.091	11.2	23.4	hard
anisole	7	8	1	0.78	0.153	0.083	12.6	26.3	hard

aromatic molecules. Anisole was not detected as such, but it represents a building block of lignin; others of the detected compounds were not affordable for extensive experiments (e.g. 5-HMF). The mixture displayed here thus nicely represented liquefied real wood and served as an excellent model mixture for long term catalyst tests.

## 5.3 Swine Manure

### 5.3.1 General

The Eidgenössische Forschungsanstalt für Agrarwirtschaft und Landtechnik, Tänikon, Switzerland provided the swine manure used in this thesis. They delivered two types: filtrated raw manure with a dry matter content of ~3 wt %, and filtrated manure, concentrated on a curved screen to a dry matter content of 15 – 20 wt %. For gasification experiments, only the concentrated manure was used, as this is a possible feedstock for a commercial plant. The raw manure has too high a water content for economic operation of a plant; for analytical purposes however, also the diluted raw manure is of value.

### 5.3.2 Dry Matter Content and Elemental Analysis

The dry matter (DM) content of the concentrated manure (as received) was 16.2 wt %. An elemental composition analysis (EA) yielded the carbon, hydrogen, oxygen, nitrogen, and sulfur content of the dry matter, see Table 5.5.

Table 5.5: Elemental analysis of the dry matter of concentrated swine manure.

element	C	H	O	N	S	sum
content / wt % of DM	35.74	5.20	40.85	2.20	0.41	84.40

These 5 elements account for about 5/6 of the composition of the dry matter. No distinction between oxygen bound in organic constituents and oxygen bound in inorganic substances is possible by this method. Complementary analyses were necessary in order to identify the amount of inorganic oxygen. The inorganic oxygen has no positive contribution to the heating value of the feedstock. If not treated separately, the estimation of the energy content in manure is wrong, and net thermal process efficiency evaluations for a hydrothermal gasification plant appear too promising.

### 5.3.3 Incineration Residue

While the ash content of wood was very low, 0.3 wt % of the dry matter, the residue after incineration of concentrated raw manure under O<sub>2</sub> at 550 °C was 26.2 wt % of the dry matter (incineration loss made of organic substances 73.8 wt %), and after incineration under O<sub>2</sub> at 890 °C, it was 24.2 wt %. Between 550 – 890 °C, the carbonates (CaCO<sub>3</sub>, MgCO<sub>3</sub>, Na<sub>2</sub>CO<sub>3</sub>, K<sub>2</sub>CO<sub>3</sub>) decomposed to CO<sub>2</sub> and the corresponding metal oxides. The mass difference was 2.0 wt %, corresponding to the CO<sub>2</sub> lost. Two inorganic oxygen atoms of the carbonates are accounted for in the CO<sub>2</sub> fraction, while the third oxygen atom is then accounted for in the metal oxide fraction, determined later. The inorganic oxygen of the carbonate fraction was thus ~1.5 wt % of the dry matter.

It is important to know the composition of the dry matter for several reasons: (i) contained salts can have a deactivating effect on the catalyst, (ii) the salts are responsible for corrosion, and, as stated before, (iii) the amount of inorganic oxygen must be identified for the accurate determination of the heating value.

The constituents of manure can be divided into sub-groups, according to a thermal or a chemical viewpoint.

### 5.3.4 Thermal vs. Chemical Viewpoint

From a thermal point of view, the manure can be divided into these three groups of constituents:

1. water content ( $\text{H}_2\text{O}$ )
2. incineration loss (IL)
3. incineration residue (IR)

Thereby, 2. + 3. represent the dry matter content (DM).

From a chemical point of view, the manure can be divided into these six groups of constituents:

1. water content ( $\text{H}_2\text{O}$ )
2. dissolved organics (DOC)
3. organic solid material ( $\text{TC} - \text{IC} - \text{DOC}$ )
4. carbonates and hydrogen carbonates (IC)
5. dissolved inorganic salts (other than (hydrogen) carbonates)
6. oxides (e.g.  $\text{MgO}$ ,  $\text{CaO}$ ,  $\text{K}_2\text{O}$ ,  $\text{Na}_2\text{O}$ ,  $\text{SiO}_2$ ,  $\text{Al}_2\text{O}_3$ )

The two different viewpoints are depicted in Figure 5.4.



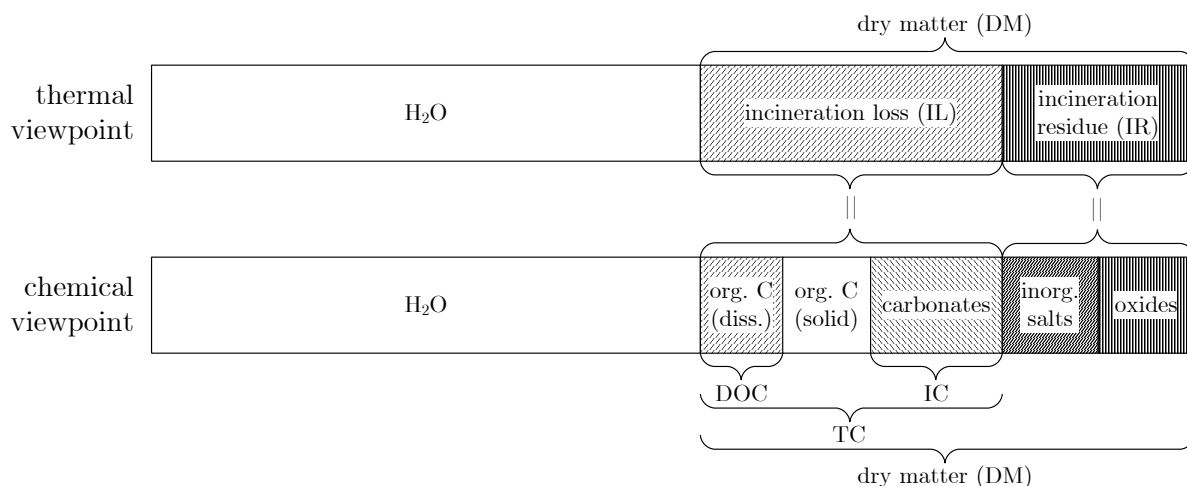


Figure 5.4: Constituents of concentrated swine manure. Thermal viewpoint (above) vs. chemical viewpoint (below). DOC: dissolved organic content, TC: total carbon, IC: inorganic carbon.

In addition to the thermal analysis (water content, incineration loss, incineration residue), soxhlet extraction combined with an HPIEC analysis was carried out to identify salts, and an ICP analysis of the incineration residue to identify the oxides.

### 5.3.5 Washing Procedure and Soxhlet Extraction

When gasification experiments with manure were carried out, a washing procedure was applied to free the manure from its salts. The idea was to set a salt-free manure as a reference material, and test the influence of the salts on gasification (conversion, gas composition, etc.) separately by adding them back before the experiment. However, the washing procedure turned out to be highly insufficient, and most salts stayed in the manure, possibly enclosed within the cells of the biomass.

The dry matter was elutriated with water ( $\chi < 0.07 \mu\text{S}/\text{cm}$ ) and mixed with a spatula for  $\sim 1$  min. After decanting the water, the residue was centrifuged. The procedure was repeated 6 times, yielding a wash water fraction and a slurry fraction. The slurry fraction was then treated by Soxhlet extraction for 5 hrs (extracting agent: water under reflux). The two phases (soxhlet extract and wash water fraction from decanting) were filtered over a membrane filter (regenerated cellulose,  $0.45 \mu\text{m}$  pore size,

Schleicher & Schuell) and analyzed by HPIEC. The washing procedure is visualized in Figure 5.5.

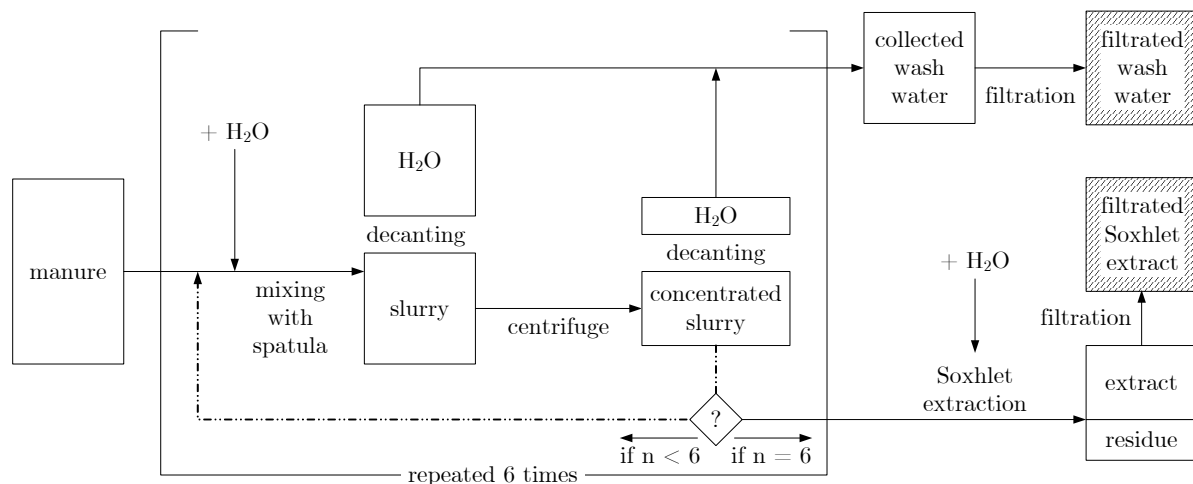


Figure 5.5: Washing procedure with manure, resulting in a filtrated wash water fraction and a filtrated Soxhlet extract.

### 5.3.6 Analysis of Ions Contained In Swine Manure

The ions contained in the concentrated swine manure were measured by high pressure ion exclusion chromatography and are tabulated in Table 5.6. The content of the untreated manure was calculated by summing up the contents of the wash water and the soxhlet extract. By measuring the two of them separately, a measure of the washing efficiency for the specific salts could be gained.

As can be seen, most salts were not extracted from the manure by the washing procedure. The sum of sulfate and thiosulfate corresponds to 0.44 wt % sulfur of the dry matter, matching nicely the amount determined by elemental analysis (0.41 wt %). By comparison, the results of the nitrogen found by the two methods, agree rather poorly: 2.20 wt % were measured by elemental analysis, while the sum of ammonium and nitrate, determined by HPIEC, yield a nitrogen content of 4.11 wt % of the dry matter. This stands in contrast to the expected value, since nitrogen should also have been found in proteins, which could not be detected by HPIEC. Hence, the amount determined by HPIEC should be lower than the one determined by elemental composition analysis, and not higher. On the other hand, ammonium could be volatilized (as  $\text{NH}_3$ ) in

the timespan starting with the drying of the manure, to the milling, the transportation and the evaporation of the sample before the elemental analysis. If this was the case, it is as expected: the amount determined by EA corresponded to the nitrogen in nitrates and proteins, and the amount determined by HPIEC to the nitrogen in nitrates and ammonium. Then, the real amount of nitrogen would be of the order of  $\sim 5.8$  wt % of the dry matter. Due to these circumstances, there is a large uncertainty attached to the value of the nitrogen content;  $\sim 5$  wt % seems to be a reasonable estimate.

Table 5.6: Ion content of the concentrated swine manure<sup>a</sup> (washed, unwashed) and washing efficiency for the specified ions.

anion	untreated conc. mg/kg	washed conc. mg/kg	washing efficiency %	cation	untreated conc. mg/kg	washed conc. mg/kg	washing efficiency %
chloride	5460	5070	7	sodium	6740	3590	47
nitrate	20780	7000	66	ammonium	46790	19600	58
phosphate	66930	10660	84	potassium	9080	7260	20
sulfate	10530	3320	69	magnesium	3810	890	84
thiosulfate	1610	0	100	calcium	2720	1690	38
oxalate	1200	0	100				
propanoate	30	0	100				
fluoride	38	22	43				

a. all concentrations are based on the dry matter.

The hydrogen of the ammonium ions made up  $\sim 1.1$  wt % of the dry matter of manure. Assuming the ammonium was lost due to volatilization prior to the elemental analysis, the total amount of hydrogen corresponded to 6.30 wt % of the dry matter.

The amount of oxygen contained in the phosphate, nitrate, sulfate, and thiosulfate detected by HPIEC was 4.51 wt %, 1.61 wt %, 0.7 wt %, and 0.07 wt % of the dry matter, respectively, adding up to 6.89 wt %.

### 5.3.7 Analysis of Metal Oxides Contained in Swine Manure

The incineration residue of concentrated swine manure was digested in a mixture of 20 mL HNO<sub>3</sub>, 20 mL HF, 200 mL H<sub>3</sub>BO<sub>3</sub> in 260 mL H<sub>2</sub>O. The resulting solution was analyzed for its metal content by ICP-OES. It is presented in Table 5.7.

Table 5.7: Elements detected in incineration residue of swine manure by ICP<sup>a</sup>.

element	conc. mg/kg	probable oxide	oxygen in oxide mg/kg
Mg	33770	MgO	22230
Ca	29980	CaO	11967
Si	14775	SiO <sub>2</sub>	16834
Al	3185	Al <sub>2</sub> O <sub>3</sub>	2833
Fe	2900	Fe <sub>2</sub> O <sub>3</sub>	1247
Mn	940	MnO	274
Zn	725	ZnO	328
Cu	135	CuO	34
Pb	3.6	PbO	0.3
Cd	1.3	CdO	0.2

a. the concentrations are based on the dry matter of manure, not its incineration residue.

Besides Si and Al (probably as sand, SiO<sub>2</sub> and Al<sub>2</sub>O<sub>3</sub>), Fe, Mn, and Zn, the majority of the metal content was made up of Ca and Mg. Na and K were not quantitized by this method due to poor reproducibility of the measurement results. While HPIEC measured ion contents of Ca<sup>2+</sup> and Mg<sup>2+</sup> of the order of 0.3 wt % each, the amount determined by ICP was ~10 times more, about 3 wt %. A possible explanation is that the earth metals are mostly present in form of oxides rather than ions in solution (CaO, MgO, part of it originally as carbonates prior to incineration; it

could be estimated that ~10 % of the Ca and Mg were present as carbonates, corresponding to the 1.1 wt % loss measured by incineration from 550 – 890 °C attributed to the earth alkali metals). For the quantification of the elements Na and K, the results of the HPIEC analysis were taken (due to the lack of reliable ICP data), while for the quantification of Ca, Mg, Si, Al, Fe, Mn, Zn, and Cu, the ICP were used.

Assuming that Ca and Mg were present as CaO and MgO, respectively (10 % of it as carbonates), and that all Si, Al, Fe, Mn, Zn, and Cu were present as SiO<sub>2</sub>, Al<sub>2</sub>O<sub>3</sub>, Fe<sub>2</sub>O<sub>3</sub>, MnO, ZnO, and CuO, respectively, the oxygen contained in these metal oxides corresponded to 5.57 wt % of the dry matter of concentrated swine manure.

### 5.3.8 Summary of Analytical Results

The total inorganic oxygen of the concentrated swine manure was determined to be ~14.0 wt % of the dry matter. About 1.5 wt % stemmed from carbonates, ~6.9 wt % from inorganic salts (phosphate, nitrate, sulfate, and thiosulfate), and ~5.6 wt % from metal oxides. Thus, only 26.9 wt % of the dry matter, or 66 % of the total oxygen, was oxygen bound in organic substances, contributing positively to the heating value of the manure. Oxalate and propanoate ions most likely exist in their acidic form and are thus gasifyable.

The distribution of oxygen on the various constituents is depicted in Figure 5.6.

The global balance closes very nicely to 99.3 wt %: C, H, O, N, S by elemental analysis make 84.4 wt %. N and H are probably underestimated due to loss of ammonia, leading to the correction of an additional ~1 wt % for H and ~3 wt % for N. Cl, Na, and K by HPIEC have a proportion of 0.55 wt %, 0.67 wt %, and 0.91 wt %, respectively. Phosphorus detected in phosphate makes 2.1 wt %, and the metals detected by ICP sum up to 6.7 wt %.

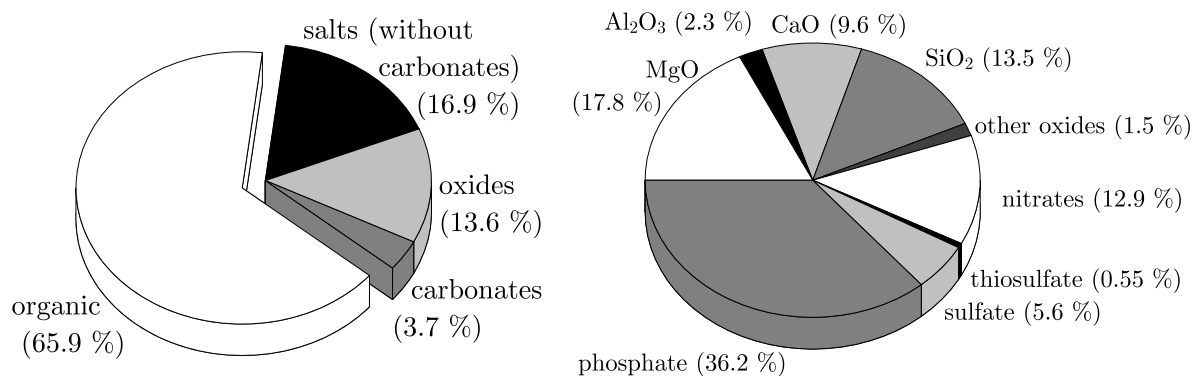


Figure 5.6: Distribution of the oxygen in concentrated swine manure. Left: Sources of oxygen (proportions relative to total oxygen). Right: Oxygen bound in inorganic substances (proportions relative to total inorganic oxygen).

Based on this analysis, the lower heating value LHV of the dry matter of concentrated swine manure is 16.3 MJ/kg (correlation: [164]), while the higher heating value HHV is 17.6 MJ/kg (correlation: [163]).

The proposed combination of analytical methods (elemental composition analysis, incineration loss, Soxhlet extraction, HPIEC, and ICP) yield the composition of manure with total balances closing nicely. It seems thus to be of reasonable accuracy.

## 5.4 Palm Oil Pyrolysis Condensate

In Southeast Asia, particularly in Malaysia, palm oil pressing residues are an abundant feedstock used for the production of pyrolysis gas. A large aqueous waste stream is generated in the pyrolysis process: palm oil pyrolysis condensate. About half of the global annual production of palm oil originates from Malaysia, corresponding to some 20 million tons a year, producing aqueous waste streams exceeding 30 million tons annually [67]. If the pyrolysis condensate could be used to produce SNG in a hydrothermal plant, the pyrolysis efficiency could be enhanced and simul-

taneously the waste stream problem associated with it would be solved. Besides its economic significance, palm oil pyrolysis condensate (short: pyrolysis condensate) is – in contrast to manure or wood slurries – an aqueous liquid phase, with salt concentrations somewhere in between the content of wood and manure. Pumping is greatly simplified in comparison to handling manure or wood slurries on a laboratory scale (throughput  $\sim 1$  kg/hr), as many problems can be avoided (segregation of the liquid and solid phase, contamination with solids on the sealing face of the pump’s valve seats, etc.). For this reason, pyrolysis condensate is the feedstock of choice for a small process demonstration unit (see chapter 8) of the order of  $1 \text{ kW}_{\text{th}}$ , or a gas production of  $200 - 400 \text{ L/hr}$ , even if the feedstock is not common in Europe.

The density of the pyrolysis condensate was determined in a 100 mL volumetric flask to slightly heavier than pure water. The electric conductivity was  $4.20 \text{ mS/cm}$ . The condensate was acidic, with a pH of  $3 - 4$ . The water content was determined by KF titration to be  $55.2 \text{ wt } \%$ . The dry matter content was determined by evaporation at  $105 \text{ }^\circ\text{C}$  and  $100 \text{ hPa}$  to be  $17.8 \text{ wt } \%$ .  $27 \text{ wt } \%$  are thus stemming from rather volatile compounds (=feed– $\text{H}_2\text{O}$ –DM). The total carbon content was measured by DC-190 (boat module) to be  $26.4 \text{ wt } \%$ , with a dissolved organic carbon proportion (DC-190 boat module after filtration over a  $0.45 \text{ } \mu\text{m}$  regenerated cellulose filter) of  $26.5 \text{ wt } \%$ . The two values are very close, thus it is reasonable to assume that all carbon of the pyrolysis condensate was dissolved organic carbon. The chemical oxygen demand (COD, determined with round cuvette quick test using potassium dichromate, Nanocolor CSB 1500, Macherey-Nagel) was very high,  $705 \text{ g}_{\text{O}_2}/\text{L}_{\text{pyrolysis condensate}}$ , or  $22 \text{ mol/L}$ . The results are tabulated in Table 5.8.

The chemical oxygen demand is the amount of oxygen needed to fully oxidize the organic content, according to (5.1):

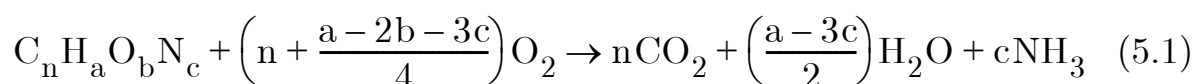


Table 5.8: Properties of the palm oil pyrolysis condensate as received.

property (at 20 °C)	value	property (at 20 °C)	value
density	1.079 kg/L	dry matter (DM)	17.8 wt %
electric conductivity	4.20 mS/cm	total carbon (TC)	26.4 wt %
pH	3 – 4	diss. org. carbon (DOC)	26.5 wt %
water content	55.2 wt %	COD <sup>a</sup>	705 g <sub>O<sub>2</sub></sub> /L
volatile substances <sup>b</sup>	27.0 wt %	HHV	8400 kJ/kg

a. chemical oxygen demand

b. 100 %–water content–dry matter

Assuming a composition similar to hydrolyzed wood, e.g.  $\text{CH}_{1.6}\text{O}_{0.7}$ , and neglecting the nitrogen content, the stoichiometric factor of oxygen becomes  $1 + 1.6/4 - 0.7/2 = 1.05$ . Thus, about  $22/1.05 \cong 21$  moles of  $\text{CH}_{1.6}\text{O}_{0.7}$  should be contained in 1 L of pyrolysis condensate, corresponding to  $\sim 25$  wt % of carbon, being in good agreement with the value determined by DC-190.

A procedure to estimate the higher heating value from the measured chemical oxygen demand was reported by Vogel [169]. From tabulated molar heat of combustion values of manifold organic substances with various C/H/O ratios [170], the chemical oxygen demand per mole substance for the total oxidation can be calculated. Surprisingly, a plot of the molar heat of combustion vs. the molar oxygen demand (i.e.  $\text{mol}_{\text{O}_2}/\text{mol}_{\text{subst.}}$ ) for the total oxidation yields a straight line with a slope of  $-411.15$  kJ/ $\text{mol}_{\text{subst.}}$  per  $\text{mol}_{\text{O}_2}/\text{mol}_{\text{subst.}}$ . Thus, by determining the chemical oxygen demand, the higher heating value HHV, corresponding to the heat of combustion, can be estimated: 1 L of pyrolysis condensate (1079 g) comprised 286 g carbon (26.5 wt %) or 23.8 mol. The COD was 705 g<sub>O<sub>2</sub></sub>/L, or 22.03 mol/L, which corresponds to 0.926 mol O<sub>2</sub> per mol of pyrolysis condensate. The higher heating value of the pyrolysis condensate is thus 380.7 kJ/mol (9060 kJ/L or 8400 kJ/kg).



Table 5.9: Ions in palm oil pyrolysis condensate, measured by HPIEC.

cation	conc. mg/kg	conc. mmol/kg	anion	conc. mg/kg	conc. mmol/kg
sodium	4560	198.3	sulfate	6710	69.9
calcium	1470	36.7	o-phosphate	890	9.4
potassium	180	4.5	chloride	440	12.5

The inorganics content of the palm oil pyrolysis condensate was determined by HPIEC (see Table 5.9). Interestingly, the charge balance did not close well; not enough anions could be detected. Nitrate was not measured due to experimental difficulties with the HPIEC setup; possibly, the balance would have closed better if nitrate had been detected. Similarly, Mg was not detected at all, but it is assumed to exist as well.

If more analytical results are needed, an approach analogous to the manure analysis is recommended.



---

# Chapter 6: Selection of Catalysts

## 6.1 Experiments for the Attainment of the Chemical Equilibrium Composition with a Skeletal Ni Catalyst

### 6.1.1 Starting Point and Aim of The Experiments

The starting point of the thesis was to procure experimental evidence that a product gas corresponding to the chemical equilibrium composition can indeed be achieved by gasifying wood slurries at process relevant concentrations (10 – 30 wt %) with a proper catalyst. Skeletal Ni catalysts are known to exhibit a high activity for reforming as well as for methanation reactions [58]. Their attractive price justified that they were selected as the first catalysts to be tested. The gasification experiments were carried out in the batch reactor described in section 3.2, together with an overview of the applied procedures for the experiments and their analysis.

### 6.1.2 Experimental Details and Overview

A total of 9 experiments were carried out with skeletal nickel catalysts and wood as feedstock. Refer to Table 6.1 for a complete list of the experimental details and results.

The codes used as abbreviations for the individual experiments are based on the convention displayed in Figure 6.1.

A commercially available slurry grade skeletal nickel catalyst was purchased (Raney<sup>1</sup> 2800 nickel, Sigma Aldrich) and used without further treatment. The slurry contained 50 wt % of solid catalyst and 50 wt % of

---

1. Raney is a trademark of Grace Davison, Inc. Raney catalysts designate skeletal catalysts after their inventor Murray Raney. The term “Raney” (instead of “Raney<sup>®</sup>”) will be used when the product was named as such; otherwise, the term “skeletal nickel” will be used throughout this work.

Table 6.1: Conditions and results of wood gasification experiments.

run no.	$w_{\text{wood}}$ wt %	$\frac{m_{\text{wood}}}{m_{\text{cat.}}}$ [-]	$T_{\text{max.}}$ °C	$p_{\text{end}}$ MPa	$t$ ( $T < T_c$ ) min.	$t$ ( $T > T_c$ ) min.	$\text{DOC}_{\text{aq.}}^{\text{a}}$ mg/L	$\text{TC}_{\text{res.}}^{\text{a}}$ mg/g <sub>res.</sub>
HB300R01	10.5	2.0	303	12.2	41	0	18'480	142.9
HB400R01	10.0	1.9	409	34.1	5	24	300	14.9
HB400R03	9.9	1.8	402	30.8	8	22	720	20.3
HB400R04	9.7	1.9	405	31.6	57	25	770	7.6
HB400R05	9.7	1.8	400	29.3	57	9	4'470	22.4
HB400R06	9.7	1.9	404	31.5	56	42	1'020	19.6
HB400R07	9.6	1.9	404	31.0	6	92	670	13.8
HB400R08	29.9	2.1	403	32.0	55	43	1'620	0.1
HB400NC1	9.6	N/A	409	29.3	6	92	14'390	871.4

a.  $\text{DOC}_{\text{aq.}}$  = dissolved organic carbon remaining in the aqueous phase,  $\text{TC}_{\text{res.}}$  = total carbon content in  $\text{mg/g}_{\text{residue}}$  by measurement with DC-190 (boat module) as defined in the notation overview on page xx.

water (due to the catalyst's pyrophoric nature). The pH of the slurry solution was  $\sim 9$ , corresponding to  $3.5 \times 10^{-9}$  mol NaOH for a typical feed, whereas about  $1.5 \times 10^{-5}$  moles of  $\text{Na}^+$  were contained in the biomass to be gasified. The amount of sodium added with the catalyst solution was thus negligible.

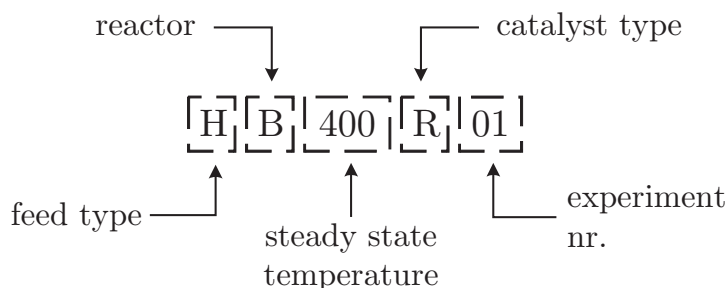


Figure 6.1: Explanation of the experimental codes used for batch experiments. Feed type: H for wood (German: Holz), G for manure (German: Gülle). Reactor: B for batch (bomb) reactor. Temperature in °C. Catalyst type: R for Raney Ni 2800 (Aldrich).

Table 6.2: (continued)

run no.	X <sub>C</sub> <sup>a</sup> %	GE <sup>a</sup> %	Y <sub>gas</sub> <sup>a</sup> L/g <sub>wood</sub>	CH <sub>4</sub> vol %	CO <sub>2</sub> vol %	H <sub>2</sub> vol %	CO vol %	Y <sub>CH<sub>4</sub></sub> <sup>a</sup> g <sub>CH<sub>4</sub></sub> /g <sub>wood</sub>
HB300R01	87.1	29	0.30	23	59	18	< 0.1	0.05
HB400R01	99.1	46	0.45	37	56	6	< 0.1	0.12
HB400R03	99.0	77	0.84	30	45	24	< 0.1	0.19
HB400R04	99.2	96	0.85	47	46	7	< 0.1	0.30
HB400R05	95.1	80	0.75	40	47	13	< 0.1	0.22
HB400R06	98.4	96	0.86	47	46	7	< 0.1	0.30
HB400R07	99.4	103	0.92	49	43	8	< 0.1	0.33
HB400R08	99.5	89	0.79	48	49	3	< 0.1	0.28
HB400NC1	85.7	21	0.19	14	61	16	9.0	0.02

a. X<sub>C</sub> = dissolved carbon conversion, GE = carbon gasification efficiency, Y<sub>gas</sub> = gas yield, Y<sub>CH<sub>4</sub></sub> = methane yield, as defined in the notation overview on page xx.

Raney 2800 nickel proved very active in the experiments. A loading of 0.5 g of catalyst (dry solid) per 1 g of wood was chosen. The reason for this rather high catalyst-to-feed ratio was to ensure the attainment of equilibrium conditions within a reasonable time before possible catalyst deactivation (e.g. due to sintering, hydrolysis, interaction with salts, etc.). Typically, the wood concentration was 10 wt %, but could be increased up to 30 wt % by using smaller feed amounts (typically ~700 mg dry wood + 6.3 g H<sub>2</sub>O for 10 wt %, 1.65 g wood + 3.85 g H<sub>2</sub>O for 30 wt %).

### 6.1.3 Results of Wood Gasification with Raney 2800 Ni (Aldrich)

The evolution of temperature and pressure during a typical experiment are depicted in Figure 6.2. For large heat-up rates, the critical point was reached after ~5 minutes and a steady state of pressure and temperature after ~15 min., and for small heat-up rates, the critical point was reached after ~56 min. with a steady state after about 75 min., indicating the end of the gasification reaction.

The carbon gasification efficiency GE was introduced:

$$\text{GE} = \frac{n_{\text{C, product gas}}}{n_{\text{C, feed}}} = \frac{\sum_i n_{\text{C},i}}{n_{\text{C, feed}}} \quad (6.1)$$

with  $i$  = typically  $\text{CH}_4$ ,  $\text{CO}_2$ ,  $\text{CO}$ , and, if detected,  $\text{C}_2\text{H}_6$  and  $\text{C}_3\text{H}_x$ . It varied between 77 and 103 %. Higher hydrocarbons were not detected. Thus, under ideal conditions, the carbon contained in the woody biomass could be completely gasified.

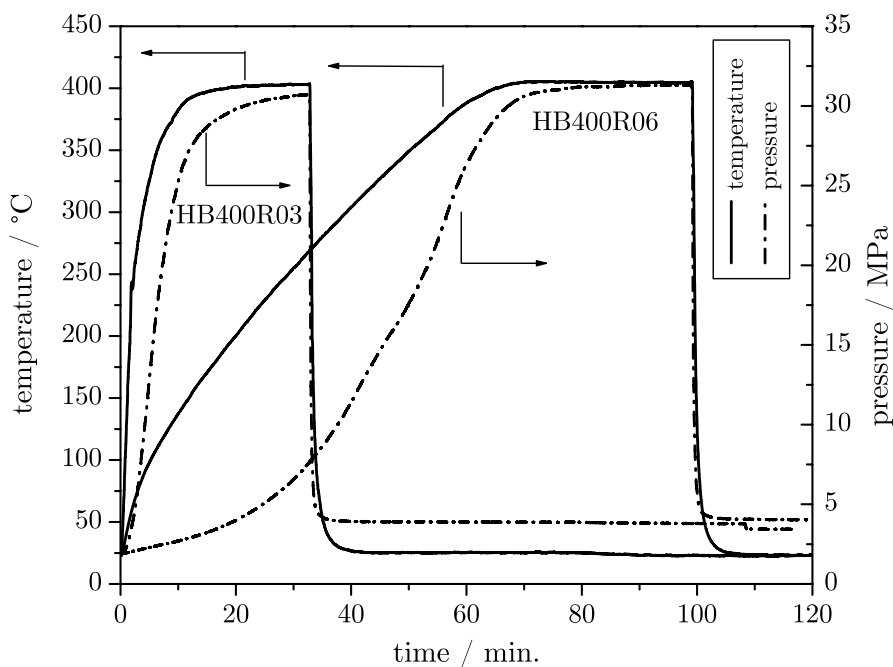


Figure 6.2: Evolution of temperature (left axis) and pressure (right axis) during the catalytic hydrothermal gasification of wood sawdust. Run no. HB400R03 used a fast heat up rate, whereas run no. HB400R06 used a slow heat-up rate (for conditions: see Table 6.1).

In all catalytic runs at supercritical conditions, no tars were present after opening the reactor, and the aqueous phase was colorless with a very low DOC content. A photograph of the feed suspension used for the experiments and the colorless water product phase after reaction can be seen in Figure 6.3.

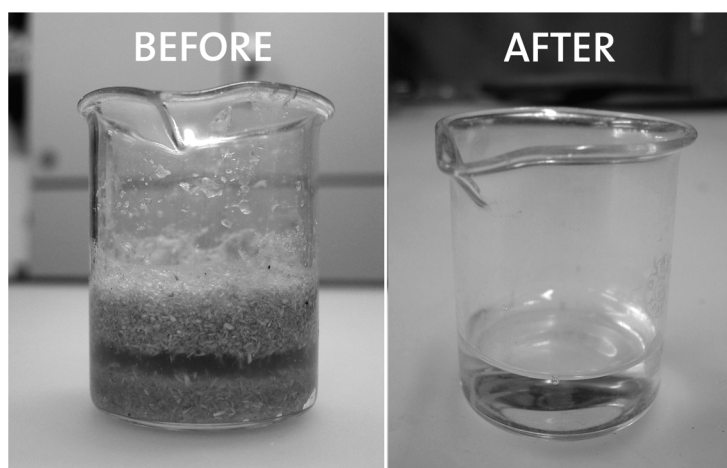


Figure 6.3: Photograph of the feed suspension (left; water-catalyst-wood mixture) and the colorless aqueous product phase (right) with very low dissolved organic carbon content.

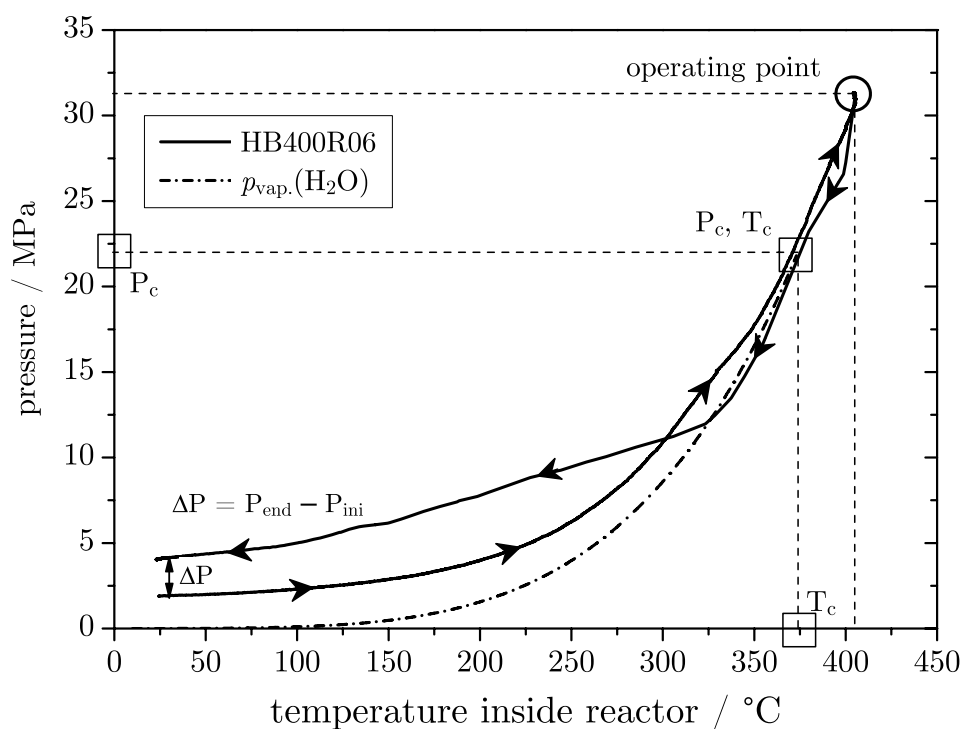


Figure 6.4:  $p$ - $T$ -trajectory for run HB400R06, in comparison to the pure water vapor pressure line (from tabulated data [147]). Note: during quenching ( $\Delta T$  ca.  $-10$  °C/s), the pressure signal (measured in the upper part) lags behind the temperature signal (measured in the lower part) due to the very thin capillary connecting the two parts, thus the pressure signal seems to follow the vapor pressure line.

A temperature of 405 °C and pressures ranging from 29 to 34 MPa, depending on the feed properties, were chosen as a starting point of operation and resulted in good gasification. No attempt was made to optimize the reaction conditions. An analysis of the pressure-temperature trajectory, shown in Figure 6.4, revealed that the reaction mixture approached the critical point of pure water before going into a supercritical state, thus the vapor region was avoided. Up to 2 MPa of argon were applied prior to heat up to always keep a dense, liquid phase in the reactor.

#### 6.1.4 Comparison Between Catalytic Liquefaction (300 °C, small $\tau$ ) and Catalytic Gasification (400 °C, large $\tau$ )

In experiment HB300R01, the reactor was slowly heated to 300 °C (heat-up rate  $\sim 6.8$  °C/min.), in presence of Raney nickel catalyst to prevent the formation of char and tars, and then rapidly quenched as soon as 300 °C were reached. This experiment yielded a liquid phase rich in dissolved organics. The liquefied wood filtrate of *liquefaction* experiment HB300R01 was analyzed by ion exclusion chromatography for its composition in order to identify some reaction intermediates. The separation quality of the analyses is presented in two chromatograms, shown in Figure 6.5 (peak numbers correspond to the ID in Table 6.3). The findings are tabulated in Table 6.3, together with the contents of the liquid phase after *gasification* experiment HB400R05. This analysis revealed which intermediates were gasified (i.e. not present anymore in the analysis of HB400R05, or their content significantly reduced), and which ones remained in the liquid phase after reaction in supercritical water (i.e. were still present or their content even increased). The data was used together with knowledge gained from the literature to elaborate the reaction network presented in section 2.4.

One run was carried out without a catalyst (run HB400NC1). A very viscous brown residue, partly liquid and partly solid, was stuck to the reactor walls. This residue consisted of 87 % carbon. The carbon gasification efficiency was only 21 %, and the gas contained 9 vol % CO and only 14



vol % CH<sub>4</sub> besides its major constituent CO<sub>2</sub>.

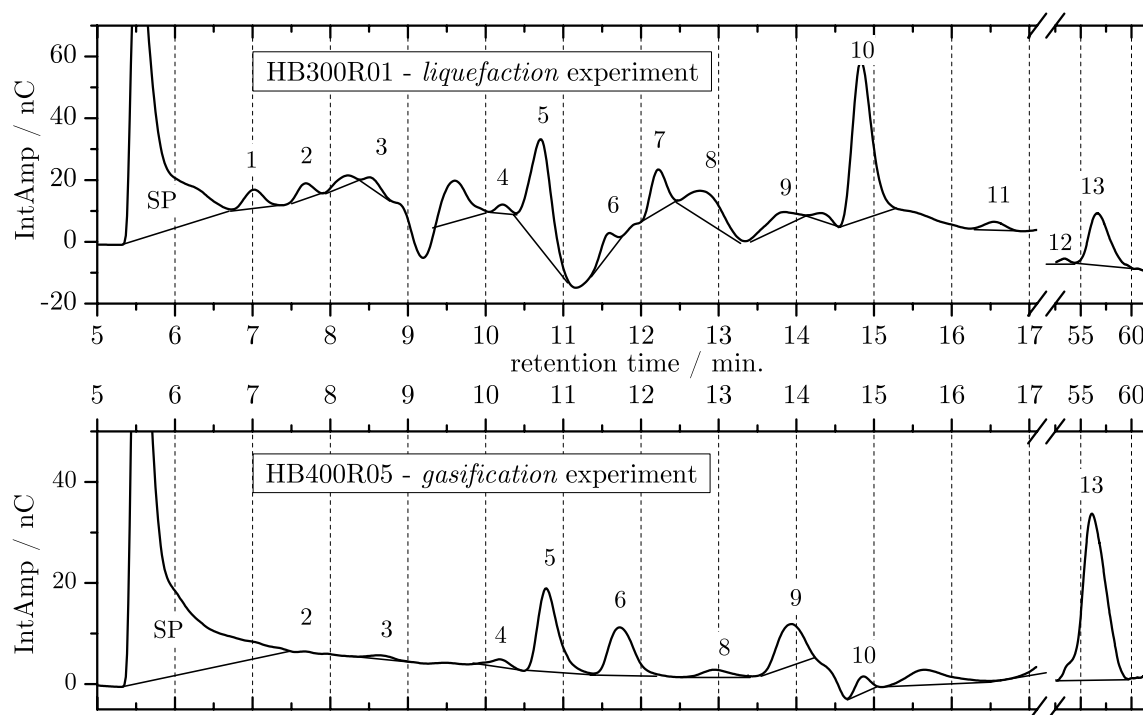


Figure 6.5: High pressure ion exchange chromatography with amperometric detection of organic compounds in the residual liquid phase after *liquefaction* experiment HB300R01 (above, dilution 1:7) and after *gasification* experiment HB400R05 (below, dilution 1:10). The peak ID numbers correspond to the compounds presented in Table 6.3, with the exception of SP designating the system peak. The compounds without ID were either not identified or quantitatively determined using a UV detector (200 – 300 nm) and thus not explicitly labeled here.

Table 6.3: Substances detected in the water phase recovered after a *liquefaction* experiment (HB300R01, left, gasification efficiency GE 29 %) and after a *gasification* experiment (HB400R05, right) where most of the feed was gasified (GE 80 %).

ID <sup>a</sup>	substance	<i>liquefaction</i> experiment (HB300R01)			<i>gasification</i> experiment (HB400R05)		
		conc. mg/L	CE <sup>b</sup> mg <sub>C</sub> /L	% DOC	conc. mg/L	CE <sup>b</sup> mg <sub>C</sub> /L	% DOC
1	D-glucose	4688	1875	10.2	0	0	0
2	pyruvic acid	57	23	0.1	3	1	< 0.1
	oxalic acid	0	0	0	220	59	1.3
3	methylglyoxal	133	67	0.4	92	46	1.0
	glycerol	1288	504	2.7	0	0	0
4	formaldehyde	8	3	< 0.1	15	6	0.1
5	formic acid	1092	285	1.5	155	40	0.9
6	acetic acid	749	300	1.6	2730	1092	24.4
7	ethylene glycol	665	257	1.4	0	0	0
8	levulinic acid	700	362	2.0	80	41	0.9
9	acetaldehyde	1701	928	5.0	5360	2924	65.4
10	methanol	4420	1658	9.0	160	60	1.3
11	ethanol	133	69	0.4	0	0	0
	5-HMF	133	76	0.4	0	0	0
12	furfural	14	10	< 0.1	0	0	0
13	phenol	42	32	0.2	290	222	5.0
	TOTAL $\Sigma$		7009	34.9		4491	100.5

a. The ID numbers correspond to the peaks shown and labeled in Figure 6.5.

b. Carbon equivalents (mg<sub>C</sub>/L).

### 6.1.5 Catalytic Gasification at 400 °C

In all other experiments, gas compositions close to equilibrium were achieved, independent of the feed concentration of wood. Varying the heating rate between 5.5 °C/min. and 47.4 °C/min. had no significant influence on the gasification results (apart from a slightly increased amount of carbonaceous compounds recovered in the methanolic fraction, i.e. tars, for slow heating rates), as opposed to the findings of Matsumura and co-workers [89]. However, the Japanese researchers used glucose as feed, applied significantly higher rates (10 – 30 °C/s) and did not add any catalyst.

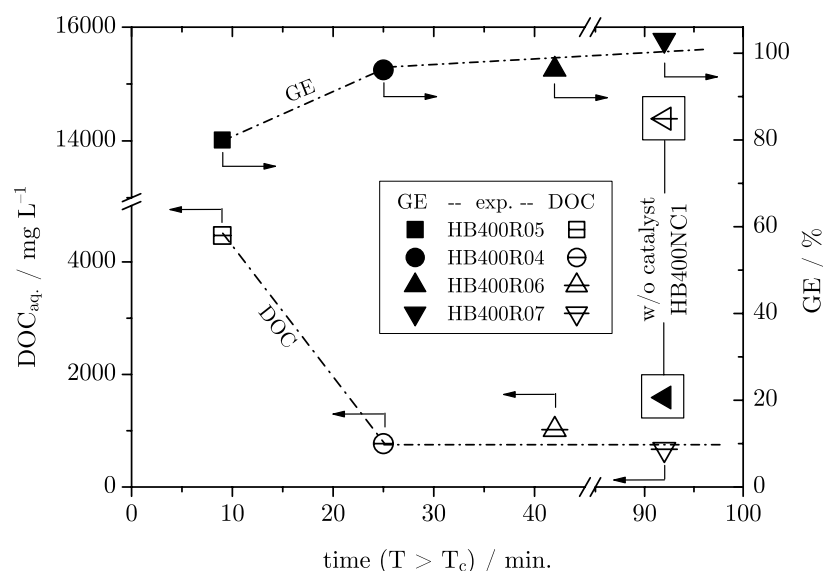


Figure 6.6: Carbon gasification efficiency (GE, filled symbols) and dissolved organic carbon in the remaining aqueous phase (DOC<sub>aq.</sub>, open symbols) vs. residence time in supercritical water. Conditions:  $T = 400$  °C,  $p \sim 30$  MPa, 10 wt % wood,  $m_{\text{wood}}/m_{\text{cat.}} = 2$ .

An important parameter was the residence time the mixture spent in supercritical water. As an approximation, supercritical state was assumed as soon as the mixture was above  $T_c$  of pure water (374 °C; the total pressure was always higher than the critical pressure of water, which is 22.1 MPa, when the critical temperature was reached). For a residence time of 9 minutes (run HB400R05), gasification was not complete, as can be seen in the gasification efficiency of only 80 % as well as the high DOC in the

residual solution (Figure 6.6). In run HB400R04, thermodynamic equilibrium was almost achieved at a residence time of 25 min. above  $T_c$  (374 °C). Longer residence times showed only a minimal increase in the methane concentration. This behavior is depicted in Figure 6.7. The fact that the increase was only minimal could be due to catalyst deactivation (skeletal nickel catalysts were later found to sinter rapidly in the hydrothermal environment).

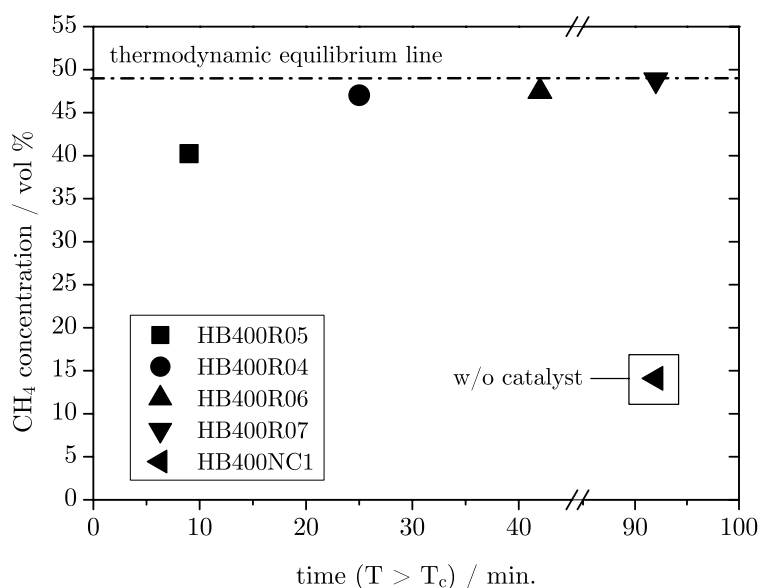


Figure 6.7: Methane concentration in the dry product gas vs. residence time at supercritical temperatures,  $m_{\text{wood}}/m_{\text{cat.}} = 2$ . The dashed line represents the equilibrium concentration calculated for 400 °C, 30 MPa and 10 wt % wood using the Peng-Robinson equation of state.

Molar balances are shown in Table 6.4. Carbon balances close mostly to more than 90 %. In some runs, balances are higher than 100 %. In experiments with lower feed loadings, small measurement errors have a larger impact on absolute numbers. Missing hydrogen and oxygen are mostly due to experimentally unrecovered water (compare with H/O ratio of around 2 for the missing moles). Frequently, some water was found in the upper, cold part of the apparatus where it was hard to be collected.

Table 6.4: Molar balances in terms of carbon, oxygen and hydrogen for all experiments reported in Table 6.1. Missing hydrogen and oxygen are mostly due to unrecovered water (compare with H/O ratio of around 2 for missing moles). Carbon balance in HB400R01 is low due to a mistake during gas sampling.

run no.	feed / mmol			products / mmol			product/feed (%)		
	C	H	O	C	H	O	C	H	O
HB300R01	26.7	650.4	325.9	23.1	218.9	117.7	86.4	33.7	36.1
HB400R01	24.3	623.9	312.8	12.2	625.3	319.3	50.2	100.2	102.1
HB400R03	24.1	621.7	311.7	19.7	533.7	271.3	81.7	85.8	87.0
HB400R04	23.8	627.5	314.6	23.8	599.2	300.7	99.7	95.5	95.6
HB400R05	24.2	642.3	322.1	24.5	571.7	288.8	101.6	89.0	89.7
HB400R06	24.2	641.7	321.7	25.0	578.5	289.6	103.1	90.2	90.0
HB400R07	24.2	647.4	324.6	26.7	623.8	310.3	110.1	96.4	95.6
HB400R08	67.8	525.9	260.4	61.7	432.2	217.2	91.3	82.2	83.4
HB400NC1	24.2	646.4	324.1	23.5	600.0	310.2	97.1	92.8	95.7

### 6.1.6 Catalyst Analysis with XPS, BET and TPO

XPS measurements revealed carbon deposits on the catalyst surface after reaction. Table 6.5 summarizes these results. Interestingly, the fresh catalyst, washed either with distilled water or distilled water and methanol, and dried in the vacuum oven prior to analysis (105 °C), had already a significant amount of carbon located on its surface. While the fresh catalyst had roughly 10 atom % of carbon on the surface, the spent catalyst after one run had about 15 atom %. As XPS is very surface sensitive, carbon deposits could result from traces of organic contaminants present in the laboratory air. Nevertheless, the values show that there is more carbon on the spent catalyst than on the fresh one. The nickel was almost exclusively oxidized; for this reason, skeletal nickel catalysts are stored in aqueous solutions. It is assumed, however, that the mechanism of biomass degradation over nickel catalysts follows a redox cycle, where Ni(0) is oxidized to NiO or Ni<sub>2</sub>O<sub>3</sub> by reduction of water to H<sub>2</sub>, and then, the oxidized

Ni species are subsequently reduced back to Ni(0) by oxidation of the biomass (Mars-van-Krevelen-mechanism) [67]. If no more biomass is present, the nickel remains in the oxidized form. Of course, the surface of the catalyst can oxidize when being exposed to air (drying, transport to the XPS device, etc.). The oxidized species of other skeletal nickel catalysts tested in a later phase of the project were additionally identified with XRD (see section 6.3.1 and Figure 6.16 on page 135).

Table 6.5: Elements detected on the catalyst surface by XPS.

element	binding energy	H480-275R04 <sup>a</sup>	fresh Raney Ni 2800, washed with H <sub>2</sub> O	fresh Raney Ni 2800, washed with H <sub>2</sub> O/MeOH
	eV	atom %	atom %	atom %
O 1s	531.4	50.5	57.4	59.5
C 1s	285.3	15.2	9.6	9.1
Al 2s	119.1	21.9	18.5	20.3
Ni 2p <sub>3/2</sub> metal	852.7	1.4	0.4	0.3
Ni 2p <sub>3/2</sub> oxide	855.8	11	14	10.8

a. Run no. H480-275R04 was carried out in a previous campaign of experiments. For details see [15].

Absolute values for carbonaceous deposits on the catalyst were determined from total carbon (TC) analyses of the dried residue (Table 6.1). The TC value of dried fresh catalyst (about 1 wt %) was subtracted from the measurements. The amount of deposits on the catalyst did not depend on the initial wood concentration; as a matter of fact, the least amount of deposits per mass of catalyst (0.01 wt %) was found for the highest wood concentration of 29.9 wt %. Comparing experiments HB400R05 through HB400R07, the amount of carbonaceous deposits is reduced with an increased residence time of the mixture in supercritical water.

For a Temperature Programmed Oxidation (TPO) analysis of the recovered catalyst after experiment HB400R06, 17.3 mg of spent catalyst

were put into an  $\text{Al}_2\text{O}_3$  crucible and dried at  $110\text{ }^\circ\text{C}$  under  $\text{N}_2$  for 30 min. Then, the sample was heated at  $11\text{ }^\circ\text{C}/\text{min.}$  up to a temperature of  $800\text{ }^\circ\text{C}$  (Figure 6.8A).

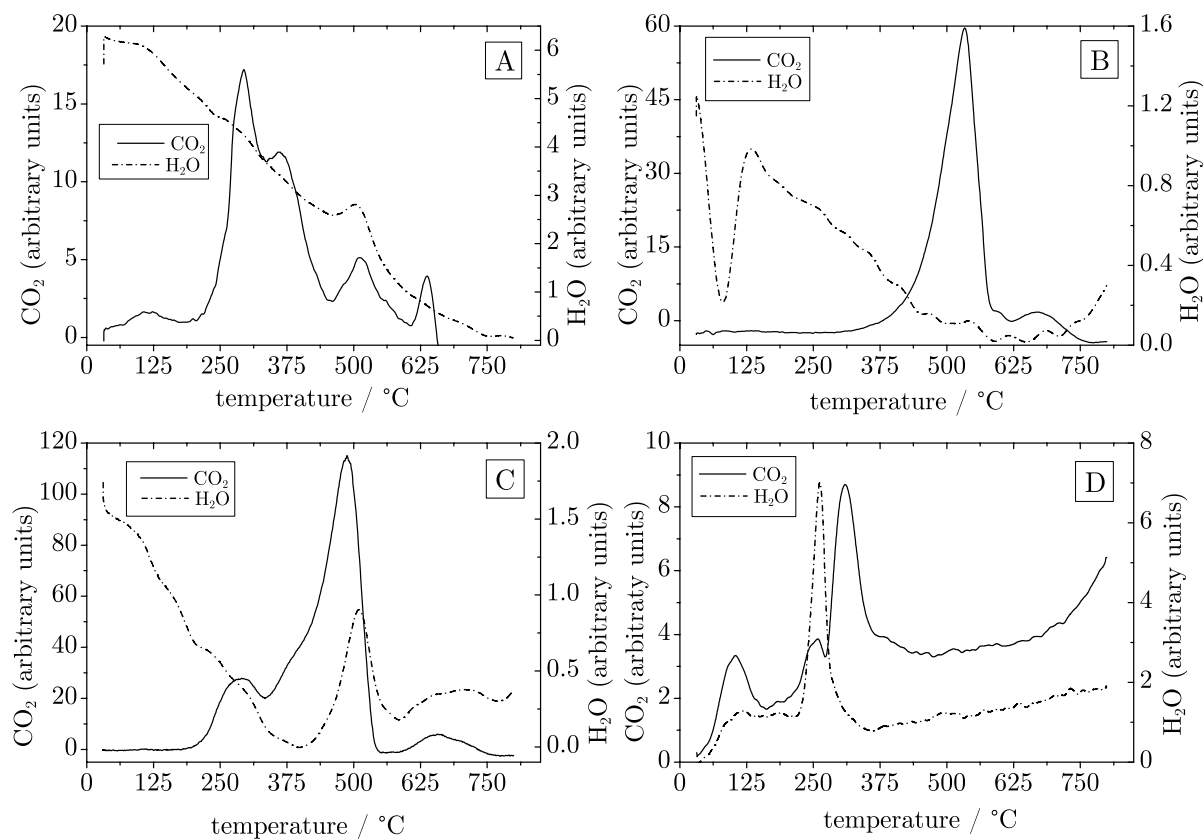


Figure 6.8: TPO analysis of the Raney 2800 Ni catalyst. A: spent catalyst after run HB400R06, heated under  $\text{N}_2$ , only. B: spent catalyst HB400R06 after treatment A, oxidatively heated under synthetic air. C: spent catalyst HB400R06, oxidatively heated under synthetic air. D: fresh Raney 2800 nickel catalyst, oxidatively heated under synthetic air.

The units of the IR signal (y-axis) are arbitrary but are the same on every graph (scaled to 1 mg of sample). Thus, the  $\text{CO}_2$  signals of each graph can be compared, and the  $\text{H}_2\text{O}$  signals can be compared to the other  $\text{H}_2\text{O}$  signals. A significant peak was measured between  $200\text{ }^\circ\text{C}$  and  $350\text{ }^\circ\text{C}$ , probably originating from sodium hydrogen carbonate (bicarbonate) deposits on the catalyst, since sodium bicarbonate releases  $\text{CO}_2$  at  $270\text{ }^\circ\text{C}$  [34]. Then, the sample was cooled to room temperature. Synthetic air was fed to the analysis chamber, and the same sample was heated

again to 800 °C within 70 min. (heat-up rate 11 °C/min.) under oxidizing conditions (Figure 6.8B). As can be seen, unlike before, there is no peak between 200 °C and 350 °C (all hydrogen carbonate was already removed), but starting at 350 °C, more CO<sub>2</sub> evolved, with a peak at 520 °C.

A third analysis was carried out with a fresh sample of 19.4 mg of the same recovered catalyst (HB400R06), with heating to 800 °C under synthetic air (Figure 6.8C). Interestingly, both peaks (the one at 300 °C and the one at 500 °C) were identified.

For a system blank, a fourth analysis with fresh catalyst, washed with deionized water and dried in the vacuum oven at 110 °C was carried out. 22.1 mg were put into the crucible and heated with the same temperature ramp under oxidizing conditions (Figure 6.8D). Surprisingly, carbon was found on the fresh catalyst as well (roughly 10 times less).

Table 6.6: BET measurement results of fresh Raney Ni 2800 (Aldrich).

	fresh Raney Ni 2800, washed with H <sub>2</sub> O	fresh Raney Ni 2800, washed with H <sub>2</sub> O/MeOH
S <sub>BET</sub> / (m <sup>2</sup> /g)	23.6	30.6
avg. pore diameter / nm	11.5	10.5
total pore volume / (cm <sup>3</sup> /g)	0.068	0.081

The BET measurements of the fresh catalyst are displayed in Table 6.6. The differences between the fresh catalyst, washed with deionized water only, and the fresh catalyst, washed with deionized water and methanol could result from chemically bound water in the pores. Although freshly manufactured Raney nickel should exhibit a BET surface area of ~80 m<sup>2</sup>/g, our catalyst was still active, despite the smaller BET surface area. According to the manufacturer, aging is an issue with Raney type catalysts and storage should not exceed one year (our catalyst was slightly older). Additionally, the catalysts had to be dried prior to BET physisorption. Due to the catalyst's pyrophoric nature, a change in structure could not be totally avoided during the evaporation and heating process,



although it was carried out with care (heat-up at 1 °C/min. to 105 °C and cool-down to room temperature under inert nitrogen atmosphere at ~100 hPa). Heating rates, pressure and composition of the atmosphere around the catalyst during the drying process are believed to be crucial parameters. When heated under air (at 100 hPa), the BET surface area decreased to 5 m<sup>2</sup>/g or below.

### 6.1.7 Differential Pressure Analysis

Before the wood can be gasified (and thereby lead to an increase in pressure inside the batch reactor), it must be decomposed to smaller molecules, as outlined before. Bobleter and Binder described in 1980 that hemicellulose from aspen wood is liquefied and broken down to smaller molecules at low temperatures (180 °C), followed by cellulose at moderate temperatures (270 °C), and lignin at higher temperatures (340 °C) [171]. These data had been gained from non-catalytic experiments in a flow-reactor at 23 MPa with slow heating. Bonn and co-workers described the decomposition of glucose to be much easier than the one of cellulose at 240 °C [172]. Minowa et al. reported the starting temperature of cellulose decomposition to be 180 °C, with a rapid increase above 260 °C, using an alkali catalyst (5 wt % sodium carbonate) [173].

While Bobleter and Binder reported only liquefaction results, it is of interest to identify the onset of gas production from the wood mixture in presence of a catalyst. For this reason, the pressure evolution of wood gasification experiments (as a function of temperature) were compared to the pressure rise of a reference experiment.

In the batch reactor, the pressure is a function of the volume of the reactor, the feed (water, catalyst, biomass), and the temperature, which in turn depends on other parameters (heat transfer, heating rate, composition, reactions, etc.), i.e.  $p = f(T)$ , and  $T = g(t, \text{feed}, \text{reactions}, T_{\text{sandbath}}, \text{etc.})$ .

If the pressure evolution of a reference experiment with similar conditions is subtracted from the pressure evolution of the gasification experiment, a differential pressure  $\Delta p$  can be calculated (temperature information was

recorded every second, and both data points were evaluated at the specific temperatures of the gasification experiment,  $T_{\text{exp.}}$ ):

$$\Delta p = P_{\text{experiment}}(T_{\text{exp.}}) - P_{\text{reference}}(T_{\text{exp.}}) \quad (6.2)$$

As the temperature  $T$  depends on the feed properties and possible chemical reactions (endothermic, exothermic), the system is rather complex and cannot be directly controlled. Thus, the temperature evolution  $T$  as a function of residence time inside the sandbath is not necessarily identical in a reference experiment and a gasification experiment.

To simulate the properties of the mixture in a gasification experiment, the approach of equal thermal diffusivity<sup>2</sup> was chosen, while interactions between individual components in the feed were neglected. The thermal diffusivity  $a_i$  of each substance  $i$  can be expressed by

$$a_i = \frac{\lambda_i}{\rho_i \cdot c_{p,i}} \quad (6.3)$$

with  $\lambda_i$  being the thermal conductivity,  $\rho_i$  the density and  $c_{p,i}$  the heat capacity at constant pressure of substance  $i$ . For this approximation, the physical properties were considered to be independent of temperature or pressure, and calculated at standard conditions. For non-interacting components, the ansatz of equal total thermal diffusivity  $a_{\text{mix}}$  holds as follows:

$$a_{\text{mix}} = \frac{\sum_i w_i \cdot a_i}{\text{gasification exp.}} = \frac{\sum_j w_j \cdot a_j}{\text{reference exp.}} \quad (6.4)$$

with  $i = \text{wood, catalyst, water}$  (gasification experiment), and  $j = \text{inert, catalyst, water}$  (reference experiment).  $w_i$  and  $w_j$  are the corresponding weight fractions.  $\text{SiO}_2$  was selected as inert substance. This catalyst-water- $\text{SiO}_2$ -mixture had approximately the same  $a_{\text{mix}}$  as a catalyst-water-

---

2. It was assumed that the reactor's content is only heated by thermal conduction through the slurry (no mixing, no convection). Then,  $a$  is the dominating parameter in the instationary energy balance.

wood-mixture.  $m_{\text{water}}$  and  $m_{\text{catalyst}}$  were identical in both the reference experiment and the gasification experiment, and thus  $m_{\text{SiO}_2}$  was adjusted to 2.3223 g to fulfill equation (6.4). The individual amounts used can be found in Table 6.7.

Table 6.7: Mass and weight fraction of the components for the reference experiment and a typical gasification experiment.

substance $i$	$\lambda_i$ W/(m K)	$\rho_i$ g/cm <sup>3</sup>	$c_{p,i}$ J/(g K)	$a_i$ m <sup>2</sup> /s	$m_i$ g	$w_i$ exp. %	$w_i$ ref. %
H <sub>2</sub> O	0.61	0.999	4.182	$1.46 \times 10^{-7}$	6.5000	85.8	70.8
catalyst	93.6	8.375	0.448	$2.495 \times 10^{-5}$	0.3531	4.7	3.8
SiO <sub>2</sub> (ref. only)	1.4	2.20	0.67	$9.50 \times 10^{-7}$	2.3223	N/A	25.3
wood <sup>a</sup> (exp. only)	0.13	0.33	2.3	$1.71 \times 10^{-7}$	0.7258	9.6	N/A

a.  $\lambda_i$  from [174],  $\rho_i$  measured.

Two reference experiments were carried out:

- with fast heating, where the reactor was immersed into the sandbath which was preheated to 405 °C (for comparison with experiments HB400R01, -R03, and -R07),
- with slow heating, where the reactor was immersed into the sandbath which was preheated to only 70 °C. Then, the sandbath setpoint temperature was increased to 405 °C, and the reactor was slowly heated to this temperature within ~50 minutes (for comparison with experiments HB400R04, -R05, and -R06).

The differential pressure evolution  $\Delta p$  as a function of the temperature inside the reactor with fast heating is depicted in Figure 6.9. A small pressure evolution can be seen between 150 and 250 °C. A possible explanation could be that part of the hemicelluloses and cellulose are hydrolyzed and readily reformed to smaller molecules (as described by Bobleter [171]), which are then decomposed to the primary gases H<sub>2</sub> and CO, and

the CO is catalytically shifted to CO<sub>2</sub> and more H<sub>2</sub>. However, below 250 °C, product gases were neither detected in wood gasification experiments during which samples were taken (section 6.5), nor visualized with the capillary technique (section 6.7).

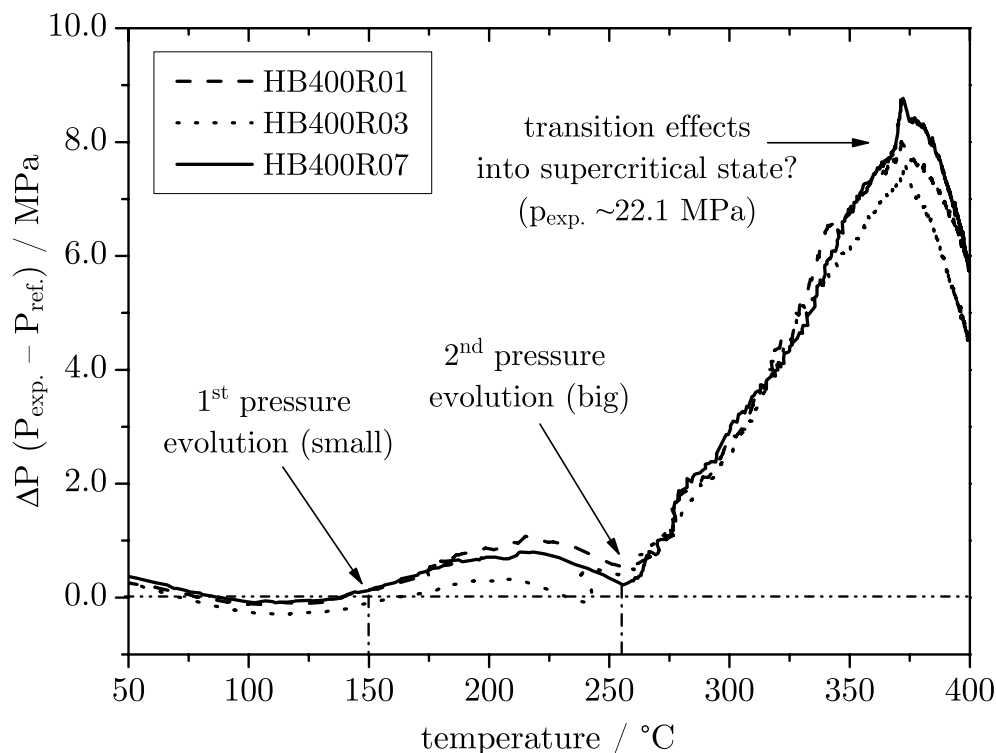


Figure 6.9: Differential pressure  $\Delta p$  of three gasification experiments with high heating rates ( $\sim 40$  °C/min.) with respect to a reference experiment, where no gasification took place. At 250 °C, a substantial pressure increase was registered, up to 8 MPa.

At  $\sim 250$  °C, a rapid increase in differential pressure was registered, up to 8 MPa. The evolution is nicely reproduced in the three individual experimental runs (HB400R01, -R03, and -R07). The wood must be hydrolyzed and readily reformed over the Raney nickel at  $T > 250$  °C. Possibly, the lignin fraction was reformed at lower temperatures than reported by Bobleter due to the presence of a catalyst. The catalyst's activity at these comparably low temperatures is surprisingly high. It is worth mentioning that the pressure difference at the end of the reaction (after cool-down of the reactor) had decreased to 2 – 3 MPa (at room temperature, corres-

ponding to less than 4 MPa at 400 °C). The reforming of wood over Raney Ni might be faster than the subsequent methanation of CO<sub>2</sub> and H<sub>2</sub>, and thus the pressure decreases again after having reached a maximum value due to the reduction in the number of moles. Then again, the reforming requires the bigger molecules to be transported to the active sites, while for the methanation, only gaseous reactants are required, which in turn are produced from the bigger molecules at the sites themselves. Thus, methanation should follow the reforming process quite immediately, given the catalyst is fully active.

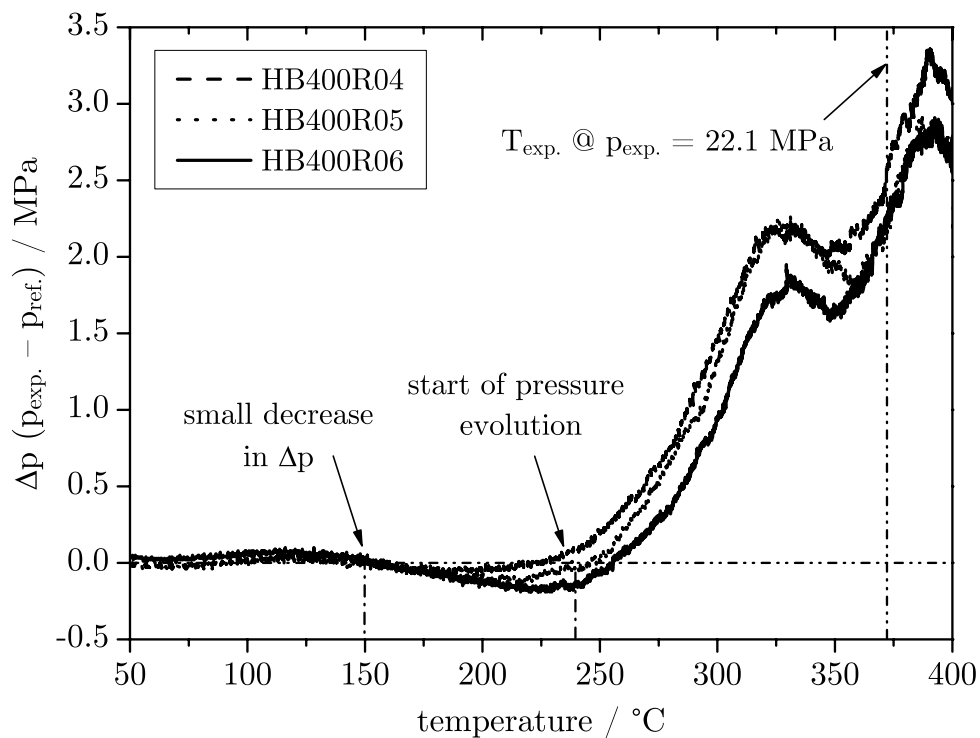


Figure 6.10: Differential pressure  $\Delta p$  of three gasification experiments with low heating rates ( $\sim 5$  °C/min.) with respect to a reference experiment, where no gasification took place. Also here, at 250 °C, the differential pressure starts to increase, but only up to  $\sim 3$  MPa.

The pressure difference evolution  $\Delta p$  at the lower heating rate is less pronounced, see Figure 6.10. A possibility could be that due to the increased residence time at each temperature, the mixture has enough time to equilibrate, and thus reforming and methanation coincide much more distinctively than at large heat-up rates. The temporary decrease at 330 °C

with subsequent increase at 355 °C cannot be explained by this speculation. The critical pressure of pure water, 22.1 MPa, was reached at ~371 °C, thus after the pressure decrease.

Nonetheless, the onset of gasification is clearly identified to be at 250 °C. Minowa and co-workers reported gas-production to start at 260 °C. They did not use a metal catalyst but sodium carbonate [173]. These findings correspond nicely, and can possibly be attributed not only to the catalyst's increased activity with increased temperature, but also to the rapid decomposition of the wood's constituents around 250 °C.

If one could take samples at the time points corresponding to the individual temperatures, more information about the underlying chemistry could be gained. Unfortunately, by taking samples and thereby removing contents of the reactor, the equilibrium would be disturbed. The attempts to take representative samples during catalytic wood gasification experiments are described in section 6.5.

#### **6.1.8 Conclusions from the Experiments with Raney Ni 2800 (Aldrich)**

- Raney nickel catalyst exhibits a high activity for gasifying wood in a hydrothermal environment around 400 °C, 30 MPa and feed concentrations of up to 30 wt %, without the formation of tars or char yielding a colorless aqueous phase with a low organic content.
- The maximum methane yield was 0.33 g CH<sub>4</sub>/g wood. The product gas contained 49 vol % CH<sub>4</sub>, corresponding to the chemical equilibrium at 404 °C and 31 MPa. Thus, the concept of hydrothermal gasification for the production of SNG is feasible.
- Several catalyst analysis methods focusing on different areas of the catalyst showed some carbon deposits on the used Raney nickel surface.
- The comparison of a catalytic liquefaction experiment with a gasification experiment allowed to identify stable reaction intermediates.

This knowledge was incorporated into the wood degradation network, presented in section 2.4.

- The onset of wood gasification at high feed concentrations with Raney nickel was identified to be at 250 °C, independent of the heating rate applied.

## 6.2 Gasification Experiments of Manure using a Skeletal Nickel Catalyst

### 6.2.1 Aim of The Experiments

After the successful gasification experiments with woody biomass as feed and a Raney nickel catalyst, the gasification of manure slurry was tackled. A titanium liner was inserted into the batch reactor to prevent corrosion (as described in section 3.2 on page 51), due to the manure's rather high content of salts such as chlorides, sulfates, and phosphates. After an initial experiment with untreated manure, the manure was washed with deionized water in order to free it from the salts it contained. For further experiments, the different salts would then be added back separately to the washed manure to test for their influence on the gasification.

The detailed composition and analysis of the manure is described in section 5.3. This elaborate analysis showed that the proposed washing of the manure with deionized water was inefficient, and most of the salts remained in the biomass, possibly entrained within its cells. To test for the influence of the salts, they would have to be added to inherently nearly salt-free biomass such as wood, rather than washed manure (which still contains a lot of salts). Unfortunately, at the time the experiments were carried out, only the elemental composition analysis of the manure was available, and this knowledge was only gained later. Nonetheless, the results of these experiments with manure shall be presented in this subchapter, as still some valuable conclusions can be drawn.

Based on the manure analysis presented in section 5.3, about 74 wt % of the dry matter is organic. The content of C, H, and  $O_{\text{org.}}$  was roughly 35.7, 5.8, and 27.0 wt %, respectively. Thus, the empirical formula of the organic part of manure (neglecting sulfur) is  $\text{CH}_{1.792}\text{O}_{0.566}$ , with a fictive molar mass of 22.99 g/mol.

### 6.2.2 Experimental Details and Overview

A total of 8 experiments were carried out with manure as feedstock and Raney Ni 2800 (Aldrich) as catalyst; see Table 6.8 for a list of the experimental details. The term “washed manure” refers to manure treated with the washing procedure outlined in section 5.3.5 on page 89, whereby, unfortunately, only parts of the salts were removed. The pH of the initial wood slurry was 8 – 9.

Table 6.8: Details of the experiments carried out with manure slurries, some of them with the addition of salts.  $T_{\text{max.}} = 405 \text{ }^\circ\text{C}$  in all experiments.

run no.	feed (manure)	$w_{\text{manure}}^{\text{a}}$ wt %	$\frac{m_{\text{manure}}}{m_{\text{cat.}}}$ [-]	$p_{\text{end}}$ MPa	$t$ ( $T < T_c$ ) min.	$t$ ( $T > T_c$ ) min.
GB400R01	washed	13.2	1.08	30.1	6	30
GB400R02	washed	15.7	1.00	30.4	6	63
GB400R03	untreated	18.5	1.00	29.4	6	61
GB400R04	washed + $\text{CaSO}_4$	14.9	1.00	28.3	7	61
GB400R05	washed + $\text{CaSO}_4$	15.2	1.01	30.1	6	61
GB400R06	washed + $\text{CaHPO}_4$	16.2	1.08	30.8	6	61
GB400R07	washed + $\text{K}_2\text{SO}_4$	16.4	1.11	30.1	6	65
GB400NC1	untreated, no catalyst	17.6	N/A	26.3	7	65

a. The weight fraction is based on the manure’s dry matter, calculated w/o the catalyst’s dry mass, but the water content of the Raney nickel slurry was accounted for in  $m_{\text{water}}$ .

The details of the salt addition for experiments GB400R04 – R07 are presented in Table 6.9.



Table 6.9: Details of the salts added to washed manure slurries.

run no.	salt	$m_{\text{salt}}$ mg	$m_{\text{water}}$ g	conc. mg/kg <sup>a</sup>		
				total	cation	anion
GB400R04	CaSO <sub>4</sub>	59.3	4.6222	12829	3777	9052
GB400R05	CaSO <sub>4</sub>	0.9	4.5481	198	158	140
GB400R06	CaHPO <sub>4</sub>	3.0	4.5545	659	194	465
GB400R07	K <sub>2</sub> SO <sub>4</sub>	11.8	4.6453	2540	1140	1400

- a. The concentrations are calculated as  $m_{\text{salt}}/m_{\text{water}}$ . The water of the catalyst slurry is included in  $m_{\text{water}}$ .  
As a reference, the salt concentrations of a typical 10 wt % wood gasification experiment were: K<sup>+</sup>: 50 mg/kg<sub>water</sub>, Ca<sup>2+</sup>: 54 mg/kg<sub>water</sub>, SO<sub>4</sub><sup>2-</sup>: 116 mg/kg<sub>water</sub>, PO<sub>4</sub><sup>3-</sup>: 6 mg/kg<sub>water</sub>.

The experimental procedure was identical to the one applied for wood slurries as feedstock. However, a catalyst-to-manure ratio of 1 was applied (dry basis). As no influence of the heating rate on the gasification was identified for wood, only the fast heating method was chosen for these experiments (i.e. the reactor content had reached a supercritical state after 6 – 7 minutes). The first two experiments served as reference experiments, to which the results from gasifying untreated manure, or manure with salt addition were compared. The only difference between GB400R01 and -R02 was the residence time: in the first experiment, the mixture spent about half an hour in supercritical water, while in the second experiment, the residence time was approximately doubled.

### 6.2.3 Results of the Manure Gasification Experiments

The analysis of the liquid and solid product phase is tabulated in Table 6.10 on page 122, and the analysis of the gas product distribution is presented in Table 6.11 on page 123. The carbon balance did not close as nicely as in the wood experiments, but it usually closed to ~90 % or even better.

Table 6.10: Analysis of the liquid and solid product phase after manure gasification. The pH of all aqueous phases was 8.0 except for GB-400NC1, it was 4.0.

run no.	DOC <sub>aq.</sub> g/L	IC <sub>aq.</sub> <sup>a</sup> g/L	TC <sub>res.</sub> mg/g <sub>residue</sub>	tars <sup>b</sup> mgC/g <sub>manure</sub>	X <sub>C</sub> %
GB400R01	1.62	2.45	15.7	25.4	93.5
GB400R02	2.94	2.25	13.8	30.9	91.5
GB400R03	3.66	2.91	18.2	42.4	91.2
GB400R04	5.13	1.46	30.2	12.8	88.5
GB400R05	3.93	2.76	30.6	30.1	89.5
GB400R06	3.50	2.05	27.9	58.4	92.0
GB400R07	3.31	3.37	18.6	31.3	90.5
GB400NC1	8.99	0.53	113.2	123.0	86.3

a. IC<sub>aq.</sub> = inorganic content remaining in the aqueous phase, as defined in the notation section.

b. tars collected in the methanolic phase (after evaporation of the MeOH), based on the manure feed mass. If their carbon content was not measured by DC-190, a proportion of 72 % C, 21.4 % O, and 6.6 % H was assumed, which is the average tar composition reported in literature.

The balance was rather poor when unwashed manure was used as feed (GB400R03): only 83 % of the initial carbon was found in the products. One has to consider the inhomogeneity of the manure slurry (larger than in dry-milled wood), as well as the fact that by using the Ti-liner, the effective reactor volume was decreased by about 25 %. For these experiments, no SKC gas sampling bags were available, and the amount of product gas was calculated with the pressure data, using equations (3.1) – (3.4) on page 53f. Thus, compared to the wood gasification experiments, an error in the pressure signal had a greater effect on the calculation of the amount of product gas. Therefore, a somewhat larger spread in balance closure had to be expected. Additionally, tarry substances and char stuck to the walls of the titanium liner. While it was easy to recover these from an open tube (such as the unscrewed stainless steel reactor tube used for the wood gasification experiments), it was much more diffi-

Table 6.11: Analysis of the gaseous product phase after gasification of manure.

run no.	C <sub>balance</sub> %	GE %	GE <sub>100</sub> <sup>a</sup> %	CH <sub>4</sub> vol %	CO <sub>2</sub> vol %	H <sub>2</sub> vol %	CO vol %	Y <sub>CH<sub>4</sub></sub> <sup>b</sup> g <sub>CH<sub>4</sub></sub> /g <sub>man.</sub>
GB400R01	93.2	75.8	81.3	46.0	43.1	10.7	0.1	0.190
GB400R02	88.2	68.9	78.2	46.4	44.2	9.2	0.1	0.171
GB400R03	82.7	59.4	71.8	39.6	45.5	14.7	0.2	0.119
GB400R04	85.3	62.0	72.7	31.9	50.1	16.9	0.5	0.104
GB400R05	92.5	65.0	70.3	42.2	45.8	11.8	0.1	0.151
GB400R06	94.6	66.4	70.2	38.5	46.3	15.0	0.2	0.129
GB400R07	97.9	74.7	76.3	41.0	45.6	13.3	0.2	0.155
GB400NC1	96.9	12.7	13.2	6.2	83.0	4.8	6.0	0.003

a. Carbon gasification efficiency if the carbon balance closed to 100 %, assuming the error is equally distributed to carbon in gas, liquid, and solid, as defined in (6.5) on page 126. This facilitates the comparison for experiments with differing carbon balances.

b. The methane yield scales with the carbon balance. Uncorrected values.

cult to retrieve them out of a container that is closed on one end such as the liner.

Nevertheless, it seems that either the carbon amount in the feed had been overestimated, or that some carbon in the product phases was not detected in those experiments where the carbon balance closed unsatisfactorily. A possible cause for unaccounted carbon could be that a larger amount of volatile carbonaceous compounds ending in the methanolic phase was formed (oils) when gasifying manure slurries, compared to the wood gasification experiments presented in section 6.1. As this methanolic phase had to be evaporated to yield the tars (usually at 45 °C and 200 hPa), volatile substances could thereby be lost.

#### 6.2.4 Product Gas Composition

The gas composition resulting from the individual manure gasification experiments is visualized in Figure 6.11.

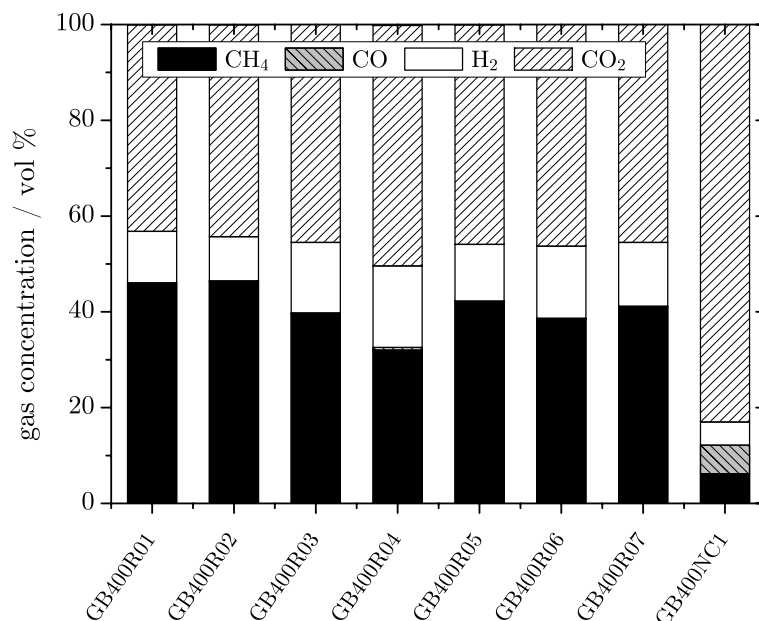


Figure 6.11: Product gas composition after gasification of manure slurries.

The gasification of washed manure yielded a gas whose composition was comparable to the one resulting from wood gasification: 46 vol % CH<sub>4</sub>, 44 vol % CO<sub>2</sub>, about 10 vol % H<sub>2</sub>, and only traces of CO. The untreated manure yielded more hydrogen and less methane, with a slightly larger proportion of carbon dioxide. Without a catalyst used, CO<sub>2</sub> was the main gaseous product, and CH<sub>4</sub>, H<sub>2</sub>, and CO were formed to equal quantities (each ~6 vol %). Still, the water gas shift reaction (not only catalyzed by the nickel but also by the alkali in manure) and the methanation did take place.

The addition of salts turned out to be unfavorable for the production of methane. The ranking of the negative influence, based on the added amount of salt, is CaHPO<sub>4</sub> > K<sub>2</sub>SO<sub>4</sub> ≅ CaSO<sub>4</sub>. The solubility of calcium salts is orders of magnitudes lower than the one of potassium salts. Possibly, the salts had precipitated and physically blocked the active catalyst sites. An alternative way of interaction is strong chemisorption of sulfur or phosphorus species to the active sites. This possibility is explained in more detail in section 7.2, where catalyst deactivation due to the co-feeding of Na<sub>2</sub>SO<sub>4</sub> was investigated.

Based on the manure analysis presented in section 5.3, which was carried out after the manure gasification experiments, the total amount of inorganics fed to the reactor could be calculated, see Table 6.12 (presented here: anions). It also illustrates that washed manure is not a good reference material, as the molar ratio of anions to surface nickel is larger than 0.3. Based on these findings, it can be deduced that the amount of salt added to the runs GB400R05 and GB400R06 was probably too low to see a clear effect. Nevertheless, as much information as possible was deduced from the experiments.

Table 6.12: Total anions present in catalytic manure experiments, based on HPIEC analysis of the manure slurry. R04–R07 include deliberately added sulfate and phosphate.

exp.	Cl <sup>-</sup> μmol	NO <sub>3</sub> <sup>-</sup> μmol	PO <sub>4</sub> <sup>3-</sup> μmol	SO <sub>4</sub> <sup>2-</sup> μmol	S <sub>2</sub> O <sub>3</sub> <sup>2-</sup> μmol	F <sup>-</sup> μmol	$n_{\text{Ni,sfc.}}^{\text{a}}$ μmol	$\frac{n_{\text{anions}}}{n_{\text{Ni,sfc.}}}$	$\frac{n_{\text{SO}_4^{2-}}}{n_{\text{Ni,sfc.}}}$	$\frac{n_{\text{PO}_4^{3-}}}{n_{\text{Ni,sfc.}}}$
R01	103	81	81	25	0	1	834	0.35	0.03	0.10
R02	122	96	96	29	0	1	1071	0.32	0.03	0.09
R03	143	335	704	109	14	2	1252	1.04	0.09	0.56
R04	116	91	91	463	0	1	1009	0.76	0.46	0.09
R05	116	92	91	35	0	1	1013	0.33	0.03	0.09
R06	126	99	121	30	0	1	1020	0.37	0.03	0.12
R07	130	103	102	99	0	1	1026	0.42	0.10	0.10

a. Assumptions: (i) catalyst consists of 92 wt % Ni. (ii) Dispersion  $D = 0.08$  (values reported by manufacturer). (iii) Dispersion does not decrease during run.

### 6.2.5 Gasification Efficiency and Dissolved Carbon Conversion $X_C$

For a better comparison of the carbon gasification efficiency  $GE$ , the carbon gasification efficiency based on a 100 % closure of the C-balance was introduced:  $GE_{100}$ . The assumption behind it is that the error in the balance is equally distributed between the carbon in the gas, liquid, and solid product fractions:

$$GE_{100} = \frac{GE}{C_{\text{balance}}}. \quad (6.5)$$

If the carbon balance did not close because of some undetected species in one particular fraction, then the scaling of GE to  $GE_{100}$  is not valid. For good, statistically sound results, more experiments would be needed (here, each experiment was carried out only once as their analysis was quite laborious). In the context of the campaign, to evaluate the influence of the salts on a semiquantitative basis, this was not necessary at the stage the experiments were carried out.

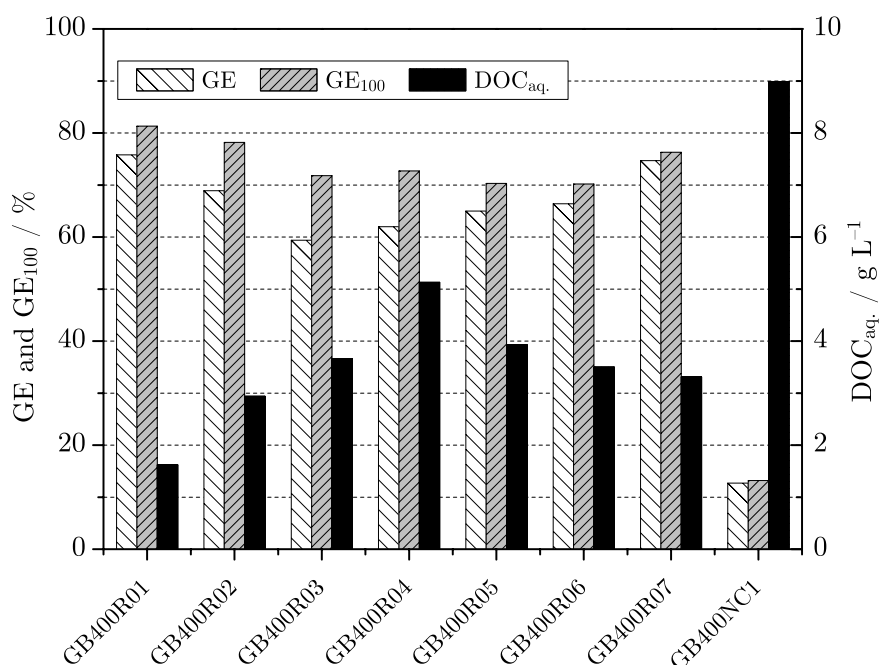


Figure 6.12: Gasification efficiency GE, scaled gasification efficiency for complete carbon balance closure  $GE_{100}$  (left y-axis) and residual carbon content in the aqueous phase (right y-axis) of the manure gasification experiments.

Clearly, without a catalyst, the gasification efficiency was poor, and the carbon content in the residual aqueous phase was comparably high. However, even in the case of GB400NC1, less than 15 % of the manure's carbon ended up in the aqueous phase as dissolved carbon; most of it was found in the form of tarry compounds and char, see section 6.2.7. The differences among individual gasification efficiencies are larger than among

the  $GE_{100}$ , and could thus also be an effect of the differing carbon balance closure. What can be seen, however, is that untreated manure as well as washed manure with back-added salts exhibits a lower gasification efficiency, indicating that salts have an adverse effect on the catalytic hydrothermal gasification.

The residual carbon content in the liquid product phase of the catalytic runs (GB400R01 to -R07) was largest in GB400R04, where the largest amount of calcium sulfate had been added. Also, in GB400R05, where only 1 mg of  $CaSO_4$  had been added,  $DOC_{aq}$  was, despite the lower amount of salt, higher than in GB400R06, where 3 mg  $CaHPO_4$  had been added. Hence, it seems that the gasification of carbonaceous compounds in the aqueous phase (such as acids, aldehydes, ketones, alcohols, ethers, etc.) is more hindered by the presence of sulfate salts than by phosphate salts.

The interpretation is complicated by the fact that the experiments were based on washed manure, a complex mixture, and not on a well-defined pure substance. Thus, the results are a combination of the washing quality, the inhomogeneity in the feed as well as the actual effect of the salts. The hindrance of the gas production from dissolved molecules in the aqueous phase could be ranked as follows:  $CaSO_4 > K_2SO_4 > CaHPO_4$ .

### 6.2.6 Volume of Gas Produced and Methane Yield $Y_{CH_4}$

For the methane yield  $Y_{CH_4}$  ( $g_{CH_4}/g_{manure, DM}$ ), the corrected measure  $Y_{CH_4,100}$  was introduced in an analogous way as in the case of  $GE_{100}$ :

$$Y_{CH_4,100} = \frac{Y_{CH_4}}{C_{balance}} \quad (6.6)$$

The trend of methane yield  $Y_{CH_4}$  was identical to the trend of corrected methane yield  $Y_{CH_4,100}$  in the experiments, see Figure 6.13. Without a catalyst, slightly more than 0.1 L (at standard conditions, 1 atm and 0 °C) gas was formed. However, the methane yield was negligible due to the large volume fraction of  $CO_2$  in the product gas.  $V_{gas}$  in catalytic runs

was at least 5 times larger than in GB400NC1: untreated manure yielded less gas and less methane, as expected, due to the larger amount of salts. Interestingly, the highest amount of gas was formed in GB400R06, in presence of  $K_2SO_4$ . While the composition was comparable to GB400R03 (untreated manure), both methane yield and gasification efficiency were higher with the addition of potassium sulfate. There is no obvious explanation for this result, and the experiment would have to be repeated to assess its reproducibility.

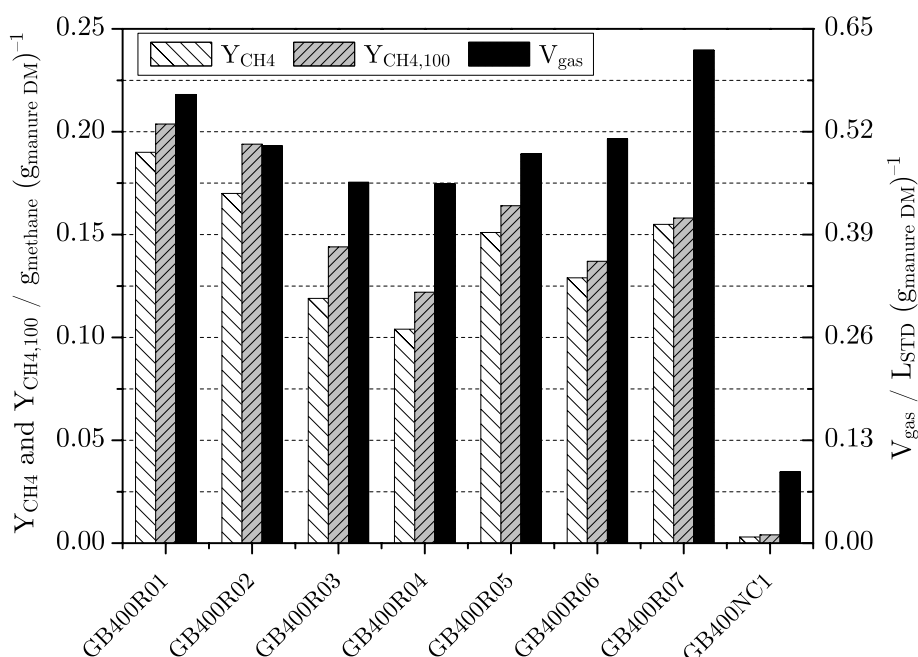


Figure 6.13: Methane yield ( $Y_{CH_4}$  as measured and  $Y_{CH_4,100}$  scaled to complete carbon closure, left y-axis) and gas volume produced at standard conditions (0 °C, 1 atm, right y-axis) of the manure gasification experiments.

As  $Y_{CH_4}$  is a combination of  $V_{gas}$  and the gas composition (and thus of GE), the ranking of the influence of sulfate and phosphate salts on  $Y_{CH_4}$  is analogous to their influence on GE:  $CaHPO_4 \cong CaSO_4 > K_2SO_4$ .

### 6.2.7 Solid Residue and Tarry Compounds After Gasification

The carbon cannot only remain in the aqueous phase in the form of dissolved organic carbon, but also in the form of tarry compounds (which



are recovered in the methanolic fraction), or as char and unconverted manure in the solid fraction, together with the catalyst particles. The two measures were in most cases reciprocally related to each other, see Figure 6.14. An increase in tars was typically accompanied by a decrease in char.

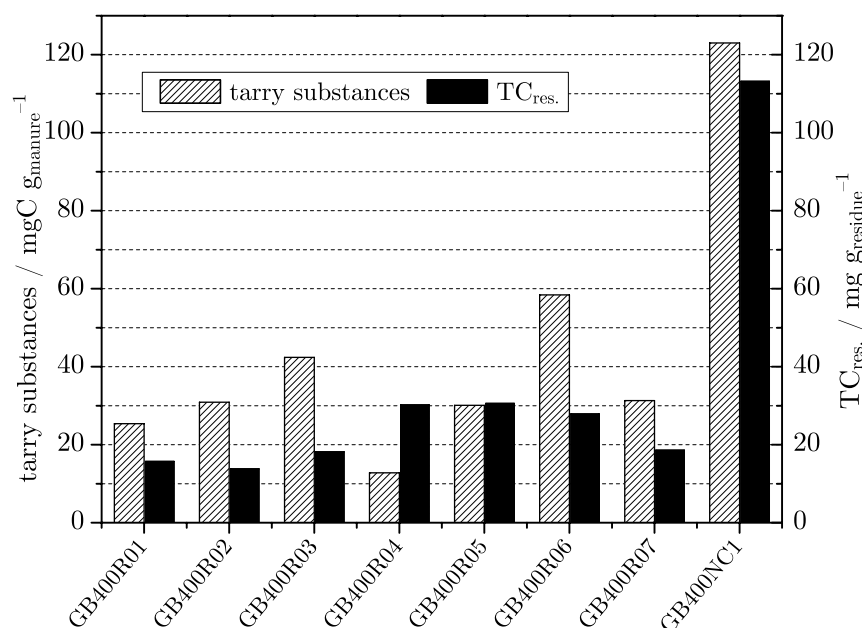


Figure 6.14: Amount of tarry substances recovered after evaporation of the methanolic fraction (left y-axis) and total carbon content of the residual solid fraction  $TC_{res.}$  (right y-axis) of manure gasification experiments.

Doubling the residence time in supercritical water from 30 to 60 minutes yielded slightly more tarry compounds but less carbon as solids, which implies that either more tars were formed due to secondary formation as a result of increased residence time (and due to partial deactivation of the catalyst, they were then not further decomposed to gas), or the manure itself was decomposed to smaller molecules to a larger extent than before, due to the increased residence time. Hence, more tars which were recovered in the methanolic fraction were formed, and less residual manure was left at the end of the experiment, leading to a lower  $TC_{res.}$ .

The gasification of untreated manure (GB400R03) yielded both a higher  $TC_{res.}$  as well as more tarry substances; thus, gasification was hindered by

the salts present in manure. The addition of  $\text{CaSO}_4$  in excess (GB400R04) led to the formation of more char, but to a decrease in tars. A reason could be that the decomposition of the manure to smaller substances (which are tar precursors) was already hindered by the presence of salts, hence a larger amount of manure remained unconverted and eventually turned into char under the harsh conditions in the reactor.

Again, calcium sulfate showed a more severe effect than potassium sulfate: a comparison of GB400R05 with GB400R07 shows that less char but equal amounts of tar were formed with  $\text{K}_2\text{SO}_4$ . The addition of the phosphate salt  $\text{CaHPO}_4$  led to a doubling of the amount of tars, and also to the formation of more char (compared to untreated or washed manure). The adverse effects can be ranked in the order  $\text{CaHPO}_4 > \text{CaSO}_4 > \text{K}_2\text{SO}_4$ , indicating that phosphates have a stronger effect than sulfates, and the less soluble calcium salts lead to a lower catalytic performance than the better soluble potassium salts.

### 6.2.8 Carbon Distribution to Gas, Liquid, Residue, and Tars

As a summary or overview of the previous findings, the carbon distribution to the product phases (gas, residual aqueous phase, solid residue, and tarry, methanol-soluble fraction) after the manure gasification experiments is depicted in Figure 6.15 (both original data representing the carbon balance closure and data scaled to 100 %).

### 6.2.9 Conclusions of the Manure Gasification Experiments

The experimental campaign with manure aimed at a first estimation of the influence of salts (sulfates, phosphates) on the catalytic hydrothermal gasification. The goal was not to assess their influence on a fully quantitative basis (much more experiments would be needed for this), but to get a first impression about the importance of salt separation in the real process.

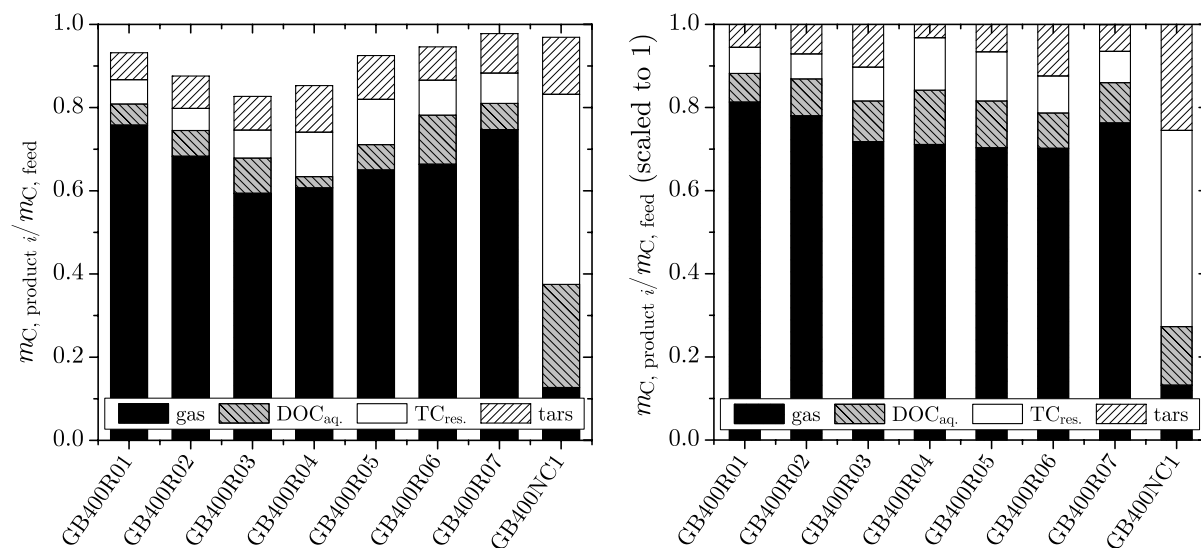


Figure 6.15: Carbon distribution after manure gasification experiments. Left: original data (total bar height represents  $C_{\text{balance}}$ ). Right: scaled to unity for more convenient comparison.

The following conclusions can be drawn:

- Wood is better suited as a reference material for testing the influence of salts on the gasification of real biomass, because wood contains less salts, and should thus be chosen instead of manure slurries. The salt concentration of the washed manure was still quite high, rendering a clear assignment of individual observations to the interaction of specific salt species difficult.
- Salts have a negative effect on the catalytic hydrothermal gasification of biomass, possibly due to precipitation phenomena as well as irreversible chemisorption of sulfur or phosphorus species (the form present inside the reactor at reaction conditions might not necessarily be sulfate or phosphate, but could also be reduced species [37]). Thus, salt separation prior to gasification and contact with the catalyst is indeed crucial.
- The negative influence of potassium and calcium salts on the gasification efficiency seems to be in the order  $\text{K}_2\text{SO}_4 > \text{CaSO}_4 > \text{CaHPO}_4$ , while the negative influence on the production of chars and tar tends to be the opposite, i.e.  $\text{CaHPO}_4 > \text{CaSO}_4 > \text{K}_2\text{SO}_4$ .

- The amount of salts added was too low in comparison to the amounts still present in washed manure. Additionally, the amount was low in comparison with the amount of active nickel surface atoms. To obtain more distinct deactivating effects, higher ratios should be chosen.

## 6.3 Batch Reactor Catalyst Screening using Wood as Feedstock

### 6.3.1 Skeletal Nickel Catalysts

Initial long term stability tests with Raney 2800 Ni (see section 7.1.2) showed that this skeletal nickel system is not stable in the hydrothermal environment. Sintering took place, and the catalyst lost its activity. There exist possibilities to enhance the stability of an alloy such as a skeletal nickel catalyst: either by co-doping of a third metal (Ru, Cu, Mo) to the Ni-Al-matrix [175, 176], or by choice of another Ni/Al ratio (lower Al contents usually lead to better stability [117]). As nickel is an abundant and cheap metal, it would be the catalyst material of choice, in addition to the good thermal conductivity and mechanical stability that pure metal catalysts exhibit.

Thus, a series of skeletal nickel catalysts were evaluated. By a cooperation with Grace Davison (W. R. Grace & Co.) and a good relationship with H.C. Starck, these two manufacturers provided several catalyst samples, of which some were especially tailored for this project.

The catalysts and the parameters of the corresponding experiments are tabulated in Table 6.13.

The first catalyst to test (in run no. R2C) was identical to the one used for the wood gasification experiments presented in section 6.1, with the addition of 0.25 wt % of Ru (composition: > 89 wt % Ni, < 9.5 wt % Al, < 0.8 wt % Fe, 0.25 wt % Ru). Ru is known to enhance the stability of skeletal nickel catalysts, as well as to increase the activity towards reforming reactions [177]. The second catalyst, Raney 6800 Ni (R3A), had a

Table 6.13: Conditions of the skeletal nickel catalyst screening experiments.

 $T_{\max.} = 405 \text{ }^\circ\text{C}$  in all runs.

run no.	catalyst	$w_{\text{wood}}$ wt %	$\frac{m_{\text{wood}}}{m_{\text{cat.}}}$ [-]	$p_{\text{end}}$ MPa	$t$ ( $T < T_c$ ) min.	$t$ ( $T > T_c$ ) min.	heat-up rate $^\circ\text{C}/\text{min}$
R2C	Raney 2800 Ni/Ru <sup>a</sup>	9.7	2.25	32.5	9	42	50
R3A	Raney 6800 Ni <sup>a</sup>	9.8	1.30	32.2	7	47	48
R4A	Amperkat <sup>®</sup> Ni <sup>b</sup>	9.4	1.58	32.8	9	43	39
R5A	Amperkat <sup>®</sup> Ni/Mo <sup>b</sup>	9.7	1.58	32.8	6	45	52
R15A	Raney Ni/Cu <sub>(high loading)</sub> <sup>a</sup>	9.1	1.89	31.6	6	47	55
R16A	Raney Ni/Cu <sub>(low loading)</sub> <sup>a</sup>	9.7	1.90	31.5	6	47	54

a. Grace Davison

b. H.C. Starck

lower Al content than Raney 2800 Ni, which might lead to enhanced stability as well (composition: 94.8 – 96.2 wt % Ni, 3.4 – 5.0 wt % Al, < 0.5 wt % Fe). The two catalysts received from H.C. Starck (Amperkat<sup>®</sup> SK-Ni 5546T, R4A, and Amperkat<sup>®</sup> SK-NiMo 5546T, R5A) were skeletal Ni catalysts, one with co-doped molybdenum (unknown amount). These catalysts were originally present as tablets in an aqueous solution, and therefore crushed in an agate mortar prior to their addition to the wood slurry. Two Raney nickel catalysts were manufactured with co-doped copper for this project by Grace Davison; one with a higher (R15A) and one with a lower (R16A) amount of copper (composition not known). Cu can increase the stability of skeletal nickel catalysts, similarly to Ru, but unfortunately, it is known to suppress hydrogenation and methanation reactions [120], leading to a trade-off between stability and selectivity.

The results of the gasification experiments carried out with these six skeletal nickel catalysts are displayed in Table 6.14.

Carbon balances closed between 97.1 and 100.8 %. Apparently, all catalysts were less selective towards the generation of methane than Raney 2800 Ni (Aldrich), as the hydrogen content of the product gas was always

Table 6.14: Analysis of the product phases after gasification of manure.

run no.	DOC <sub>aq.</sub> mg/L	X <sub>C</sub> %	tars % <sup>a</sup>	TC <sub>res.</sub> mg/g <sub>res.</sub>	GE %	CH <sub>4</sub> vol %	CO <sub>2</sub> vol %	H <sub>2</sub> vol %	CO vol %	Y <sub>CH<sub>4</sub></sub> g/g <sub>wood</sub>
R2C	1460	98.0	1.4	20.8	95.0	46	44	10	0.3	0.31
R3A	1470	97.2	1.8	18.4	94.6	42	42	15	0.7	0.28
R4A	860	99.0	1.7	20.7	95.9	45	44	11	0.2	0.32
R5A	2700	97.7	11.4	21.0	84.0	41	44	15	< 0.1	0.24
R15A	1020	97.4	0.4	28.4	94.9	40	42	16	0.2	0.25
R16A	580	98.8	0.4	40.6	97.9	42	44	12	0.4	0.26

a. carbon in tars, in % of initial carbon of the wood slurry.

higher than in the gas obtained from the experiments presented in section 6.1. The skeletal nickel catalyst with the lower aluminum content, R3A, yielded a product gas quite rich in hydrogen, 15 vol %. Thus, a shift in selectivity was registered, leading to a decreased methane yield, despite its high activity. By comparing the molybdenum doped catalyst (R5A) to the undoped skeletal nickel catalyst (R4A), it can be seen that the addition of Mo decreased the catalyst's activity, leading to a higher residual carbon content in the aqueous phase, as well as to a large amount of unconverted tars. The carbon gasification efficiency was the lowest of this test series: only 84 % of the initial carbon were collected as gas at the end of the experiment. Doping of copper shifted the product gas phase as expected to more hydrogen (R15A, R16A). 1.0 – 1.5 vol % of ethane were detected as well in these two runs. Due to the lowered methane content of the gas, the methane yield was lower than for the undoped skeletal nickel catalysts. While reduced activity and selectivity could possibly be accepted, stability is the crucial catalyst parameter in the hydrothermal environment.

To assess stability, X-ray diffractograms of fresh and used catalysts were recorded. They can be found in Figure 6.16.

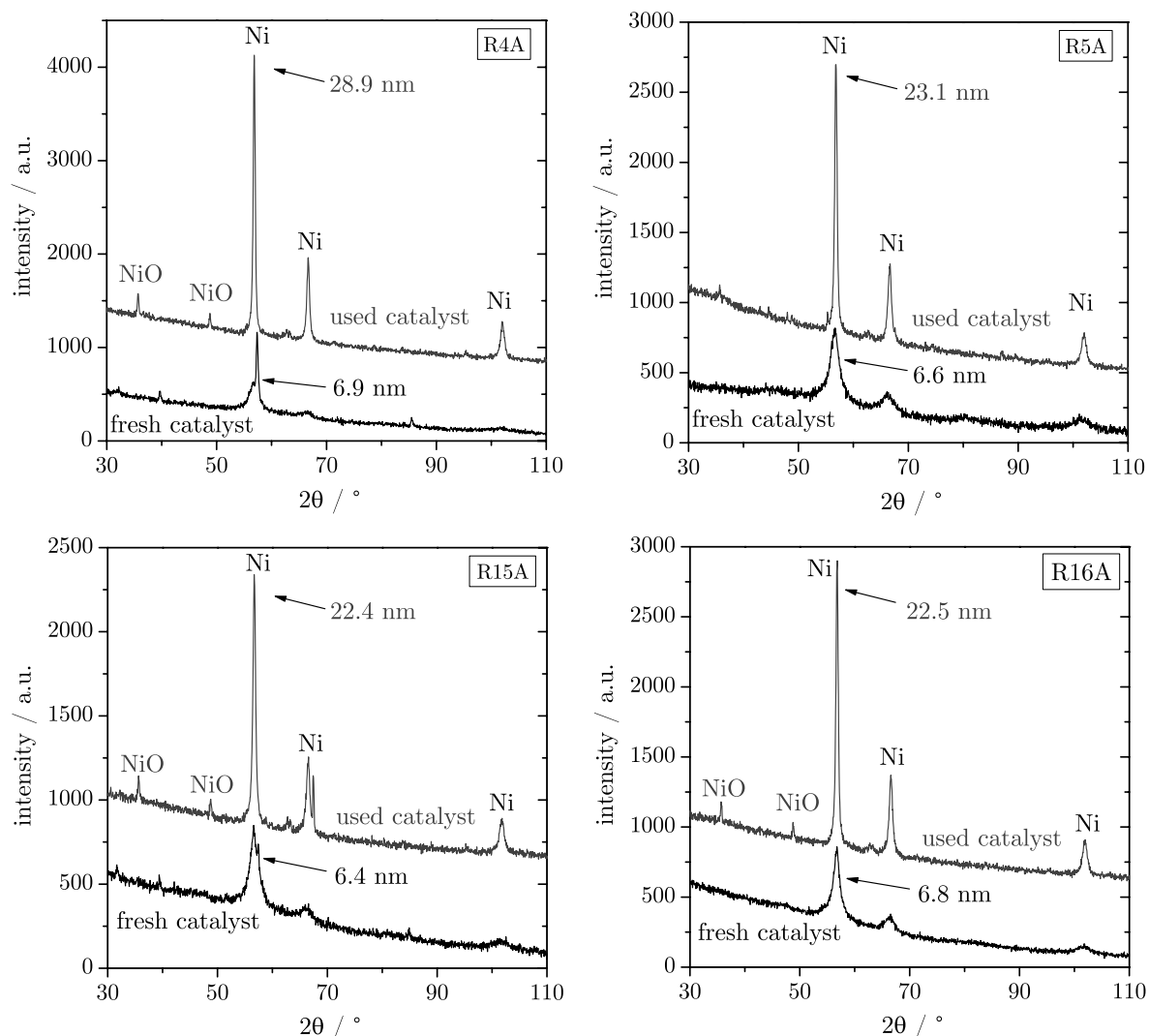


Figure 6.16: X-ray diffractograms of fresh and used skeletal nickel catalysts after a hydrothermal gasification experiment ( $\tau = 1$  hr). R4A: Amperkat<sup>®</sup> Ni; R5A: Amperkat<sup>®</sup> Ni/Mo; R15A: Raney Ni/Cu(high); R16A: Raney Ni/Cu(low).

All catalyst samples sintered already after this short period of about 1 hour: the nickel crystallites grew 2 – 4 times bigger, accompanied by loss of active metal surface area. The initial growth rate is thus very high. Nickel oxide was identified (except for R3A and R5A), being an indication of the Mars-van-Krevelen redox mechanism of biomass oxidation (outlined in section 6.1.6 on page 110). A diffractogram of Raney 2800 Ni/Ru can be found in Figure 7.5 in section 7.1.3, where a long-term stability experiment with this catalyst is described. It sintered as well, with similar crystallite growth. As outlined in section 4.9, the sizes have to be

understood as minimum sizes, because the smallest particles govern the reflections of the diffractogram. The crystallite sizes and growth factors are tabulated in Table 6.15 (Raney 2800 Ni/Ru included as well).

Table 6.15: Crystallite sizes of fresh and used skeletal nickel catalysts by XRD.

catalyst	run no.	crystallite size/nm		growth factor	runtime/min.
		fresh	used		
Raney 2800 Ni/Ru	long-term <sup>a</sup>	8.8	44.9	5.1	5760
Raney 6800 Ni	R3A	13.5	27.4	2.0	54
Amperkat <sup>®</sup> Ni	R4A	6.9	28.9	4.2	52
Amperkat <sup>®</sup> Ni/Mo	R5A	6.6	23.1	3.5	51
Raney Ni/Cu <sub>(high load.)</sub>	R15A	6.4	22.4	3.5	53
Raney Ni/Cu <sub>(low load.)</sub>	R16A	6.8	22.5	3.3	53

a. long term experiment carried out in the continuously operating catalyst test rig, see section 7.1.3 and the X-ray diffractogram (Figure 7.5) on page 177.

### 6.3.2 Supported Ruthenium Catalysts

As concluded in the previous section, skeletal nickel catalysts sinter rapidly in a hydrothermal environment and lose their very high initial activity quickly (based on long-term data, see section 7.1 for details). Different catalyst systems should therefore be evaluated. As supported ruthenium catalysts and unsupported RuO<sub>2</sub> were reported to be active for the hydrothermal degradation of waste biomass [25, 47, 48, 58, 176, 178], these systems were also tested. Based on the literature search presented in section 2.3.2, TiO<sub>2</sub> (rutile),  $\alpha$ -Al<sub>2</sub>O<sub>3</sub>, and carbon are the most stable supports in hot compressed water. Carbon supported catalysts have a very large surface area, and the active metals are usually well dispersed on it. They are very active for hydrogenation reactions. Several Ru/C and one Ru/TiO<sub>2</sub> catalyst were evaluated in wood gasification experiments in the batch reactor. For the applied experimental conditions, see Table 6.16, and for the results Table 6.17.



Table 6.16: Conditions of the supported ruthenium catalyst screening experiments.  $T_{\max.} = 405$  °C in all runs.

run no.	catalyst	$w_{\text{wood}}$ wt %	$\frac{m_{\text{wood}}}{m_{\text{cat.}}}$ [-]	$p_{\text{end}}$ MPa	$t$ ( $T < T_c$ ) min.	$t$ ( $T > T_c$ ) min.	heat-up rate °C/min
RuTi1	1 wt % Ru/TiO <sub>2</sub> (Degussa)	9.1	0.94	28.5	7	52	54
RCC	5 wt % Ru/C <sub>pwd.</sub> (fresh) <sup>a</sup>	9.4	2.06	31.8	6	46	51
RCA	5 wt % Ru/C <sub>pwd.</sub> (fresh) <sup>a</sup>	9.4	2.05	32.5	7	45	48
RCB	solid residue of RCA	8.9	2.06	29.1	7	45	46
RCD	solid residue of RCB	6.8	2.06	29.8	7	46	45
R13A	3 wt % Ru/C <sub>extr.</sub> <sup>b</sup>	9.3	0.98	29.5	6	100	57
R14A	2 wt % Ru/C <sub>gran.</sub> <sup>c</sup>	9.4	1.90	31.6	7	86	55
R14B	2 wt % Ru/C <sub>gran.</sub> <sup>c</sup> (crushed)	7.9	1.93	30.8	7	85	49
R14C	2 wt % Ru/C <sub>gran.</sub> <sup>c</sup>	9.1	0.96	32.6	6	86	56
RGA	7 wt % Ru/C <sub>grph. pwd.</sub> <sup>d</sup>	9.7	2.06	31.5	6	45	54
R18A	7 wt % Ru/C <sub>pwd.</sub> <sup>e</sup>	9.2	2.01	29.1	7	46	47
R19A	2 wt % Ru/C <sub>gran.</sub> <sup>f</sup>	8.9	0.85	30.0	7	53	56

a. support = activated carbon powder of unstated origin; manufacturer: Aldrich.

b. support = activated carbon extrudates of unstated origin; manufacturer: Alfa Aesar.

c. support = activated carbon granules, 6 – 12 mesh, made from coconut shell; manufacturer: Engelhard.

d. support = graphite powder (BET 500 m<sup>2</sup>/g, manufacturer: Timcal). Catalyst prepared in-house, see appendix A.

e. support = activated carbon powder from coconut shell (manufacturer: Engelhard). Catalyst prepared in-house, see appendix A.

f. support = activated carbon granules from coconut shell, 6 – 12 mesh (manufacturer: Engelhard). Catalyst prepared in-house, see appendix A.

For catalysts with low ruthenium loadings, or for those in granular or extrudate form, a lower wood-to-catalyst ratio was chosen (around 1) to avoid long reaction times until the attainment of the equilibrium; for powdered catalysts, wood-to-catalyst ratios of around 2 were applied.

Table 6.17: Analysis of the product phases after gasification of wood with different catalysts. N/D = not determined.

run no.	DOC <sub>aq.</sub> g/L	X <sub>C</sub> %	tars % <sup>a</sup>	TC <sub>res.</sub> mg/g <sub>res.</sub>	GE <sup>b</sup> %	CH <sub>4</sub> vol %	C <sub>2</sub> H <sub>6</sub> vol %	CO <sub>2</sub> vol %	H <sub>2</sub> vol %	CO vol %	Y <sub>CH<sub>4</sub></sub> g/g <sub>wood</sub>
RuTi1	6.36	90.8	24.0	76.4	53	34	N/D	56	10	< 0.1	0.13
RCC	0.55	99.0	5.5	640	83	43	1.2	47	9	0.3	0.23
RCA	1.70	97.3	2.7	N/D	80	47	1.6	44	7	0.6	0.24
RCB	2.30	97.5	2.1	N/D	53	30	2.5	52	15	1.5	0.11
RCD	4.64	87.7	13.4	852	59	20	1.6	52	25	1.3	0.09
R13A	0.75	98.6	1.3	875	55	27	0.0	59	13	0.7	0.10
R14A	1.39	97.5	0.5	966	80	45	1.7	47	6	0.6	0.23
R14B	0.81	98.2	0.4	966	90	42	2.1	49	7	0.8	0.24
R14C	0.61	98.8	1.3	942	93	48	0.0	45	6	0.7	0.29
RGA	8.39	91.0	5.4	831	66	28	0.0	53	18	0.9	0.13
R18A	2.5	95.2	1.9	838	63	32	3.3	54	9	1.4	0.13
R19A	N/D	N/D	N/D	N/D	34	31	0.0	57	11	0.3	0.09

a. carbon of the tars collected in the MeOH fraction after evaporation of MeOH, in % of initial carbon of the wood slurry (C in support not accounted for), i.e.  $n_{C,tars}/n_{C,wood}$ .

b. carbon gasification efficiency based on carbon input by wood (C in support not accounted for), i.e.  $n_{C,gas}/n_{C,wood}$ .

The carbon balance was adapted in a way that not only the carbon of the wood was accounted for feed carbon, but also the carbon of the catalyst:

$$C_{balance} = \frac{n_{C, products}}{n_{C, feed}} = \frac{n_{C, gas} + n_{C, solid residue} + n_{C, tars} + n_{C, aqueous phase}}{n_{C, wood} + n_{C, catalyst}} \quad (6.7)$$

For this purpose, the carbon content of the catalysts was measured by DC-190 in the boat module to yield  $n_{C, catalyst}$ . The carbon gasification efficiency GE was then calculated by reference to the carbon input of wood, only (GE =  $n_{C, gas}/n_{C, wood}$ ) as was done in all previous campaigns, i.e. it was assumed that the carbon of the catalyst was inert. It was shown in later experiments that the catalyst supports were gasified to

some extent when exposed to the hydrothermal environment (see section 6.3.3 for the blank tests carried out). The amount of self-gasification determined in these tests could be subtracted to yield a corrected GE value for the gasification experiments. However, self-gasification is a competing reaction with wood substrate gasification. From this fact follows that in the presence of hydrolyzed wood, the catalyst may preferentially gasify this feedstock rather than the carbon of the support, and thus the correction made by comparison with a blank experiment would also be affected by a certain error. For this reason, the carbon gasification efficiencies reported in Table 6.17 were calculated without any correction.

**1 wt % Ru/TiO<sub>2</sub> (Degussa)** was crushed in an agate mortar to particle sizes below 125  $\mu\text{m}$ . Compared to the skeletal nickel catalysts tested so far, it exhibited a poor gasification efficiency (53 %), left a rather large amount of ungasified dissolved carbon in the aqueous phase, and yielded a large amount of tars and carbon deposits on the solid catalyst residue. The methane to carbon dioxide ratio was low, and thus the methane yield was also low. 1 wt % Ru/TiO<sub>2</sub> is therefore not an active catalyst. Either the active metal loading is too small, or the ruthenium crystallites are rather large and the dispersion is low, all resulting in a small surface area of active sites.

**5 wt % Ru/C (Aldrich)** was tested in experiments RCA to RCD. The carbon was in powder form and very fine. The catalyst used in RCA was reused in RCB and then in RCD. As no measurement of the solid residue after RCA could be made, the experiment was repeated (RCC), which also helped to assess reproducibility. The fresh catalyst (RCA and RCC) exhibited reasonable gasification efficiencies (over 80 %), yielding a product phase rich in methane and low in hydrogen. The residual carbon content in the aqueous phase was comparably low.

When reused, however, the catalyst performed poorly. The methane content in the gas product phase decreased from run to run, while both hydrogen and carbon dioxide increased, i.e. the selectivity was lost over repetitive runs. The gasification efficiency decreased and levelled off

between 50 and 60 %. This behavior is depicted in Figure 6.17.

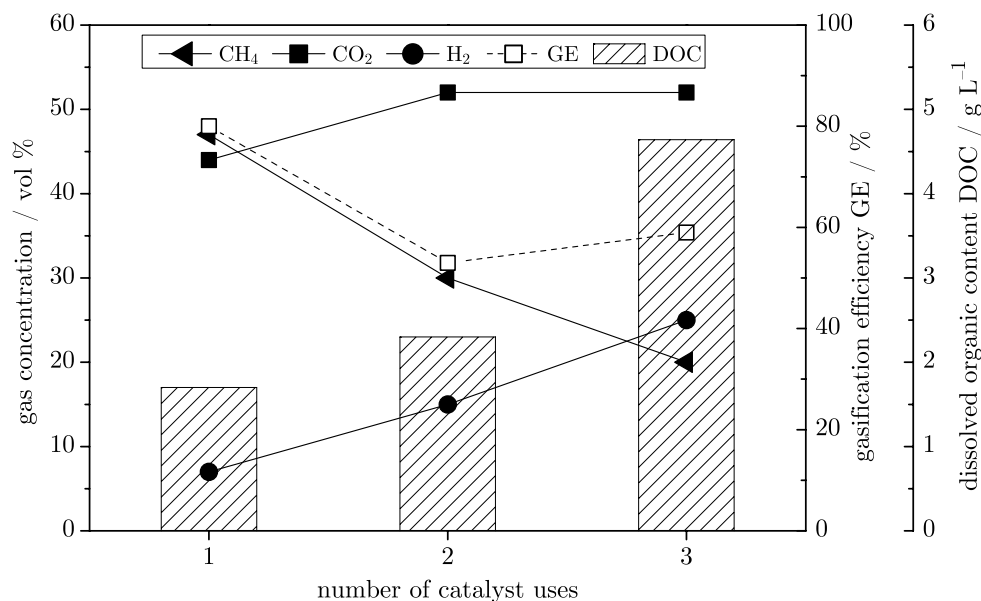


Figure 6.17: Comparison of the catalytic performance of 5 wt % Ru/C in repetitive runs. Use 1: run no. RCA; use 2: run no. RCB; use 3: run no. RCD.

First, the repetitive heat-up and quenching phases might not be advantageous for the catalyst in the sense of a seasoning to the environment (variable pressures, variable temperatures, variable solubilities, high cooling and heat-up rates, etc.). Second, the catalyst might have been increasingly poisoned by inorganics (sulfates, phosphates, etc.) that are present in the wood, which accumulated in the dry residue (the only treatment was the washing procedure with methanol, where salts would not be dissolved and extracted). Third, the catalyst was subjected to various manipulations from one run to the other, whose influence is not very clear:

(1) After each experiment, the solid residue was filtered and washed with methanol. To assess that this treatment had no adverse effect, fresh catalyst was mixed with water, filtered, and rinsed with MeOH. The aqueous phase was then analyzed for its carbon content: 0.3 % of the catalyst's carbon had dissolved into the aqueous phase. Thus, some carbon of the

fresh catalyst dissolves in water even when not exposed to hydrothermal conditions, probably due to abrasion.

(2) The solid residue was dried in the vacuum oven at 105 °C after each gasification experiment. This manipulation might influence the later catalytic activity, e.g. carbonaceous deposits on the catalyst surface might harden and be difficult to be gasified or washed off in supercritical water in the following runs, and all ruthenium sites could be fully oxidized, which can lead to a lower initial activity.

(3) To ensure that leaching of the ruthenium from the support into the aqueous or methanolic phase was not the cause for the loss in activity, ICP analyses of the aqueous and methanolic phases of the first gasification experiment RCA and the washing procedure were carried out. Only the MeOH phase of RCA contained 3 µg Ru (or 0.02 % of the ruthenium input by the catalyst). Thus, Ru leaching was not the cause of the decreasing activity.

To conclude, the initial activity and product selectivity of 5 wt % Ru/C (Aldrich) seems to be good, while repetitive usage of the spent catalyst in the batch reactor suggests a deactivation. An experiment in the continuously operating catalyst test rig could assess the long-term stability. However, other catalysts were favored due to better overall performance.

**3 wt % Ru on carbon extrudates (Alfa Aesar)** was tested next (run no. R13A). The extrudates were not crushed, but used as delivered. However, the wood-to-catalyst ratio was decreased to 1. Despite the long residence time of 100 minutes in supercritical water, the methane yield was very low,  $0.10 \text{ g}_{\text{CH}_4}/\text{g}_{\text{wood}}$  (only 30 % of the yield expected for 100 % GE and a methane concentration corresponding to the thermodynamic equilibrium concentration). However, the low dissolved organic content and the low amount of tars indicate that mass transfer restrictions might have played a role: the catalyst was not ground, and the reactor's content was not actively mixed; mixing can only take place by free convection within

the reactor. If product gases are more likely to be in the upper, cold part of the reactor (in the lower, hot part, one-phase-behavior of the fluid is assumed), and the mixing process in the hot part is impaired, then the gases cannot equilibrate, and the wood might not be completely gasified. Further indications that fluid mixture in the batch reactor is an issue were gained from experiments with gases, see section 6.4.3. Nevertheless, other non-ground granular catalysts performed much better, while the same mass transfer limitations must have existed for these catalysts as well. To conclude, 3 wt % Ru/C (Alfa Aesar) cannot be a catalyst of choice for the hydrothermal gasification of wood.

**2 wt % Ru on granular carbon from coconut shell (Engelhard)** performed quite well. Coconut shell carbon is reportedly one of the most stable carbons [125]. Three experiments were conducted: R14A, R14B, and R14C. The first run was carried out with a wood-to-catalyst ratio of 2, while R14C had a ratio of 1 (to test the influence of mass transfer limitations). R14B was crushed in an agate mortar to increase the surface area of the carbon. However, the crushing might flake off the ruthenium, which could counterbalance the increased surface area. The mixture was held in supercritical water for a longer time than in the tests with skeletal nickel catalysts. While a steady state in pressure was reached rather quickly with skeletal nickel catalysts, the pressure was still slowly increasing after one hour with 2 wt % Ru/C, indicating the lower activity of the supported ruthenium catalysts. The rate of pressure increase/decrease is displayed in Figure 6.18 for a gasification experiment with 2 wt % Ru/C, and an experiment with a skeletal nickel catalyst, with which a steady state in pressure was reached after 25 minutes. The residence time for gasification experiments with 2 wt % Ru/C was therefore adapted to around 90 minutes. The results of these experiments are depicted in Figure 6.19.

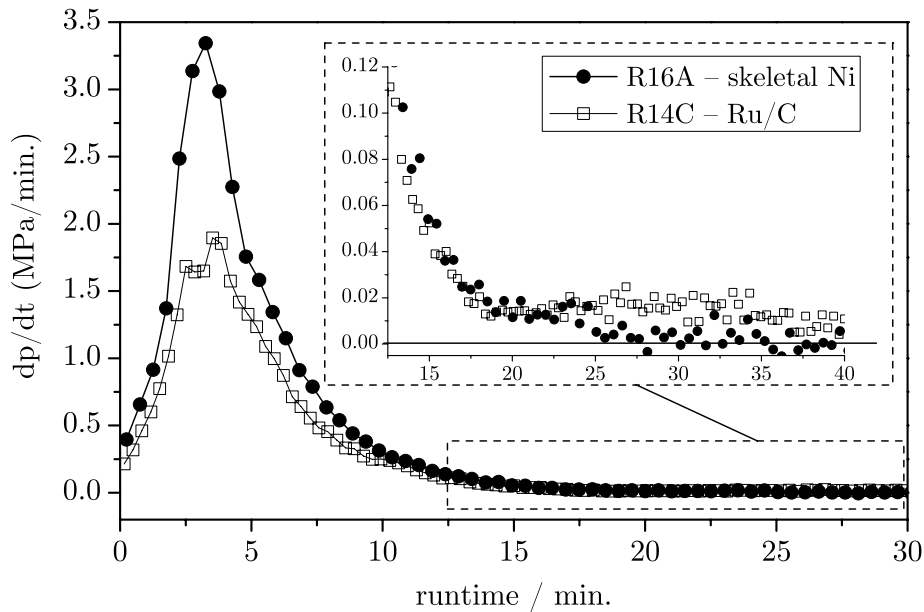


Figure 6.18: Difference in pressure per minute (rate of pressure increase/decrease) for a wood gasification experiment with a skeletal nickel catalyst (R16A) and a Ru/C catalyst (R14C). Data points averaged over 40 seconds to smooth recorded values.

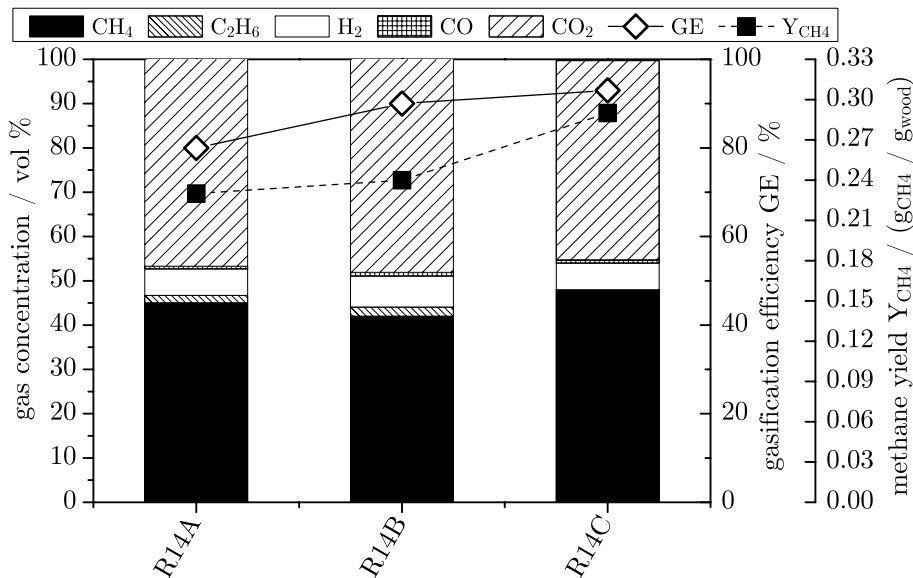


Figure 6.19: Gas phase composition, gasification efficiency and methane yield of wood gasification using 2 wt % Ru/C (Engelhard).

The crushing or the decreasing of the wood-to-catalyst ratio had nearly no effect on the product gas composition. Only slightly less methane was

detected with the crushed catalyst. However, the gasification efficiency was increased to 93 % by decreasing the wood-to-catalyst ratio to 1. In terms of GE, the performance of this Ru/C catalyst is comparable to the one of skeletal nickel catalysts. The low hydrogen content was additionally favorable, resulting in a methane yield of  $0.29 \text{ g}_{\text{CH}_4}/\text{g}_{\text{wood}}$ . The crushed catalyst yielded slightly more carbon dioxide and less methane, probably due to abrasion (the crushing process produced some carbon dust from attrition, which could be gasified to  $\text{CO}_2$ ). To conclude, 2 wt % Ru/C (Engelhard) turned out to be a promising candidate for the process and was chosen for tests in the continuously operating catalyst test rig to assess its long-term stability and performance (see section 7.1.5).

Three catalysts were synthesized in-house with potassiumpentachlororuthenate(III) as precursor,  $\text{K}_2\text{RuCl}_5$ , with the anion-deposition method described by Hoffer et al. [119], for which the resulting dispersion is reported to be high. The preparation of the three catalysts is outlined in appendix A. Three different supports were chosen:

- (i) A graphitic type carbon in powder form from Timcal ( $S_{\text{BET}}$   $500 \text{ m}^2/\text{g}$ , research grade, yielding the catalyst used in run no. RGA).
- (ii) An activated carbon from coconut shell in powder form ( $S_{\text{BET}}$   $1000 \text{ m}^2/\text{g}$ , received from Engelhard, yielding the catalyst used in run no. R18A).
- (iii) An activated carbon from coconut shell in granular form ( $S_{\text{BET}}$   $850 - 1000 \text{ m}^2/\text{g}$ , received from Engelhard, yielding the catalyst used in run no. R19A; this support is identical to the support used by Engelhard to manufacture their 2 wt % Ru/C catalyst).

The catalysts were prepared with 7 wt % Ru loading for both RGA and R18A, and with 2 wt % Ru loading for R19A (to have a 1:1 comparison to the industrially manufactured catalyst, as it used the same support).



**7 wt % Ru/C<sub>graphite</sub> (in-house)** performed quite poorly, despite its high precious metal loading (run no. RGA). The residual carbon in the aqueous product phase was high (8.4 g/L, most probably originating from the catalyst support and not from the carbon contained in the wood, see the blank tests described in section 6.3.3). The low methane content of the product gas, accompanied by almost 20 vol % of hydrogen are indications of its low selectivity towards SNG. This catalyst is not suited for the hydrothermal gasification of wood due to its low activity and gasification efficiency (although present as a powder), which leads to a methane yield of only  $0.13 \text{ g}_{\text{CH}_4}/\text{g}_{\text{wood}}$  (40 % of the maximum thermodynamic yield).

**7 wt % Ru/C<sub>powder</sub> (in-house)** yielded similar results (run no. R18A): the dissolved organic content of the aqueous product phase and the amount of tars were lower than in RGA, with a similar gasification efficiency and methane yield. Slightly more methane and substantially less hydrogen were formed, with equal amounts of CO<sub>2</sub>. The ethane detected at the end of this experiment probably stems from wood decomposition products, and not via Fischer–Tropsch synthesis. C<sub>2</sub>H<sub>6</sub> was typically detected in long-term runs in the continuously operating test rig, but only during the start-up phase. Hence ethane is assumed to be an intermediate product (not being further decomposed while the catalyst was adapting to the environment). Also Sharma and co-workers reported ethane to be a decomposition product of phenol degradation, rather than a Fischer–Tropsch synthesis product [68]. However, Ru is known to catalyze the Fischer–Tropsch reactions as it catalyzes hydrogenation steps.

**2 wt % Ru/C<sub>granules</sub> (in-house)** was tested in run no. R19A and performed worse than the other two catalysts synthesized in-house. The product gas was nearly identical to the one obtained in R18A, but had a lower content of CO and no ethane, and therefore produced a methane yield of  $0.09 \text{ g}_{\text{CH}_4}/\text{g}_{\text{wood}}$  despite the poor gasification efficiency of only 34 %.

One of the reasons for the poorer performance of the catalysts prepared in-house, compared to the commercially available ones, could be the non-ideal reduction temperature, at which the deposited  $\text{RuCl}_3$  was reduced under flowing hydrogen to  $\text{Ru}(0)$  and  $\text{HCl}$ . The applied temperature was  $150\text{ }^\circ\text{C}$ ; at a later stage of the project, however, Engelhard revealed that the reduction temperature should be  $170$  to  $220\text{ }^\circ\text{C}$  [179]. Thus, the reduction could have been incomplete and thus, the catalyst less active. Dispersion and ruthenium crystallite size distribution are other important parameters where the commercial catalysts might be better.

To sum up, supported ruthenium catalysts are suitable for the hydrothermal gasification of wood to SNG. While  $1\text{ wt } \%$   $\text{Ru}/\text{TiO}_2$  (Degussa) was not active enough, some  $\text{Ru}/\text{C}$  catalysts performed well and produced a methane yield almost as high as skeletal nickel catalysts. The best catalyst was  $2\text{ wt } \%$   $\text{Ru}/\text{C}$  (Engelhard), which was therefore selected for thorough testing in the continuously operating rig, see section 7.1.5. Figure 6.20 shows an activity versus selectivity plot for the tested  $\text{Ru}/\text{C}$  catalysts.

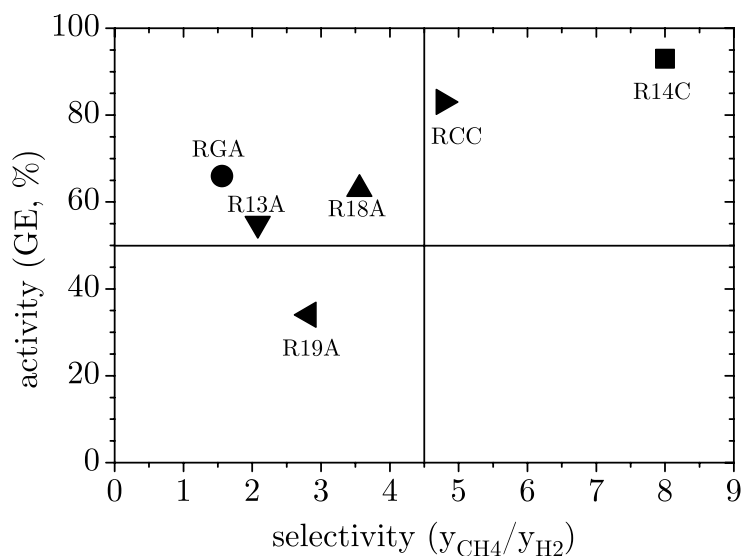


Figure 6.20: Activity (in terms of gasification efficiency) vs. selectivity (ratio of methane to hydrogen in the product gas) of the various tested  $\text{Ru}/\text{C}$  catalysts. Despite its moderate precious metal loading,  $2\text{ wt } \%$   $\text{Ru}/\text{C}$  (run R14C) performed best.

### 6.3.3 Stability Experiments with Supported Ruthenium Catalysts and Carbon Supports in the Batch Reactor

Although some Ru/C catalysts gasified wood quite well, they are all prone to self-gasification. Before carrying out rather time-consuming long-term stability tests in the continuously operating test rig, initial clarifications with short-term batch experiments were made. For this, four blank-tests with catalysts (support plus active metal), and four blank tests only with carbon supports were carried out.

For each experiment, about 300 mg of sample were loaded into the reactor, together with 6 g of water. The reactor was then pressurized with around 20 MPa Ar after its evacuation. This loading is comparable to the amount used when gasifying wood with a wood-to-catalyst ratio of 2. The mixture was heated to 400 °C (within 6 – 7 min., at ~53 °C/min.) and held at this temperature for 45 minutes. The resulting pressure was between 26.8 and 27.7 MPa.

The results of this hydrothermal treatment are displayed in Table 6.18. Due to the low amount of gas formed ( $GE < 10\%$ ), the products were highly diluted in argon. Thus, the actually measured absolute gas concentrations were much lower than the values reported here, which were calculated on an argon-free basis. The detection limit for hydrogen by TCD using N<sub>2</sub> as the carrier gas, however, is around 2 vol %. Thus, in those experiments where the absolute hydrogen concentration was lower, no H<sub>2</sub> was detected at all, although it is assumed to have been present to some extent as well.

As can be seen, the catalysts are, as expected, more prone to self-gasification than the supports alone (e.g. GE is 6 % for T-RGA and 2.1 % for its support T-CGA; 2.9 % for the commercial catalyst tested in T-R14A and 2.6 % for its support T-C14A). The amount of Ru loading seems to have an adverse effect on self-gasification (the key parameter is believed to be the surface area of active sites, which is a function of metal loading, dispersion, and crystallite size distribution). As shown, the difference in self-gasification efficiency of the most promising 2 wt % Ru/C (Engelhard, T-R14A) and its support (T-C14A) is only 0.3 %. Most probably,

Table 6.18: Gas phase analysis after self-gasification experiments of different Ru/C catalysts and carbon supports.

	run no.	sample	GE <sup>a</sup> %	CH <sub>4</sub> vol %	CO <sub>2</sub> vol %	H <sub>2</sub> vol %	CO vol %	Y <sub>gas</sub> <sup>b</sup> L/g
catalysts (T-Rxx)	T-RCA	5 wt % Ru/C <sub>pwd.</sub> (Aldrich)	5.0	14	86	N/D	0	0.07
	T-RGA	7 wt % Ru/C <sub>grph.</sub> (in-house)	6.0	4	38	56	2	0.22
	T-RGB	solid residue of T-RGA	3.5	9	29	62	0	0.13
	T-R14A	2 wt % Ru/C <sub>gran.</sub> (Engelhard)	2.9	26	25	49	0	0.06
supports (T-Cxx)	T-CGA	graphite (Timcal) 500 m <sup>2</sup> /g	2.1	23	77	N/D	0	0.03
	T-C3A	graphite (Timcal) 100 m <sup>2</sup> /g	1.2	49	50	N/D	1	0.02
	T-C14A	activated C <sub>gran.</sub> (Engelhard)	2.6	9	30	61	0	0.10
	T-C18A	activated C <sub>pwd.</sub> (Engelhard)	1.7	50	50	N/D	0	0.02

a. carbon gasification efficiency based on carbon input by catalyst or support, as determined in advance by DC-190 (boat module), i.e.  $n_{C, \text{gas}}/n_{C, \text{sample}}$ .

b. gas yield in L/g<sub>sample</sub> (dry), at 1 atm and 0 °C.

mainly carbon from attrition due to storage, shipping, etc. was gasified and had led to an increase in DOC. This is also indicated by repetitive usage: a second hydrothermal treatment for the catalyst synthesized in-house showed that the self-gasification decreased (GE from 6.0 % in T-RGA to 3.5 % in T-RGB). Also the dissolved organic content of the residual aqueous phase decreased substantially from 4.55 g/L to 0.11 g/L. This behavior could thus exemplify the adaptation to the hydrothermal environment. Interestingly, the dissolved organic content as well as the content of tars was always larger after the blank-test of the supports than after the blank-test of the corresponding catalyst, see Table 6.19. This behavior was expected, since the presence of the active noble metal gasifies the dissolved organic carbon and tars. The support for the commercially available catalyst used in T-RCA was not available for testing. To conclude, self-gasification in absence of a gasifiable feed can be an issue for Ru/C catalysts. From the pressure signal of T-R14A for instance, an average increase of 3.6 kPa/min. was recorded from the time

Table 6.19: Analysis of the liquid residue phase after self-gasification blank-tests carried out with Ru/C catalysts and carbon supports.

	catalysts				supports			
	T-RCA	T-RGA	T-RGB	T-R14A	T-CGA	T-G3A	T-C14A	T-C18A
DOC <sup>a</sup>	0.12	4.55	0.11	0.36	1.72	1.04	2.31	0.58
tars <sup>b</sup>	6.3	0.3	0.9	1.0	2.7	0.1	1.9	1.1

a. dissolved organic carbon content in g/L.

b. content of tarry compounds (methanol solubles), in % of feed carbon ( $n_{C,tars}/n_{C,feed}$ ).

when a steady state in temperature was reached (~20 min.) to the quenching (after ~50 min.). Small temperature variations during this period were accounted for. By application of the ideal gas law (for simplicity), this amount corresponds to ~0.019 mmol<sub>gas</sub>/min. For a gas phase with 1/4 of CH<sub>4</sub>, 1/4 of CO<sub>2</sub>, and 1/2 of H<sub>2</sub> (as measured), the pressure increase corresponds to an average decrease in carbon over the period recorded of 0.114 mg/min., or 0.39 ‰/min. of the initial carbon fed to the reactor. Hence, 10 ‰ of the catalyst would be gasified within 4 – 6 hours (shrinking core model).

However, it must be pointed out that 2 wt % Ru/C (Engelhard) was thoroughly tested in the continuously operating rig, and there, self-gasification was not identified as a problem at all. Thus, heat-up, adaptation to the new environment, and quenching might be factors which are much more important (and can lead to a certain degree of gas production) than the steady state behavior in supercritical water itself. Moreover, carbon catalysts can adsorb a substantial amount of CO<sub>2</sub> from the air (activated carbon is used in pressure swing adsorption to free gases from CO<sub>2</sub>). If the catalyst was not stored moist, it is possible that a significant amount of the CO<sub>2</sub> obtained from the blank-tests originated from adsorbed carbon dioxide.

## 6.4 Experiments using Gas Mixtures as Reactants Instead of Biomass

### 6.4.1 Overview of the Experiments

Several experiments were carried out where water and catalyst (or support only) were filled into the batch reactor, after which it was flushed three times with Ar before being pressurized with reactant gas, e.g. with CO, or with gas mixtures, e.g. CO<sub>2</sub> and H<sub>2</sub> to ~1.2 MPa (2.0 MPa for mixtures). The experimental matrix for these experiments can be seen in Table 6.20.

Table 6.20: Matrix of experimental conditions for batch reactor experiments using gaseous reactants (or formic acid). T<sub>max.</sub> = 405 °C.

run no.	CO mmol	CO <sub>2</sub> mmol	H <sub>2</sub> mmol	solid (dry) <sup>a</sup> mg	$n_C/n_{Ru}$ <sup>b</sup> –	H <sub>2</sub> O mmol	remarks
G1	10.1	–	–	218	234	404	
G2	9.7	–	–	25	1972	398	10 × less catalyst
G3	9.6	–	–	2312	21	404	10 × more catalyst
G4	9.6	–	–	2312	N/A	403	support only
G5	10.8	–	8.8	222	204	468	
G6	–	8.4	12.6	228	161	422	
A1	–	–	–	228	339	468	705.4 mg HCOOH as feed <sup>c</sup>

a. 2 wt % Ru/C (Engelhard) was used as catalyst; in run no. G4 only its carbon support was used.

b. based on 2 wt % (of dry catalyst) as stated by the manufacturer.

c. 705.4 mg HCOOH (included water traces were accounted for) corresp. to 15.3 mmol CO and H<sub>2</sub>O each, or CO<sub>2</sub> and H<sub>2</sub> each, resp. (by decarbonylation or decarboxylation of the formic acid, resp.). 0.76 MPa Ar were added.

The molar amount of the added gas reactants was calculated from the pressure signal, using the ideal gas law with the addition of compressibility factors. The carbon dioxide dissolution in the water, if applicable, was accounted for using Henry's law. The ratio of carbon from reactants to

ruthenium on the catalyst was roughly the same as in the wood gasifying experiments. The gas reactant's total concentration was 4 – 5 wt %. The residence time of the reactor in the hot fluidized sandbath was 60 min.

#### 6.4.2 CO/CO<sub>2</sub>, (H<sub>2</sub>), Ru/C (or support)

Run no. G1 was expected to shift the CO with water over the catalyst to CO<sub>2</sub> and H<sub>2</sub>, which would then be methanated ( $0.25 \text{ CO}_2 + \text{H}_2 = 0.25 \text{ CH}_4 + 0.5 \text{ H}_2\text{O}$ ). The resulting gas phase should thus be composed of 75 vol % CO<sub>2</sub> and 25 vol % CH<sub>4</sub>, with some traces of hydrogen (thermodynamic equilibrium). The actually measured product gas, however, contained only a small amount of H<sub>2</sub> (8 vol %) and CO<sub>2</sub> (11 vol %), and traces of CH<sub>4</sub> (< 0.1 vol %), while the majority of the product gas was unreacted CO, see Figure 6.21.

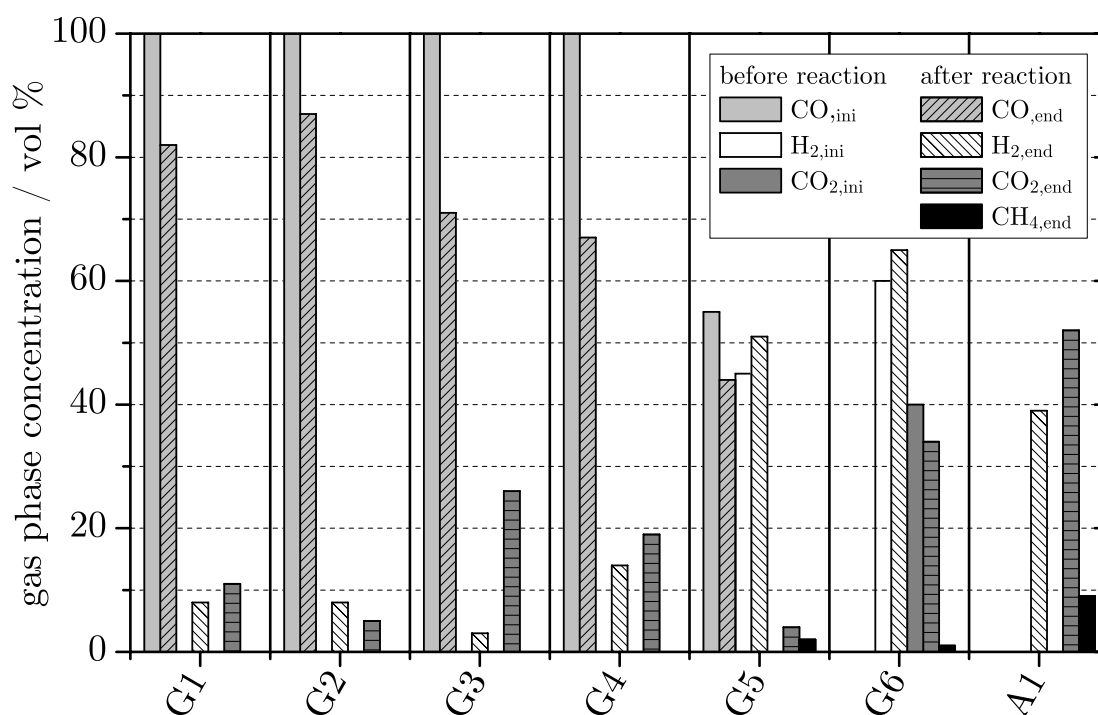


Figure 6.21: Gas concentrations before (calculated based on pressure) and after reaction (measured by gas chromatography).

Decreasing the amount of catalyst tenfold (run no. G2) did not lead to a significant change in the product composition. Increasing the amount of

catalyst by a factor of 10 (run no. G3) produced more  $\text{CO}_2$  and less  $\text{H}_2$ , but still, virtually no  $\text{CH}_4$  was detected.

The non-catalytic (neglecting the wall effects of the stainless steel reactor) water gas shift experiment in run no. G4 interestingly produced more hydrogen and more carbon dioxide than by using 2 wt % Ru/C.

Supplying both carbon monoxide and hydrogen to the reactor prior to heat up (run no. G5) should increase the methane yield, and indeed some  $\text{CH}_4$  was formed (2 vol %). Nevertheless, 79 % of the initial carbon monoxide had neither shifted to carbon dioxide nor was it methanated. Starting from  $\text{CO}_2$  and  $\text{H}_2$  (run no. G6) also produced some methane, but to a lesser extent (only 1 vol %) than by using CO and  $\text{H}_2$ , despite the higher  $\text{H}_2/\text{CO}_x$  ratio.

### 6.4.3 Mixing Problem of the Batch Reactor

These findings can only be explained by mass transfer limitations. Up to these experiments, it had always been believed that, although the reactor's content was not actively mixed by a stirrer or by a tumbling mechanism, the convective streams inside the vessel would suffice to provide a significant mixing. Especially when a supercritical state is reached, there are supposedly only one fluid (water and gas) and a solid catalyst phase. Thus, the gases should be well solubilized in the hydrothermal environment, and readily react over the noble metal catalyst.

Before these experiments with gaseous reactants were started, the lower, hot part of the reactor (making about 82 % of its total volume), which is immersed into the fluidized sand bath, contained water and catalyst. The gases are in the upper, cold part of the reactor (18 % of the reactor's volume), as well as in the residual volume of the lower part which is on top of the water phase (water + catalyst occupy about 1/3 of the lower part at room temperature). Now, during the heat-up phase, the water vapor pressure rises, the water expands in the lower part of the reactor, and compresses the gases (which do not significantly expand as they are not heated) in the upper, cold part, so that the pressure is equal in every part of the apparatus. The density in the lower part of the reactor decreases as



the water is heated to 400 °C. However, the density of the cold gases in the upper part of the reactor is always lower than the one of the supercritical water phase in the hot part: At a pressure of 30 MPa, the density (at 50 °C as in the upper cold part) is 190 kg/m<sup>3</sup> for CH<sub>4</sub>, 275 kg/m<sup>3</sup> for CO, and only 19.2 kg/m<sup>3</sup> for H<sub>2</sub>. In contrast, the density of the supercritical water phase in the lower, hot part is 357 kg/m<sup>3</sup> at 400 °C (and larger at lower temperatures) [35]. Thus, there is no real driving force leading to the mixing of the two compartments in direction of the hot part, only in direction of the cold part. However, if water is transferred to the upper, cold part, it condensates, because  $T \ll T_c$  (even if  $p > p_c$ ). Hence, the capillary connecting the lower, hot part of the reactor to the upper, hot part acts like a reflux cooler, and as a consequence the fluid phase from below is not being sucked into the upper part (it only happens to some degree when one of the high-pressure valves is opened to withdraw a sample of the reactor's content, which induces a large pressure difference). Thus, while the lower, hot part is assumed to be mixed by convective streams within the supercritical fluid, gas molecules which are not already dissolved in this phase (e.g. in the upper, cold part) have no tendency to go there, are not in contact with the catalyst, and remain unreacted.

#### 6.4.4 Formic Acid, H<sub>2</sub>O, Ru/C

If the reacting gases (CO, H<sub>2</sub>, CO<sub>2</sub>) were formed *in-situ*, out of a dissolved compound, inside the aqueous part of the reaction media, then the gas would not be separated from the liquid phase from the beginning, and much more methane should be formed. As formic acid can decompose to CO, CO<sub>2</sub>, H<sub>2</sub>, and H<sub>2</sub>O, it was used at a concentration of 10 wt % in run no. A1. To always keep a dense phase inside the reactor and avoid dry-out during heat-up, the reactor was pressurized with 0.76 MPa of Ar before its immersion into the fluidized sandbath. During the heat-up, the formic acid certainly went preferentially into the gas phase, compared to water (vapor-liquid-equilibrium), but nevertheless, when starting from HCOOH(aq.), much more gas should be present in the fluidic phase when a supercritical state has been reached. Furthermore, formic acid is a reac-

tion intermediate of the  $\text{CO}_2$  methanation, as pointed out in section 2.2.5 on page 33. And in fact, the gas phase at the end of the experiment was composed of 39 vol %  $\text{H}_2$ , 52 vol %  $\text{CO}_2$ , and 9 vol %  $\text{CH}_4$ . Still, the composition was not in equilibrium, but the methane yield was significantly higher (more than 10 times as high compared to starting from  $\text{CO}_2$  and  $\text{H}_2$  in the gas phase). Considering the methanation mechanism, where several neighboring adsorbed hydrogen atoms are required, it follows that still some  $\text{CO}_2$  and especially  $\text{H}_2$  (large diffusion coefficient) must have escaped into the upper, cold part of the reactor, while the reaction mixture in the lower, hot part must have been in equilibrium.

#### **6.4.5 Conclusions of the Experiments Using Gas Mixtures as Reactants**

In light of these experiments, it can be deduced that the mixing of the reactor's contents by free convection is insufficient, and that gases, once in the cold part of the reactor, are not easily mixed back with the hot content in the lower part of the reactor. This may also explain why it takes so long to reach equilibrium in the batch reactor.

The larger and heavier the catalyst particles are, the less are they carried with fluid streams in the hot part. Certainly, catalysts in powder form such as skeletal nickel catalysts, or some of the Ru/C, are expected to be better mixed due to their small particle size. Especially in the early stage of gasification, where still unconverted wood and a viscous wood hydrolysis phase coexist, the larger particles such as 2 wt % Ru/C (Engelhard) are expected to be more impeded to travel through the reactor compared to catalyst particles in powder form.

The separation of the reactor into two compartments which are barely mixed explains why with 2 wt % Ru/C (Engelhard) as catalyst, the product gas composition after the batch gasification experiments did not correspond to the thermodynamic equilibrium composition, while the same catalyst gasified synthetic liquefied wood in the continuously operating test rig (see section 7.1.5) completely to a gas which actually did correspond to the equilibrium condition.

Therefore, for experiments carried out in the batch reactor, only those with catalysts having similar physical properties can be one-to-one compared to another, e.g. skeletal nickel catalysts in powder form, Ru/C in powder form, Ru/C in granular form. Nonetheless, the commercially available supported granular ruthenium catalyst was, despite its mixing impediment, better than Ru/C in powder form, and the preliminary catalyst evaluations presented in section 6.3 are still valid.

Unfortunately, these experiments with gases were conducted at an advanced stage of the project, when most of the batch experiments had already been carried out.

## 6.5 Comparison of the Reactivity of Wood to Synthetic Liquefied Wood

Instead of actual wood slurries, a mixture of five organic liquids, so called synthetic liquefied wood (refer to section 5.2 for its composition), was used as the organic feed in the continuously operating catalyst test rig. Although the composition of the synthetic liquefied wood was based on the outcome of wood slurry liquefaction experiments, its five substances (acetic and formic acid, ethanol, phenol, and anisole) are small molecules, whereas wood consists of (hemi-)cellulose and lignin, i.e. of macromolecules, whose linkages must be broken before the constituents can access the catalytic sites and be gasified. Thus, the synthetic liquefied wood is expected to exhibit a higher reactivity, as the hydrolysis steps in which the linkages are broken had already been taken. To assess the reactivity of synthetic liquefied wood (SLW) in comparison to the one of real wood slurries, gasification experiments were carried out in the batch reactor.

To have information about the evolution of gas concentrations, gas phase samples should be taken during the reaction. The most elegant way to achieve this goal would be to continuously withdraw a small amount of the reactor's content and analyze it with a mass spectrometer (which has

a much faster measuring time than a gas chromatograph, for instance). However, the mass spectrometer needs a continuous input gas flow (ideally  $\sim 5$  mL/min), which is difficult to achieve when the pressure inside the vessel changes from 2 MPa at immersion into the fluidized sandbath to around 30 MPa after the reaction.

### 6.5.1 Possibilities to Take Samples During Reaction

A capillary, connected to the upper cold part of the reactor, could generate a pressure drop so that on its other end, the pressure is reduced to a slightly higher level than the atmospheric pressure. However, the pressure inside the batch reactor is not constant during the heat-up phase (and during gas-evolution), and so the pressure at the end of the capillary would vary, and with it the gas flow out of the system.

The pressure drop  $\Delta p$  of a pipe with laminar flow can be described by [180]:

$$\Delta p = \frac{32 \cdot \eta \cdot v \cdot L}{d_i^2} \quad (6.8)$$

with  $\eta$  being the dynamic viscosity of the gas mixture,  $v$  its velocity through the pipe, and  $L$  and  $d_i$  the length and internal diameter of the pipe, respectively. Splitting the calculation into sections of 1 MPa pressure drop under the condition that at the end of the pipe, a throughput of 5 mL/min. is given at atmospheric pressure, the total length  $L$  increases impressively with the inner diameter  $d_i$ , see Table 6.21 for examples.

The limiting factor is not so much the inner diameter than the ability to withstand a pressure of 30 MPa. The smallest high pressure tubings available have an inner diameter of 508  $\mu\text{m}$  (HiP Company, USA). HPLC steel capillaries have a typical inner diameter of 100  $\mu\text{m}$  (Supelco), which would still lead to a tube 44 m long, where significant backmixing phenomena would take place over time.

Table 6.21: Capillary length to generate a pressure drop of 30 MPa for various pipe inner diameters  $d_i$ .

inner diameter $d_i$ $\mu\text{m}$	length $L$ m
50	3
100	44
500	27'300
1000	437'000

These preliminary calculations led to a different approach: the sampling over a hatch, see Figure 6.22.

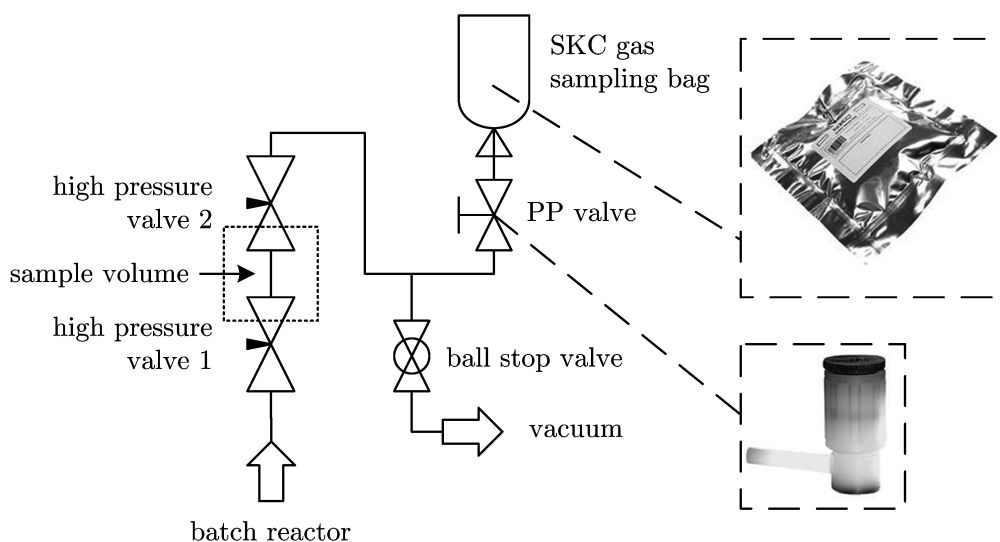


Figure 6.22: Gas sampling section added to the batch reactor.

During the experiment, both high pressure valves are first closed, and the transfer line had previously been evacuated. Then, high pressure valve 1 was opened, and gas flowed into the transfer line. Hereby, the pressure dropped slightly and so did the temperature (due to expansion), see Figure 6.23. At higher pressures, hot reactor content was sometimes sucked into the upper cold part, which was inevitable especially after the critical point had been reached. After the filling of the transfer line, high pressure valve 1 was closed, and valve 2 opened. The gas expanded into the previously evacuated gas sampling bag (Grab Foil Bag, SKC Inc.,

USA). Its content was then analyzed by gas chromatography (injection by a syringe through the septum port of the PP valve attached to the bag) and its volume determined by evacuation into a plastic syringe with a scale in mL. The dead volume of the system was accounted for as well.

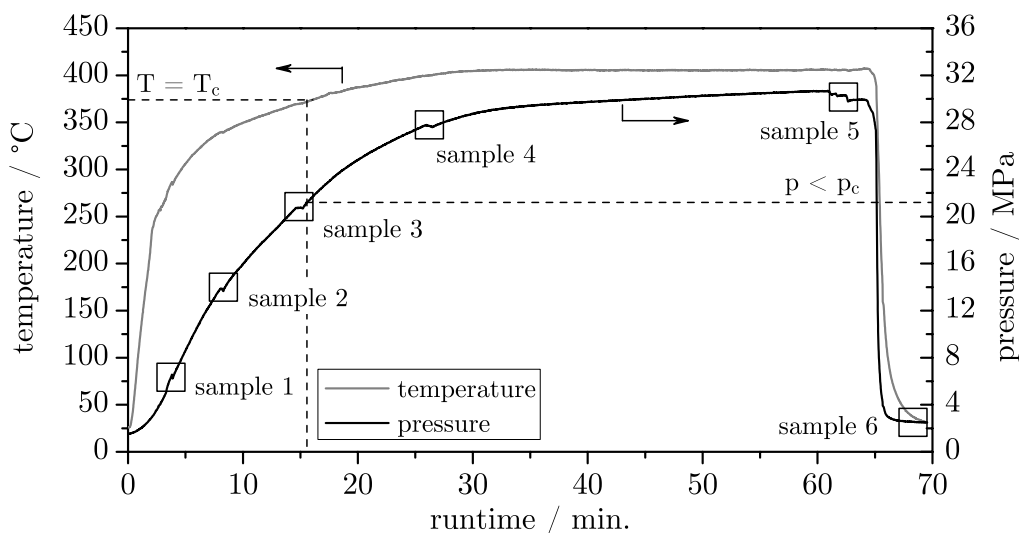


Figure 6.23: Pressure and temperature diagram of an exemplary wood gasification experiment with simultaneous high-pressure sampling.

### 6.5.2 Comparison of Spruce Slurries to Synthetic Liquefied Wood (catalyst: 2 wt% Ru/C)

The comparison of wood gasification experiments (conc. 10 wt %) and experiments with synthetic liquefied wood (SLW, conc. 10 wt %) is depicted in Figure 6.24 in a gas phase concentration vs. time plot, and in Figure 6.25 in a gas phase concentration vs. temperature plot. All gasification experiments were carried out with 2 wt % Ru/C (Engelhard). Prior to reaction, the reactor was flushed two times with Ar (instead of being evacuated), and then subjected to around 1.5 MPa of Ar before reaction. For these experiments, the sandbath was preheated to 350 °C. Upon immersion of the reactor, a new setpoint temperature (405 °C) was selected. This ensured a gradual heat-up time of around 25 min., which facilitated the sampling procedure.

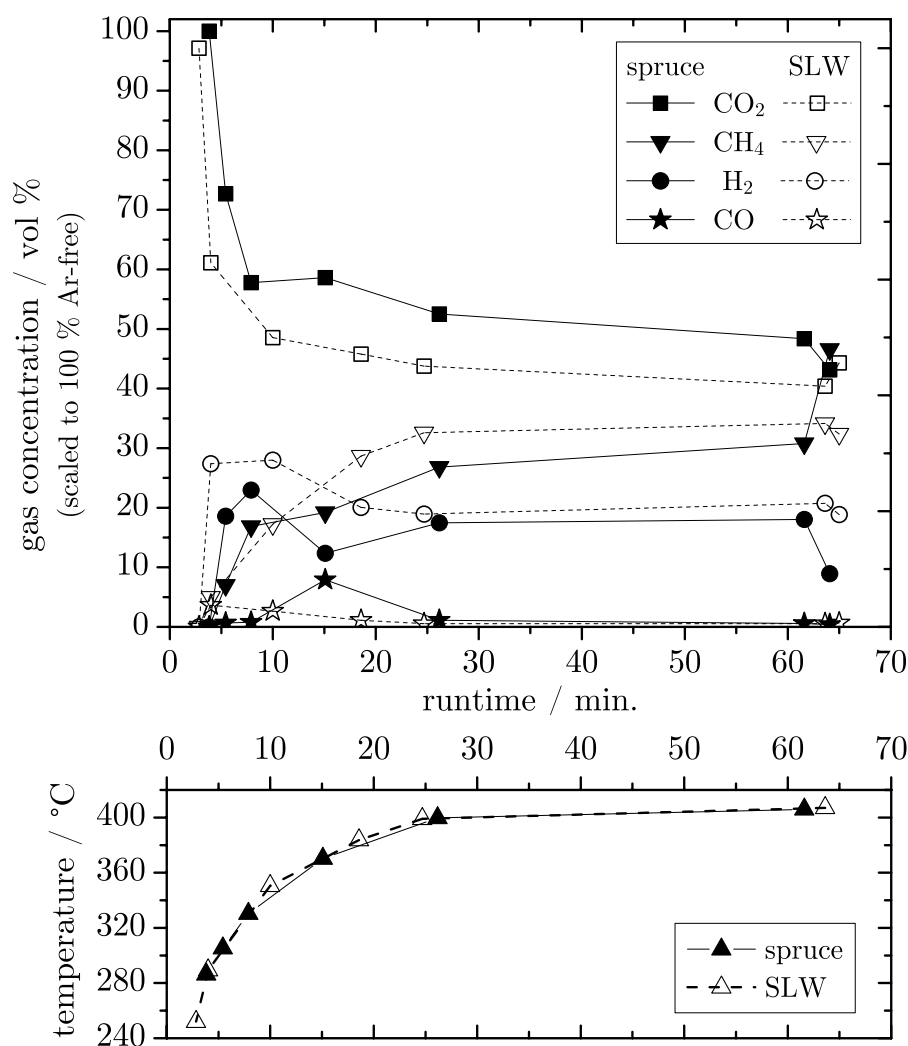


Figure 6.24: Comparison of the product gas composition as a function of time.

The general trend is quite comparable, justifying the use of synthetic liquefied wood for real wood slurries to test for the long term activity of catalysts in the continuously operating test rig. However, the gasification of SLW starts at slightly lower temperatures. While skeletal nickel catalysts started to produce gas from real wood slurries at 250 °C (compare section 6.1.7), no gas was formed below 270 °C using Ru/C as catalyst. With SLW, the hydrogen concentration increases faster than the methane concentration, whereas with wood as feed this behavior is less distinct. This can be explained by the faster reforming to the primary gases CO/CO<sub>2</sub> and H<sub>2</sub>, while the methanation from these gas molecules is carried out equally fast in both systems.

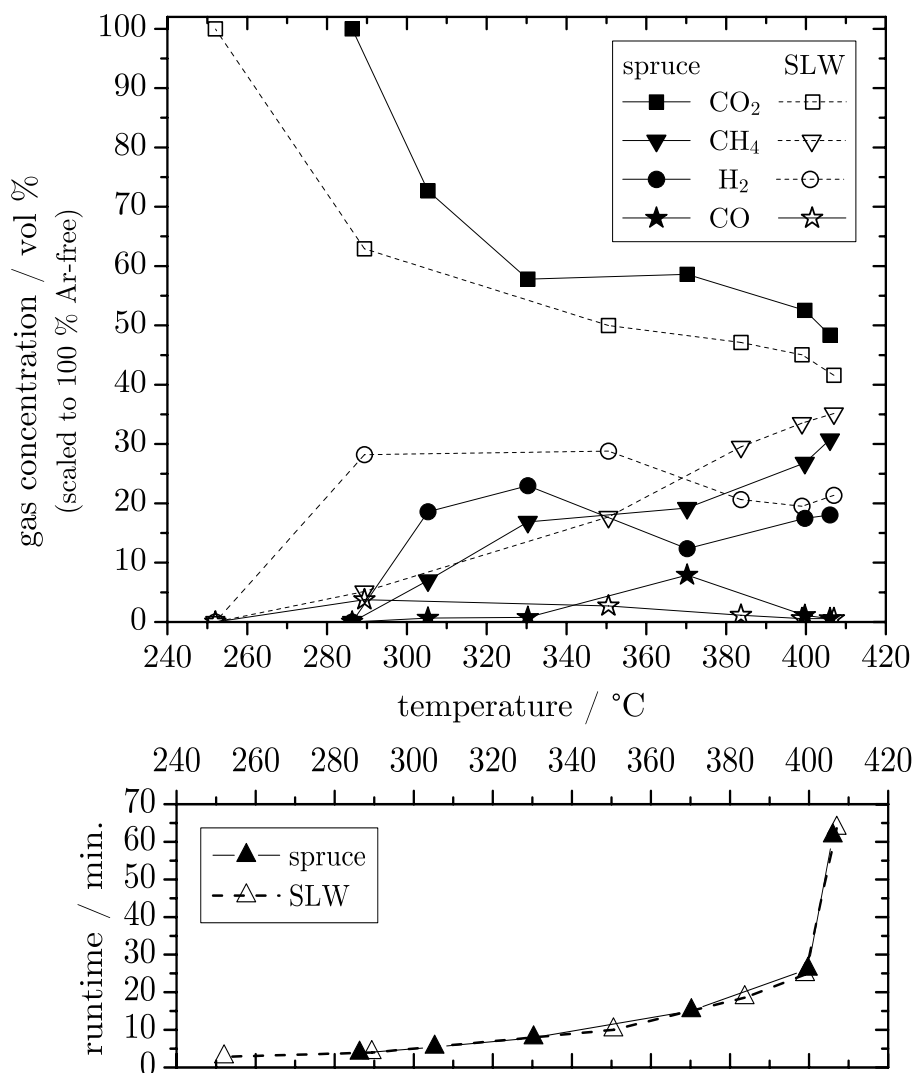


Figure 6.25: Comparison of the product gas composition as a function of temperature inside the hot, lower part of the reactor.

The difference in concentration from the last measuring point which was taken after cool-down of the reactor and the second last one, which had been taken at 405 °C, just before the quenching of the reactor, illustrates the problem of the component distribution within the batch reactor system outlined in section 6.4.3. During hot sampling, the Ar fraction in the gas was significantly lower than after cool-down, indicating that Ar preferentially stayed in the supercritical water, while the lighter gases, especially hydrogen, stayed preferentially in the upper, cold part of the reactor. Thus, the hydrogen content during hot sampling was larger than the average hydrogen content inside the whole apparatus.



If the Ar were equally distributed in the reactor, both in a cold and a hot status, then molar amounts could have been backwards calculated by reference of argon. However, as the sampling was not equally representative for all gas components, this approach failed. Thus, only concentration evolutions could be drawn and compared. Nevertheless, as gasification with real wood slurries and with synthetic liquefied wood were both carried out in the same system, the comparison of the product gas composition as a function of temperature and/or time is valid, although the actually measured concentration might be affected by an error due the distribution of the individual gases at specific conditions.

### 6.5.3 Conclusions of the Comparison Experiments

- Despite the non-ideal distribution of product gases inside the hot and cold part of the reactor, gas sampling during reaction permitted a comparison of reactivity between spruce slurry and synthetic liquefied wood.
- Synthetic liquefied wood exhibits a slightly higher gasification reactivity over Ru/C, starting at lower temperatures (250 °C for SLW vs. 270 °C for spruce), but leads to a product gas very similar in composition.
- The evolution of the product gas composition is comparable, indicating that SLW is a valid liquid substitute biomass for real wood slurries which are exceedingly difficult to pump continuously on a laboratory scale.

## 6.6 Batch Gasification of Palm Oil Pyrolysis Condensate with Ru/C

As pointed out in section 5.4, palm oil pyrolysis condensate is an abundant waste stream in Malaysia, and can be used as feed for the continuously operating process demonstration unit that was built (see section 8). To assess its reactivity and to test for its gasification, a batch experiment was carried out with the pyrolysis condensate (concentration 28.3 wt %) using 2 wt % Ru/C (Engelhard) as catalyst.

For this experiment, 2.8500 g of pyrolysis condensate were premixed with 0.7610 g of water and 2.3085 g of moist catalyst, and loaded into the reactor. The catalyst-to-organics ratio on a dry basis was 1.10. Prior to heat-up, the reactor was flushed with Ar twice before being pressurized with the same gas to 1.1 MPa.

The heat-up time to 405 °C was 10 minutes, with a subsequent residence time at this temperature of 62 min. In contrast to gasification experiments with wood, the pressure rose steadily during the isothermal residence time, from 26.1 MPa at  $t = 25$  min. to 28.1 MPa at  $t = 72$  min., when the system was quenched. The rate of pressure evolution versus time is depicted in Figure 6.26, together with the rate of a wood gasification experiment. The pyrolysis condensate (PC) was almost three times more concentrated, however.

The reason for this reduced reactivity could be in the content of inorganics present in the pyrolysis condensate. Sulfate was later determined to act as a catalyst poison (see section 7.2). The sulfate-to-ruthenium ratio of this experiment was 0.72. The gasification efficiency GE was merely 72.4 %. However, the carbon balance did not close well (only to 74 %). The scaled gasification efficiency  $GE_{100}$  was 97.8 %. Only 7.6 mg (or 1 % of the feed's carbon) were found in tars, and 4.5 mg of carbon (or 0.6 % of the feed's carbon) were found in the residual liquid phase with a TOC of 1.2 g/L. As the catalyst's support was coconut shell carbon, the carbon content of the residual solid phase was not determined. Since the carbon balance did not close that well, a certain amount of the feed's carbon might have been transformed to coke and deposited on the catalyst,

where it was not measured and accounted for. However, coke formation had not been observed so far in catalytic hydrothermal gasification. The product gas was composed of 48.7 vol %  $\text{CO}_2$ , 45.9 vol %  $\text{CH}_4$ , 1.2 vol %  $\text{C}_2\text{H}_6$ , 3.7 vol %  $\text{H}_2$ , and 0.5 vol %  $\text{CO}$ .

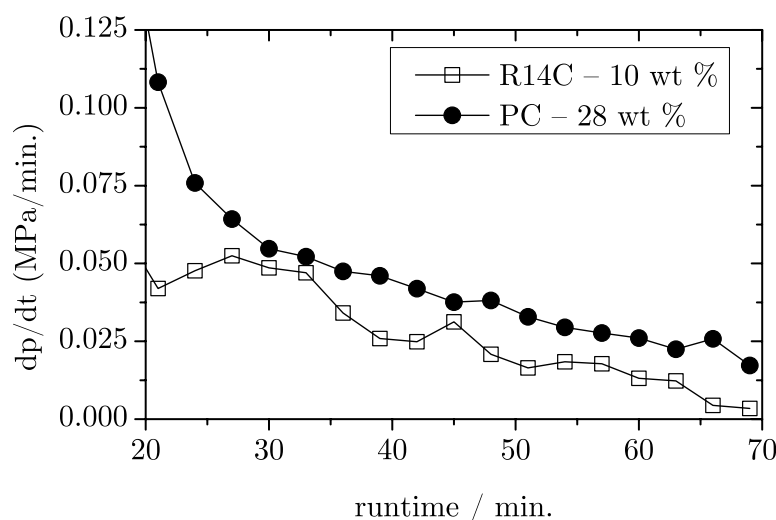


Figure 6.26: Difference in pressure per minute for a wood gasification experiment (R14C) and the pyrolysis condensate gasification experiment (PC).

Based on this batch experiment, the catalytic hydrothermal gasification of palm oil pyrolysis condensate with 2 % Ru/C yields a product gas close to the equilibrium composition, with very few tars, and an aqueous product phase with a low carbon content.

## 6.7 Experiments using Quartz-Capillaries as Micro-Reactors

### 6.7.1 Capillary Gasification Experiment with Wood Slurry and Raney 2800 Nickel

The onset of wood gasification was visualized in a catalytic quartz capillary experiment, carried out by S. Rabe, PSI [181]. The visual results are depicted in Figure 6.27.

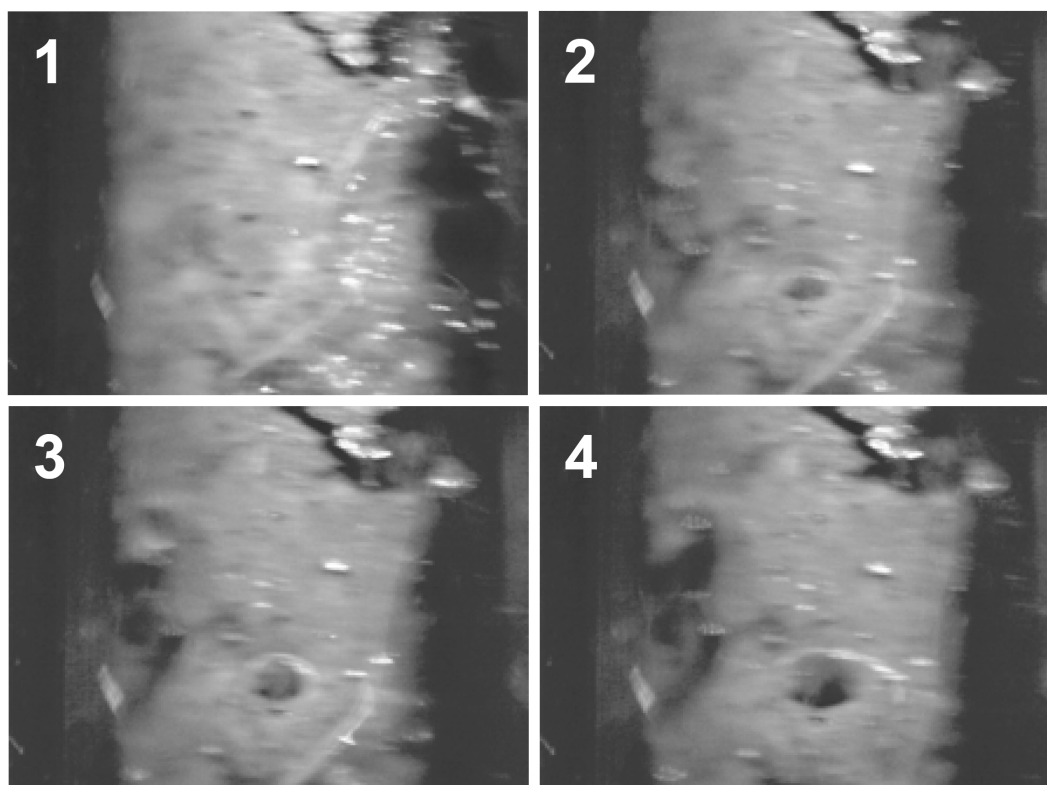


Figure 6.27: Formation of a gas bubble at 295 °C from wood slurry above a catalyst grain (skeletal nickel). Time elapsed between image 1 and 4 is about 1 min.

About 70 mg of wood slurry and 20 mg of Raney 2800 Ni (Grace Davison) were loaded into a quartz capillary (i.d. = 1.4 mm, o.d. = 6 mm, L = 145 mm) and sealed by welding, as described in section 3.4. The capillary was put into the heating block and heated to 350 °C. The first gas bubbles were formed at 295 °C, when the pressure inside the capillary was around 8 MPa (calculated based on the feed amount with data of pure water). In contrast, gas formation was observed in the batch reactor already at 250 °C (refer to section 6.1.7). However, in the batch reactor, the pressure at this temperature was slightly higher, and thus hydrolytic power of the water was higher. The gasification continued, and more and more wood was converted. However, at a certain time, the capillary exploded and the experiment had to be stopped.

### 6.7.2 Capillary Experiment with Pure Water

The transition of pure water from the two phase region into the supercritical one phase region was visualized with the capillary technique by filming the process. Some snapshots of this movie are displayed in Figure 6.28.

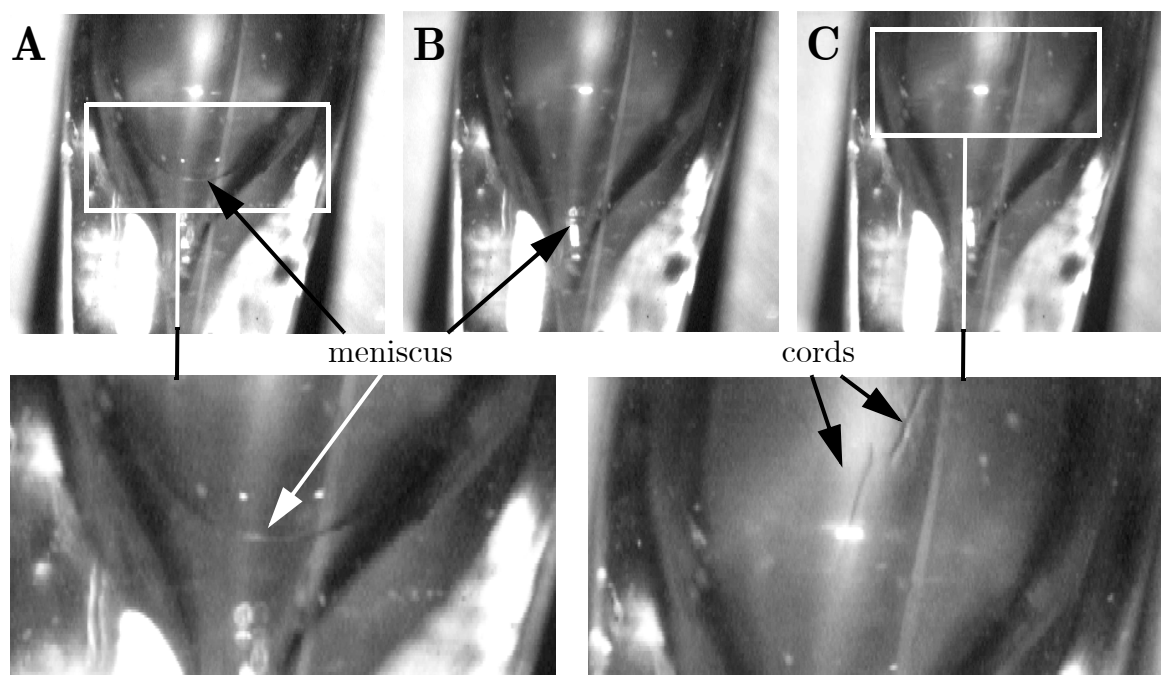


Figure 6.28: Capillary experiment with pure water (magnification of one of the tips). A: 372 °C, two phases: liquid below the meniscus, vapor above it. B: 375 °C: the meniscus moved towards the capillary tip. C: 378 °C: one phase, with commotion and cords on the upper side of the capillary.

During the heat up phase, the water evaporated, and the meniscus of the liquid phase boundary slowly moved towards the capillary tip. When the brass heating block reached a temperature of 378 °C, the phase boundary inside the quartz tube disappeared, and the content became less transparent, as if it turned into a haze. There was heavy commotion inside the quartz tube from one second to the other, made visible by quickly moving cords on the upper side of the capillary. Probably, the upper side was slightly cooler, as it was not in contact with the heating block, and some of the supercritical water might have condensed on the glass at these

locations, because there, the temperature was locally below  $T_c$ . Unfortunately, the transition is not as nicely and clearly visible on these snapshots as it is in the movie. The movie can be downloaded at:

[http://cpe.web.psi.ch/scwg\\_movie.html](http://cpe.web.psi.ch/scwg_movie.html).

### 6.7.3 Capillary Experiment with 5 wt % NaCl in Water

The addition of salts is reported to shift the critical point of the mixture typically to higher temperatures [182]. To confirm this phenomenon visually, 200 mg of a solution of NaCl (conc. 5 wt %) were sealed into a quartz capillary (i.d. = 2.0 mm, o.d. = 6.0 mm), and heated in the heating block. The visual observations made during the experiment are tabulated in Table 6.22 on page 167.

The vapor phase (with possibly entrained air) moved to the middle section of the capillary, and was surrounded by two liquid phases on either side, forming two menisci. However, only one is visible on the snapshots taken from the corresponding movie, see Figure 6.29.

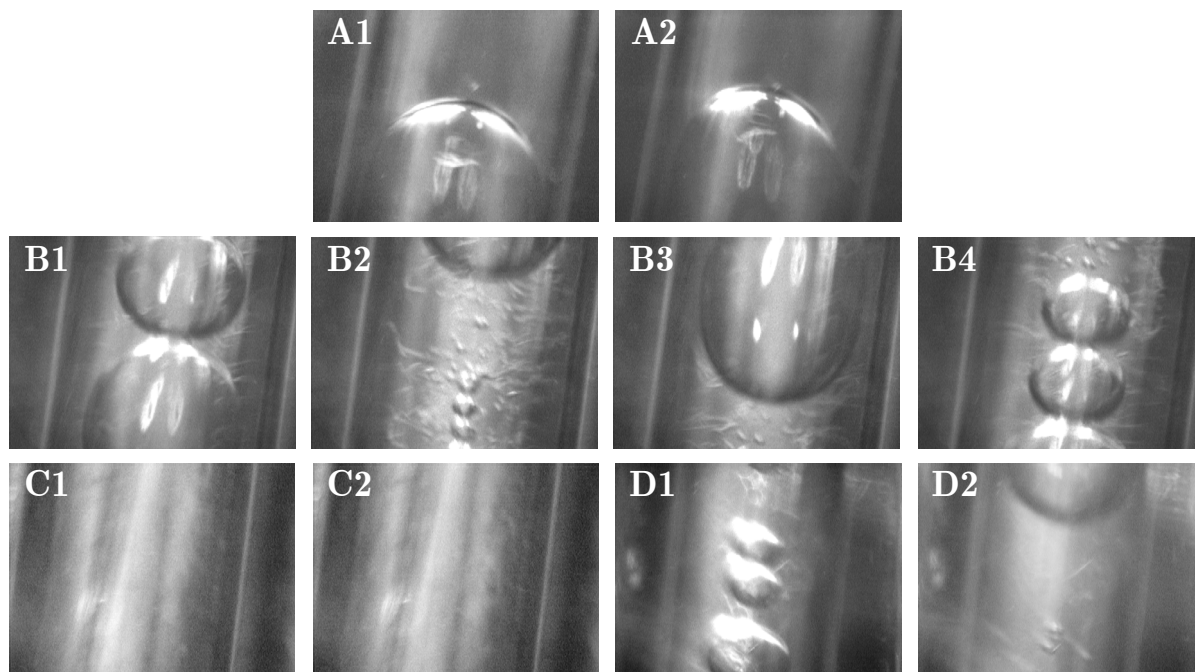


Figure 6.29: Snap shots from capillary heating movie with 5 wt % NaCl solution. Images A1 – A2: 381 °C, time between snap shots: 6 sec. B1 – B4: 404 °C, time between snap shots: 1 sec. C1 – C2: 445 °C, salt brine sticking to the upper wall; very hazy. D1 – D2: 393 °C, time between snap shots 2 sec. Bubbles reappeared.

Table 6.22: Visual observations during a capillary experiment with a 5 wt % aqueous NaCl solution.

$T_{\text{block}}$ °C	observations
$\leq 381$	slow movement of the meniscus and an entrained air bubble (A1 – A2) <sup>a</sup>
400	streamlines of some internal current visible
404	heavy commotion, gas bubbles swirling around (B1 – B4)
414	the solution gets hazy; gas bubbles still present
430	only now disappearance of the meniscus; no gas bubbles visible anymore
445	precipitated salt cords are visible on the upper side of the capillary (C1 – C2)
455	salty cords become more numerous and thick / heating switched off
393	all salty cords have redissolved, the fluid is clear again; bubbles are visible (D1 – D2)

a. A1, A2, B1, etc. refer to the snap shots depicted in Figure 6.29.

Interestingly, up to 390 °C, neither chords on the upper side of the tube were visible, nor commotion, nor did the content turn hazy, in contrast to the experiment with pure water described in the previous section. At around 400 °C, some sort of streamlines were observed. At 404 °C, suddenly some intense commotion was detected, with gas bubbles swirling around: the images B1 – B4 are taken over a period of only 4 seconds, and depict the rapid change inside. However, still two phases were present at these conditions. In the bulk fluid phase in the middle of the tube, some sort of threads or cords were formed (they could be salt brine), best visible on snapshot B2.

When the capillary was further heated, the bubbles disappeared at 430 °C, the mixture became more hazy, and some sort of brine cords were visible on the upper side of the capillary. At 445 °C, the brine cords became more distinct (snap shots C1 – C2); they almost seemed to build a crust at 455 °C so that the contrast of the images deteriorated.

When the heating was switched off, and the capillaries were allowed to cool, the bubbles reappeared at around 415 °C, and the brine was com-

pletely redissolved at 393 °C (snapshots D1 – D2). The solution inside the capillary stayed a bit hazier than at the beginning of the experiment.

These observations are congruent with the data presented by Armellini, who stated that sodium chloride solutions form from the one-phase fluid a vapor-liquid phase at 387 °C and 25 MPa, which has its boundaries then at around 450 °C and sodium chloride contents of 0.03 wt % [182]. Based on the mass of water inside the capillary (95 % of the feed), the pressure at 404 °C (onset of the commotion) was 23 MPa. According to Armellini, the sodium chloride solubility decreases nearly asymptotically around 390 °C: from several wt % at 388 °C to around 0.1 wt % at 400 °C. It decreases further to 400 ppm at 430 °C and 300 ppm at 450 °C (all data at 25 MPa) [182]. Based on this data, the threads and cords that appeared around 405 °C could well have been the visualization of salt brine.

#### 6.7.4 Conclusions of the Capillary Experiments

- Capillary experiments served as visual confirmation of the hydrothermal gasification of wood slurries in the presence of a skeletal nickel catalyst.
- The transition into the supercritical state could be nicely visualized. It differed quite impressively between pure water and a sodium chloride solution (5 wt %).
- Despite the advantages of visualizing the processes, it took numerous attempts to carry out these experiments. Only about 20 % of the capillaries did not explode during heat-up. When they exploded, the capillary frequently destroyed also the protecting quartz disk, as well as any other capillaries inside the block. Thus, filling all eight notches with capillaries did not make sense as long as the failure rate was so high.
- Catalyst stability experiments (catalyst and water sealed into the capillary) were attempted for Ru/C catalysts in powder form. Unfor-



---

tunately, all tests failed due to explosion, either because of gas production from self gasification, or from tensile stress of the quartz tube. Plans for any further tests were then abandoned due to safety reasons.



# Chapter 7: Catalyst Testing and Characterization

## 7.1 Towards a Hydrothermally Stable Catalyst

### 7.1.1 Starting Point and Aim of The Experiments

The gasification efficiency (GE) and selectivity towards methane ( $Y_{\text{CH}_4}$ , methane yield) could be tested for with the catalyst screening experiments run in the batch reactor (as outlined in section 6.3), but no information about long-term stability in the hydrothermal environment could be gathered, as typical reaction times were only around 1 hr. Thus, experiments with the most promising catalysts were carried out in the continuously operating test rig presented in section 3.3.

As it is very difficult to pump slurries containing solids (e.g. wood sawdust slurries) reliably on the laboratory scale (i.e. at small throughputs,  $< 1$  L/hr), synthetic liquefied wood (see section 5.2 for its analysis), SLW, approximating the chemical composition of real spruce and fir slurries, was chosen as an alternative feed for most of the experiments. The comparability of synthetic liquefied wood and real spruce slurries had been justified in experiments in the batch reactor, refer to section 6.5.2. For long-term experiments with low carbon conversion, the phenol fraction of SLW was replaced by adding more anisole to avoid excessive exposure to phenol vapors (during sampling and temperature profiling).

Preliminary experiments that were carried out at a time when SLW was not available yet were run with aqueous ethanol solutions as feed. Ethanol is cheap, abundant, pure, and the pathways of its gasification reaction are well-defined.

In order to reach high methane yields and to be able to transfer know-

ledge gained with this test rig to a pilot plant, high concentrations (10 – 20 wt %) were endeavored.

### 7.1.2 Gasification of Synthetic Liquefied Wood over Raney 2800 Ni

Synthetic liquefied wood with a concentration of 17.5 wt % was gasified with Raney 2800 Ni (Grace Davison) in a 50 hrs experiment, at 30 MPa and with a weight hourly space velocity<sup>1</sup> (WHSV) of 4.4 g<sub>org.</sub>/(g<sub>cat.</sub>, dry hr), at 400 °C (for 17 hrs), 425 °C (for 24 hrs), and 450 °C (for 11 hrs). The experiments with skeletal nickel catalysts were carried out at a time when it was not yet clear that this type of catalysts deactivated quickly over time due to chemical sintering.

The resulting gas production rate was nearly independent of temperature, being equal to 5.55 L/hr at atmospheric temperature (25 °C) and pressure (~980 hPa), or 0.377 L/g<sub>SLW</sub> fed, see Figure 7.1.

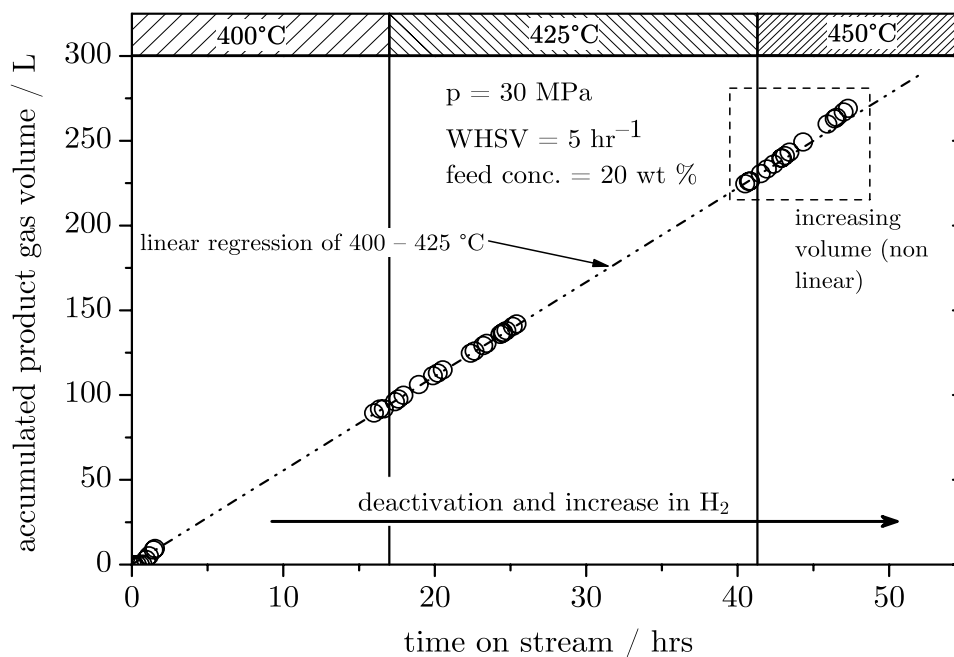


Figure 7.1: Total volume of gas produced during a 50 hours run with synthetic liquefied wood as feed. The indicated temperature is the reactor's oven setpoint temperature;  $p = 30$  MPa,  $WHSV = 4.4$  hr<sup>-1</sup>, feed concentration = 17.5 wt %.

1. The weight hourly space velocity is based on the mass of hydrocarbons in the feed, not on the total mass of the feed. Its units will further be referred to as [hr<sup>-1</sup>] instead of [g<sub>org.</sub>/(g<sub>cat.</sub>, dry hr)].

Only at 450 °C, or after 41 hours, did the gas production rate increase, due to a change in gas composition (more H<sub>2</sub>, leading to more moles of gas). As can be seen in Figure 7.2, the product gas composition changed over time, probably due to catalyst deactivation. At the beginning of the experiment, the gas composition was 50 vol % CH<sub>4</sub>, 47 vol % CO<sub>2</sub>, and 3 vol % H<sub>2</sub>, thus very close to the equilibrium composition (at 400 °C, 30 MPa, and conc. 20 wt %: 50 vol % CH<sub>4</sub>, 48 vol % CO<sub>2</sub>, and 2 vol % H<sub>2</sub>). The hydrogen content steadily increased to > 30 vol %, while the methane concentration decreased to ~25 vol %. The concentration of CO remained always < 0.1 vol %.

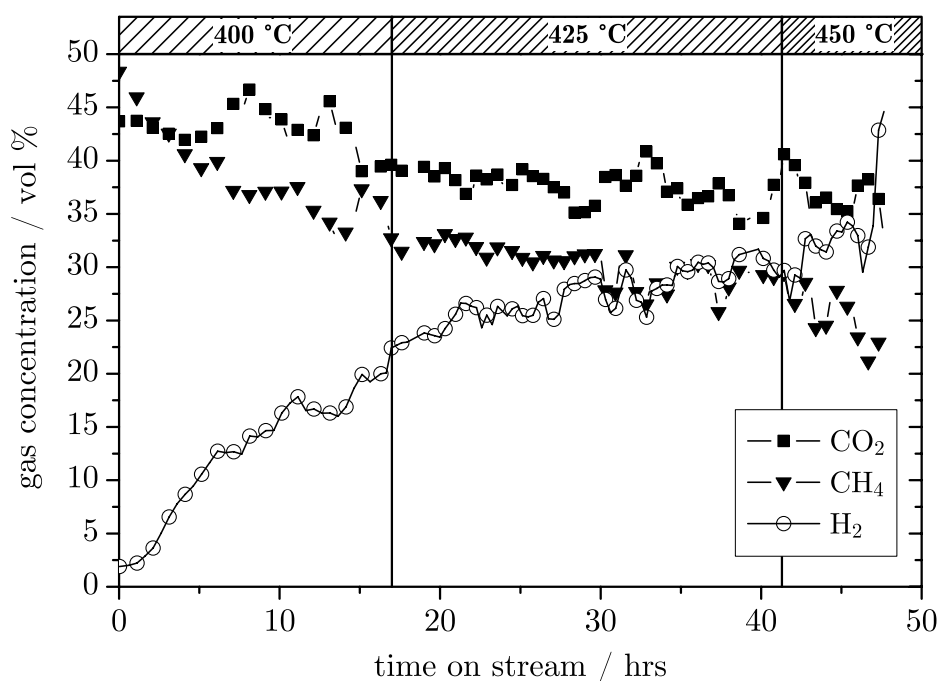


Figure 7.2: Dry gas composition versus time on stream for the gasification of synthetic liquefied wood with Raney 2800 Ni,  $p = 30$  MPa.

The temperature profile along the reactor revealed information about the location of endothermic reactions (Figure 7.3). The catalytic bed was located between 3 and 18 cm from the reactor inlet with  $\alpha$ -Al<sub>2</sub>O<sub>3</sub> before and after it. A cold spot of ~8 °C at the beginning of the catalytic bed (oven setpoint 400 °C) indicated the predominance of endothermic reforming reactions with CO<sub>2</sub> and H<sub>2</sub> as main products. The temperature profile varied only very little over time. At the higher oven setpoints

(425 °C / 450 °C) no distinct cold spot at the beginning of the catalyst bed could be observed. This could indicate that the reforming reactions were slowed down by catalyst deactivation. Interestingly, the profile at 425 °C (runtime 17 – 41 hrs on stream) did not change at all over time. Additionally, the temperature profile did not show a moving front, as it would be observed if the catalyst had deactivated due to poisoning (a moving front was detected with Ru/TiO<sub>2</sub> as catalyst, outlined in section 7.1.4). Thus, the deactivation of Raney 2800 Ni must have taken place simultaneously and progressively in every part of the reactor; an observation that could be explained by sintering. To remedy this phenomenon, the skeletal nickel catalyst should be stabilized (e.g. by co-doping of Ru). Such a co-doped Raney catalyst was tested next.

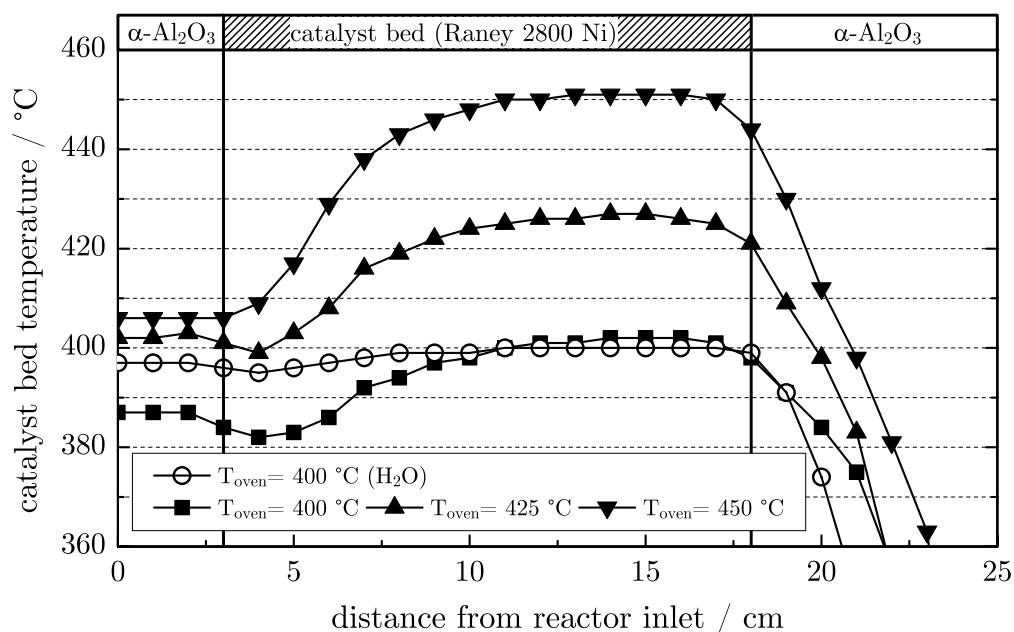


Figure 7.3: Temperature profile along the reactor with Raney 2800 Ni as the catalyst. Catalyst was located between 3 and 18 cm. Fluid flow is from left to right.

### 7.1.3 Gasification of Synthetic Liquefied Wood over Raney 2800 Ni/Ru

As a remedy to the loss of methanation activity over time, a ruthenium stabilized Raney nickel catalyst<sup>2</sup> was tested in a long-term SLW gasification experiment (conc. 20 wt %, WHSV = 2.3 hr<sup>-1</sup>). Elliott and co-workers reported the co-doping of ruthenium to enhance catalyst stability by suppressing the sintering of the nickel phase [175]. However, they used rather high amounts of the precious metal, 1 – 5 wt %. Due to the high price of ruthenium, the co-doped amount should ideally be lower, as for these amounts, a supported ruthenium catalyst could be used instead of co-doping this metal to nickel<sup>3</sup>. A co-dopant proportion of 0.25 wt % was arbitrarily chosen. Grace Davison supplied a sample of Raney 2800 Ni/0.25 wt % Ru for this experiment. In addition to the on-line measurement of the gas phase composition, samples of the liquid product phase were taken and analyzed with respect to their organic and inorganic carbon content (by DC-190), as well as to their Ni content (by ICP).

This catalyst showed comparable performance and similar stability as regular Raney 2800 nickel; despite the co-doping, it still deactivated rather quickly, as can be seen from the product gas composition and carbon conversion  $X_C$ , depicted in Figure 7.4.

After 22 hrs, problems with the backpressure regulator forced the test rig to be stopped. After the replacement of the defective part, the plant was flushed with distilled water prior to switching back to feeding SLW (start of campaign 2). Again, product gas compositions close to the thermodynamic equilibrium were reached (e.g. at run time 25 hrs; hydrogen was only measured after 30 hrs on stream due to technical difficulties), but over time, the hydrogen concentration increased towards ~30 vol %, whereas the methane concentration decreased towards a stable level of ~30 vol %. The concentration of carbon monoxide was always below 2 vol %.

---

2. For the corresponding experiment in the batch reactor, refer to run no. R2C on page 126.

3. Thus, 1 wt % Ru/TiO<sub>2</sub> was tested next, see section 7.1.4.

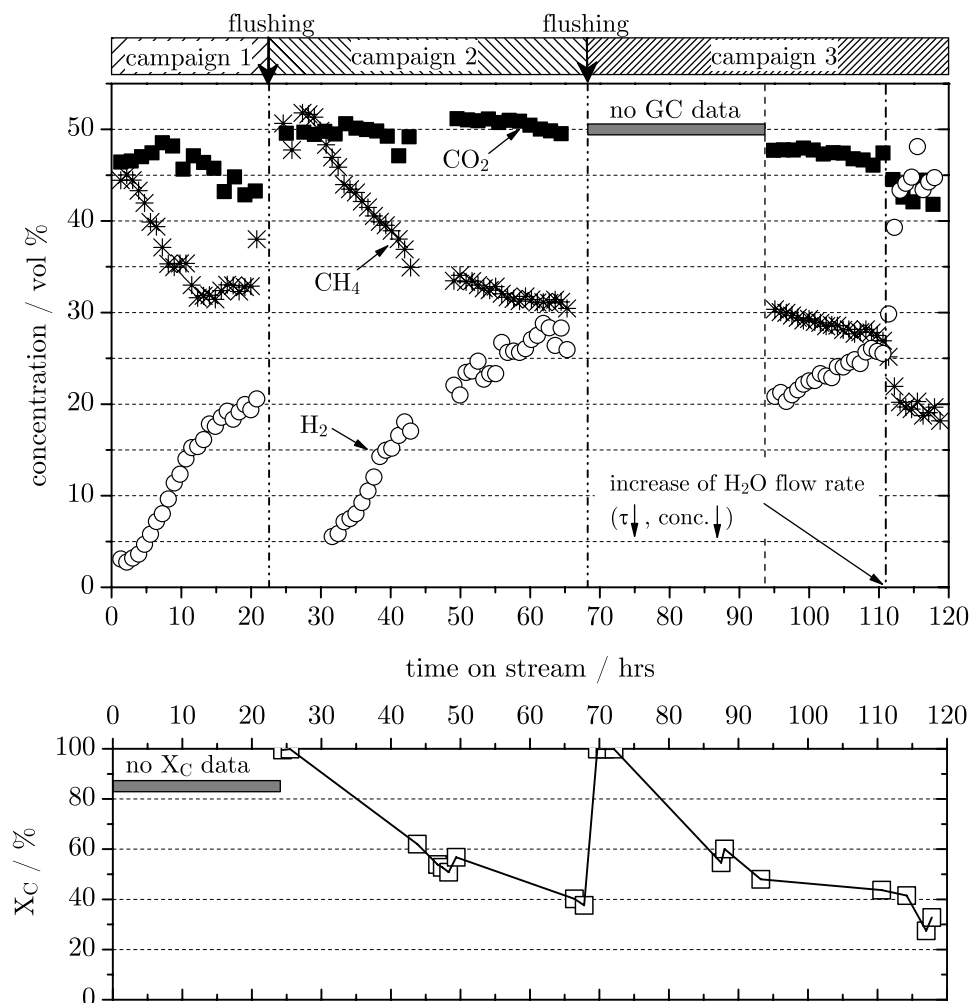


Figure 7.4: Concentration of gaseous products (above) and carbon conversion  $X_C$  (below) during 120 hours gasification experiment with synthetic liquefied wood over Raney 2800 Ni/Ru (3 campaigns with identical process conditions: conc. = 20 wt %, WHSV =  $2.3 \text{ hr}^{-1}$ ,  $T = 400 \text{ }^\circ\text{C}$ ,  $P = 30 \text{ MPa}$ .). At 102 hrs, the water flow rate was increased.  $\text{CO}$  concentration was always below 2 vol %.

After another minor problem at 68 hrs on stream, the plant was again flushed with distilled water. Also this time (begin of campaign 3), the catalyst gasified the SLW completely during the first thirty to forty minutes, followed by a similar decrease in activity as before: The carbon conversion  $X_C$  dropped to 60 % within 20 hrs, and decreased further to about 40 %. At 112 hrs, the water flow rate was increased by a factor of ca. 2, leading to a reduced residence time of the feed in the reactor (no decrease of the WHSV). The feed concentration was thereby lowered from 20 to 10 wt %. The carbon conversion dropped slightly more, due to the



lowered residence time, to 30 %. The methane concentration decreased from 27 to 17 vol %, and the hydrogen concentration increased from 25 to 45 vol %.

It can be clearly seen that the mixture did not spend enough time over the catalytic bed in order for the methanation to be fully completed. In addition, the diluting effect of increasing the water flow rate lead, governed by thermodynamics, to an additional shift towards hydrogen rather than methane (compare with Figure 2.1 on page 27, calculated for wood as feedstock). However, the catalyst still exhibited residual methanation activity, while it showed a decreased activity for the gasification ( $y_{\text{CH}_4} = 30$  vol %, but  $X_{\text{C}}$  only 40 % at 110 hrs on stream).

Post-reactionem analysis of the spent Raney 2800 Ni/Ru catalyst by means of X-ray diffraction revealed the deactivation mechanism: chemical sintering of the nickel crystallites, see Figure 7.5, as was already outlined in section 6.3.1 on page 135. No nickel leaching was detected by ICP.

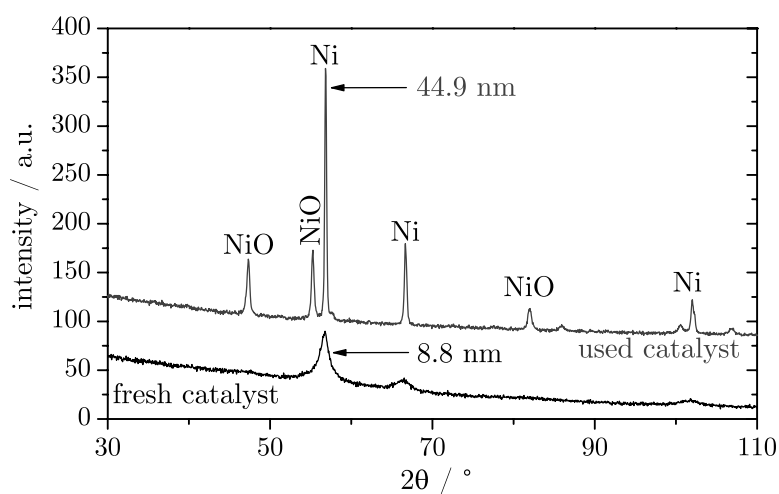


Figure 7.5: XRD of fresh Raney 2800 Ni/Ru (below) vs. XRD of the same catalyst after 120 hrs of gasification of synthetic liquefied wood (above). Crystallite growth and loss of BET surface area indicate sintering.

The crystallites grew from an initial size of 9 nm to 45 nm. In addition, the BET surface decreased from 29  $\text{m}^2/\text{g}$  to  $< 5$   $\text{m}^2/\text{g}$ , i.e. below the limits of the instrument and method employed. The timescale of sintering

is of the order of a few hours or less, as catalyst samples after batch experiments with only 1 hr runtime showed similar crystallite growth (refer to Table 6.15 on page 136).

#### 7.1.4 Gasification of Ethanol over 1 wt % Ru/TiO<sub>2</sub>

As skeletal nickel catalysts sintered quickly in the hydrothermal environment, a noble metal catalyst was chosen. TiO<sub>2</sub> (rutile) was reported to be stable in supercritical water [65], thus suitable as support, and ruthenium is known to catalyze both the gasification and the methanation reaction, as outlined in section 2.3.1. Therefore, the commercially available 1 wt % Ru/TiO<sub>2</sub> catalyst (Degussa) was tested next. The catalyst was delivered in the form of tablets, which were crushed to 125 – 250 μm prior to being filled into the fixed bed reactor. In preceding experiments, this catalyst had been tested in the batch reactor with wood slurries and performed at a middle-rate level ( $GE = 53\%$ ,  $Y_{CH_4} = 0.13 \text{ g}_{CH_4}/\text{g}_{\text{wood}}$ , see run no. RuTi1 in Table 6.17 on page 138). As the focus of this test was on catalyst stability rather than on good comparability to a real feed, ethanol (conc. 30 wt %) instead of SLW was chosen as feed. The catalytic bed ranged from 3 to 11 cm of the reactor tube, which was embedded within zones of packed α-alumina (particle sizes 100 – 150 μm).

The total runtime was over 70 hrs, at three different gasification temperatures to bracket the reactivity of the catalyst: first at 455 °C for 26 hrs, then at 345 °C for 24 hrs, and last at 400 °C for 23 hrs.

Table 7.1: Results from ethanol gasification over 1 wt % Ru/TiO<sub>2</sub>.

avg. cat. temp. °C	$\Delta T^a$ °C	$t$ on stream hrs	WHSV hr <sup>-1</sup>	$V_{\text{gas}}$ L/g <sub>EtOH</sub>	CH <sub>4</sub> vol %	H <sub>2</sub> vol %	CO <sub>2</sub> vol %	CO vol %
455 – 440	73	26	35.1	1.09	65	13	22	1
345	15	24	35.2	0.11	66	19	9	4
400	24	23	18.5	0.58	60	20	17	4

a. temperature difference within catalyst bed between cold spot (entrance) and hot spot (exit).

The WHSV was quite large,  $35.1 \text{ hr}^{-1}$  and  $35.2 \text{ hr}^{-1}$  for  $455 \text{ }^\circ\text{C}$  and  $345 \text{ }^\circ\text{C}$ , respectively, and  $18.5 \text{ hr}^{-1}$  for  $400 \text{ }^\circ\text{C}$  (see Table 7.1 for details). Again, at the first part of the catalytic bed (entrance), the fluid was significantly cooler than in the last section of the bed (exit), indicating the location of predominating endothermic reactions followed by exothermic reactions, as can be seen in Figure 7.6.

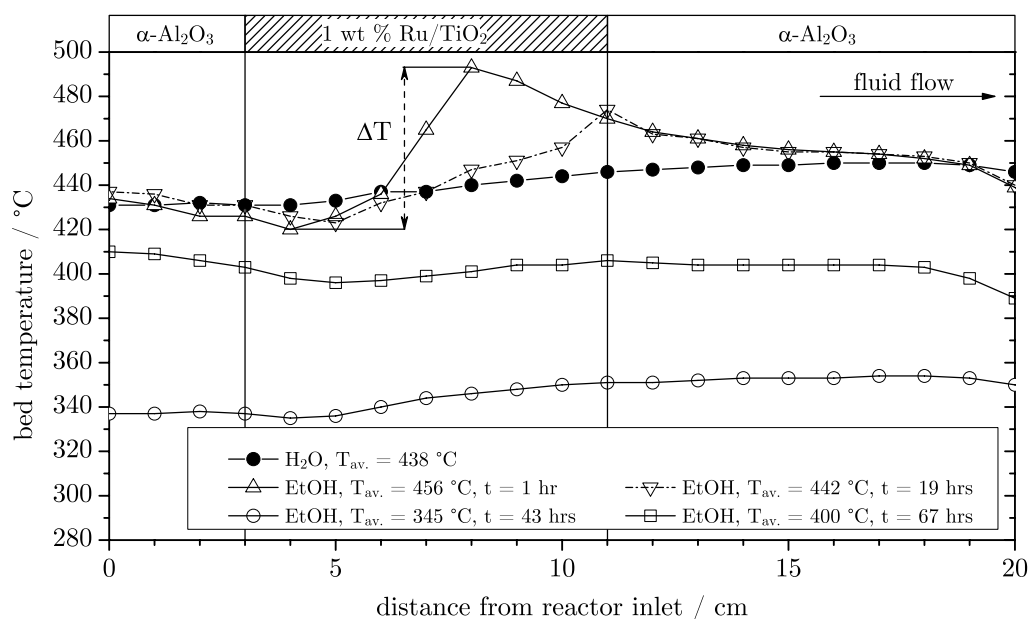


Figure 7.6: Temperature profile along the reactor with 1 wt % Ru/TiO<sub>2</sub> as catalyst. The catalyst was located between 3 and 11 cm. Fluid flow is from left to right.

The temperature difference  $\Delta T$  between the coolest part (entrance) and the hottest part (exit) was  $73 \text{ }^\circ\text{C}$  at the average catalyst temperature of  $455 \text{ }^\circ\text{C}$ , due to the large WHSV chosen. Over time,  $\Delta T$  became less pronounced, and the hotspot shifted towards the end of the catalytic bed, which indicates a decrease in activity which moves like a front, probably due to a seasoning to the hydrothermal environment. However, it does not seem like sintering, as was the case with skeletal nickel catalysts. An explanation could be that the TiO<sub>2</sub> rearranged in presence of hydrogen and formed layers that partially covered the ruthenium crystallites, leading to a decreased activity<sup>4</sup>. A steady state in temperature was attained only after some time. The average catalyst temperature decreased from

456 °C (at time on stream = 1 hr) to 442 °C (at time on stream = 19 hrs).

As expected, more gas was formed over time and higher carbon conversions were achieved at higher temperatures. The accumulated gas volume vs. time on stream is depicted in Figure 7.7.

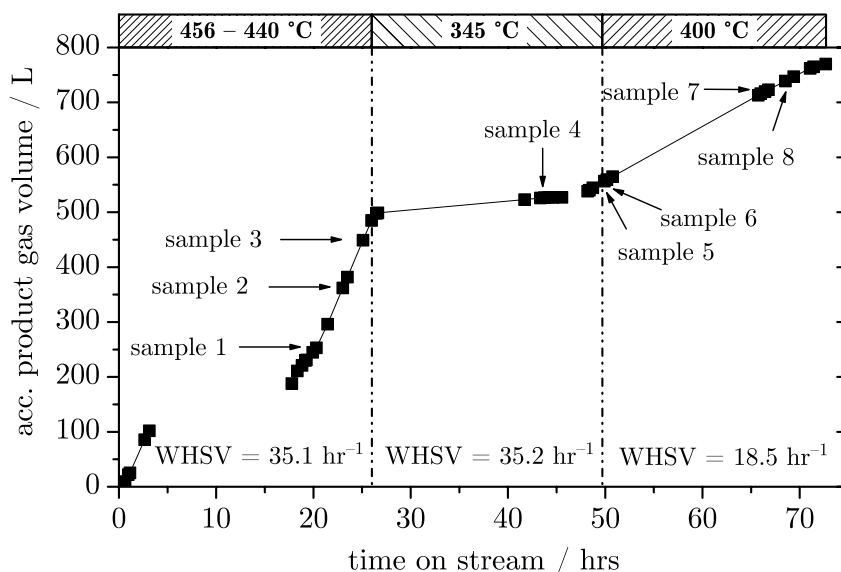


Figure 7.7: Accumulated product gas volume over 70 hrs of ethanol gasification over 1 wt % Ru/TiO<sub>2</sub>. P = 30 MPa, ethanol feed conc. = 30 wt %.

There was a problem with the gas/liquid separator after 4 hours, which was only detected the next morning after 17 hours time on stream, leading to a gap in the graph. Although hydrogen is thermodynamically favored at higher temperatures (leading to an increase in the total number of moles of gas), the concentration in hydrogen was lower at 450 °C than at 400 °C, depicted in Table 7.1. An explanation for this could be that the catalyst deactivated gradually and the methanation reaction was suppressed. The deactivation is also indicated by the decreasing carbon conversion over time: during the experiment, samples of the residual liquid phase were collected and analyzed in terms of their carbon content,

4. The catalyst manufacturer recommended to reduce the catalyst only at temperatures below 150 °C, and stated that such a rearrangement might take place in presence of hydrogen at temperatures exceeding 300 °C (not in the hydrothermal environment).

see Table 7.2 (sampling times are depicted in Figure 7.7). However, as the activity of the catalyst depended largely on the temperature, a decrease of 15 °C (i.e. from sample 1 to sample 2 and 3) can significantly lower the carbon conversion. The decreased temperature itself, however, can only be explained by a reduced methanation activity, which in turn produced less heat of reaction (methanation is exothermic).

Table 7.2: Carbon content in the residual liquid phase of ethanol gasification over 1 wt % Ru/TiO<sub>2</sub>.

sample no.	T °C	DOC <sub>aq.</sub> g/L	X <sub>C</sub> %	sample no.	T °C	DOC <sub>aq.</sub> g/L	X <sub>C</sub> %	sample no.	T °C	DOC <sub>aq.</sub> g/L	X <sub>C</sub> %
1	455	3.5	97.8	4	345	123.7	20.7	6	405	75.0	51.9
2	440	15.5	90.1	5	345	125.9	19.3	7	400	89.7	42.5
3	440	15.4	90.1					8	400	86.7	44.4

No post-reactionem analyses of the catalyst were conducted, as this experiment was carried out before the infrastructure for such an analysis was available. According to thermodynamics, the lowest possible temperature is best for the production of SNG, as the methane-to-hydrogen product gas ratio decreases with increasing temperature. However, the reactivity decreases with decreasing temperature, and in addition, solid carbon formation might occur at low temperatures. Thus, an intermediate temperature around 400 °C represents a good trade-off. At these conditions around 400 °C, the activity of 1 wt % Ru/TiO<sub>2</sub> was too small to yield full conversion of ethanol. Either the flow rate (WHSV) has to be decreased, or the loading in noble metal has to be increased to get full conversion at these desired conditions. Elliott and co-workers for instance used a higher ruthenium loading of 3 wt % on rutile-TiO<sub>2</sub> when gasifying an aqueous phenol solution (conc. 10 wt %) at 350 °C and 21 MPa in a microscale tubular fixed bed reactor during 19 weeks ( $V_{\text{reactor}} = 39.8$  mL,  $\text{LHSV} = 1.47$  hr<sup>-1</sup>, corresponding to a mass flow rate of 58.5 g hr<sup>-1</sup>, or a  $\text{WHSV}^5$  of 0.1 hr<sup>-1</sup>) [176]. They attained a carbon conversion of 99.99 %, however their WHSV was 180 – 360 times lower.

Table 7.3: Physical properties of the 1 wt % Ru/TiO<sub>2</sub> catalyst (Degussa).

property (meas.)	value	property (calc.)	value
dispersion $D^a$	0.25	solid density	2323 kg/m <sup>3</sup>
$S^a$	135 m <sup>2</sup> /g <sub>Ru</sub>	skeletal density <sup>b</sup>	4339 kg/m <sup>3</sup>
$A_s^a$	1.35 m <sup>2</sup> /g <sub>cat.</sub>	bulk density	1420 kg/m <sup>3</sup>
avg. crystallite size $l^a$	3.6 nm	avg. particle diameter	185 μm
$S_{\text{BET}}$	9.44 m <sup>2</sup> /g <sub>cat.</sub>	bed porosity $\epsilon$	0.39

a. measured by oxygen chemisorption at room temperature.

b. calculated from tabulated literature values ( $w_{\text{Ru}} \cdot \rho_{\text{s, Ru}} + w_{\text{TiO}_2} \cdot \rho_{\text{s, TiO}_2}$ ).

The low dispersion of the catalyst used here (fresh, before reaction), measured with the oxygen chemisorption method outlined in section 4.8 on page 75, is a likely cause for the rather low activity at temperatures below 450 °C (and especially when real biomass, such as wood slurries, was used in batch reactor experiments). The chemisorption results are presented in Table 7.3, together with a summary of the physical properties of this catalyst. Possibly, a minimum active metal loading is necessary to gasify biomass at high feed concentrations and WHSV (the residence time  $\tau$  inside the reactor was  $< 1$  min, thus much lower than in Elliott's case) or a minimum of active sites surface area  $A_s$  is needed, which itself is coupled to the metal loading and the dispersion  $D$ . Thus, another way to improve the results would be to change the catalyst's support (for a higher dispersion and better accessibility of reactants, etc.), which was tried next.

### 7.1.5 Gasification of Synthetic Liquefied Wood over 2 wt % Ru/C

Guided by the previous experiments, an alternative support, possibly with better stability and better catalyst performance for real feeds, had

---

5. Assuming the reactor was completely filled with Ru/TiO<sub>2</sub> with a bulk density of 1420 kg/m<sup>3</sup> as reported in Table 7.3, yielding  $m_{\text{cat.}} = 56.5$  g.

to be found. The most promising ruthenium system tested in batch experiments with wood as feedstock was 2 wt % Ru/C (Engelhard). The results of its oxygen chemisorption and BET analysis are presented in Table 7.4. The ruthenium dispersion  $D$  found by the O<sub>2</sub>-chemisorption method was >95 %, with an average Ru crystallite size  $l$  of ~0.9 nm, corresponding nicely to the findings by HAADF-STEM, shown later (page 187). The BET surface area was 890 m<sup>2</sup>/g, with a macro- and mesopore area of 170 m<sup>2</sup>/g (i.e. 80 % of the surface lies within the micropores), measured by nitrogen adsorption. The specific Ru surface area  $A_s$ , determined by the proposed oxygen chemisorption method, was 11 m<sup>2</sup>/g<sub>cat.</sub> (thus roughly 10 times as large as in 1 wt % Ru/TiO<sub>2</sub> tested in section 7.1.4). The average pore size (by BET) was very small, only 1.9 nm.

Table 7.4: Physical properties of the 2 wt % Ru/C catalyst (Engelhard).

property	value	property	value
dispersion $D^a$	>0.95	$S_{\text{BET}}^b$	890 m <sup>2</sup> /g <sub>cat.</sub>
total metal surface $S^a$	550 m <sup>2</sup> /g <sub>Ru</sub>	avg. pore size <sup>b</sup>	1.9 nm
specific metal surface $A_s^a$	11.0 m <sup>2</sup> /g <sub>cat.</sub>	micropore area <sup>b</sup>	80 %
avg. crystallite size $l^a$	0.9 nm	bulk density (dry) <sup>c</sup>	260 kg/m <sup>3</sup>

a. measured by oxygen chemisorption at room temperature.

b. measured by nitrogen adsorption at -195.8 °C.

c. calc. based on tapped bulk density (0.45 g/cm<sup>3</sup>) and water content (42 %, measured).

For the tests, a wider reactor tube was used (12 mm i.d. instead of 5.2 mm i.d.), and no temperature information was available along the first 30 mm of the bed, as the thermowell did not reach the entry of the reactor tube. Synthetic liquefied wood at a concentration of 20 wt % was used as feed. The experiment was divided into two phases:

In a first phase, the plant was run for 120 hrs at a comparably small WHSV of 1.56 hr<sup>-1</sup>. The average temperature in the catalytic bed was

around 400 °C (entrance ~380 °C, outlet 410 °C). The temperature when feeding pure water varied from 395 °C to 405 °C. The gas production over time was constant in terms of volumetric flow (1.06 L/g<sub>org.</sub>), and in terms of composition, near the chemical equilibrium composition (54 vol % CH<sub>4</sub>, 42 vol % CO<sub>2</sub>, 4 vol % H<sub>2</sub>, <0.1 vol % CO, no higher hydrocarbons). The CO<sub>2</sub> fraction in the gas was thus slightly lower than predicted by equilibrium calculations. Possibly, this was not exclusively due to dissolved CO<sub>2</sub> in the aqueous phase (usually ~200 mgC/L, measured with DC-190, corresponding to 16.7 mmol CO<sub>2</sub> per L, in contrast to ~5.2 mol CO<sub>2</sub> in the gas phase per L effluent produced). The methane yield was 0.36 g<sub>CH<sub>4</sub></sub>/g<sub>SLW</sub>, thus 10 % above the expected thermodynamic equilibrium yield of 0.33 g<sub>CH<sub>4</sub></sub>/g<sub>SLW</sub>. One possible explanation is that the gas was not in the equilibrium state; more likely, however, there was a systematic measurement error in the GC when measuring methane for this run, as the next campaign showed more sensible concentrations, see below. Nevertheless, no signs of catalyst deactivation were detected.

After the successful completion of this 120 hrs run, where no catalyst deactivation was detected, a second phase of 100 hrs was started without changing the catalyst, to study the effect of variations in the WHSV and the temperature. The gas composition and applied WHSV vs. time on stream is shown in Figure 7.8, and the gas production over time is depicted in Figure 7.9 and Table 7.5 (for various WHSVs and for identical WHSVs overnight). A mixture of ~50 vol % CH<sub>4</sub>, 2 – 3 vol % H<sub>2</sub>, and 47 – 48 vol % CO<sub>2</sub> was formed. CO was always below 0.1 vol %, and no higher hydrocarbons were detected, except during start-up of the rig when ~1 vol % C<sub>2</sub>H<sub>6</sub> was measured. The composition corresponded to the chemical equilibrium composition. Increasing the WHSV from 1.56 hr<sup>-1</sup> to 4 hr<sup>-1</sup> did not change the gas composition. At WHSV above ~7 hr<sup>-1</sup>, a slight decrease in the methane concentration was observed, but even at WHSV equal to 22 hr<sup>-1</sup>, the methane concentration was still 47 – 48 vol %.



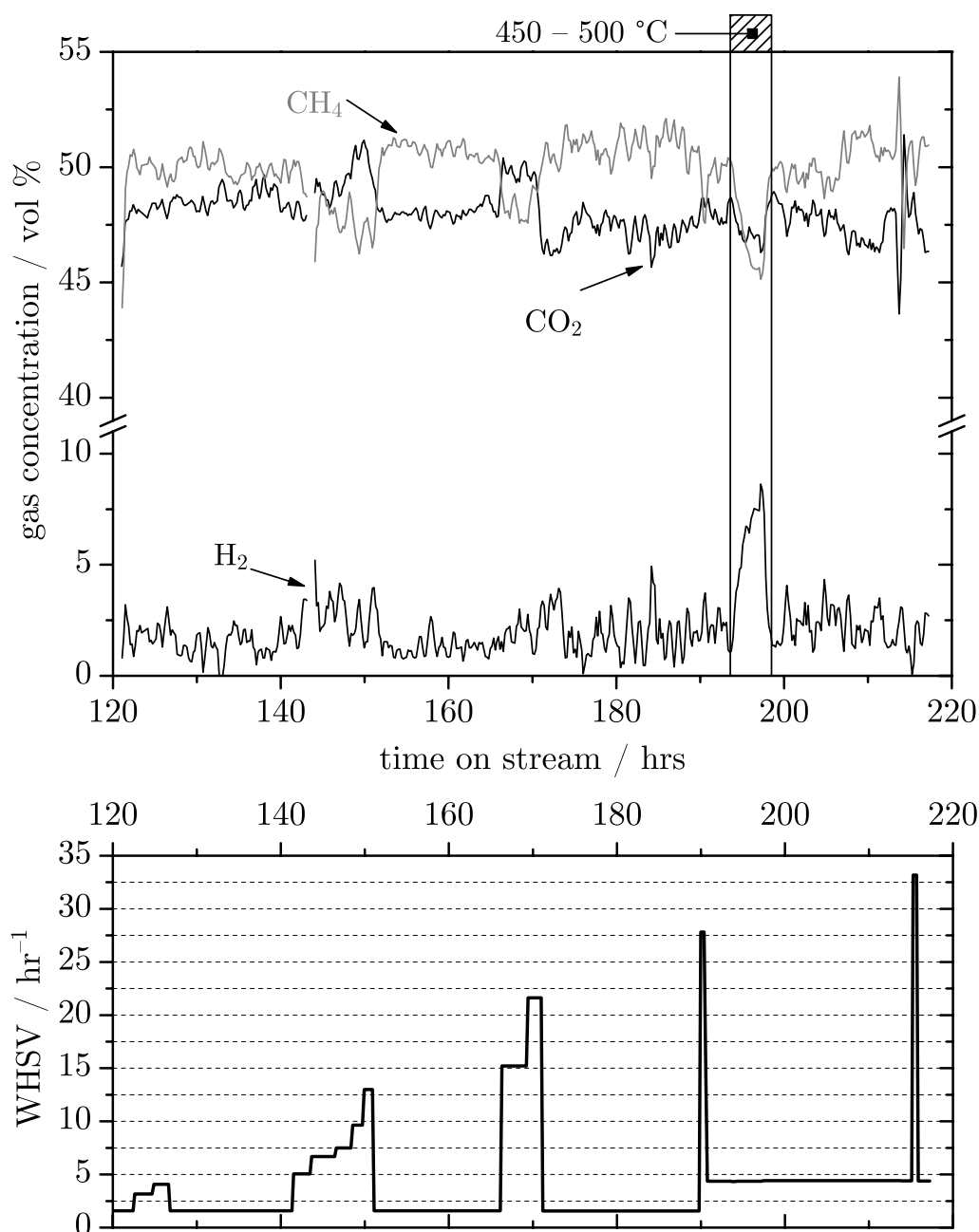


Figure 7.8: The dry product gas composition of SLW gasification over Ru/C (above) was nearly independent of the WHSV applied (below), up to  $22 \text{ hr}^{-1}$ . At runtime 193 hrs, the temperature was increased from  $400 \text{ }^\circ\text{C}$  to  $450 \text{ }^\circ\text{C}$  and then to  $500 \text{ }^\circ\text{C}$ . Pressure = 30 MPa. CO was always  $< 0.1 \text{ vol } \%$ .

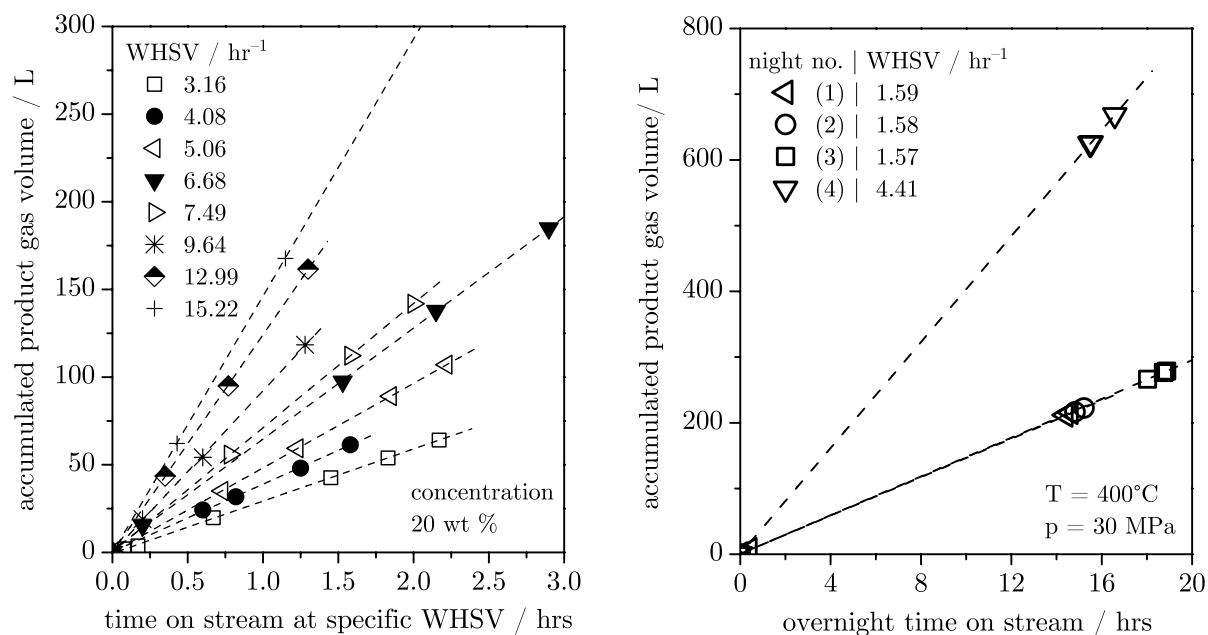


Figure 7.9: The gas production from SLW over Ru/C was strictly linear in time and WHSV, indicating no signs of catalyst deactivation. Left: gas production at various space velocities. Right: Overnight runs with reproducible gas production.

Table 7.5: Hourly and specific gas volume produced from synthetic liquefied wood gasification over Ru/C at various WHSV (right side: overnight runs).

WHSV $\text{hr}^{-1}$	$dV/dt$ L/hr	$V_{\text{gas, spec.}}$ L/gSLW	night	WHSV $\text{hr}^{-1}$	$dV/dt$ L/hr	$V_{\text{gas, spec.}}$ L/gSLW
3.16	29.47	1.02	1	1.59	14.73	1.01
4.08	38.68	1.03	2	1.58	14.58	1.01
5.06	48.10	1.04	3	1.57	14.72	1.02
6.68	63.78	1.04	4	4.41	40.24	0.99
7.49	70.81	1.03				
9.64	91.79	1.04				
12.99	124.10	1.04				
15.22	146.28	1.05				

Increasing the temperature to 500 °C produced a gas consisting of 45 – 46 vol % CH<sub>4</sub>, 7 – 8 vol % H<sub>2</sub>, and 47 vol % CO<sub>2</sub>, again in accordance with the calculated equilibrium values. Switching back to 400 °C at a WHSV equal to 4 hr<sup>-1</sup> produced the same gas composition as before. At all these operating conditions, the carbon conversion in terms of dissolved organic carbon was > 99.9 %. In order to obtain a gas composition indicative for incomplete conversion, the WHSV was increased drastically to 28 – 33 hr<sup>-1</sup> at 400 °C. Since for reaching these high space velocities, the water flow rate could not be increased to the same proportion as the organic flow rate, the concentration in organics was 30 wt %, and 35 wt %, respectively during this period. Only at these conditions did the carbon conversion decrease to 99.2 %, and 98.5 %, respectively. Interestingly, the gas composition remained almost unaffected. This might be an effect of the higher concentration counter-balancing the shorter residence time, or the methanation reactions are much faster than the gasification to primary gaseous products. Overnight, the rig was run without changing the WHSV (3 nights at ~1.58 hr<sup>-1</sup>).

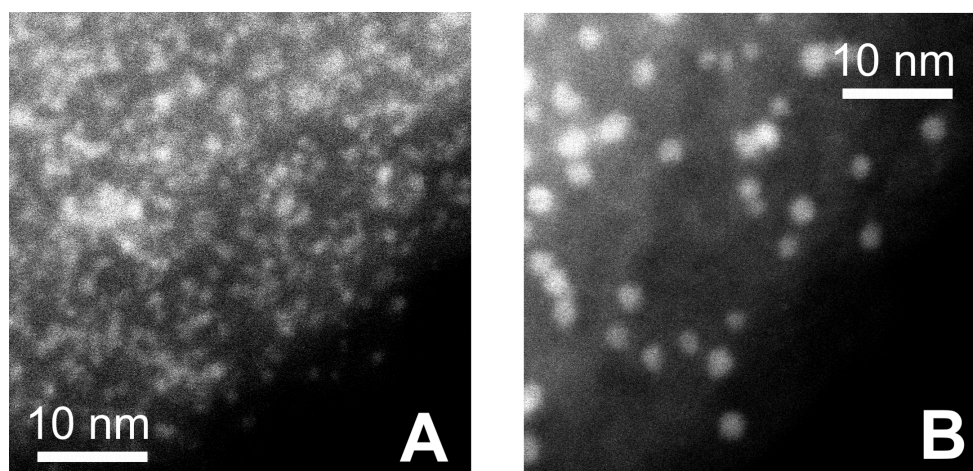


Figure 7.10: HAADF-STEM images of both fresh (A) and 220 hrs hydrothermally used (B) 2 wt % Ru/C catalyst. Some sintering was detected, with particle growth from 0.7 – 1 nm to 2 – 3 nm.

Comparison of HAADF-STEM images of both fresh and 220 hrs hydrothermally used catalyst showed some weak sintering effects, see Figure 7.10. The particles grew from 0.7 – 1 nm at a uniform, nearly

monodisperse distribution to 2 – 3 nm. As no ruthenium was detected in the reactor’s effluent phase by means of ICP, all Ru must have remained on the catalyst and formed less finely distributed crystallites. Assuming that by scanning transmission electron microscopy, their projection area is seen, a growth in detected size (the diagonal of a side surface of the Ru cubes) by the factor 2.5 represents a volumetric growth by the factor 15.6. Thus more than 15 times fewer crystallites should be seen on an image of the same size. This criterion is fulfilled for the tested catalyst, again corroborating the hypothesis of no ruthenium leaching. According to the manufacturer, the sintering phenomenon in a less harsh aqueous environment is known to stop at a certain level, which barely affects the catalytic performance in that particular application, which seems also to be true for the hydrothermal gasification of synthetic liquefied wood.

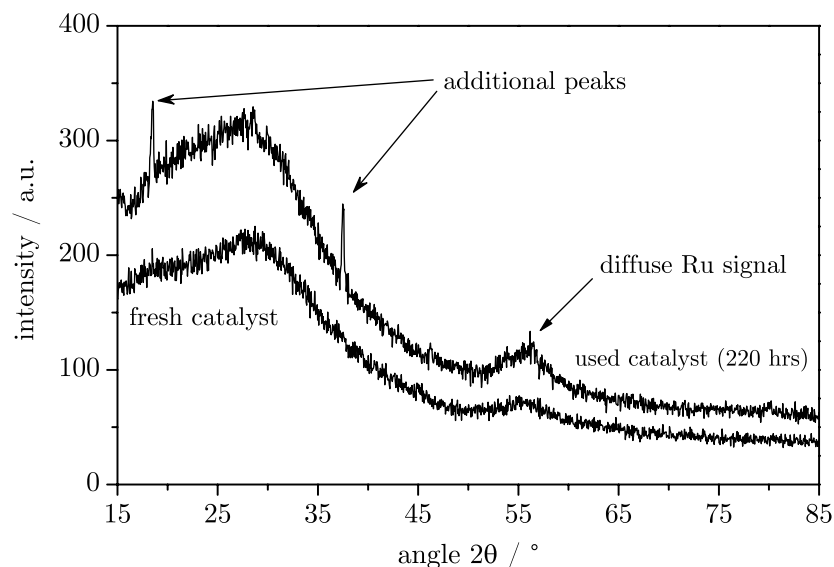


Figure 7.11: XRD scans of fresh (below) and 220 hrs hydrothermally used (above) 2 wt % Ru/C catalyst. Two non-identifiable sharp peaks of low intensity arose.

XRD measurements showed no distinct (broad) peaks, as the concentration of metal was low (2 wt %), and the average crystallite size had to be very small (e.g. < 4 nm), being another indication that no severe sintering took place, see Figure 7.11. There were two additional, sharp peaks present in the diffractogram of the used catalyst, but the signal intensity

was small, and no known compound could be attributed to the peaks (corrosion products neither).

Table 7.6: XPS analysis of fresh and 220 hrs hydrothermally used catalyst. Some traces of Na were detected as well.

atom	220 hrs used, scaled <sup>a</sup> atom %	O in oxides atom %	w/o oxides atom %	without oxides, scaled <sup>a</sup> atom %	fresh atom %
C <sub>1s</sub>	43.8	0.0	43.8	73.4	77.8
O <sub>1s</sub>	38.6	0.0	12.7	21.3	18.6
Ru <sub>3p3/2</sub>	0.8	1.7 <sup>b</sup>	0.8	1.4	1.1
Fe <sub>2p3/2</sub>	4.8	7.3	–	–	–
Ni <sub>2p3/2</sub>	6.1	7.6	–	–	–
Cl <sub>2p</sub>	1.3	0.0	1.3	2.1	0.7
S <sub>2p</sub>	0.3	1.3	–	–	–
P <sub>2p</sub>	2.4	9.7	–	–	–
sum	98.2		58.6	98.2	98.2

a. to have the same basis for comparison, the results were scaled to the atomic sum of elements present in the fresh sample (98.2 atom %).

b. not accounted for in subtracting corrosion oxides as RuO<sub>2</sub> is also present in the fresh sample.

The surface of the catalyst was analyzed by XPS. The results are presented in Table 7.6. As for all XPS results, the fraction of specific atoms identified are scaled to 100 % of all atoms found, a 1:1 comparison between samples is not straightforward. Some corrosion products were detected on the used catalyst, mainly iron and nickel. The sulfur 2p band corresponded to the signal of sulfate. Sulfate was present as a contaminant in the synthetic liquefied wood, originating from formic acid, where up to 5 ppm SO<sub>4</sub><sup>2-</sup> and up to 10 ppm SO<sub>3</sub><sup>2-</sup> were present. If one considers iron to be in the form of Fe<sub>2</sub>O<sub>3</sub> and nickel both in NiO and Ni<sub>2</sub>O<sub>3</sub> (1:1 proportion assumed), 14.8 atom % of the oxygen stem from sulfate, iron and nickel oxide. Subtracting the contribution of these substances leaves a

"corrected" amount of ruthenium, allowing for better comparison between fresh and used catalyst. Considering measurement errors and errors by random selection of catalyst grains, the amount of ruthenium before and after hydrothermal usage is identical, again indicating no leaching. The corrosion products were also visualized with SEM, see Figure 7.12.

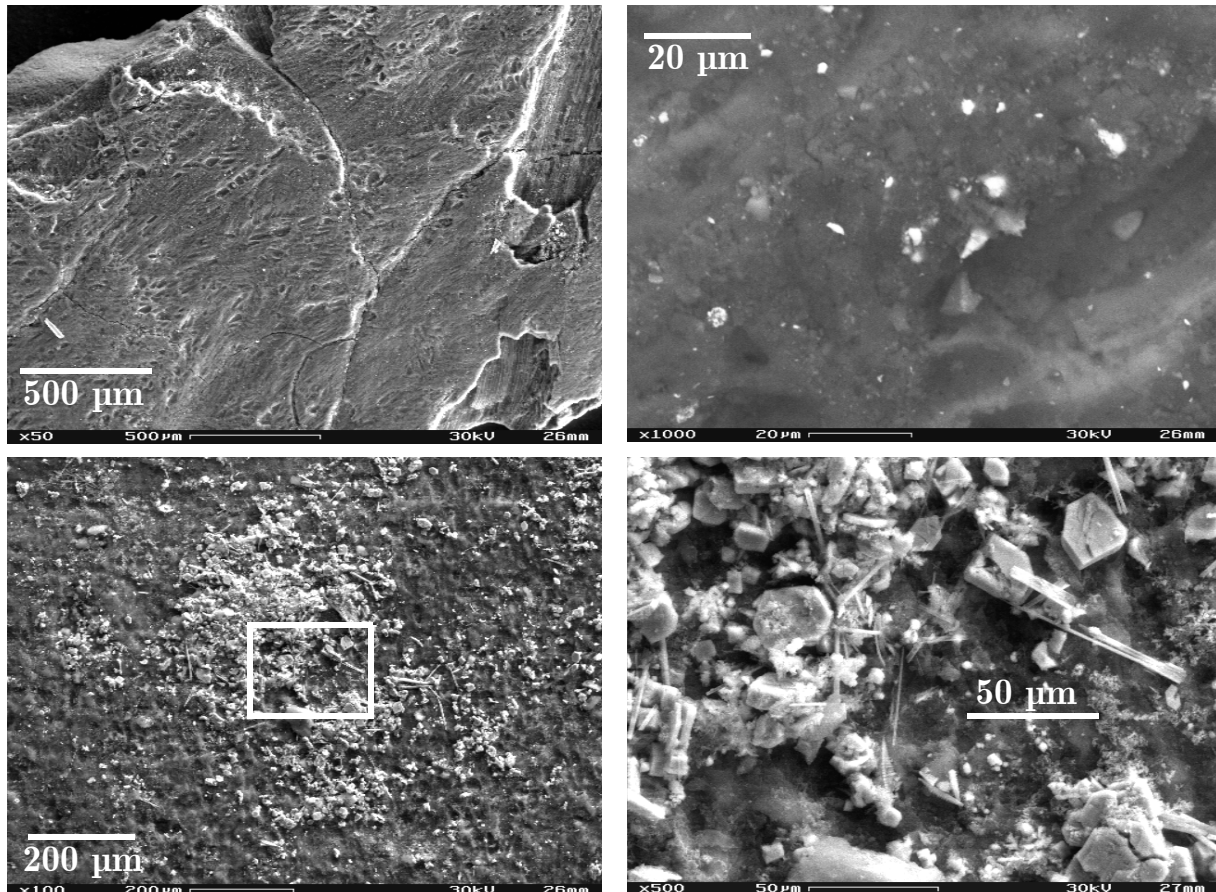


Figure 7.12: Scanning Electron Microscopy images of fresh 2 wt % Ru/C catalyst (above) and 220 hrs hydrothermally used catalyst (below). The used catalyst was covered with chunks and needles containing P, N, and corrosion products such as Fe, Ni, Cr.

The SEM images revealed some severe deposition of corrosion products, possibly from the superheater, the mixing cross, and the reactor walls. While the fresh catalyst (Figure 7.12 above) was rather free of impurities, the catalyst after 220 hrs of hydrothermal gasification (Figure 7.12 below) was covered with blocks and needles of different sizes, ranging from 1 to 50 – 100 micrometers. They consisted of Fe, Ni, P, and N. Na, Mg, and

Cr were found in traces ( $< 2$  atom % without C, analyzed by EDXS. In order to calculate the percentages, carbon was disregarded, as the support consisted of carbon, and the samples had to be treated with a carbon spray). It is suspected that the feed water was not pure (the ion exchanger that was used to purify the desalinated water was due to be replaced by that time) and contained some phosphate and nitrate, which co-precipitated with corrosion products such as  $\text{Fe}_2\text{O}_3$  or  $\text{NiO}/\text{Ni}_2\text{O}_3$ , deposited on the outer shell of the catalyst. It should be noted that the catalyst was still active at the time of sampling. Due to the presence of these corrosion products, the oxygen chemisorption method could not be applied to measure the dispersion of the used catalyst, as the corrosion products would be oxidized and reduced as well. A remedy could be to wash the corrosion products from the samples with acidic solutions prior to the oxygen chemisorption. However, by crystallite growth in the hydrothermal environment from  $l = 1$  nm to  $l = 3$  nm, as observed by STEM, the resulting dispersion  $D$  can be calculated: it is reduced from near 1.0 to 0.33, according to equation (4.10) and (4.11) presented in section 4.8. All observations indicate that 2 wt % Ru/C (Engelhard) is a very suitable and stable catalyst for the hydrothermal gasification of organics at high feed concentrations, which is an important milestone, as much effort has been directed towards finding a stable catalyst by many researchers [66-69, 79, 176], most of which operated at much lower organic feed concentrations, run times or space velocities. Applying low concentrations (e.g. 4 wt %) and low space velocities (liquid hourly space velocity LHSV =  $1.7 \text{ hr}^{-1}$ ) as for example Elliott and co-workers [176], the amount of SLW fed during this 220 hrs run corresponds to a time on stream of over 2500 hrs.

The results gained from the gasification of synthetic liquefied wood contradict the findings of Osada et al. who stated that their Ru/C catalyst (5 wt % Ru,  $D = 51$  % (fresh), Wako Pure Chemical Industries, Ltd.) showed a decrease in gasification performance in two subsequent lignin gasification experiments (conc. 3.2 wt %) in a stainless steel batch reactor, where the catalyst was re-used ( $p_{\text{H}_2\text{O}} = 37.1$  MPa,  $T = 400$  °C) [183]. They did not suggest a deactivation mechanism, but it is conceiv-

able that the sulfur species within the lignin have poisoned the catalyst. During the 220 hrs on stream of our long-term experiment presented here, a total of 5005 g synthetic liquefied wood was successfully gasified over 9.183 g of catalyst (dry), thus the ratio of organics to catalyst was  $m_{\text{org.}}/m_{\text{cat.}} = 545$ , or  $m_{\text{org.}}/m_{\text{Ru}} = 27'250$ , with no signs of deactivation. Thus, 2 wt % Ru/C (Engelhard) appears to be superior to other Ru/C catalysts, confirming the trend that had already emerged from the batch reactor catalyst screening experiments presented in section 6.3.2.

### 7.1.6 Blank Test Gasification of Synthetic Liquefied Wood over $\alpha\text{-Al}_2\text{O}_3$

To assess the carbon conversion and decomposition of synthetic liquefied wood (conc. 10 wt %) in a non-catalytic<sup>6</sup> experiment at 400 °C and 30 MPa, the tubular reactor was filled with  $\alpha\text{-Al}_2\text{O}_3$  beads only (1 mm diameter, 99.8 % metal basis, Alfa Aesar). The phenol fraction in the SLW was replaced by anisole (to avoid excessive exposure to phenol vapors), which then made 31 wt % of the synthetic liquefied wood. The flow rates corresponded to a WHSV from previous experiments of 27.2  $\text{hr}^{-1}$  for 1.5 hrs on stream, and 7.1  $\text{hr}^{-1}$  for 2.3 hrs on stream. As there was no catalyst present, the numbers represented a pseudo space velocity, meaning the fluid spent the same amount of time in the reactor as during the corresponding catalytic experiments (equal fluid residence time  $\tau$ ).

The product gas composition was similar for both space velocities: 39 vol %  $\text{CO}_2$ , with less than 0.2 vol %  $\text{CH}_4$  and  $\text{C}_2\text{H}_6$ . The hydrogen content at the higher WHSV was higher, while the opposite was the case for carbon monoxide, see Table 7.7.

This could indicate that for higher space velocities, the reverse water gas shift reaction becomes less pronounced, or just slightly less feed was gasified to the primary product carbon monoxide, resulting in a lower CO concentration. However, the carbon conversion was in both cases  $\sim 27\%$ , invalidating the above option. The aqueous product effluent from the

---

6. The stainless steel reactor walls and the bed filling material  $\alpha\text{-Al}_2\text{O}_3$  might exhibit some catalytic activity, despite the term “non-catalytic”.



Table 7.7: Carbon conversion  $X_C$  and product gas composition of “non-catalytic” gasification of SLW. Only  $\alpha$ - $\text{Al}_2\text{O}_3$  was present in the reactor.

WHSV $\text{hr}^{-1}$	$X_C$ %	$\text{CO}_2$ vol %	$\text{CH}_4$ vol %	$\text{C}_2\text{H}_6$ vol %	$\text{H}_2$ vol %	CO vol %
27.2	26.9	39	< 0.2	< 0.2	41	20
7.1	27.2	39	< 0.2	< 0.2	38	23

plant at this low carbon conversion was a two-phase mixture and needed to be largely diluted for analysis (anisole is very poorly miscible with water). HPLC analysis showed that there was no formic acid present in the effluent anymore, thus 20 % of the carbon conversion originated from formic acid gasification<sup>7</sup>, while the other 7 % mostly stemmed from ethanol and anisole gasification. About 0.3 % (at  $\text{WHSV} = 27 \text{ hr}^{-1}$ ), or 0.9 % (at  $\text{WHSV} = 7 \text{ hr}^{-1}$ ) of the anisole molecules were hydrolyzed to phenol. Acetic acid, however, was measured at nearly the feed concentration. For a completely deactivated catalyst, the above effluent and gas phase compositions at the outlet of the test rig would be expected, as they were received with only the bed-filling material  $\alpha$ - $\text{Al}_2\text{O}_3$ .

The formic acid in the feed can either decarbonylate/dehydrate to CO and water (7.1), as already outlined in section 2.2.7, and then shift with water to  $\text{CO}_2$  and  $\text{H}_2$ , or it can decarboxylate to form  $\text{CO}_2$  and  $\text{H}_2$ , which can then form CO and water via the reverse water gas shift reaction (7.2):



Which way is more pronounced depends mostly on the temperature and the pH of the reaction medium [108, 184]. Based on this background, the carbon monoxide in the gas phase would not only be a primary product gas out of the synthetic liquefied wood, but also a secondary one via the

7. Formic acid represents 20 wt % of the SLW’s carbon content, refer to Table 5.4 on page 86.

reverse water-gas shift reaction (rWGS) from  $\text{CO}_2$  and  $\text{H}_2$  formed. If one assumes 100 % conversion for the decomposition of  $\text{HCOOH}$ , which is reasonable as no formic acid was detected in the outlet phase, then the gas phase would be composed of 100 vol %  $\text{CO}$  for case (7.1), or 50 vol %  $\text{CO}_2$  and 50 vol %  $\text{H}_2$  for case (7.2). In order to end up with a gas phase composition as obtained in the experiments (roughly 40 vol %  $\text{CO}_2$ , 40 vol %  $\text{H}_2$ , and 20 vol %  $\text{CO}$ ), the subsequent WGSR in case (7.1) would have to be carried out at 67 % conversion, but the subsequent rWGSR in case (7.2) at only 33 % conversion. At the higher WHSV of  $27 \text{ hr}^{-1}$ , the  $\text{CO}$  content of the product gas phase was lower. It is reasonable that for higher WHSVs, the conversion will be lower. Yet, more data at even higher space velocities would be needed to corroborate this hypothesis, as the difference in  $\text{CO}$  concentration was rather low (23 vol % vs. 20 vol %) for the two WHSVs. The experimental evidence would support pathway (7.2), but as the chemical equilibrium composition includes no  $\text{CO}$ , but only  $\text{H}_2$  and  $\text{CO}_2$ , there is no driving force for mechanism (7.2b), as the primary products from (7.2a) are already  $\text{CO}_2$  and  $\text{H}_2$ . Thus, the  $\text{CO}$  must mostly stem from decarbonylation of  $\text{HCOOH}$ , and not via a reverse water gas shift reaction. The two options are also depicted in Figure 7.13.

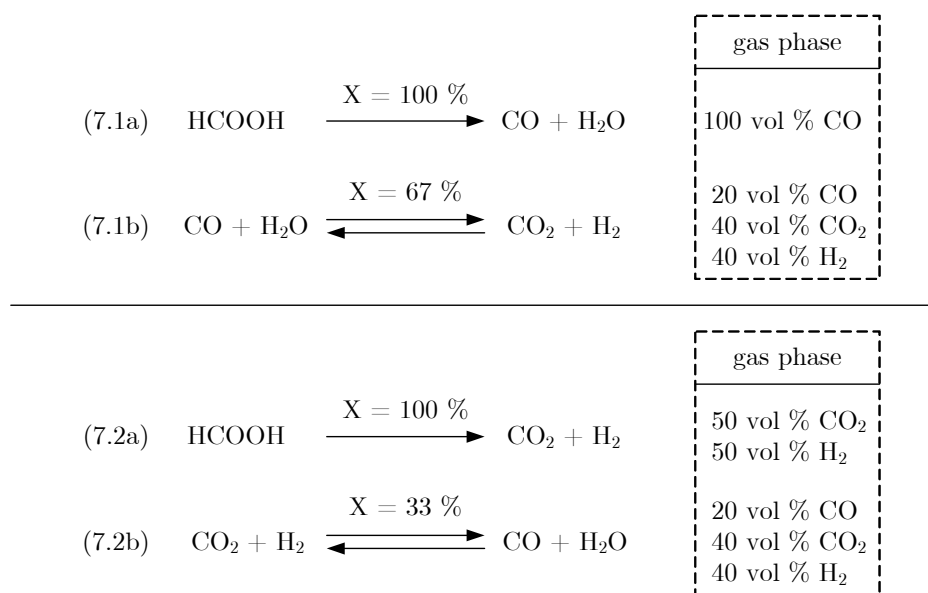


Figure 7.13: Possible reaction schemes of formic acid degradation to yield a product gas composition as obtained in the experiments.

However, these considerations are not consistent with the theory presented in section 2.2.7, where it was outlined that the decarboxylation is the dominating pathway of formic acid decomposition in supercritical water.

### 7.1.7 Conclusions of the Long-Term Stability and Activity Experiments with Various Catalysts

- Skeletal nickel catalysts are not suitable for the hydrothermal gasification of biomass. They exhibit high initial activity but sinter rapidly, accompanied by loss of metal surface area. Stabilization by doping of other metals such as Ru, (or Fe, Mo or Cu as investigated in batch reactor experiments) was not successful.
- Ru/TiO<sub>2</sub> can be a suitable catalyst in supercritical water, if it provides a sufficient active metal surface area. Generally, the dispersion of Ru/TiO<sub>2</sub> is lower than the one of Ru/C, and hence a higher metal loading is needed to achieve the same surface area of active metal, which negatively affects the overall price of the catalyst system. Moreover, catalysts with higher metal loadings are usually less dispersed, so that the required increase of metal loading is disproportionate.
- 2 wt % Ru/C (Engelhard) was long-term active (220 hrs) in the hydrothermal environment, for both gasification and methanation at 400 °C and 30 MPa, at high feed concentrations (20 wt %) and with space velocities as large as 20 hr<sup>-1</sup>. The product gas corresponded to the thermodynamic equilibrium composition (50 vol % CH<sub>4</sub>, 2 – 3 vol % H<sub>2</sub>, 47 – 48 vol % CO<sub>2</sub>, < 0.1 vol % CO).
- “Non catalytic” gasification of SLW in the test rig used for the long-term experiments described in this thesis yielded around 27 % of carbon conversion, with a product gas composition of ~40 vol % CO<sub>2</sub>, ~40 vol % H<sub>2</sub>, and ~20 vol % CO.

## 7.2 Methodology for Testing the Sodium Sulfate Tolerance of the 2 wt % Ru/C Catalyst

Real waste biomass streams contain inorganics such as metal oxides and salts. As their solubility in water decreases sharply around the critical point, most of them should precipitate and be separated in a device where the fluid is quickly brought to the supercritical state (i.e. in a salt separator). Although such a stage could substantially reduce the salt load, there will always remain a residual salt concentration entering the reactor, corresponding to the solubility at the pressure and temperature of the salt separator. It is important to understand the possible interaction of dissolved salts with the catalyst. Separation studies with sodium sulfate have been carried out previously (in phase equilibria studies [182, 185], and recently with neutron radiography, carried out at the Paul Scherrer Institute [30]). Hence, sodium sulfate was chosen as the model substance, added to the synthetic liquefied wood, for the salt tolerance experiments described in this section. In addition, sulfate is contained to ~1.1 wt % in the dry matter of swine manure solids, and it is also present in many other types of biomass.

The concentration of  $\text{Na}_2\text{SO}_4$  was chosen so that it was presumably below the maximum solubility at conditions within the reactor. All concentrations (in  $\text{mg}_{\text{Na}_2\text{SO}_4}/\text{kg}_{\text{mixture}}$ , or ppm) refer to the mixed fluid phase that entered the reactor, thus after the mixing of the cold model biomass stream with the hot water stream in the cross of the test rig above the tubular reactor. The solubility of sodium sulfate in complex mixtures such as synthetic liquefied wood is not known. Only data at slightly lower pressure (25 MPa) in pure water are presented in the literature for typical reaction temperatures around 400 °C [182, 185-187]. The solubility is exponentially dependent on temperature. Lower concentrations than those reported on the solubility curve were chosen: typically 8 – 16 ppm at 400 °C, and up to 40 ppm below 360 °C (the solubility at 25 MPa and 400 °C is reported to be ~200 ppm, and at 25 MPa and 360 °C to be ~3 wt %).

### 7.2.1 Gasification of Synthetic Liquefied Wood with Increasing Sodium Sulfate Content

After the successful gasification experiments with 2 wt % Ru/C, sodium sulfate (Merck, p.a., water free) was added to the synthetic liquefied wood, and 23 gasification experiments were carried out (most of them with SLW, some with ethanol or water and sulfate only). A list of these experiments is presented in Table 7.8 on page 198f, where the process conditions and some results are presented. Initial clarifications revealed catalyst deactivation due to the addition of sulfate (exp. no. 1 – 5). Subsequent experiments (no. 6 – 23) served to identify the mechanism of this deactivation. Details to the individual runs are presented in the following paragraphs.

Experiments no. 1 – 5 were carried out with a fixed WHSV of  $4 \text{ hr}^{-1}$ . 9.2 g of catalyst (dry) were present in the reactor. After the initial gasification of sulfate-free synthetic liquefied wood (conc. 10 wt %; 125 g SLW fed within 3.2 hrs, exp. no. 1), sodium sulfate was added to yield a concentration of  $4 \text{ mg}_{\text{Na}_2\text{SO}_4} / \text{kg}_{\text{mixture}}$ , later referred to as ppm, at the entrance of the reactor, after mixing with the water phase. To prevent the sulfate fed with the cold SLW from precipitating in the mixing cross upon contact with supercritical water (the local concentration before mixing could exceed the solubility), the water phase was preheated to only  $360 \text{ }^\circ\text{C}$ . The fluid was then heated to  $400 \text{ }^\circ\text{C}$  within the first 11 cm of the catalytic bed, after which the temperature was kept constant. The solution was fed for 2.1 hrs, with no identifiable effect ( $\sim 100 \%$  carbon conversion, exp. no. 2). Overnight, the rig was flushed with cold water. The next experiment (no. 3) was carried out at 8 ppm for 2.5 hrs, followed by 16 ppm for 2.9 hrs (exp. no. 4). The rig was then again flushed with cold water overnight. After an additional 5.5 hrs at 16 ppm (exp. no. 5), the carbon conversion decreased from 100 % to 98 %, with a distinct odor of unconverted feed in the effluent.

Table 7.8: Experimental conditions of the 23 experiments carried out to identify the mechanism of deactivation for 2 wt % Ru/C, grouped into 4 campaigns.

exp. no.	feed	conc. wt %	runtime hrs	$m_{\text{org.}}$ g	WHSV $\text{hr}^{-1}$	$\text{Na}_2\text{SO}_4$ ppm	$n_{\text{SO}_4^{2-}}$ mmol	$\frac{n_{\text{C, fed}}}{n_{\text{Ru}}}$	$\frac{n_{\text{SO}_4^{2-}}}{n_{\text{Ru}}}$	$T_{\text{cat.}}$ $^{\circ}\text{C}$	$X_{\text{C}}$ at end %
details: catalyst bed pos.: 0 – 18 cm   $m_{\text{cat., dry}}$ : 9.18 g   $n_{\text{Ru}}$ : 1.82 mmol											
1	SLW	10	3.2	125	4.3	0	0.00	2747	0.00	400	99.9
2	SLW	10	2.1	78	4.0	4	0.02	1714	0.01	400	99.9
3	SLW	10	2.5	105	4.1	8	0.06	2307	0.03	400	99.8
4	SLW	10	2.9	106	4.0	16	0.12	2329	0.07	400	99.5
5	SLW	10	5.5	215	4.04	16	0.24	4724	0.13	400	98
1 - 5	SLW	10	16.2	629	4.0 – 4.3	0/4/8/16	0.44	13821	0.24	400	98
details: catalyst bed pos.: 17.5 – 22.5 cm   $m_{\text{cat., dry}}$ : 2.22 g   $n_{\text{Ru}}$ : 0.44 mmol											
6	SLW	10 – 20	50.1	841	7 – 27	0	0	76417	0	400	99.4
7	SLW	10	5.8	323	25	16	0.37	29349	0.83	400	~45
8	SLW	10	7.5	316	7 – 27	0	0	28726	0	400	~50
details: catalyst bed pos.: 17.5 – 22.5 cm   $m_{\text{cat., dry}}$ : 2.02 g   $n_{\text{Ru}}$ : 0.40 mmol											
9	SLW		26.5	497	30/15/10/7.5	0	0.00	49620	0.00	350 – 400	99.3
10	SLW	10	19.6	311	7.8	8	0.18	31053	0.44	355	~40
11	SLW	10	7.5	115	7.6	0	0.00	11529	0.00	396	80

Table 7.8: Experimental conditions of the 23 experiments carried out to identify the mechanism of deactivation for 2 wt % Ru/C, grouped into 4 campaigns.

exp. no.	feed	conc. wt %	runtime hrs	$m_{\text{org.}}$ g	WHSV $\text{hr}^{-1}$	$\text{Na}_2\text{SO}_4$ ppm	$n_{\text{SO}_4^{2-}}$ mmol	$\frac{n_{\text{C, fed}}}{n_{\text{Ru}}}$	$\frac{n_{\text{SO}_4^{2-}}}{n_{\text{Ru}}}$	$T_{\text{cat.}}$ $^{\circ}\text{C}$	$X_{\text{C}}$ at end %
12	SLW	10	18.1	279	7.6	8	0.16	27871	0.39	354	~25
13	SLW	10	8.6	136	7.9	0	0.00	13629	0.00	399	30
14	SLW	10	13.4	206	7.6	8	0.12	20573	0.29	355	31
15	SLW	10	7.1	111	7.7	0	0.00	11073	0.00	396	32
9 – 15	SLW	10	100.8	1656	7.5 – 30	0 / 8	0.45	165346	1.12	350 - 400	32
details: catalyst bed pos.: 16.5 – 20.0 cm   $m_{\text{cat., dry}}$ : 1.97 g   $n_{\text{Ru}}$ : 0.39 mmol											
16	H <sub>2</sub> O	N/A	25.5	N/A	N/A	40.1	1.05	N/A	2.71	200	N/A
17	SLW	10	3.9	62	8.1	0	0.00	6298	0.00	400	99.8
18	H <sub>2</sub> O	N/A	18.2	N/A	N/A	40.1	0.75	N/A	1.93	290	N/A
19	EtOH	10	5.1	69	6.9	0	0.00	7677	0	400/290	99/55
20	EtOH	10	16.0	225	7.2	40	0.64	25103	1.63	290	~5
21	EtOH	10	6.1	86	7.1	0	0.00	9532	0.00	400	~90
22	EtOH	10	17.9	252	7.1	40	0.71	28074	1.83	320	3
23	EtOH	10	5.1	71	7.0	0	0.00	7940	0.00	400	~20
19 – 23	EtOH	10	50.2	703	6.9 – 7.2	0 / 40	1.35	78326	3.46	290/320/400	~20

The test rig was flushed with hot water and depressurized while still at 400 °C to evaporate the liquids and keep any salts on the catalyst. After cool-down, the catalytic bed was carefully removed from the reactor, split into an entrance and an exit fraction, and analyzed with XRD, XPS, ICP, and HAADF-STEM. The findings did not differ significantly from the results gained after 220 hrs of gasification described in section 7.1.5, when no sulfate had been deliberately added to the feed. Thus, the sulfate feeding had to be prolonged until a significant decrease in carbon conversion would be detected (the sulfate-fed-to-ruthenium ratio of this campaign, exp. no 1 – 5, was  $n_{\text{SO}_4^{2-}}/n_{\text{Ru}} = 0.24$ ).

### 7.2.2 Possible Catalyst Deactivation Mechanisms

These findings suggest a deactivating effect of the sodium sulfate on the Ru/C catalyst. Some sodium is present in the carbon matrix of the fresh catalyst (EDXS analysis revealed the amount to be roughly one third of the amount of ruthenium, thus corresponding to ~0.5 – 1 wt %). Sodium must be continuously extracted in the hydrothermal environment over time, as in used samples its quantity had decreased by orders of magnitude (measured with XPS and EDXS). During this sodium leaching, sodium must have been present in solution, and passed the vicinity of the active ruthenium sites on its way out of the reactor, without affecting macroscopic variables such as carbon conversion or gas composition.

Thus, the deactivating effect of the addition of sodium sulfate had to be attributed to the anion sulfate, and not the sodium cation. This deactivation process could be governed by several mechanisms:

- (i) regular usage and exposure to hydrothermal water that dissolves ruthenium and carries it out of the system,
- (ii) possible dissolution with re-precipitation, accompanied by a loss of dispersion and metal surface area over time,
- (iii) precipitation of sodium sulfate which physically blocks the active ruthenium sites, or



- (iv) chemical bonding of a sulfur species to the ruthenium sites (sulfate as ligand is conceivable as well as a preceding reduction of sulfate to sulfide, which then acts as a ligand for the ruthenium sites; both possibilities will be discussed in section 7.2.6).

These four possible deactivation mechanisms are visualized in Figure 7.14. The following experiments were carried out to identify the governing mechanism.

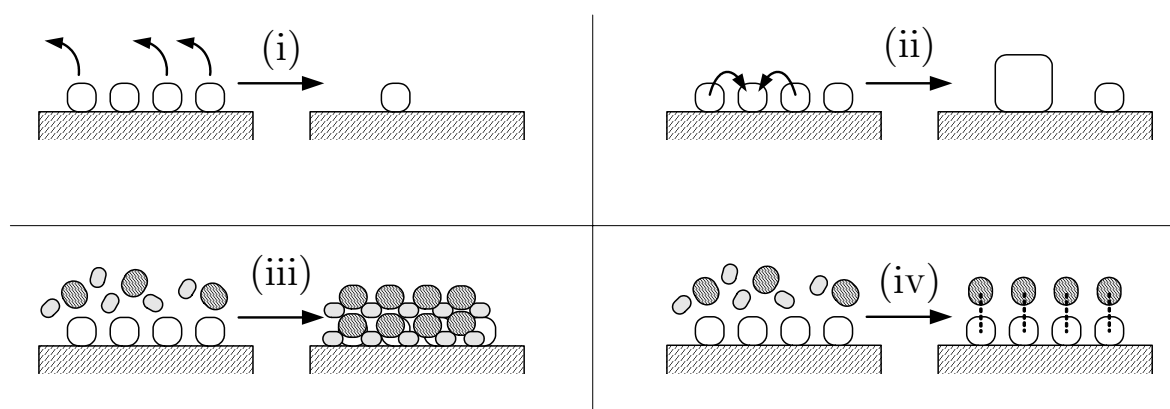


Figure 7.14: Four possible catalyst deactivation mechanisms: (i) dissolution of ruthenium and carry-out of the system, (ii) sintering of the crystallites and loss of active metal surface area, (iii) precipitation of sodium sulfate leading to physical blockage of the active sites, or (iv) irreversible chemical bonding of sulfate to  $\text{Ru}^{\text{III}}$  (or sulfide to  $\text{Ru}^{\text{II}}$ ), masking the active sites.

### 7.2.3 Identification of the Governing Deactivation Mechanism – Hypothesis of Deactivation due to Ru Leaching (i)

To verify that the deactivation was not due to regular usage leading to Ru leaching (i), the reactor was filled with fresh catalyst (amount  $\sim 4$  times less) and experiment no. 6 was carried out. A total of 76'400 moles of carbon per mole of ruthenium were gasified within 50 hours, with complete feed conversion and the gas phase corresponding to the chemical equilibrium composition. In the previous 220 hrs stability experiment (section 7.1.5), a total of 109'900 moles of carbon per mole of ruthenium were completely gasified. Therefore, if deactivation takes place in the fol-

lowing experiment no. 7 (which it did indeed), the deactivation effect has to be attributed to an interaction with sulfate, and option (i) can be ruled out, as the catalyst should be capable of gasifying at least an additional 33'000 moles of carbon. Furthermore, no Ru was detected by ICP in the effluent phase, which also speaks against hypothesis (i).

#### **7.2.4 Hypothesis of Deactivation due to Loss of Active Metal Surface Area (ii)**

Thus, without changing the catalyst, experiment no. 7 was carried out: By adding sodium sulfate in a concentration of 16 ppm at the reactor entrance, the catalytic performance at 400 °C decreased steadily within only 6 hrs towards a carbon conversion of 50 %. Total exposure to hydrothermal water was 56 hrs until deactivation, 4 times less than in the 220 hrs stability experiment. STEM images of the catalyst differed not from the images of the catalyst after 220 hrs of gasification without sulfate. Mild sintering did occur during exposure to hydrothermal water, as was depicted in Figure 7.10 on page 187, but no additional loss of surface area was detected due to the co-feeding of sulfate, and option (ii) was disproved.

#### **7.2.5 Hypothesis of Deactivation due to Physical Blockage by Precipitated Sodium Sulfate (iii)**

The plant was flushed overnight (17 hrs) with cold water. In case sodium sulfate had precipitated and masked the ruthenium crystallites, these precipitates should have been re-dissolved and carried out of the system during this flushing procedure applied between experiment no. 7 and 8. The subsequent gasification experiment (no. 8, 400 °C, SLW fed, no sulfate added) showed no increase in catalytic performance, but no further decrease either. The product gas composition of these two experiments is depicted in Figure 7.15. After three hours on stream, the methane concentration started to drop, and decreased steadily towards 20 vol % after six hours, when the SLW/sulfate feeding was switched off, and pure water was fed to the plant (at the end of exp. no. 7).

The methane concentration decreased even further in experiment no. 8, from 20 to 15 vol %, accompanied by an increase of the hydrogen concentration, which indicates reduced methanation activity. The CO concentration did not reach the level of the blank test described in section 7.1.6 (20 vol %), thus some residual gasification and water gas shift activity remained.

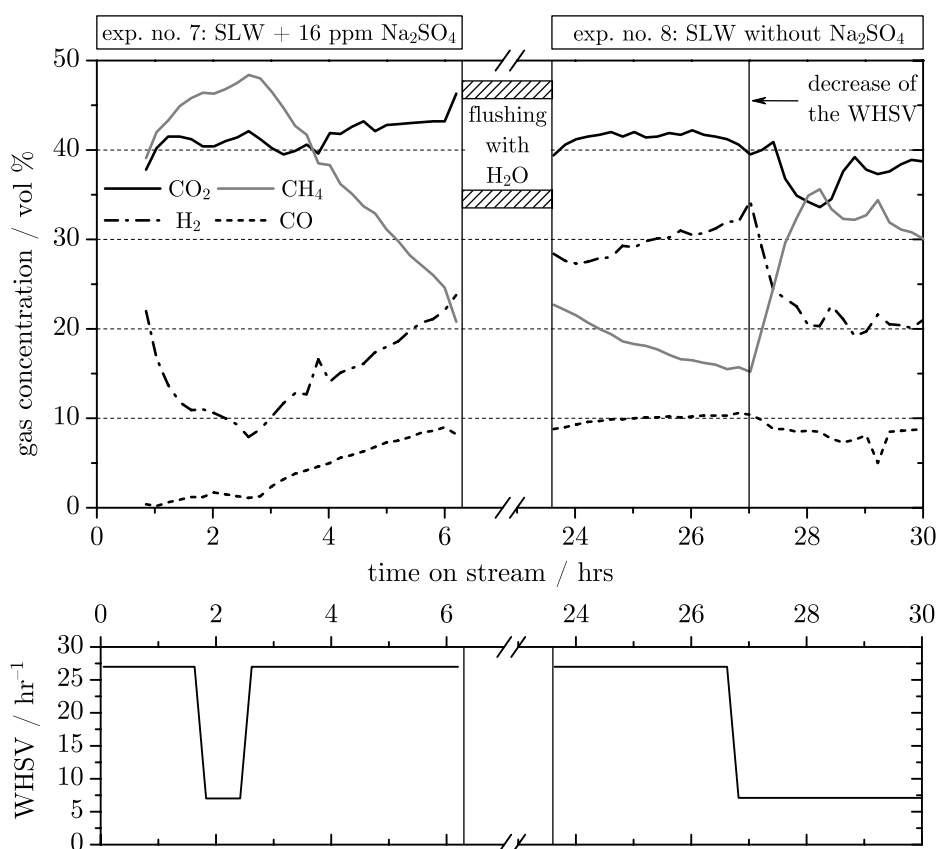


Figure 7.15: Product gas concentration of SLW gasification in experiments no. 7 and 8. The flushing procedure with water did not recover the catalyst's activity.

While the product gas composition changed over time, the carbon conversion  $X_C$  decreased to ~45 % during experiment no. 7, and stayed at this level throughout experiment no. 8 at  $\text{WHSV } 27 \text{ hr}^{-1}$ . It only increased to ~50 % after reduction of the weight hourly space velocity to  $7 \text{ hr}^{-1}$ . Also the methane concentration increased by reducing the WHSV, and the hydrogen concentration decreased, again indicating some residual catalytic activity. The content of carbon monoxide in the gas, however, was

not affected.

As the washing procedure with pure water between experiments no. 7 and 8 did not regenerate the catalyst, option (iii) – deactivation by physical blockage due to salt precipitates – was unlikely: the precipitates should have been re-dissolved and washed off the catalyst. However, if the sodium sulfate precipitated inside the pores of the carbon support rather than on the catalyst surface, the time required for re-dissolution might exceed the flushing time applied (slow pore diffusion of cold water), and further investigation was needed.

The campaign with experiments no. 9 – 15 was carried out to gain clearer evidence to exclude option (iii) as the governing catalyst deactivation mechanism. The aim was to operate the plant during these runs at conditions where precipitation would certainly not occur, and check for a decrease in activity. If the catalyst still deactivated, then precipitation could not be the cause for it. However, since the exact solubility of sodium sulfate in a complex biomass-water-mixture is not known, a safety margin has to be applied to the concentration of sulfate and the temperature of the catalyst bed.

Precipitation is influenced by temperature and concentration, and can be avoided by lowering both (in the temperature range of 300 – 400 °C, the solubility of sulfate is decreasing with increasing temperature). Yet the co-presence of organics influences the solubility, as was shown in a sulfate-water-methanol system at ambient temperatures of 10 – 50 °C: the solubility of sulfate in 20 wt % MeOH was reduced by a factor of 3 [188]. In addition, the production of gas at the catalyst surface additionally lowers the local solubility, and precipitation might still take place at these locations, whereas in pure water, the salts would still be dissolved. These considerations again speak for a margin of safety, which should be added to the solubility data of sodium sulfate in pure water that was taken from the literature.

As the activity of the catalyst depends on temperature, a reference temperature of 400 °C was chosen to identify the degree of deactivation in the following experiments; a completely active catalyst is then expected to yield full conversion. However, at 400 °C, precipitation of sodium sulfate

can take place. To avoid this, the temperature was always lowered to max. 355 °C before sodium sulfate was added to the feed. At this temperature, the solubility of Na<sub>2</sub>SO<sub>4</sub> in pure water is about 5 wt % [182] (at 25 MPa, no data at higher pressures is available; however, at 30 MPa, the solubility is possibly even higher due to the denser fluid phase). Even in a complex biomass-water-mixture (biomass conc. 10 wt %) and with ongoing gas production, the sulfate (conc. 8 ppm, factor 6200 lower than reported solubility in pure water) is expected to be completely dissolved at these conditions. Thus, by lowering the temperature to 355 °C prior to sulfate addition, precipitation can be prevented, and if deactivation takes place, it cannot be attributed to option (iii). This approach was followed in the next experiments (no. 9 – 15).

At first, the carbon conversion of synthetic liquefied wood at a temperature of 355 °C was assessed (in experiment no. 9), as it would certainly be lower than at 400 °C. A plot of  $X_C$  vs. time on stream is depicted in Figure 7.16, covering experiments no. 9 – 15. At 400 °C,  $X_C$  was 100 %, as expected. By reducing the temperature to 355 °C, it decreased from 80 % (initially) to ~60 % (overnight). The reason for the difference between the conversion at the beginning and at the end of the period was due to the slow response of the system; the first effluent samples were taken shortly after the temperature reduction. In addition, the effluent at incomplete conversion was a two phase mixture (anisole is hardly miscible with water at ambient conditions), and the samples had to be strongly diluted prior to analysis in DC-190. A scatter of 5 – 8 % in the data points was observed. Exp. no. 9 showed that after a period at 355 °C, the conversion settled back to 100 % when raising the temperature back to 400 °C (at around 22 hrs on stream, compare Figure 7.16).

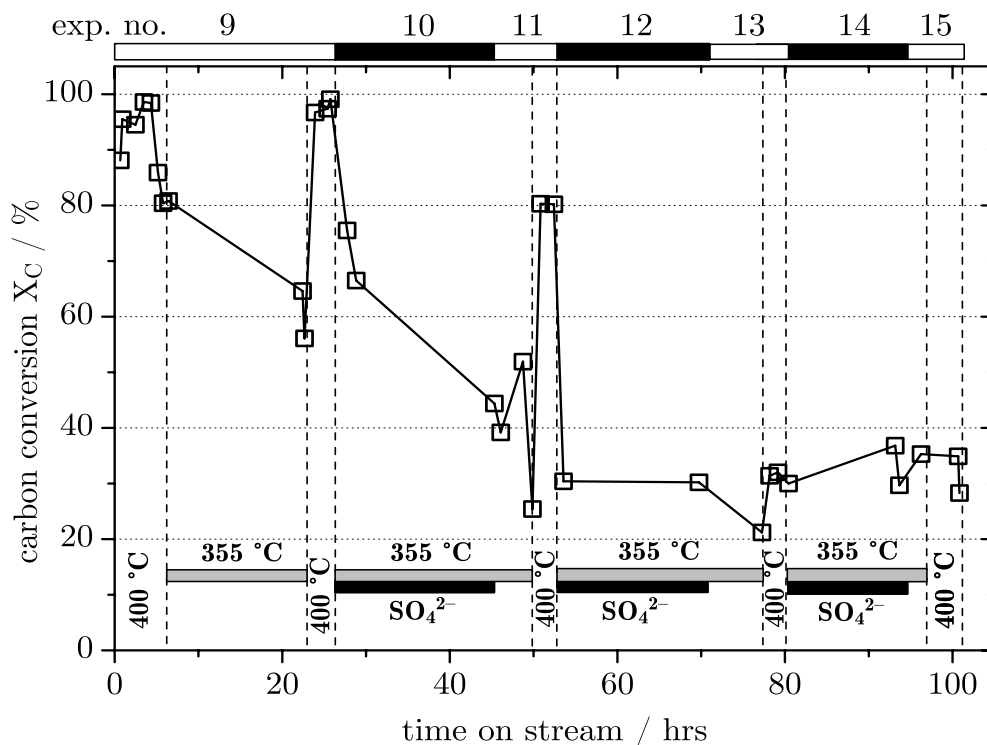


Figure 7.16: Catalyst deactivation with SLW (conc. 10 wt %) and sodium sulfate (conc. 8 ppm at reactor entrance). Gasification yielded ~60 % carbon conversion at 355 °C, and ~100 % at 400 °C (without sulfate). After exp. no. 10, conversion at 400 °C was reduced to ~80 %, while after exp. no. 12, conversion was near the value expected without catalyst (~27 %), because of  $\text{SO}_4^{2-}$ .

In the following experiments 10 – 15, feeding SLW with sulfate (always at 355 °C to avoid precipitation) and without sulfate (at 400 °C) was alternated. During the sulfate feeding experiments no. 10, 12, and 14, the carbon conversion steadily decreased over time. After each experiment, the feed was switched to sulfate free SLW, and after a holding time of 2 hrs, the temperature was raised again to 400 °C (experiments no. 11, 13, and 15). By doing so, it was ensured that no more sulfate was present in the fluid phase before the temperature increase. The conversion at 400 °C was higher than at 355 °C (as expected), but only up to experiment no. 12. There, the catalyst seemed to be fully deactivated ( $X_C$  was reduced to 20 – 30 %). A carbon conversion around 27 % can be expected even with only  $\alpha\text{-Al}_2\text{O}_3$  packed in the tubular reactor, without any Ru/C, as described in section 7.1.6. Also, the composition of the gaseous product

phase slowly progressed from the chemical equilibrium composition towards the gas composition measured with an  $\alpha$ -alumina packing only, see Figure 7.17.

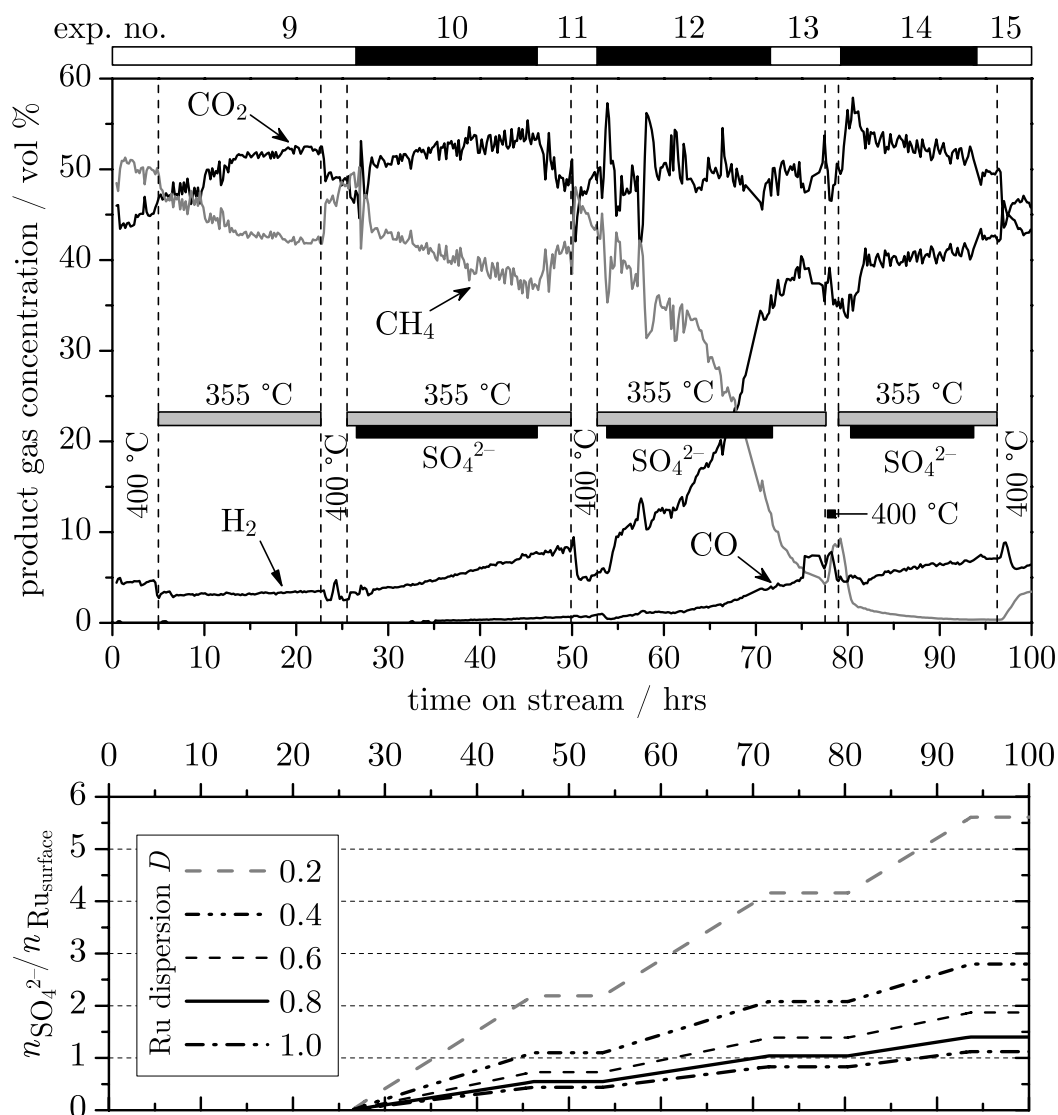


Figure 7.17: Catalyst deactivation by sulfate (conc. 8 ppm at reactor entrance) during gasification of SLW. Above: the progressive deactivation is seen by a shift of the product gas composition away from the chemical equilibrium composition towards the primary products  $\text{CO}$ ,  $\text{CO}_2$ , and  $\text{H}_2$ . Below: molar sulfate-to-surface-ruthenium-ratio.

The molar sulfate-to-ruthenium-ratio after experiment no. 12 was 0.83. Considering a reduction of the dispersion from 1.0 to 0.33 by seasoning to the hydrothermal environment (as outlined on page 191), the molar ratio

of sulfate fed to surface ruthenium,  $n_{\text{SO}_4^{2-}}/n_{\text{Ru}_{\text{surface}}}$ , was around 2 after experiment no. 12, as can be seen in Figure 7.17. Hence, enough sulfate was fed to irreversibly bind to all ruthenium surface sites, even at a stoichiometry of  $\text{Ru}_{\text{surface}}-(\text{SO}_4^{2-})_2$ . The fluid properties at 355 °C and 30 MPa ensured that no precipitation of the salts could take place. Thus, the deactivating effect of sodium sulfate was due to an irreversible interaction of sulfate with the catalyst (iv), and not due to physical blockage of the sites by precipitates.

### 7.2.6 Hypothesis of Deactivation due to Chemical Interaction of Ru with a Sulfur Species (iv), i.e. $\text{SO}_4^{2-}$ or $\text{S}^{2-}$

To study this deactivating effect in more detail, fresh catalyst was loaded into the reactor, and experiments no. 16 to 23 were conducted. First, in experiment no. 16, pure water with sodium sulfate (conc. 40 ppm at the reactor's inlet) was fed at 200 °C catalyst bed temperature. The molar ratio of sulfate-to-ruthenium of 2.71 surmounted the ratios of preceding deactivation experiments. After this conditioning, SLW was gasified in exp. no. 17 at 400 °C with nearly 100 % carbon conversion. The procedure was repeated in exp. no. 18, where again water and sulfate were fed at a higher temperature of 290 °C. The effluent's electrical conductivity was measured (Schott pH-LF Handylab 12). The conductivity leveled off at 84  $\mu\text{S}/\text{cm}$  within 2.2 hrs after the response lag of the rig (see Figure 7.18), corresponding to the level of the sulfate feed solution. After having switched to feeding pure water, the conductivity dropped over a similar period of time. If sulfate bonded to the catalyst, a lower conductivity would be expected until saturation, followed by an increase of the conductivity to the level of the feed solution after saturation of the catalyst.



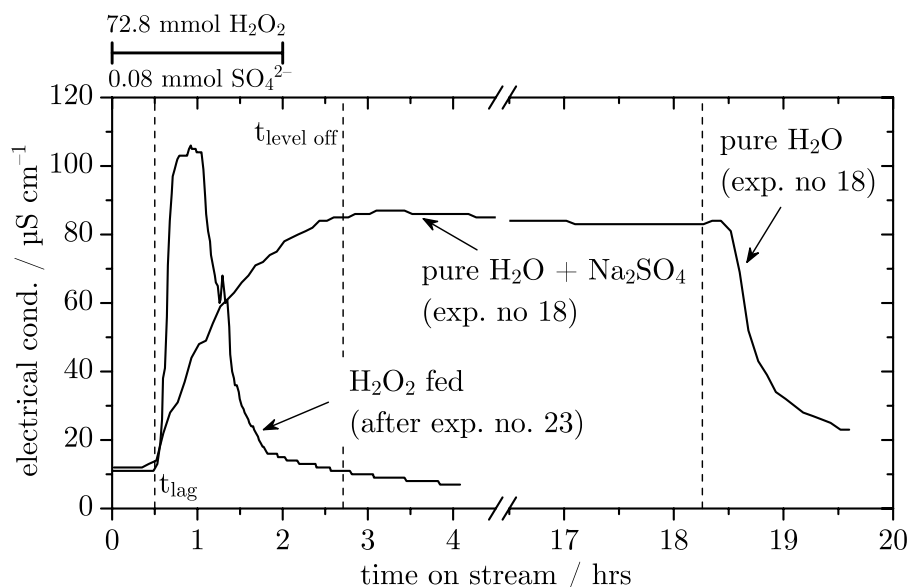


Figure 7.18: Measurement of the reactor effluent's electrical conductivity (after the cooler, at 25 °C) of experiment no. 18, where  $\text{Na}_2\text{SO}_4$  was fed (conc. 40 ppm), and of the catalyst regeneration experiment with  $\text{H}_2\text{O}_2$  (conc. 1 wt %).

After this sulfate-in-water conditioning at 290 °C, ethanol was gasified in experiments no. 20 – 23. The feed was changed to ethanol as the effluent is then a one phase mixture even at low conversions (in contrast to aqueous solutions of anisole, a major component of SLW). To monitor the progress of the deactivation, the temperature was, as in the previous campaign, periodically increased to 400 °C (with no sulfate fed, experiments no. 19, 21, and 23) where complete gasification is expected as long as the catalyst is fully active.

After gasification of ethanol + sulfate at 290 °C (exp. no. 20), no severe loss in catalytic activity was detected ( $X_C$  in exp. no. 21 still  $> 90\%$ ), although 1.63 times more sulfate was fed than ruthenium present. In experiment no. 23, however, the carbon conversion was significantly reduced ( $X_C$  around 20 %). The reason for this must be connected to the temperature inside the reactor: from exp. no. 20 to 22, the temperature was raised from 290 °C to 320 °C. It can be assumed that at 290 °C, biomass gasification did not take place ( $X_C$  after cool-down to 290 °C overnight  $\sim 5\%$ ), while at 320 °C, biomass conversion did indeed take place until the catalyst deactivated. The difference in activity can be estimated

from the initial level of conversion before complete cool-down of the reactor (55 % at 290 °C vs. 65 % at 320 °C). This behavior is shown in Figure 7.19.

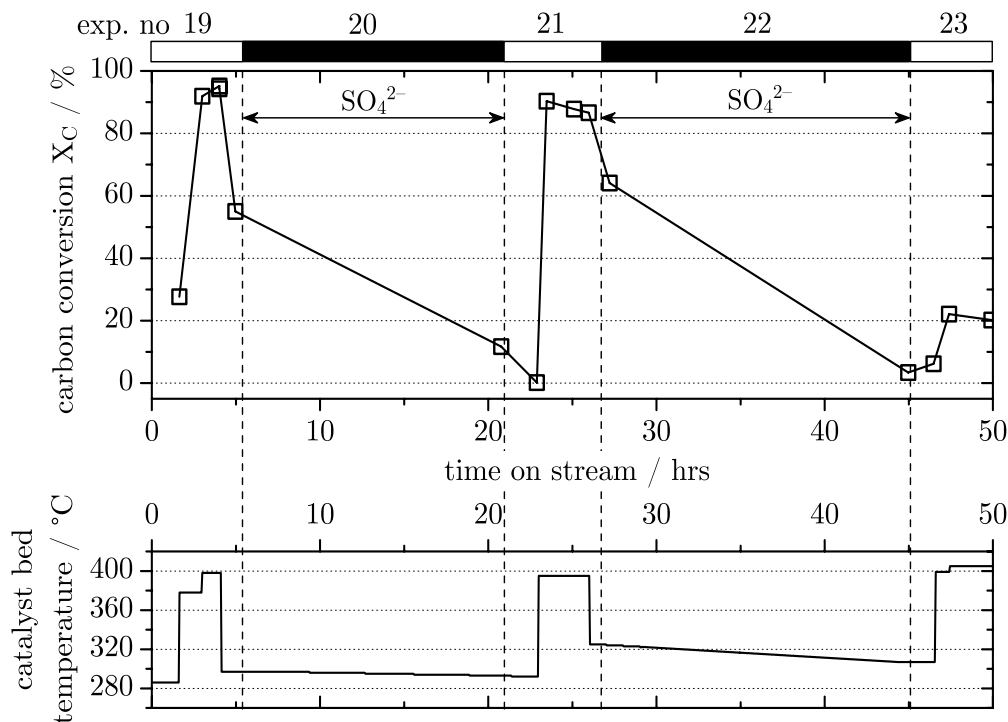
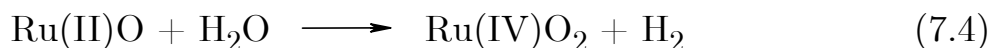
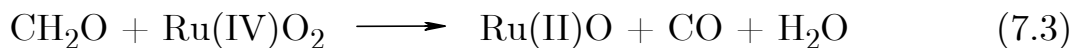


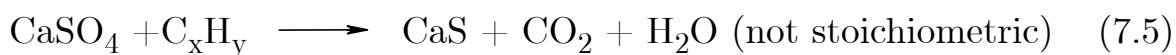
Figure 7.19: Carbon conversion (above) and average catalyst bed temperature (below) during experiments 19 – 23. After the first conditioning with sulfate at 290 °C, the conversion at 400 °C was still near complete. In contrast, catalyst deactivation took place after conditioning at 320 °C (exp. no. 22).

Biomass (here for simplicity CH<sub>2</sub>O) is assumed to be oxidized by reduction of Ru(IV) to Ru(II), as outlined in (7.3). Ru(II) is then re-oxidized to Ru(IV) by reduction of water to hydrogen (7.4) [25]:



As long as this postulated redox cycle is inactive (i.e. at low temperatures or in the absence of biomass as reducing agent), sulfate has no deactivating effect on the Ru/C catalyst. Ru is then present as Ru(IV), and sulfate

is not known to act as a ligand for Ru(IV). However, sulfate is known to form stable compounds with Ru(III) [189], which is expected to exist as an intermediate in the redox cycle. No evidence was found in the literature that Ru(II) does not form stable sulfate complexes such as  $\text{RuSO}_4$  as well. Another possible route is the reduction of sulfate to sulfide (e.g. catalyzed by the reactor's steel walls and the hydrogen that is produced by gasification, or reduced by the biomass itself). In a high temperature gasification system, there was recently evidence found at PSI that calcium sulfate could be reduced to calcium sulfide with biomass ( $\text{C}_x\text{H}_y$ ) as the reducing agent, according to (7.5) [190]:



It is not clear, however, if this reduction by 8 oxidation states from S(+6) to S(-2) can take place also in supercritical water, which itself is more of oxidative nature. Elliott et al. found similar poisoning of a ruthenium catalyst when processing waste water that contained residual amounts of sulfate [191], but they did not carry out systematic experiments as presented here. They suspected without experimental evidence that sulfate is reduced to sulfide which then poisoned the catalyst due to its strong interaction with ruthenium, which is also a conceivable mechanism. Kritzer summarized in a review on corrosion in high temperature and supercritical water that both sulfate might be reduced to sulfide, but also sulfide oxidized to sulfate in the hydrothermal environment, without stating process conditions or prerequisites where each pathway is favored [37].

Therefore, *in-situ* EXAFS experiments are planned at the Paul Scherrer Institut to study this mechanism in more detail, beyond the scope of this thesis. The current hypothesis is that the sulfate bonds irreversibly to Ru(III) and thereby interrupts the redox cycle, which deactivates the catalyst, or that sulfate is precedingly reduced to sulfide by either the biomass itself or evolving hydrogen, which then irreversibly bonds to Ru(II) with the same effect of interrupting its redox cycle.

### 7.2.7 Catalyst Regeneration with Hydrogen Peroxide Solution

To regenerate the catalyst, the sulfate–ruthenium<sup>8</sup> bond needs to be broken, and the sulfate has to be extracted from the system. Either a reductive or an oxidative treatment of the catalyst is conceivable. Here, the oxidative treatment was selected: an aqueous solution of hydrogen peroxide (conc. 1 wt %) was fed into the reactor with the completely deactivated catalyst at 30 MPa, at a temperature of 50 °C for 3 hrs, and 90 °C for an additional 3.3 hrs (in total 776 g solution fed, corresponding to 0.23 mol H<sub>2</sub>O<sub>2</sub>). The temperature was chosen low to prevent the oxidation of the carbon support and of the ruthenium to RuO<sub>4</sub>, which is volatile and would therefore be extracted out of the system. The electrical conductivity of the effluent was measured. It increased quickly to 105 μS/cm, and dropped back to below 20 μS/cm within one hour, as depicted in Figure 7.18 on page 209. This pulse-type response indicates that an ionic species had been released and carried out of the system. As the electrical conductivity dropped back to the baseline conductivity, the regeneration was assumed to be complete after ~2 hours. After three hours, the temperature was increased to 90 °C and the feeding prolonged for another 3.3 hrs to check for the release of more ionic species at higher oxidation temperatures, but the effluent's conductivity stayed below 10 μS/cm.

After this mild oxidation with diluted peroxide, the plant was flushed with water for 3 hrs. Then, ethanol (conc. 10 wt %) was fed at 400 °C to estimate the catalytic activity after the regeneration step. Initially, the carbon conversion was near 100 %, with the product gas close to the chemical equilibrium composition (68 vol % CH<sub>4</sub>, 28 vol % CO<sub>2</sub>, 4 vol % H<sub>2</sub>, no CO). Then, the carbon conversion steadily decreased to 80 % within 24 hrs at a WHSV of 7 hr<sup>-1</sup>. The product gas changed slightly in composition to 62 vol % CH<sub>4</sub>, 26 vol % CO<sub>2</sub>, 10 vol % H<sub>2</sub>, 1 vol % CO, and 0.5 vol % C<sub>2</sub>H<sub>6</sub>.

---

8. or sulfide-ruthenium-bond, depending on the actual sulfur species acting as catalyst poison.

It seems that after the initial regeneration, a slow re-deactivation took place. A possible reason could be that some of the sulfate was not completely washed off the catalyst, but stayed inside the porous matrix of the activated carbon. Therefore, sulfate was in the vicinity of the ruthenium sites and could quickly re-bond as soon as ethanol was gasified and the redox cycle again active.

### 7.2.8 Catalyst Characterization after Sulfate Deactivation and H<sub>2</sub>O<sub>2</sub>

#### Regeneration

To support the hypothesis of deactivation by a strong sulfate-ruthenium bond rather than any of the other hypothesized deactivation mechanisms, the catalyst was analyzed with various techniques, the results of which are presented here.

HAADF-STEM imaging was carried out at the Laboratory of Inorganic Chemistry at ETH Zurich for catalyst samples after experiment no. 5 (slight deactivation), 15 (full deactivation), and after the treatment with H<sub>2</sub>O<sub>2</sub>. Representative high-angular annular dark field scanning transmission electron microscopy images are shown in Figure 7.20 on page 214.

As the images were taken from several areas and different catalyst granules, they are assumed to be representative. As can be seen, the crystallite size distribution did not change with deactivation. It seems that by regeneration with hydrogen peroxide, the crystallites might have slightly grown, about 10 – 20 %. However, as the catalyst samples experienced different conditions during their campaigns, such a difference in size might not be a sole effect of the H<sub>2</sub>O<sub>2</sub> treatment. Most crystallites were 2 – 4 nm in size, while a few larger particles had diameters of up to 10 nm. Even though these images cannot explain the catalyst deactivation, they provide the visual proof that neither ruthenium leaching took place, nor severe sintering, which would have led to a loss in active metal surface area.

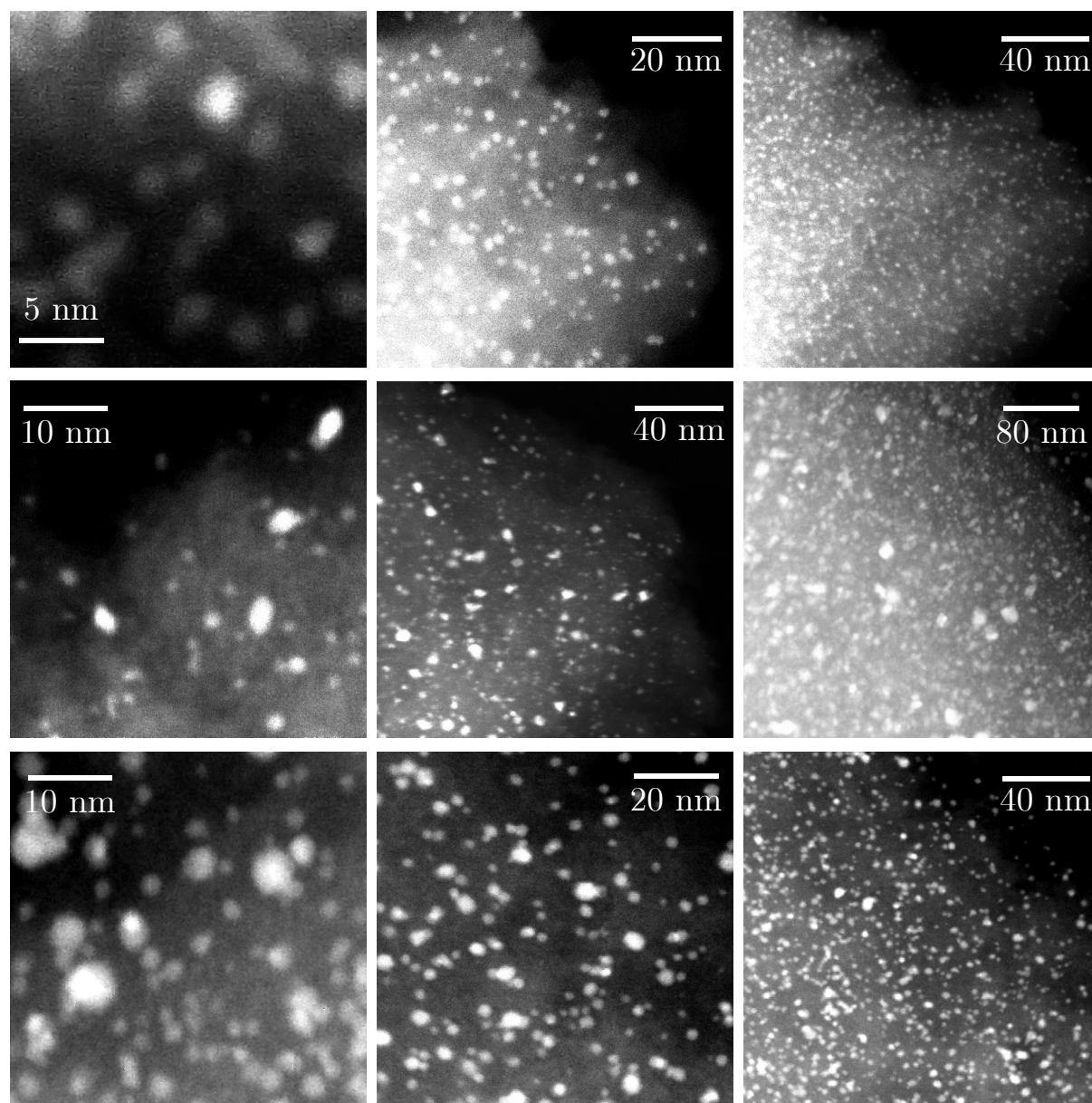


Figure 7.20: STEM images of 2 wt % Ru/C samples. Top row: Catalyst after exp. no. 5 (partly deactivated). Middle row: Catalyst after exp. no. 15 (fully deactivated). Bottom row: Catalyst after regeneration with H<sub>2</sub>O<sub>2</sub>.

In addition to the HAADF-STEM analysis, TEM imaging was conducted for catalyst samples after experiment no. 15. On these pictures, even the lattice layers of a ruthenium crystallite could be visualized, see Figure 7.21.

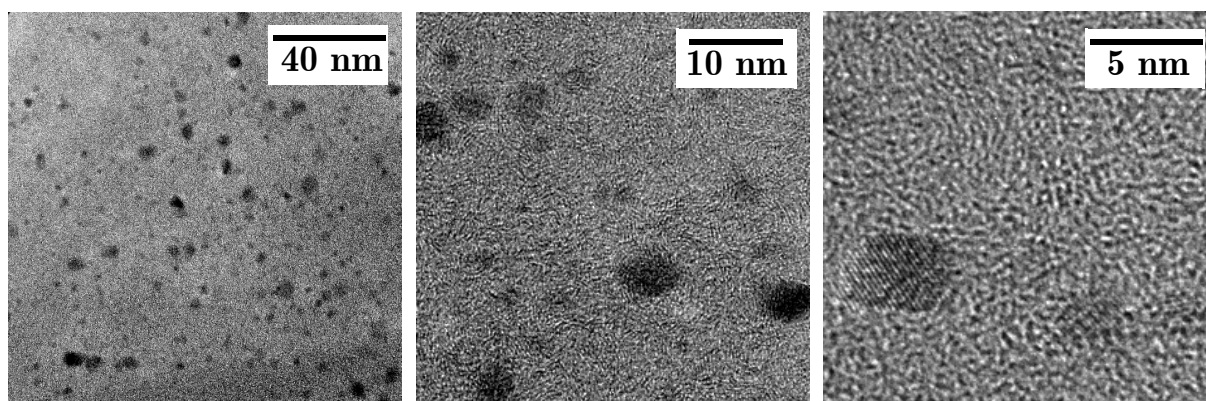


Figure 7.21: Transmission electron microscopy images of 2 wt % Ru/C after experiment no. 15. At the largest magnification, the lattice layers of a ruthenium crystallite are visible.

The catalyst samples were also examined with a stereo microscope (Leica Wild M3Z). The images show significant differences between fresh and used catalyst, depicted in Figure 7.22.

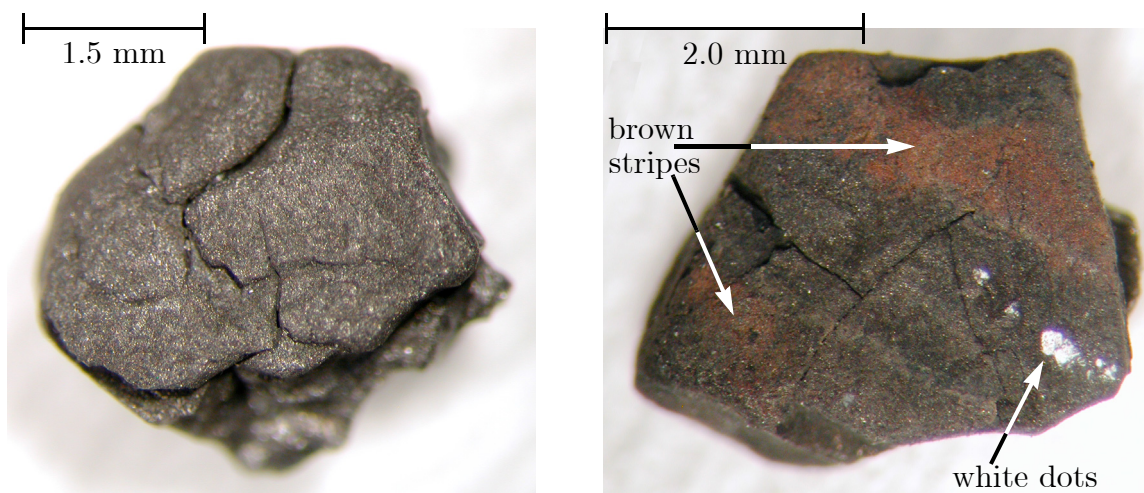


Figure 7.22: Microscope images of 2 wt % Ru/C. Left: fresh catalyst, shiny and glimmering. Right: used catalyst after exp. no. 8. The catalyst is matt, with brown stripes (iron oxide, EDXS) and white dots (aluminum oxide, EDXS).

The used catalyst had two brown stripes, white shiny dots on one corner, and was generally matt, whereas the fresh catalyst was glimmering and uniform in color. The stripes were later analyzed by EDXS as layers of corrosion products, and the white dots as areas of alumina, see

Figure 7.23. It is not clear whether these products have deposited out of dissolved species in the fluid phase during reaction, or whether they got there from direct contact with the walls of the reactor, or whether the corrosion products had been in dissolved form during the process and deposited only when the plant was stopped and the water evaporated (by pressure reduction at 400 °C). The alumina on the catalyst most probably originated from the  $\alpha$ - $\text{Al}_2\text{O}_3$  bed upstream of the Ru/C catalyst bed. While the Fe, Cu, Co, and Al signals were related to specific areas of the sample, the ruthenium was dispersed over the whole catalyst grain, as was expected (HAADF-STEM showed no severe sintering, thus the active metal should be evenly distributed over the whole sample). The sulfur signal, however, was also distributed over the whole sample. Therefore, it is likely that the sulfur species was either adsorbed on the carbon matrix of the catalyst, or bound to the ruthenium sites, both leading to a similar coverage as Ru. Elliott and co-workers showed EDXS analyses of a cleaved Ru/C pellet after subcritical gasification of manure slurries at 350 °C and 20 MPa in a series of tubular reactors [65]. In that application, both the ruthenium and the sulfur signal were distributed over the whole radius of the pellet, and both elements were surface enriched, indicating a strong correlation of the two (e.g. due to a chemical bond).

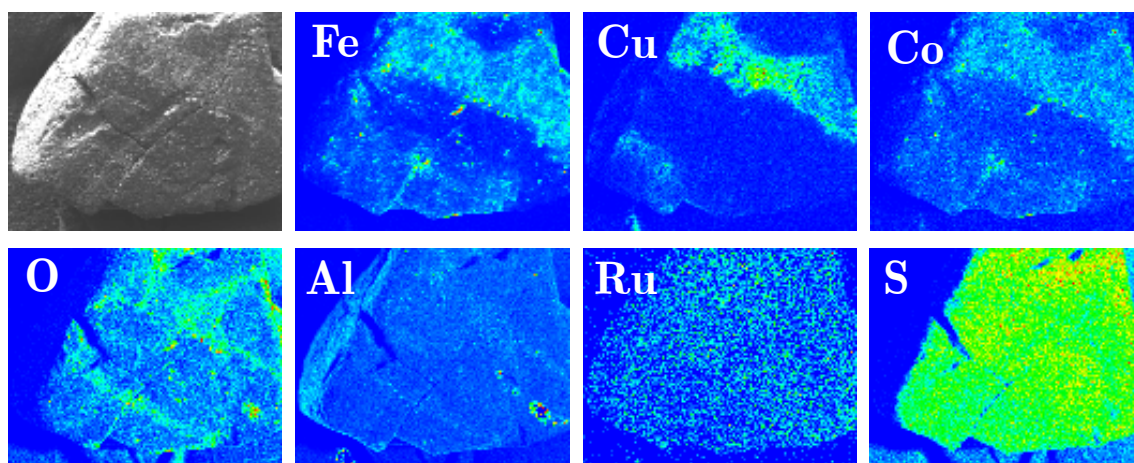


Figure 7.23: EDXS mapping of the Ru/C catalyst grain photographed in Figure 7.22 (after exp. no. 8). The brown stripes consisted of Fe, Cu, Co, and O (thus corrosion products), while the white dot in the lower right corner consisted of Al and O (likely  $\text{Al}_2\text{O}_3$ ). Ruthenium and sulfur were equally distributed over the whole grain.



The  $\alpha$ - $\text{Al}_2\text{O}_3$  beads from the layer upstream of the Ru/C catalyst bed showed some minor coverage with brownish stripes, as depicted in a photograph in Figure 7.24. The  $\alpha$ - $\text{Al}_2\text{O}_3$  beads from the layer downstream of the Ru/C bed, however, were covered with layers of black, hard material. Some particles showed even signs of pitting. By EDXS analysis, the predominating elements found on these particles were Fe (3.15 atom %) and Cu (0.26 atom %), besides the original material Al (34.88 atom %) and O (60.76 atom %). However, the SEM image of the  $\text{Al}_2\text{O}_3$  particle did not show any dark spots, and thus these dark spots are likely made of carbon dust (giving a much weaker signal than the heavier metals), originating from the carbon matrix of the catalyst (e.g. due to attrition in the catalyst bed; during the first experiments with Ru/C in the process demonstration unit, attrition of the carbon support was detected as well). This could explain why only the alumina particles downstream of the catalyst were covered with such a black layer, but not the ones upstream. These findings were also supported by XPS (see Table 7.9), where the black spots were identified as a mixture of carbon and different metal oxides, and the alumina bead downstream of the catalytic bed showed an increase in Fe and Cu.

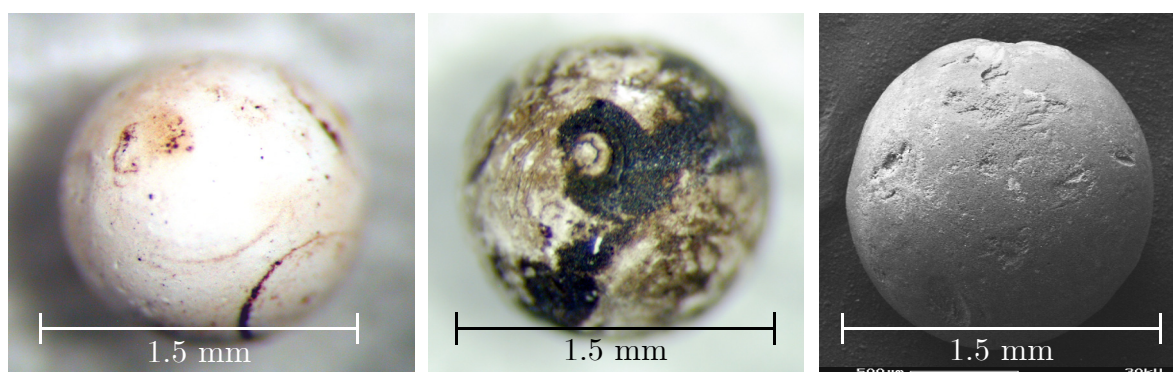


Figure 7.24: Microscope images (left, middle) and SEM image (right) of  $\alpha$ - $\text{Al}_2\text{O}_3$  beads from the reactor tube after exp. no. 8. Left: particle from the bed upstream of the Ru/C catalyst bed. Middle and right: particle from the bed downstream of the Ru/C catalyst bed.

As outlined before, iron was found on the alumina beads downstream of the Ru/C bed, but not upstream. Thus, biomass gasification (inside the

catalytic bed) seems to have an adverse effect on corrosion (e.g. due to the presence of H<sub>2</sub>, etc.). Otherwise, also the alumina beads upstream of the Ru/C would be covered with corrosion products, as also there, super-critical conditions were present.

Table 7.9: XPS analysis of a Ru/C catalyst grain and two  $\alpha$ -Al<sub>2</sub>O<sub>3</sub> beads upstream and downstream of the Ru/C catalyst bed after exp. no. 8.

element	$\alpha$ -Al <sub>2</sub> O <sub>3</sub> bead upstream	Ru/C grain	$\alpha$ -Al <sub>2</sub> O <sub>3</sub> bead downstream
	atom %	atom %	atom %
C <sub>1s</sub>	15.0 <sup>a</sup>	39.1	22.4 <sup>a</sup>
O <sub>1s</sub>	53.2	44.8	48.4
Al <sub>2p</sub>	28.3	5.7	20.1
Ru <sub>3d5/2</sub> / Ru <sub>3p3/2</sub>	0.4 <sup>b</sup>	0.2	0.5 <sup>b</sup>
S <sub>2p</sub>		0.8	
Fe <sub>2p3/2</sub>	1.0	7.8	3.7
Ni <sub>2p3/2</sub>	0.7	1.7	0.6
Cr <sub>2p3/2</sub>	0.8	N/D	1.3
Cu <sub>2p3/2</sub>	0.3	N/D	2.6
Zn <sub>2p3/2</sub>	0.4	N/D	0.3

a. The alumina beads were glued on an alumina sample holder with carbon tape, which possibly influenced the measurement.

b. As the sample upstream already seemed to contain Ru, this quantification is considered to be affected with some error.

SEM/EDXS analysis was carried out for Ru/C catalyst samples after exp. no. 8, 15, and after the H<sub>2</sub>O<sub>2</sub> treatment. The catalyst sample after exp. no. 8 (deactivated after sulfate feeding) was covered with corrosion products, depicted in Figure 7.25. The coverage was similar to the catalyst sample after 220 hrs of hydrothermal gasification, where no sulfate had been deliberately added to the feed yet (compare to Figure 7.12 on page 190).

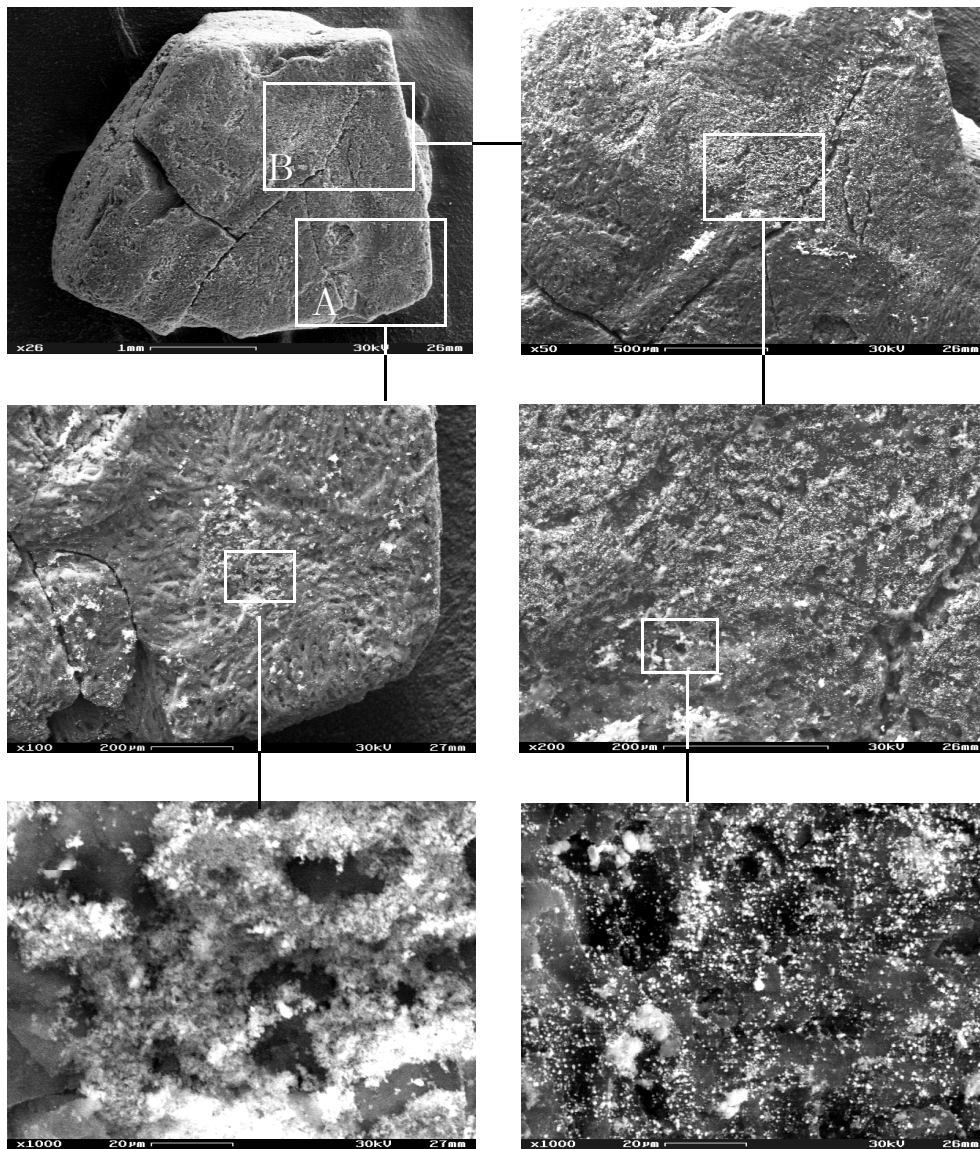


Figure 7.25: SEM images of the used Ru/C catalyst after exp. no. 8. The white dots in area A (left column) were identified by EDXS as aluminum and oxygen (thus likely  $\text{Al}_2\text{O}_3$ ), while area B (right column, brown stripes) showed various deposits of corrosion products.

However, on the sample after exp. no. 8, neither nitrogen nor phosphorus were found (most probably because the ion exchanger of the water purifier had been exchanged). Many small dots of  $\sim 1 \mu\text{m}$ , and larger sites of  $\sim 10 \mu\text{m}$  were detected, consisting of Fe, Ni, Al, and Cu. It is probable that the catalyst after 220 hrs of gasification depicted in Figure 7.12 on page 190 was covered with a comparable layer like this specimen after exp. no. 8, but on top of that, it was additionally clogged with P and N,

which masked the layer below. Taking this into account, both catalyst samples were covered with similar layers of corrosion products, and these products could not be responsible for the deactivation, as one catalyst was still active, while the other was deactivated. As a matter of fact, the active catalyst was more severely covered than the deactivated one. Besides, it is assumed that the corrosion products stuck only on the outer surface, but not within the pores of the carbon matrix, where they could lead to a physical blockage of the ruthenium sites that are inside the pores. The majority of the ruthenium sites, however, lies on the outer shell of the catalyst [179], as sketched in Figure 7.26. Otherwise, the pores (determined to be of an average size of 1.9 nm by nitrogen adsorption) would be easily blocked by ruthenium crystallite growth within the pores from 1 to 3 nm (as depicted by HAADF-STEM), and the catalyst would lose its activity much faster, independent of sulfate addition to the feed.

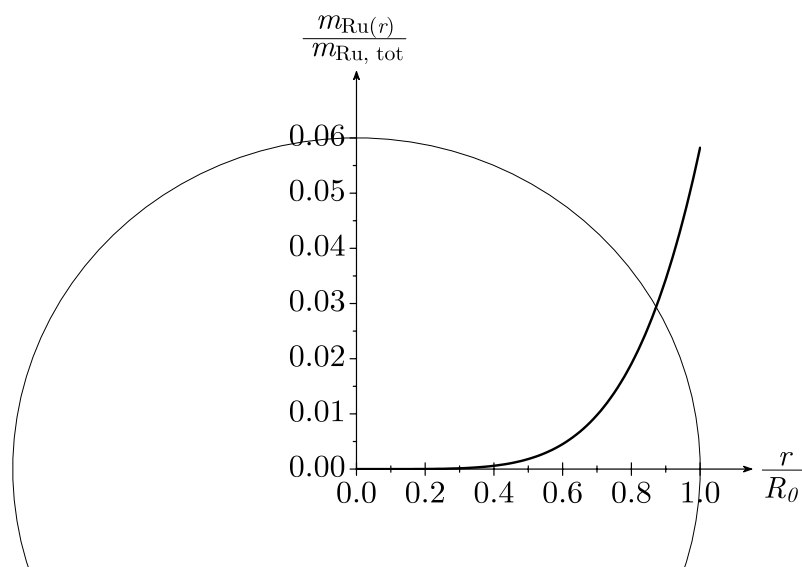


Figure 7.26: Qualitative location of the ruthenium over a Ru/C catalyst grain.

More importantly, apart from these corrosion products, an increase in sulfur content was detected from fresh catalyst to the catalyst after 220 hrs of hydrothermal gasification, to the ones recovered after the sulfate deactivation exp. no. 8 and 15, as depicted in Table 7.10 (determined both with EDXS and ICP). Thus, the sulfur species indeed did interact with

the catalyst. The ICP data produced huge scatter and showed signs of systematic errors or sulfur contamination from one sample to the other. Moreover, the chemical digestion method prior to analysis might need to be revised. Therefore, the conclusions were primarily drawn from the EDXS analysis.

Table 7.10: Measurement of the S/Ru ratio with EDXS averaging and ICP.

catalyst (2 wt % Ru/C)	status	EDXS <sup>a</sup>	ICP	ICP	ICP
		S/Ru (molar)	S/Ru (molar)	Ru wt %	S wt %
fresh	active	0.06	246±99 <sup>b</sup>	0.55±0.06 <sup>b</sup>	5.89±0.42 <sup>b</sup>
220 hrs hydrothermal gasification (no SO <sub>4</sub> <sup>2-</sup> added)	deactivated	0.19	25.06 <sup>b</sup>	1.99 <sup>b</sup>	15.80 <sup>b</sup>
after exp. no. 8 ( $n_{\text{SO}_4^{2-},\text{fed}}/n_{\text{Ru}} = 0.83$ )	deactivated	0.91	0.51	2.68	0.44
after exp. no. 15 ( $n_{\text{SO}_4^{2-},\text{fed}}/n_{\text{Ru}} = 1.12$ )	deactivated	1.00	13.71 <sup>b</sup>	1.79 <sup>b</sup>	7.76 <sup>b</sup>
after H <sub>2</sub> O <sub>2</sub> treatment	reactivated	0.30	0.29	2.73	0.25

- a. averaged with reference spectra over a representative area of the catalyst grain (ca. 250 × 150 μm).
- b. The ICP measurement produced huge scatter, and these values need to be reconfirmed. From the original ICP data, a sulfur contamination of the device is probable: after one sample, the Ru content of all succeeding samples was very low, and the S content very high. Also the chemical digestion method prior to analysis might need to be revised.

The fresh catalyst already contained some traces of sulfur, stemming most likely from the carbon support. After 220 hrs of hydrothermal gasification of synthetic liquefied wood, the ratio of sulfur-to-ruthenium had increased to ~0.2 (by EDXS analysis), probably due to the trace sulfate present in formic acid. After exp. no. 8, where a molar ratio of 0.83 SO<sub>4</sub><sup>2-</sup> per ruthenium had been fed, the molar S/Ru ratio determined by EDXS was ~0.9, or ~0.5 by ICP, or even 4 by XPS (see Table 7.9 on page 218). Assuming some loss of dispersion due to the sintering described before (e.g. only 30 % of the ruthenium contributed to the active metal surface

area), every ruthenium surface site was blocked by sulfate, and the catalyst had become deactivated. These findings support the hypothesis that the redox cycle was interrupted due to the bonding of the sulfate to the active sites, or the sulfide, which ever is the sulfur species that is present *in-situ*. By XPS analysis, the sulfur species on the catalyst corresponded to sulfate. However, this cannot be judged as clear indication for sulfate being the actual poisoning species, as after the unloading of the catalyst, sulfide could have been re-oxidized to sulfate, as the samples were exposed to air before analysis; then, the sulfur species detected by XPS would correspond to sulfate, even if *in-situ*, the deactivating agent was sulfide, instead of sulfate.

The molar S/Ru ratio after the H<sub>2</sub>O<sub>2</sub> regeneration step was significantly reduced, indicating that the method had worked. However, there was still more sulfur on the catalyst than on fresh or 220 hrs hydrothermally used Ru/C, indicating that the regeneration step was not complete, which could explain the slow decrease in catalytic performance from 100 % carbon conversion towards 80 % when gasifying ethanol after the hydrogen peroxide treatment.

While the EDXS mapping of the deactivated catalyst after exp. no. 8 (Figure 7.23 on page 216) showed a clear overlap of the Ru and S signal, this correlation could not be found for the regenerated catalyst, see Figure 7.27 below, which is another indication that much of the sulfate was extracted from the system. The so called bulb of penetration of the electrons shot onto the sample to produce the SEM image and the EDXS analysis is about 30 – 50 μm deep at 30 kV; thus the amount determined by EDXS originates from the outer shell of the catalyst. As the molar S/Ru ratio determined by EDXS and ICP is ~0.3 for the regenerated catalyst by both methods, it seems that the sulfur left on this species originated from the outer shell. To clarify this assumption, a catalyst grain could be cut in halves (difficult as carbon from coconut shell is extremely hard), glued into a sample holder and polished, which was not deemed necessary for the scope of this analysis.

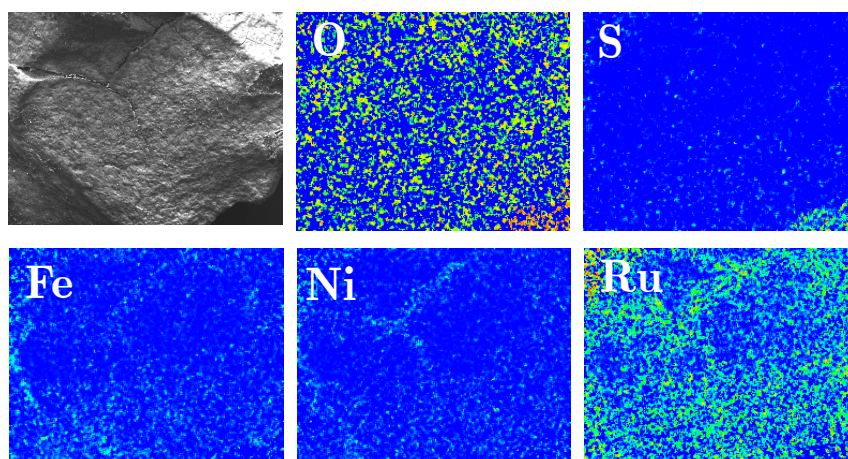


Figure 7.27: EDXS mapping of a 2 wt % Ru/C catalyst grain after deactivation by  $\text{SO}_4^{2-}$  (in exp. no. 19 – 23), followed by  $\text{H}_2\text{O}_2$  treatment. The sulfur signal in the lower right corner is a measurement artifact, as there was no catalyst surface (see upper left image).

### 7.2.9 Conclusions

- The results presented here are consistent with the redox mechanism for biomass gasification postulated by Park and Tomiyasu [25].
- The tolerance of the 2 wt % Ru/C catalyst towards sulfate was rather low. The hypothesis of catalyst deactivation due to the formation of a stable ruthenium sulfate complex, most probably with Ru(III), or a stable ruthenium sulfide complex, and not due to physical blockage by precipitation of  $\text{Na}_2\text{SO}_4(\text{s})$ , was consistent with the experimental evidence.
- Catalyst characterization with ICP, HAADF-STEM, and SEM-EDXS supported the proposed deactivation mechanism (hypothesis (iv)).
- To clarify the exact mechanism of deactivation with identification of the oxidation states of the interacting species involved, i.e. sulfate vs. sulfide, *in-situ* EXAFS experiments would be needed.





# Chapter 8: Process Demonstration Unit (PDU)

## 8.1 Introduction

The batch reactor system was suitable and sufficient for carrying out experiments with real biomass slurries as feed (chapter 6). However, the setup was not designed for long term studies, and typical feed amounts were very small.

The continuously operating catalyst test rig could be used to test catalysts for their stability and activity in the hydrothermal environment over extended periods of time (chapter 7). However, only liquid biomass model substances could be used as feed. Ideally, a plant should be capable of running continuously and process real biomass slurries. Therefore, a process demonstration unit (PDU) was built. There, the biomass is pumped to high pressure, liquefied in a liquefaction unit, freed from its inorganic constituents in a reverse-flow vessel, the so called “salt separator”, and gasified in a catalytic reactor. Then, the product phases should be separated, ideally under pressure, in order to take advantage of the high solubility of carbon dioxide in water.

The basic requirements for this laboratory scale process demonstration unit were:

- Small throughputs, 0.5 – 1 kg/hr, up to a pressure of 35 MPa (which leads to a gas production of ~200 L/hr for a feed concentration of 20 wt %, or ~400 L/hr for 40 wt %, respectively).

- Liquefaction of the feed should be on a continuous basis (no pre-liquefaction and storage)
- Incorporated salt separation
- 120 hrs experiment possible (“long-term” test)
- Continuous on-line gas sampling
- Incorporated option for liquid high-temperature sampling (e.g. upstream and downstream of the salt separator)

A basic block diagram of the process is depicted in Figure 8.1.

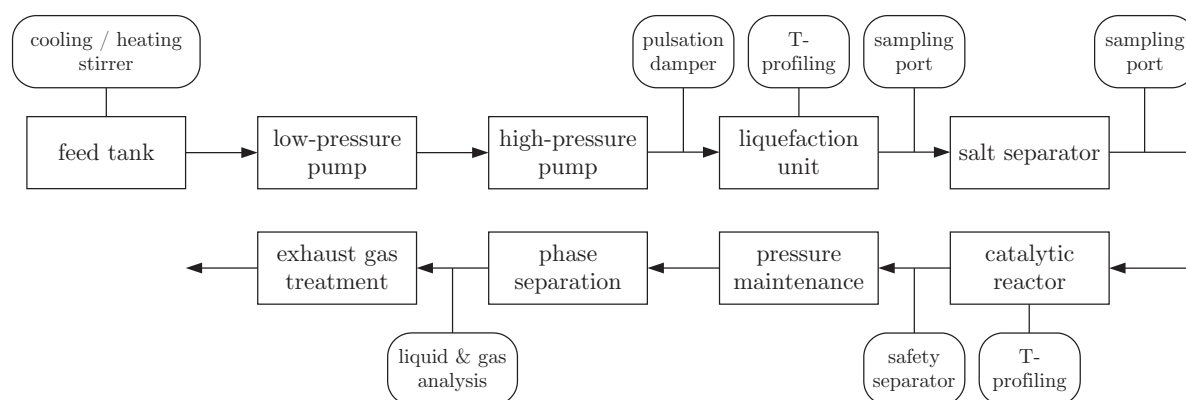


Figure 8.1: Basic block diagram of the process demonstration unit.

The most critical parts of such a plant are the pump (it turned out to be a real challenge to find a suitable pump on the laboratory scale), the salt separating vessel, and the exhaust gas treatment (initially, the safety policy required a catalytic oxidation reactor to convert all gas to  $\text{CO}_2$  and  $\text{H}_2\text{O}$  in contrast to a simple torch). At the beginning of the project, wood and manure slurries were typical target biomass types, selected for their abundant nature in Switzerland. Based on these considerations, spruce and fir liquefaction was studied in the batch reactor, with the goal to bracket suitable conditions and residence times to dimension the liquefaction unit of the PDU (presented in section 8.2). However, due to prolonged problems with the pumps (outlined in section 8.4), the feed had to be replaced by a liquid in the course of the project (i.e. ethanol for start-

ing experiments of the plant, and palm oil pyrolysis condensate for the actual process demonstration, as soon as the basic operability of the plant is ensured).

For the salt separating vessel, the reverse flow principle was selected, which was invented by Modar, Inc., USA, for an SCWO (supercritical water oxidation) application [192]. This system was preferred because preliminary experiments with this type had already been carried out [30].

A fixed bed system was chosen for the reactor due to its low cost and simplicity. The experience gained in the continuously operating catalyst test rig (100 % conversion of SLW at 20 wt % at a WHSV of  $20 \text{ hr}^{-1}$  over Ru/C) was used to dimension the reactor. As hydrolyzed biomass is expected to be harder to gasify (outlined in section 6.5), the maximum WHSV was assumed to be lower than  $20 \text{ hr}^{-1}$  as with SLW. It was chosen well low enough, i.e.  $4 \text{ hr}^{-1}$ ; it could then still be increased by diluting the catalytic bed with  $\alpha\text{-Al}_2\text{O}_3$ . For a mass flow rate of 1 kg/hr (assuming  $\rho=1.0 \text{ kg/dm}^3$ ), 50 g Ru/C<sub>dry</sub> are required. The moist catalyst has a measured bulk density of  $0.74 \text{ kg/dm}^3$ . Thus, for a reactor tube (i.d. = 12 mm) with a concentric thermowell (o.d. = 3 mm), the catalyst bed has to be 105 cm long. As the upper and lowest part of the tube could not be easily heated, a tube length of 135 cm was selected, with 15 cm of non-heated sections on both ends.

In larger applications, monoliths are preferable, as they are less susceptible to plugging, but they require an advanced coating technology for the selected catalyst (stability in the hydrothermal environment). A continuously stirred tank reactor, CSTR, is also conceivable, where the catalyst could be placed in a basket. However, due to the residence time distribution in a CSTR, secondary coking of tar-precursor molecules (i.e. polyphenols) might occur, if they spend too much time inside the vessel. A supercritical fluidized bed as targeted in micro-reactors by Potic et al. is still far from an application stage [76].

## 8.2 Experiments to Identify Suitable Conditions for the Non-Catalytic Liquefaction of Wood (Batch Reactor)

### 8.2.1 Starting Point and Aim of The Experiments

There are several reports describing (non-catalytic) liquefaction of biomass [87, 91-93, 105, 171-173, 193, 194]. One problem for the comparison of these reports is that either the pressure level is different (possibly operating in the steam region rather than in a condensed phase), or the biomass itself is of another nature. Thus, the liquefaction problem had to be tackled in own experiments, carried out in the batch reactor system.

The experiments were conducted at a time when the goal was still to feed wet-milled spruce slurries into the process demonstration unit. At a later stage of the project, it turned out that our pumping system was not able to handle wood-containing slurries. Nevertheless, a crucial experiment showed that liquefaction and gasification can be carried out in two separate consecutive steps, leading to near complete gasification of the wood (up to then, liquefaction and gasification had been carried out in one step, in presence of a skeletal nickel catalyst).

To reach the desired pressure of  $\sim 30$  MPa, a larger amount of argon (10 MPa) than for the wood gasification experiments described in chapter 6 had to be pressed into the reactor prior to heat-up. During liquefaction, there should ideally no gas be formed that would then additionally contribute to the pressure evolution.

Two phases of the experiments could be distinguished:

- heat up phase: the time from the immersion of the reactor into the preheated sandbath until the reaching of the desired temperature. Typical heat-up times were  $\sim 6$  minutes.
- holding phase: as soon as the desired temperature was reached, the holding time started. Three holding times were applied: 0, 10, or 20 minutes. After this, the reactor was quenched to room temperature in the water bath.

### 8.2.2 Experimental Details and General Observations

A total of 12 experiments were carried out ( $w_{\text{wood}} = 10 \text{ wt } \%$ ). The corresponding experimental conditions are displayed in Table 8.1. For two experiments, zinc oxide was added ( $m_{\text{ZnO}}/m_{\text{wood}} = 1.4$ ) to test its influence on the liquefaction of wood. In previous experiments at PSI, the addition of zinc oxide to manure yielded very little solid residues [195]. As a consequence, it was concluded that ZnO could act as a liquefaction catalyst.

Table 8.1: Conditions of wood liquefaction experiments carried out in the batch reactor.

run no.	$T_{\text{max.}}$ °C	heat-up time min.	holding time min.	additive	GE %	LE %
HB240V01	240	6	120	–	5.2	13
HB300V02	300	7	10	–	3.8	42
HB300V03	300	8	23	–	6.5	33
HB315V01	315	8	10	–	8.4	35
HB330V01	330	8	13	–	11.1	29
HB330V02	330	10	4	–	5.4	51
HB330V03	330	10	21	–	4.5	34
HB350V01	350	6	0	–	5.1	56
HB350V02	350	6	7	–	8.9	52
HB330Z01	330	9	12	ZnO	12.4	59
HB400Z01	400	10	40	ZnO	8.7	53
HB330/400R01	330/400 <sup>a</sup>	8/11	13/19	–/RaNi <sup>b</sup>	6.2/84	N/A

a. 330 °C during non-catalytic liquefaction, 400 °C during catalytic gasification.

b. Raney nickel 2800/Ru (GraceDavison).

Ideally, most of the organic carbon should be liquefied and then collected either in the aqueous phase (as dissolved organic carbon), or in the methanolic phase (as gasifiable tarry compounds) at the end of the experi-

ment. As a measure for this quantity, the carbon liquefaction efficiency LE was introduced:

$$\text{LE} = \frac{n_{\text{C, H}_2\text{O}} + n_{\text{C, tars}}}{n_{\text{C, feed}}} \quad (8.1)$$

A problem herewith is that polyphenols tend to solidify at temperatures lower than  $\sim 80$  °C. Hence, in a real, continuous process, these substances would be present in the liquid form, they could pass the salt separator and enter the catalytic reactor, where they would be gasified. In the batch reactor, however, they solidify during the quenching procedure at the end of the experiment, are dissolved in methanol during the recovery and accounted for in the methanol soluble fraction (i.e. tars after evaporation of the methanol). Similar values of LE were reported by Yilgin and Pehlivan, who liquefied poplar wood in presence of formic acid [92]. They received almost 40 % of gas, however (possibly due to decomposition of the formic acid).

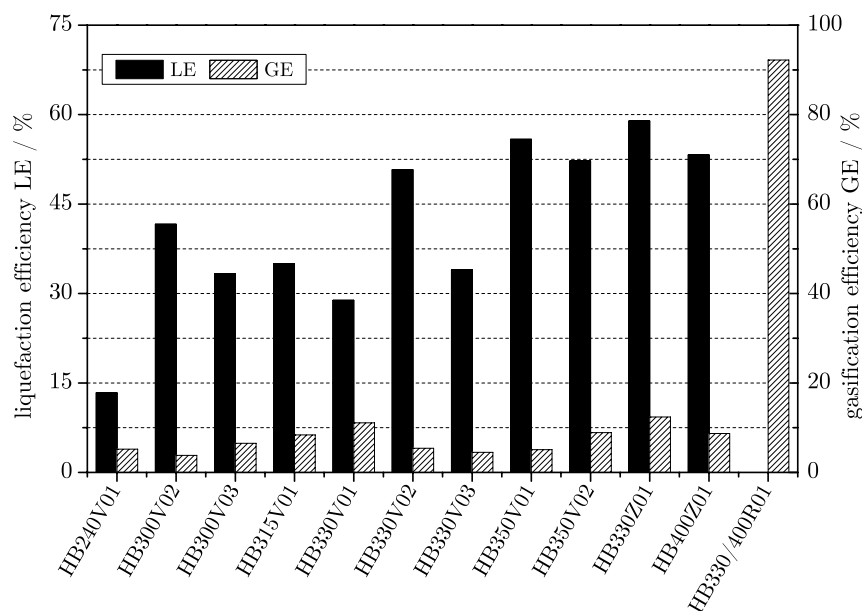


Figure 8.2: Liquefaction efficiency (LE, black bars, left y-axis) and gasification efficiency (GE, striped bars, right y-axis) of the wood liquefaction experiments.

Table 8.2: Visual description of the product phases after the liquefaction of wood slurry in the batch reactor.

run no.	aqueous residue	MeOH fraction	solid residue
HB240V01	transparent, golden-yellow	light yellow	dark brown, no black spots, clumped to chunks
HB300V02	inhomogeneous, dark yellow	very dark, yellow greenish	light brown, homogeneous, fine
HB300V03	inhomogeneous, dark yellow	more transparent, reddish	slightly darker, homogeneous, fine
HB315V01	brownish, reddish, fine particles	milky, dark, reddish	brown olive, soft, blackened spots
HB330V01	yellow, dark particles suspended	dark, yellow green, fine particles	brown olive, soft powder
HB330V02	copper, light brown particles	milky brown, dark particles	brown olive, soft powder
HB330V03	yellow, dark particles suspended	dark yellow green, fine particles	brown olive, soft powder
HB350V01	copper, fine particles suspended	dark brown	very fine, black shiny powder
HB350V02	copper, fine particles suspended	dark brown	dark brown and black chunks
HB330Z01	brown, golden, transparent	dark brown	whitish, green olive with brown spots
HB400Z01	yellow	light brown	whitish, greyish
HB330/400R01	clear, transparent	clear, transparent	catalyst (grey) with dark spots

A description of the visual observations of the product phases is displayed in Table 8.2. At 240 °C, virtually no liquefaction took place despite the long holding time, but approximately 5 % of the feed carbon were gasified to CO<sub>2</sub>. The liquefaction and gasification efficiency for the individual experiments are depicted in Figure 8.2. The carbon content in the residual aqueous phase was around 8 g/L in almost all experiments (exceptions: at 240 °C, it was below 2 g/L and with ZnO at 330 °C, it was 11

g/L, indicating the activity of zinc oxide as liquefaction catalyst). Differences in LE were mostly due to an increased or decreased amount of tarry substances. The amount of carbon in the solid fraction was between 30 % and 12 % of the feed carbon in the non-catalytic experiments (best values at 350 °C), or around 8 % with ZnO. These results are better than in experiments reported in the literature for non-catalytic liquefaction at 350 °C by Fang et al. (57 %) [105], or by Karagöz and co-workers (42 %) [91]. However, with the addition of potassium carbonate, Karagöz could reduce the solid residue to as little as 4 %.

The carbon content of the solid residue and the tars increased with temperature and residence time, from ~50 to over 70 %, indicating that either secondary polymerization took place, or more phenolic compounds with a higher C/H and C/O ratio were liquefied. Similar findings are reported by Minowa et al., who liquefied cellulose in the presence of sodium carbonate [173]. They found that the C/H ratio was increased from 0.56 in cellulose to 1.1 in the solid residue, and C/O was even increased from 1 in cellulose to 5 in the solid residue.

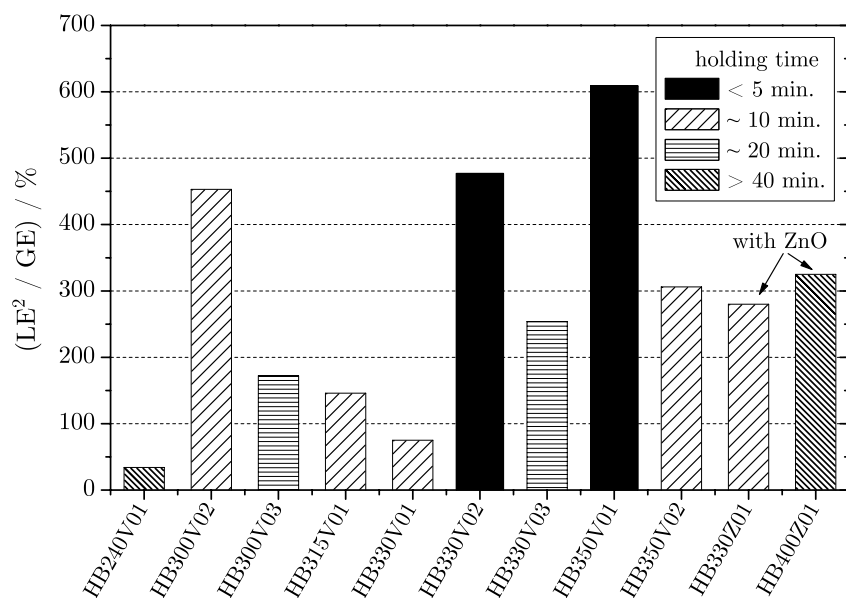


Figure 8.3: Weighted liquefaction to gasification ratio  $LE^2/GE$  of the wood liquefaction experiments.



Generally, the liquefaction efficiency in the experiments was larger at higher temperatures, but then also more carbon gasified, which is undesirable. Thus, the ratio of liquefaction efficiency to gasification efficiency,  $LE/GE$ , is a suitable measure to quantify this trade-off. As the actual target quantity was the liquefaction of the wood,  $LE/GE$  was weighted with the liquefaction efficiency itself, i.e.  $LE^2/GE$  was the measure of choice to quantitatively describe the quality of liquefaction. It is displayed in Figure 8.3.

The product gas was typically composed of more than 90 vol %  $CO_2$ , and about 5 to 10 vol %  $CO$ , except for the experiments with  $ZnO$ , where at 330 °C, 4 vol %  $CO$  and 2 vol %  $CH_4$  were formed, and at 400 °C, 6 vol %  $CO$ , 10 vol %  $CH_4$  and 19 vol %  $H_2$  were formed. Zinc oxide thus not only acted as a liquefaction catalyst, but also enhanced the gasification of the feedstock.

As can be seen in Figure 8.3, short residence times (accompanied by large heat-up rates) are favorable for the liquefaction of wood, which is in agreement with literature reports [88]. However, at 350 °C, where  $LE^2/GE$  is maximized, the solid residue was black and shiny (compare Table 8.2), which is an indication of the formation of char. It is not clear whether the char would be properly gasified when carried into the catalytic reactor in the real process, or whether it would be separated from the fluidic phase in the salt separator, together with the salt brine. Thus, a temperature between 330 and 350 °C should be chosen, and the quality of liquefaction should be verified in the process demonstration unit by high-temperature sampling (minimum 90 °C, to avoid the solidification problem). As outlined in section 6.4.3, the mixing inside the batch reactor is not guaranteed by free convection, as was previously assumed. Moreover, the feed could segregate to an aqueous phase and a solid phase (see Figure 8.4 on page 239). The wood which was in direct contact with the reactor's walls might preferentially form char when not readily solubilized by water. Thus, the results can be largely affected by mass transfer limitations (e.g. leading to more char for longer residence times). The liquefaction experiments should therefore be repeated in a stirred vessel to exclude the effect of unsatisfactory mixing, if more data is needed.

The addition of zinc oxide led to higher values of LE. However, if added to the milled wood for an improved liquefaction behavior, ZnO would probably be separated out of the system in the salt separator, and would contaminate the salt brine. Additionally, the biomass-ZnO-mixture was very sticky, and also the residues after liquefaction were very clammy. As a consequence, it was quite difficult to retrieve them out of the reactor. However, used as a fixed bed catalyst with larger particle size, or coated onto a monolith, the addition of zinc oxide is feasible due to its favorable nature for liquefaction, as long as plugging problems can be avoided.

### 8.2.3 Successful Liquefaction with Subsequent Gasification

A crucial experiment was HB330/400R01: it confirmed the possibility to carry out liquefaction and gasification in two separate steps, as it will be done in a continuously operating plant using real biomass slurries as feed. Up to this run, all gasification experiments were carried out by heating biomass in presence of a gasification catalyst (such as Raney Ni 2800), and simultaneously gasifying it to SNG.

In HB330/400R01, wood (conc. 10 wt %) was loaded into the batch reactor and liquefied at 330 °C, by applying the same procedure as in HB330V01 (8 min. heat-up, 14 min. holding time). After this liquefaction stage, the reactor was quenched and depressurized (about 6 % of the initial carbon was gasified to CO<sub>2</sub>), and Raney Ni 2800/Ru (Grace Davison, 0.25 wt % Ru) was added to the reactor content ( $m_{\text{cat.}}/m_{\text{wood}} = 1$ ).

The previously liquefied wood was then successfully gasified ( $t_{(T < T_c)} = 9$  min.,  $t_{(T > T_c)} = 21$  min.). The residual carbon content in the aqueous phase was very low (0.36 g/L), the methanolic phase was free from tars, and the solid fraction at the end of the experiment was low in carbon (6.2 % of the initial carbon of the wood). The gasification efficiency was 84 %, or more than 90 % if the carbon dioxide formed during the liquefaction step is accounted for as well.

The product gas composition was very close to the composition obtained when wood was gasified in one step, without the quenching after the liquefaction (1 vol % more H<sub>2</sub>): 39 vol % CO<sub>2</sub>, 45 vol % CH<sub>4</sub>, and 16

vol % H<sub>2</sub>, with no CO detected. Hence, the liquefaction can be carried out non-catalytically, with subsequent catalytic gasification. The yielded gas is very similar to the gas composition received from the one step process.

#### 8.2.4 Basic Dimensioning of a Preheater for the Liquefaction in the PDU

For a process demonstration unit, the preheater should be built as simple as possible. The simplest system is an electrically heated and insulated pipe, where the biomass is heated while flowing through. On the way from the inlet to the outlet of this preheater, the biomass' temperature will increase, and its viscosity and density decrease. Thus, the volumetric flow rate will increase along the pipe, and its residence time for a given pipe length will decrease. Given the mass flow rate  $\dot{m}$  and total time  $t_{\text{tot}}$  from the inlet to the outlet of the preheater ( $t_{\text{tot}} = t_{\text{heat}} + t_{\text{hold}}$ ,  $t_{\text{heat}} =$  time to heat the fluid to the desired temperature  $T_{\text{end}}$ , and  $t_{\text{hold}} =$  residence time at  $T_{\text{end}}$ ), the length  $L$  of the pipe can be calculated as follows:

$$L = L_{\text{heat}} + L_{\text{hold}} = \frac{4 \cdot \dot{m}}{d_i^2 \cdot \pi \cdot \varepsilon} \left( \int_{t=0}^{t=t_{\text{heat}}} \frac{1}{\rho(T(t))} dt + \frac{t_{\text{hold}}}{\rho(T_{\text{end}})} \right) \quad (8.2)$$

with  $d_i$  the internal diameter of the pipe,  $\rho(T)$  the density of the fluid as a function of temperature (and hence of time, via  $T = f(t)$ ), and  $\varepsilon$  the void fraction of the preheater (1.0 for an empty pipe, 0.85 to 0.9 if static mixing elements are used). As a first estimation for the length of such a preheater, the following assumptions were made:

- (i) The initial density of the feed at room temperature is 900 kg/m, hence  $\rho(25 \text{ }^\circ\text{C}) = 0.9 \cdot \rho_{\text{water}}(25 \text{ }^\circ\text{C})$ . The density of the mixture is assumed to behave at all temperatures as  $\rho(T) = 0.9 \cdot \rho_{\text{water}}(T)$ . All data are calculated at 30 MPa.
- (ii) The desired heating temperature is  $T_{\text{end}} = 350 \text{ }^\circ\text{C}$ .

- (iii) The biomass is assumed to be heated from 25 °C to  $T_{\text{end}}$  within 5 minutes ( $t_{\text{heat}} = 300$  sec, temperature ramp linear in time, i.e.  $T(t) = (T_{\text{end}} - 25) \cdot t / t_{\text{heat}}$ ), and then to be held at  $T_{\text{end}}$  for 2 minutes ( $t_{\text{hold}} = 120$  sec), after which it leaves the preheater. Thus,  $t_{\text{tot}} = 7$  min.
- (iv) The inner tube diameter is 12 mm, as most tubular units used in the PDU are made of this size.

Based on these assumptions, the length of the preheater is 1.45 m for an empty tube, or 1.65 m for a tube with static mixing elements ( $\varepsilon = 0.88$ ). The actually measured temperature profile of the preheater is depicted in Figure 8.16 on page 261, justifying the above estimations.

While in a small process demonstration unit, the preheater can be made of a simple tube due to its simple nature and large wall area per volume of slurry ratio, for larger plants, static mixing elements should be used to improve the heat transfer from the pipe's wall to the fluid, as well as to prevent coking on the walls (which in turn impairs the heat transfer). A suitable system is available from Sulzer ChemTech in Switzerland: the static mixing system SMF (the thinner SMX-L is not suited for fluids containing solids). Besides the function of mixing, it also ensures plug flow of the feed. The smallest commercially available version has an inner diameter of 21 mm.

### 8.2.5 Conclusions of the Wood Liquefaction Experiments

- Wood could be liquefied non-catalytically in the batch reactor at concentrations of 10 wt %.
- Good liquefaction parameters are high heating rates to temperatures between 330 and 350 °C (e.g. within 5 min.), accompanied by short residence times at these temperatures (e.g. 2 min.) before the catalytic gasification to avoid secondary polymerization as well as coking.

- Non-catalytic liquefaction and catalytic gasification could be carried out separately, leading to results nearly as good as in a one-step process. This is the basis for the operation of a continuous plant without a significant loss in utilization of the heating value of the feed.
- For larger process demonstration units, static mixers should be used to improve the heat transfer to the fluid and to prevent local coking.

### 8.3 Feed Conditioning (Milling)

The conditioning of the biomass has an impact on several stages of its transformation to SNG. A crucial process step is the milling, especially on a laboratory scale, where the size of the apparatuses is generally small. The finer the feed is milled, the less prone it is to lead to plugging problems in the pump. Also the liquefaction step is somewhat dependent on the particle size, as smaller particles have a larger surface to volume ratio, and are thus more easily attacked by water in the hydrolysis step. In larger process demonstration units, a trade-off between good liquefaction and pumpability, and energy consumption for milling should be chosen. On the laboratory scale, however, the milling should be carried out to yield a minimal particle sizes with a narrow distribution if ever possible. It turned out that wood needed to be milled wet in order to yield a suspension that did not segregate over time. For this, bark-free spruce and fir chips were pre-milled at PSI to a size of 1 – 2 cm with a knife mill, and then moisted with water to a dry matter content of about 25 wt %. Milling experiments with these tapped chips were then carried out at Romaco FrymaKoruma (Neuenburg, DE). Good milling parameters were identified as follows (the setpoints of the mills are tabulated in Table 8.3):

- An initial size reduction was achieved by milling with a toothed colloid mill (FrymaKoruma type MZ-110).

- A further size reduction was achieved by milling with a perforated disk mill (FrymaKoruma type ML-180): 1<sup>st</sup> pass with a disk with hole diameter 40 mm, 2<sup>nd</sup> pass with a disk with hole diameter 20 mm.
- A last size reduction was achieved by milling with a corundum stone mill (FrymaKoruma type MZ-180), in 2 – 4 passes.

Table 8.3: Mill types used and applied for the wet milling of wood chips.

pass no.	mill type	milling elements	milling gap mm	T <sub>in</sub> °C	T <sub>out</sub> °C
1	toothed colloid mill MZ-110	N/A	+2U	30	41
2	perforated disk mill ML-180 hole Ø 40 mm	20/20	-0.1	30	40
3	perforated disk mill ML-180 hole Ø 20 mm	20/20	-0.3	40	59
4	corundum stone mill MZ-180	20/20	-0.1	22	29
5	corundum stone mill MZ-180	20/20	-0.3	29	45
6	corundum stone mill MZ-180	36/46	-3.0	40	56

During the milling process, water was added to avoid plugging of the mills. The final water content of the wood suspension was around 96 wt %, but could be lowered to 90 – 70 wt % by decanting and heating the slurry to 50 °C.

While suspensions of dry-milled wood segregated rather quickly (depending on the water content within minutes), the wet milled wood from the above milling campaign was stable for months. Photographs of wood dry and wet milled wood slurries are depicted in Figure 8.4. No measurement of the particle size distribution was carried out as the device was temporarily unavailable at FrymaKoruma; however, the experienced process engineers suspected an average size below 100 µm upon visual inspection with a microscope.

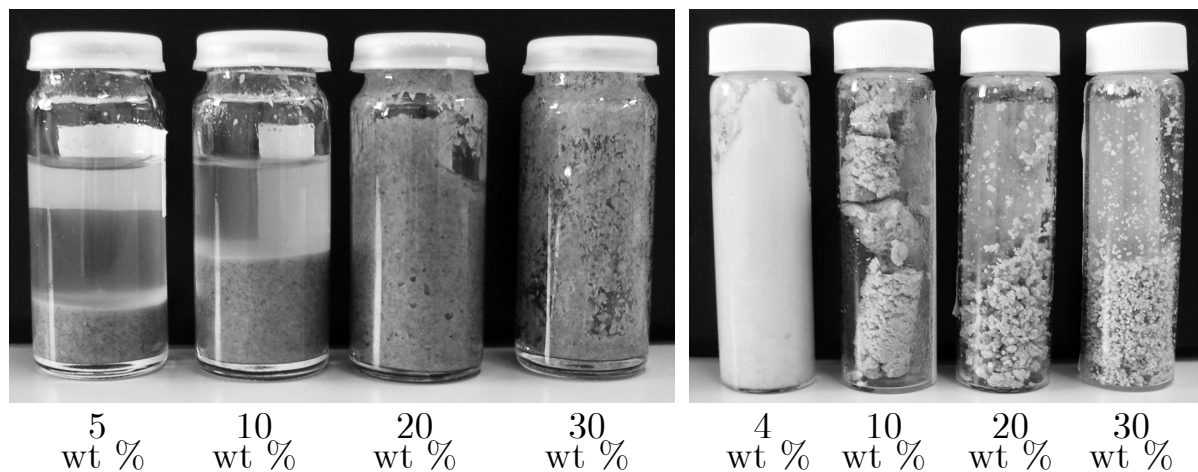


Figure 8.4: Comparison of dry milled wood slurries (left,  $x_D = 300 \mu\text{m}$ ) to wet milled wood slurries (right,  $x_D < 100 \mu\text{m}$ ). The dry milled slurry segregated within minutes, while the wet milled was stable for months.

## 8.4 Suitable Pump Systems for the PDU

Several types of pumps were evaluated. Most of them failed due to the combination of requirements: very low throughput ( $\sim 1 \text{ kg/hr}$ ), high pressures (up to 35 – 40 MPa), and the ability to pump solids, such as wood slurries, that can be of abrasive or corrosive nature, or tend to segregate. Some of the evaluated pumping systems are described in the following section, together with an overview of their advantages and disadvantages.

### 8.4.1 Gear Pumps

Both the low throughput and the desired pressure level can be achieved with a gear pump, but the pump requires the feed to have automatic lubrication character in order to work properly. The addition of oil residues or rapeseed oil to the biomass was not considered an option, since their greasing properties are not sufficient [196]. Bitumen, in contrast, has such greasing characteristics, but its hydrothermal decomposition would have to be examined prior to its application, and therefore, this option

was dismissed. It would be better to choose a pump which does not need any additive to the feed. In addition, the fibres of the wood and the sand inside the manure can cause significant problems to the gear-wheel. For these reasons, the gear pump was not chosen.

#### **8.4.2 Twin-Screw Extruders**

Twin-screw extruders, especially counter-rotating models, are less susceptible to plugging than many other types of pumps. However, most extruders are used in food and plastics applications, and are thus often not specifically protected against corrosion and abrasion (manure slurries contain sand). Moreover, at pressures exceeding 20 MPa, bearing problems are common, leading to a short lifetime of the affected parts of the pump (increasing running costs). Usual throughputs are also much larger, starting at 100 kg/hr. Mini models do exist, but all tested models failed.

#### **8.4.3 Eccentric Screw Pumps**

Eccentric screw pumps are widely used for conveying solid containing slurries. Typically, either small screws or low rotational speeds result in low throughputs. However, small screws often lead to blockage and plugging, and low rotational speeds to segregation of the feed (see Figure 8.5). They are conceivable as primary pressure pump (i.e. to generate a certain pressure level often required on the intake side of a high pressure pump), but also as high pressure pump. For the latter, a multiple-stage pump was proposed by process engineers. However, for 30 MPa design pressure, the pump would have consisted of about 5 individual stages with a total length of several meters, at a price that exceeded the budget by far. Thus, eccentric screw systems were mainly considered as primary pressure pumps.

#### **8.4.4 Piston Diaphragm Pumps**

Piston diaphragm pumps are reliable systems to pump slurries with high solid fractions including aggressive and abrasive media, due to their sepa-



ration of the feed from mechanical parts by a diaphragm. However, pressures exceeding 30 MPa can commonly only be obtained in combination with large throughputs (larger than 50 kg/hr). Smaller units are more prone to plugging, and thus such a type is only recommended for a larger process demonstration unit, beyond the laboratory scale, as no manufacturer was willing to design a high pressure diaphragm pump for our application at a reasonable price.

#### **8.4.5 Piston / Plunger Pumps**

Plunger pumps are quite reliable and common in laboratory scale applications. Piston pumps produce pressure surges, which need to be absorbed by a pulsation damper in order for the controlled back-pressure regulator and the salt separator to work; however, pulsation dampers might plug with slurries. In addition, the check valves must not be susceptible to plugging. Due to their availability, scale and simplicity, this type of pump is relatively low priced (e.g. Novados N-P31 around € 7'000).

#### **8.4.6 Evaluation Process towards a Suitable Pump for the PDU**

The evaluated pump systems are tabulated in Table 8.4. Generally, extruders are the pump system that is ideally suitable to handle slurries with high concentrations of solids; however, for throughputs of 1 kg/hr, the number of revolutions of the screw would have to be reduced to below 10/min., even for small pumps, which lead to segregation of the wood slurry inside the storage funnel or the screw itself. This behavior was observed even for low pressure pumps (evaluated as primary pump for the high pressure pump, see section 8.5 and Figure 8.5 on page 244).

After an extensive evaluation phase of numerous pump manufacturers (a total of 18 enterprises were inquired), and a few pumping tests of wet milled wood slurries at various concentrations (5, 7.5, 10, and 15 wt %, respectively, 50 – 100  $\mu\text{m}$  particle size), Bran+Luebbe GmbH, Germany, was willing to develop a plunger pump specifically designed to convey wood slurries with solid concentrations of up to 10 wt %, at a pressure of

Table 8.4: Pump types considered.

pump type	pro	contra
gear pump	<ul style="list-style-type: none"> <li>– pressure level reachable</li> <li>– relatively low priced</li> </ul>	<ul style="list-style-type: none"> <li>– min. throughput &gt; 10 kg/hr</li> <li>– automatic lubrication needed</li> <li>– slurries with solids problematic</li> </ul>
twin-screw extruder	<ul style="list-style-type: none"> <li>– conveying generally reliable</li> </ul>	<ul style="list-style-type: none"> <li>– corrosion resistance low</li> <li>– short lifetime at 35 MPa</li> <li>– at small throughputs extremely low rotation speed</li> <li>– feed segregation possible</li> </ul>
piston diaphragm pump	<ul style="list-style-type: none"> <li>– abrasive and highly viscous slurries with high solids concentrations possible</li> </ul>	<ul style="list-style-type: none"> <li>– min. throughput &gt; 50 kg/hr</li> <li>– price around € 50'000</li> </ul>
piston pump	<ul style="list-style-type: none"> <li>– small throughputs possible</li> <li>– relatively low priced</li> </ul>	<ul style="list-style-type: none"> <li>– pressure surges</li> <li>– sealing problems with solids</li> <li>– feed segregation possible</li> </ul>
double piston with positively controlled valves	<ul style="list-style-type: none"> <li>– non-sensitive towards variable solid concentrations</li> <li>– no plugging</li> <li>– reliable, up to 50 wt % solids</li> </ul>	<ul style="list-style-type: none"> <li>– min. throughput 50 – 100 kg/hr</li> <li>– costly</li> </ul>

max. 40 MPa (model Novados N-P31). This plunger pump was selected as feed pump for the PDU, since it was the only affordable solution to the problem that had been offered.

It has to be noted that for a larger process demonstration unit with mass flow rates of 50 – 100 kg/hr, several commercially available pumps could have been selected (e.g. Feluwa piston diaphragm pump, Abel SH solid pump); the pumping is only a problem on the laboratory scale at which this PDU had to be designed.

## 8.5 Novados N-P31 Plunger Pump Testing

The plunger pump Novados N-P31, constructed by Bran+Luebbe, SPX Process Equipment, Germany, was designed to convey wood slurries using cone valves up to a solid concentration of 10 wt %, at a maximum operating pressure of 40 MPa. However, the pump required a primary pressure of 0.5 MPa on the intake side. Thus, a second low-pressure pump was needed. The extruder-type pumps are best suited for this task.

Tests with an eccentric screw pump (stator: NBR, rotor: stainless steel 1.4571) to provide this primary pressure failed due to segregation of the feed, leading to a build-up of biomass dry matter and blockage, as depicted in Figure 8.5 on page 244, even with atmospheric pressure at the exit (in contrast to 0.5 MPa for the application with the Novados N-P31 high pressure pump).

The major problem with eccentric screw pumps and very low mass flow rates is the low rotation speed of the screw (i.e. only 8/min. during the test). An alternative would be to use eccentric screw pumps with higher screw rotation speeds, leading to higher throughputs, e.g. 10 kg/hr, and the application of a by-pass, so that only 1/10 is fed to the high pressure pump. However, this by-pass might also lead to a segregation and structural change of the wood slurry, thus only shifting the problem from the pump to the by-pass system.

Therefore, this alternative was not followed, but another approach used: The wood slurry was filled into a disc shaped pressure expansion vessel (butylrubber bladder, Pneumatex statico PND8, volume 4 L), which is frequently used in household heating systems. By pressing gas (e.g. Ar) into the vessel between its shell and the bag, the latter is scrunched and its content forced into a tube which was previously filled with water and attached to the intake side of the high pressure pump. Unfortunately, feeding could only be sustained for about 3 hours with this method, but at least this allowed to test the high pressure pump.

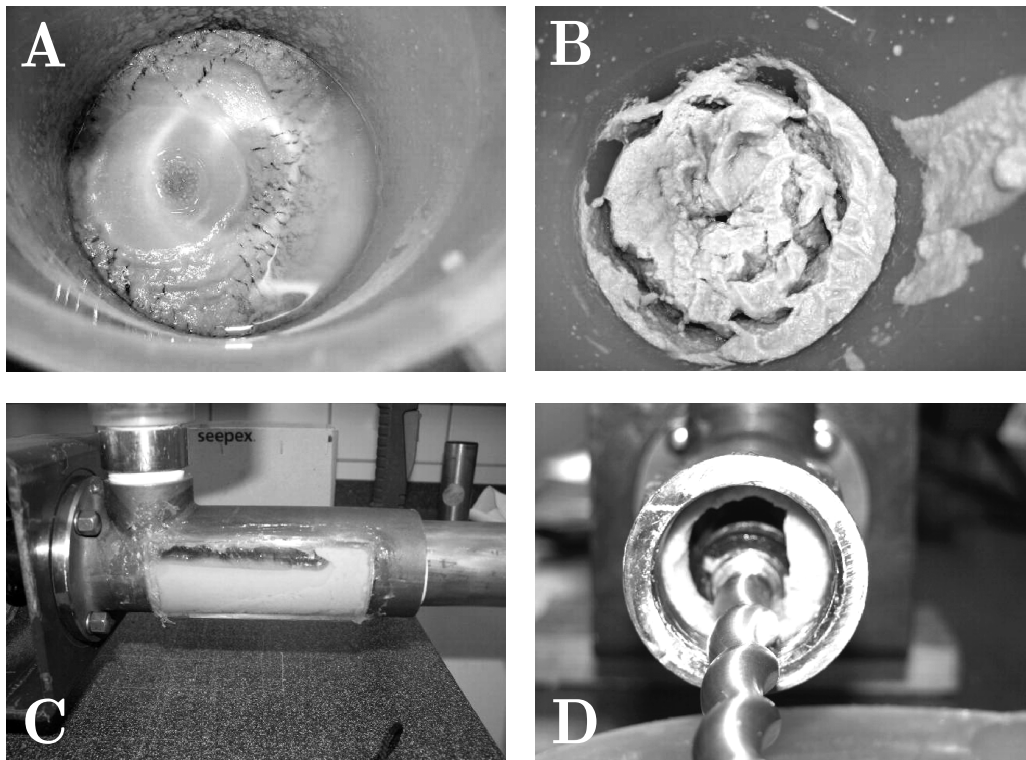


Figure 8.5: Eccentric screw pump test as primary pressure pump for wood slurries (conc. 7 wt %). Conditions:  $n=8$  rev./min., pressure at exit  $p_2 = 1$  atm., feed in funnel above the extruder. A and B: Feed segregation in the supply funnel, caused by dewatering in the entry section of the rotor/stator. C: Dewatering of the feed inside the compounding area. D: Build-up of the feed's dry matter in the entry section of the stator.

A short test with this pressure vessel connected to the Novados N-P31 high pressure pump revealed that the pump was not capable of feeding the wood slurry (conc. 4.5 wt %) at all; as soon as the first wood particles were sucked into the valves of the pump, the pressure could not be held, and the pump stopped conveying. The slurry inside the valve had been dewatered, and wood fibres were deposited on the seatings of the cone valve.

The manufacturer tried to fix the pump by exchanging its head with a model using ball valves instead of cone valves, and by increasing the throughput to 4 – 5 kg/hr. Only then was the pump able to convey the slurry, at a throughput of 3.6 kg/hr, compared to 4.6 kg/hr when feeding

pure water. The throughput could not be varied down, as the pump would immediately stop conveying. But also when running the pump at maximum throughput, a segregation of the feed on the inlet side was visible after 55 min., and the pump stopped working, having acted as a separating unit.

### 8.5.1 Alternatives to the Novados N-P31

In the form as delivered, the Novados N-P31 pump was useless for pumping slurries containing solids (e.g. manure, wood, sewage sludge, etc.). Therefore, alternatives had to be evaluated:

One possibility was the stabilization of the wood slurry with corn starch, which was reported in the literature to yield very stable suspensions [61]. To test this, a suspension of dry-milled wood sawdust in water was used (the typical feed for wood gasification experiments in the batch reactor) instead of wet-milled wood: the former type segregated within minutes when not stirred, while the latter was stable over months. Indeed, by adding corn starch (conc. 4 wt %) to boiling water, and then adding wood sawdust to it to get a wood concentration of 10 wt %, the feed did not segregate within the observation period of three days. However, preliminary pumping tests with this stabilized feed using an eccentric screw pump (Netzsch Mini pump, Häny AG, Switzerland) had failed, as the biomass still segregated in the pump, and biomass dry matter was built up in the stator area. Apart from that, the wood-starch-mixture turned very hard and sticky when dried; so it was expected to cause severe problems inside the plant (e.g. plugging of parts). Considering this, a test of the high pressure pump by filling the biomass into the butylrubber bladder did not make sense.

Another option was to replace the high pressure pump by a pressurized vessel, in which the feed was filled batch-wise, providing material for about 10 hours on stream (depending on its volume). Thus, for long-term experiments, a second vessel would be needed, with the possibility to

switch between the two. A 35 MPa bladder accumulator (Olaer AG, Switzerland) is an example of such a pressurized vessel, of which a cross section can be seen in Figure 8.6.

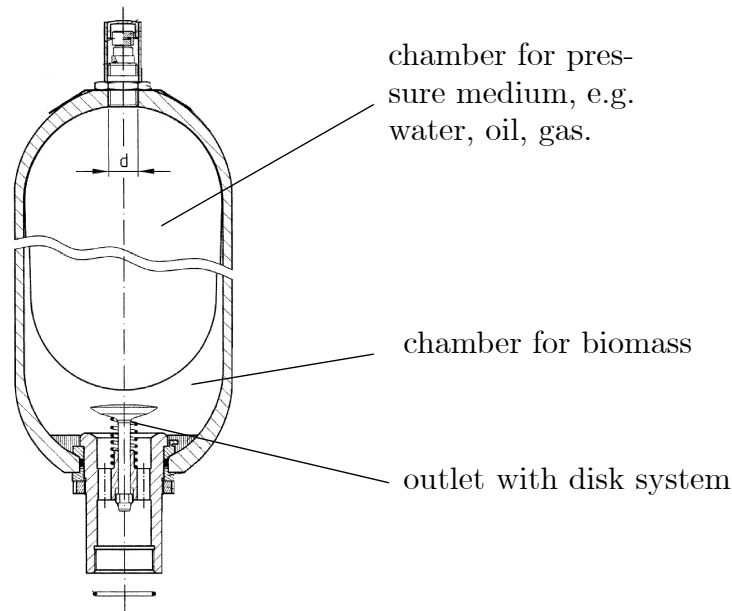


Figure 8.6: Cross section of a high pressure bladder accumulator (Olaer).

A problem could be the outlet system with a disk, which is susceptible to plugging when using biomass with solids; thus, a tailored version would be needed, which in turn would boost its costs. The Novados N-P31 high pressure pump could be used as a means to press a suitable medium into the bladder, e.g. oil or water. However, the start-up of the plant would be difficult, as the plant would have to be filled with water prior to switching to one of the pressurized vessels, making manipulations or an additional pump necessary.

A similar idea was proposed by H. Bieri Engineering GmbH, Winterthur, Switzerland: the biomass is filled into a cylinder with a piston. The piston is moved by pressing oil against it, pumped by the existing Novados N-P31 pump. There is a stirrer integrated into the cylinder to mix the biomass and avoid segregation, and a low-pressure pump, whose only task is the conveying of the biomass, but not the simultaneous establishment of a pressure level, which is realized externally by the oil acting on the piston.

Given the small pressure difference inside the vessel, commercially available low-priced pumps could be used. The setup is depicted in Figure 8.7.

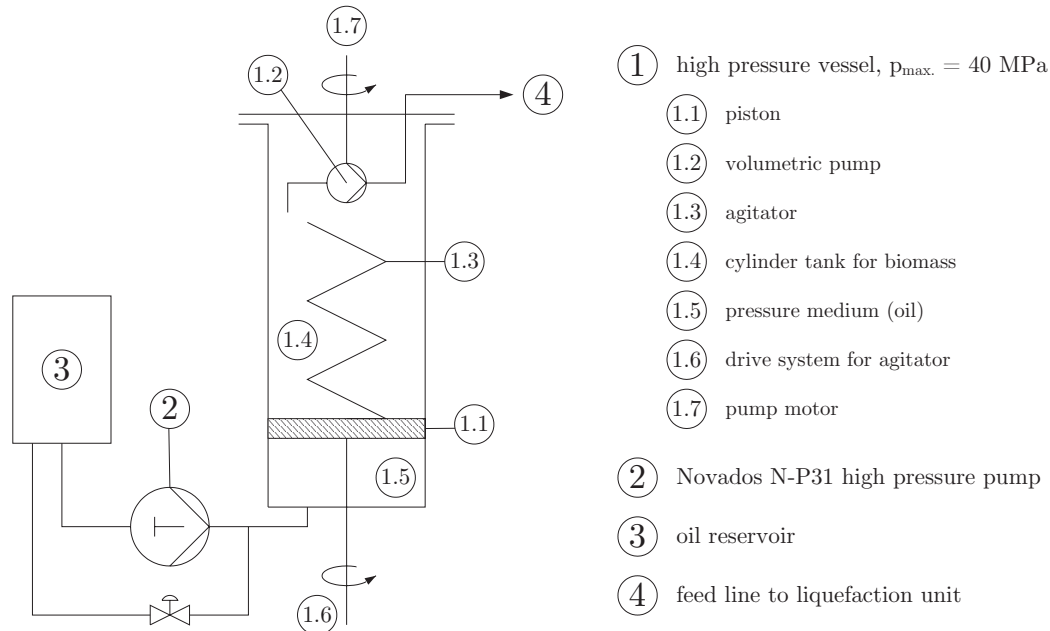


Figure 8.7: Conveying unit proposed by H. Bieri Engineering GmbH.

Unfortunately, this device was rather costly (€ 20'000) and could not be considered for the process, as the conveying would be limited to one filling of the cylinder, providing biomass for about 10 hours on stream, only. A second unit and switching between them would have exceeded the budget by far.

### 8.5.2 Final Solution

The only alternative left was to change the biomass so that it could be pumped with the existing Novados N-P31 pump. Wood slurries would have the advantage of representing an abundant feedstock, being well characterized and analyzed, having low salt concentrations, and preliminary experience from the batch reactor could have been used. With the change of the biomass, the liquefaction experiments described in section 8.2 had thus no direct application anymore. The disadvantages of wood slurries – its fibers, its non-greasing character, and the occurring phase separation – clearly outweighed the advantages. After the wet-

milled wood stock was used up, and a new milling campaign had failed (a new batch of spruce wood could only be milled to a coarser size distribution, despite the application of the same procedures), the feed was changed to a liquid: palm oil pyrolysis condensate. With this feed, the original pump head (with throughputs from 0.5 – 1.0 kg/hr and cone valves) could be used again. However, due to the high biomass concentration (around 40 wt %), a larger gas production of around 400 L/hr for a gas corresponding to the chemical equilibrium had to be expected, or up to 600 L/hr for a gas produced over a partly deactivated catalyst (assuming 100 % conversion and a gas rich in hydrogen, carbon dioxide and monoxide). But the process could still be demonstrated, as a real biomass waste stream served as feed. While rather unknown in Europe, it is very common in Indonesia, and contains inorganics so that the salt separation can also be studied.

## 8.6 Setup and Process Flow Sheet

The PDU consists of several units, each of which is assigned to a specific task. It was assembled by E. De Boni, PSI, and could be controlled over a WAGO system with a LabView<sup>®</sup> interface (P. Hottinger, E. De Boni, PSI), of which screenshots are presented in Figure 8.8.

The units of the PDU are tabulated in Table 8.5, and the process flow sheet is depicted in Figure 8.9 on page 250.



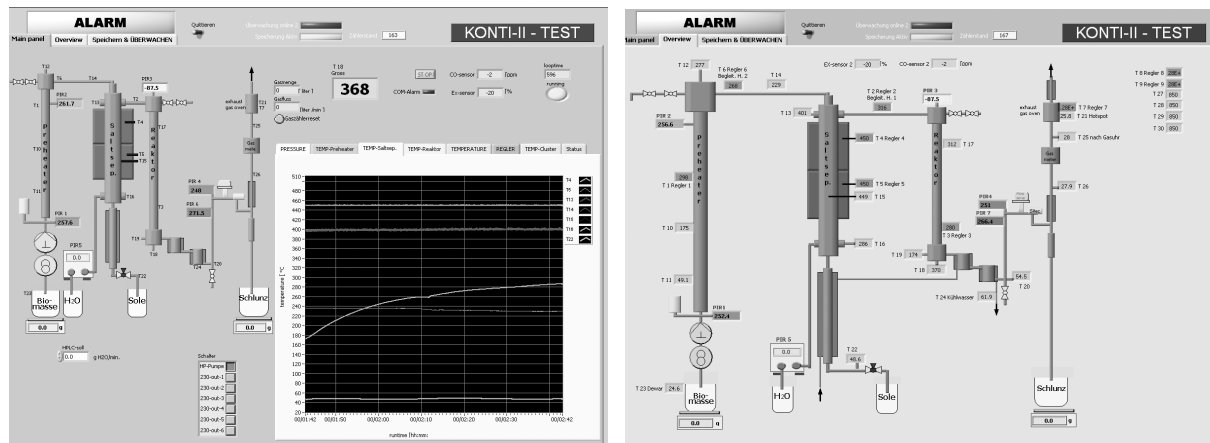


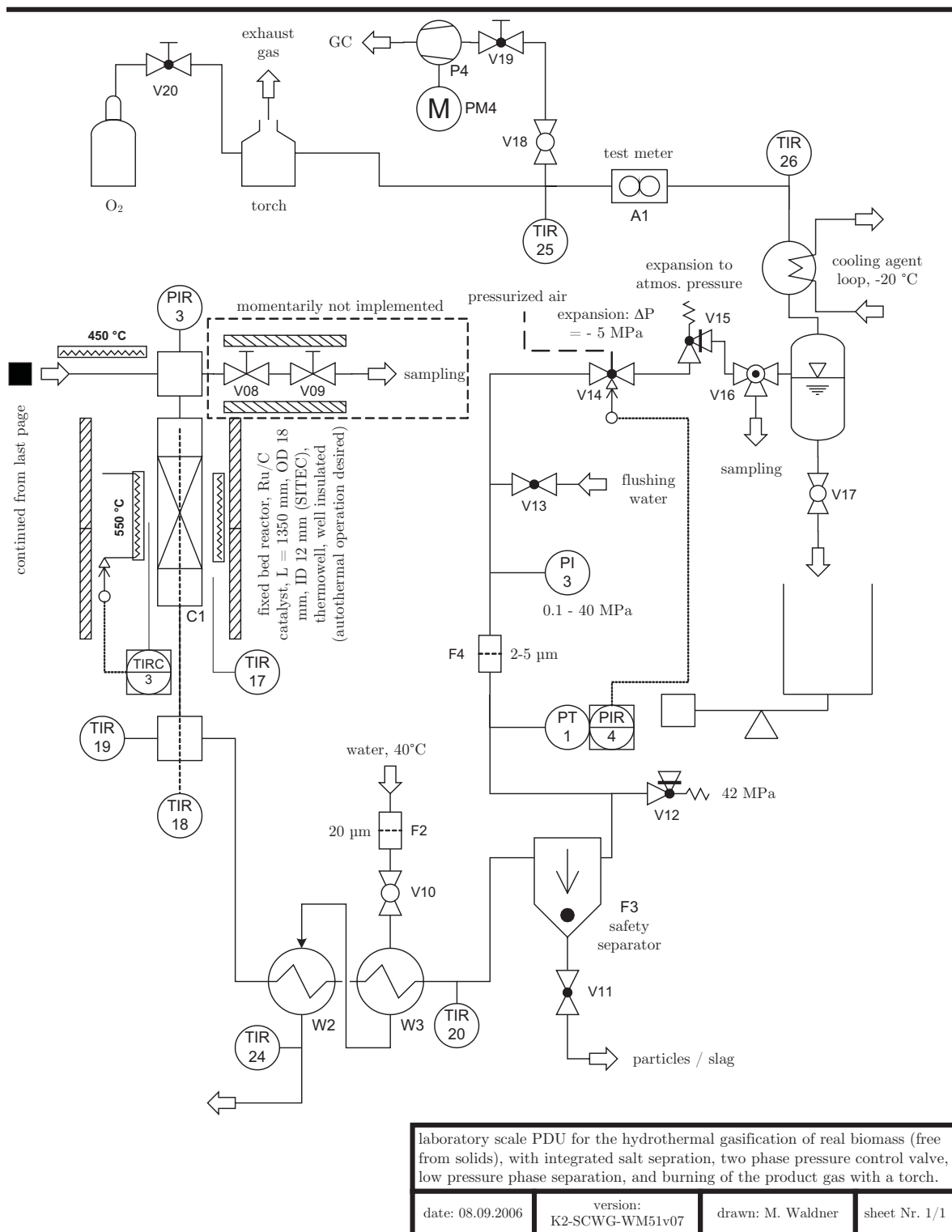
Figure 8.8: Screenshots of the LabView interface (total 3 layers).

Table 8.5: Units of the PDU.

unit	type	material	dimensions
feed tank	stirred Dewar vessel	–	i.d.=29 cm, H=75 cm, V=40 L
conveyance	1a) gear pump <sup>a</sup> 1b) peristaltic pump 2) piston pump	–	–
liquefaction	heated pipe	stainless steel 1.4435	12×18 mm, L=1.70 m
salt separation	reverse flow vessel	titanium grade 5, brass heating block	12×50 mm, L=694 mm
reactor	tubular fixed bed	stainless steel 1.4435	12×18 mm, L=1.35 m
condensation	two helix coolers in series	stainless steel 1.4571	coiled tube, L=2 m each
pressure control and letdown	pneumatic control valve (Kämmer) + spring loaded relief valve (SITEC)	stainless steel 1.4571	$k_{vs}=3.9 \times 10^{-4} \text{ m}^3/\text{hr}$
phase separation	laboratory equipment	glass	V=0.5 L
exhaust gas treatment	burner/torch	–	not installed yet

a. The gear pump was later replaced by a peristaltic pump.





### 8.6.1 Storage and Conveying

The storage and conveying section of the plant is shown on photographs in Figure 8.10.

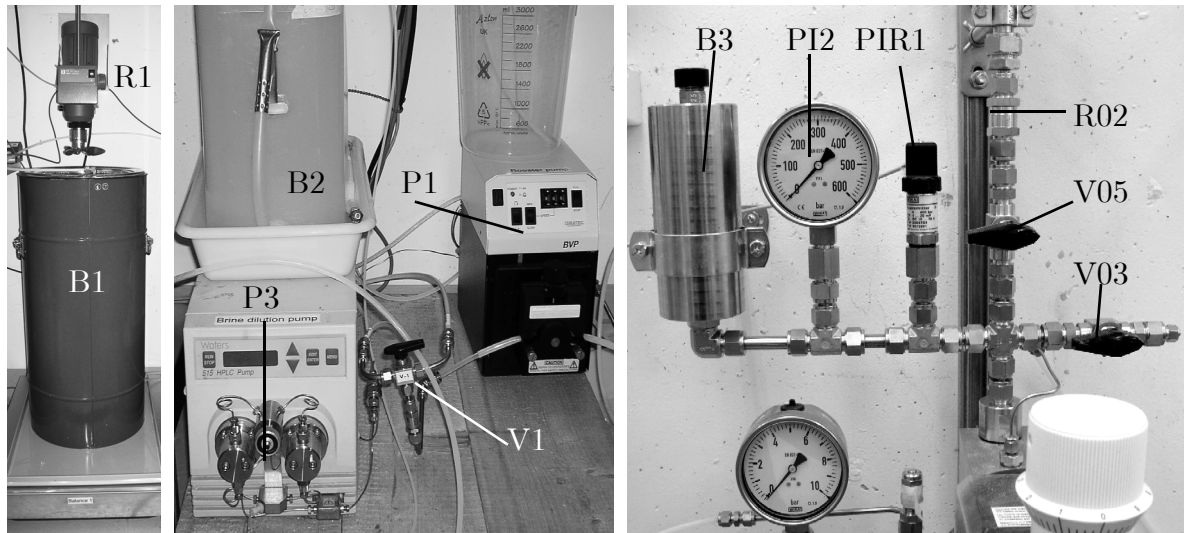


Figure 8.10: Storage and Conveyance section. Left: feed tank B1 (Dewar) with stirrer R1. Middle: primary feed pump P1, brine dissolution pump P3, water tank B2, feed switching valve V1. Right: section downstream of the high pressure pump. Flushing water ball valve V03, ball valve V05, check valve R02, pressure sensor PIR1, manometer PI2, and pulsation damper B3.

The feed is filled batch-wise into a stirred Dewar vessel B2<sup>1</sup> (KGW Isotherm, volume 40 L; stirrer R1: IKA RW 28 basic, RI 1388 propeller stirrer). It was first pumped with a gear-type pump P1 (Ismatec BVP), later with a peristaltic pump P1 (Cole Palmer Masterflex 77390-00) through a polytetrafluoroethylene (PTFE) tube (i.d. = 4 mm, o.d. = 6 mm) over an overflow spring relief valve V02 (Swagelok, preset to 0.5 MPa) to the inlet section of the high pressure pump P2 (Bran+Luebbe Novados N-P31, pump direction vertically up, due to the design of its cone valves requiring gravity), which was built on a wood block screwed onto the floor. The second exit of the overflow spring relief valve is connected to the feed

1. The abbreviations of some of the components (e.g. P1, W2, V06, etc.) correspond to the symbols used in the process flow sheet on page 250.

tank, acting as a by-pass. Thereby, the two pumps do not need to have exactly the same mass flow rate, and minor fluctuations can be balanced. The pressure side of the high pressure pump is connected over a cross to a vertically mounted pulsation damper B3 (Olaer, OLG0,1-690/00-RF, nitrile bladder, gas volume 0.1 L at 23 MPa), to a pressure sensor PIR1 (WIKA LR110686-1) and to a manometer PI2 (WIKA EN 837-1).

### 8.6.2 Preheater

Vertically above the cross is the preheating tube (SITEC, i.d. = 12 mm, o.d. = 18 mm, L = 1.50 m, 1.4435 stainless steel), heated on a length up to 1.30 m by heating bands (Hillesheim HSQ60, 600 W/m) and insulated by mineral wool (thickness: 42 mm). The preheating tube is connected to a cross (SITEC, 1.4571 stainless steel) with a high-temperature pressure sensor PIR2 (Dynisco MDT462F, Inconel 718, with optional NaK brine, type B171), where over a tube (SITEC, i.d. = 12 mm, o.d. = 18 mm, L = 40 mm, 1.4543 stainless steel) a second, identical cross is connected, to which a high-temperature sampling port is attached, consisting of 2 valves V06, V07 (SITEC, 1/4 " micro, ASI 316.Ti 1.4571 SS) connected by a tube (i.d. = 1/16 " , o.d. = 1/4 " , L = 50 mm).

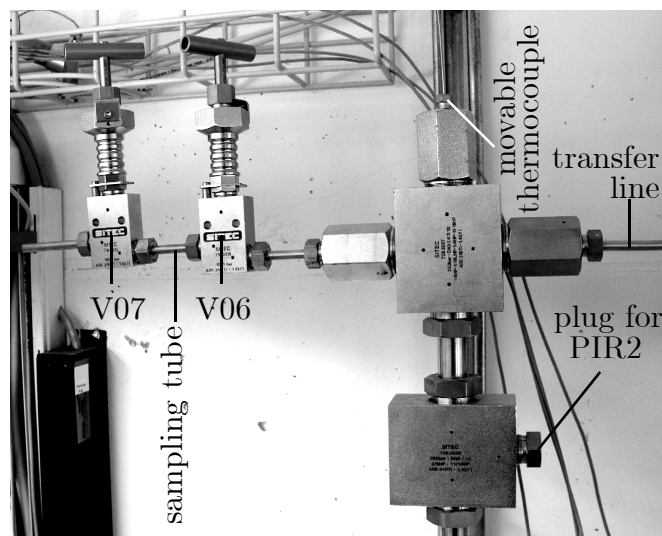


Figure 8.11: Upper (non-heated) part of the preheater, consisting of two crosses and two high-temperature valves V06 and V07 for sampling.

A thermowell (i.d. = 1/16 ", o.d. = 1/8 ", L = 1.40 m ) is built from the top part of the upper cross, into which a type K movable thermocouple (d = 1 mm) can be inserted, allowing for the measurement of a temperature profile along the preheater. The upper part of the preheater is depicted in Figure 8.11.

### 8.6.3 Salt Separator

The double cross is connected over a heated and insulated tube (i.d. = 1/8 ", o.d. = 1/4 ", L = 30 cm, 1.4543 stainless steel) to the salt separator (SITEC, titanium grade 5, i.d. = 12 mm, o.d. = 50 mm, L = 694 mm), of which a cross section and a photograph can be seen in Figure 8.12. Its design was deduced from a prototype used for the neutron imaging salt separation studies carried out in another project at PSI [30].

The biomass stream enters the salt separator through a dip tube (i.d. = 1.4 mm, stainless steel 1.4543) which extends for 248 mm into the vessel. The biomass reverses its flow direction inside the salt separator vessel and leaves at the top part of the vessel, through a side part.

The vessel is jacketed by four brass heating shells (manufactured in-house), heated with 8 heating cartridges (Probag, d = 10 mm, L = 80 mm, upper part 4×400 W, lower part 4×315 W) and insulated by mineral wool (thickness: 70 mm). The division into two upper, hotter shells, and two lower, cooler shells (each 230 mm long) was necessary to allow for the heating of the biomass stream to a temperature of around 450 °C in the upper region to induce precipitation (hereby, the salts precipitate depending on their solubility and are drawn by gravity to the bottom), and for the re-dissolution of the salts in the lower section at around 350 °C. The lowest section is not heated at all, but only insulated (the heat conduction keeps it hot enough).

An optional water stream can be introduced by means of an HPLC pump P3 (Waters 515) to the bottom side part of the separator, to enhance the dissolution of the salts and ease their extraction out of the system. The

salt stream leaves the salt separator at its bottom section through a stainless steel tube (i.d. = 1/8 ", o.d. = 3/8 ", L = 1 m), which is cooled by a jacket cooler (o.d. = 1 ") over a length of 75 cm, and attached to an overflow spring relief valve (Swagelok), where the flow rate can be manually adjusted.

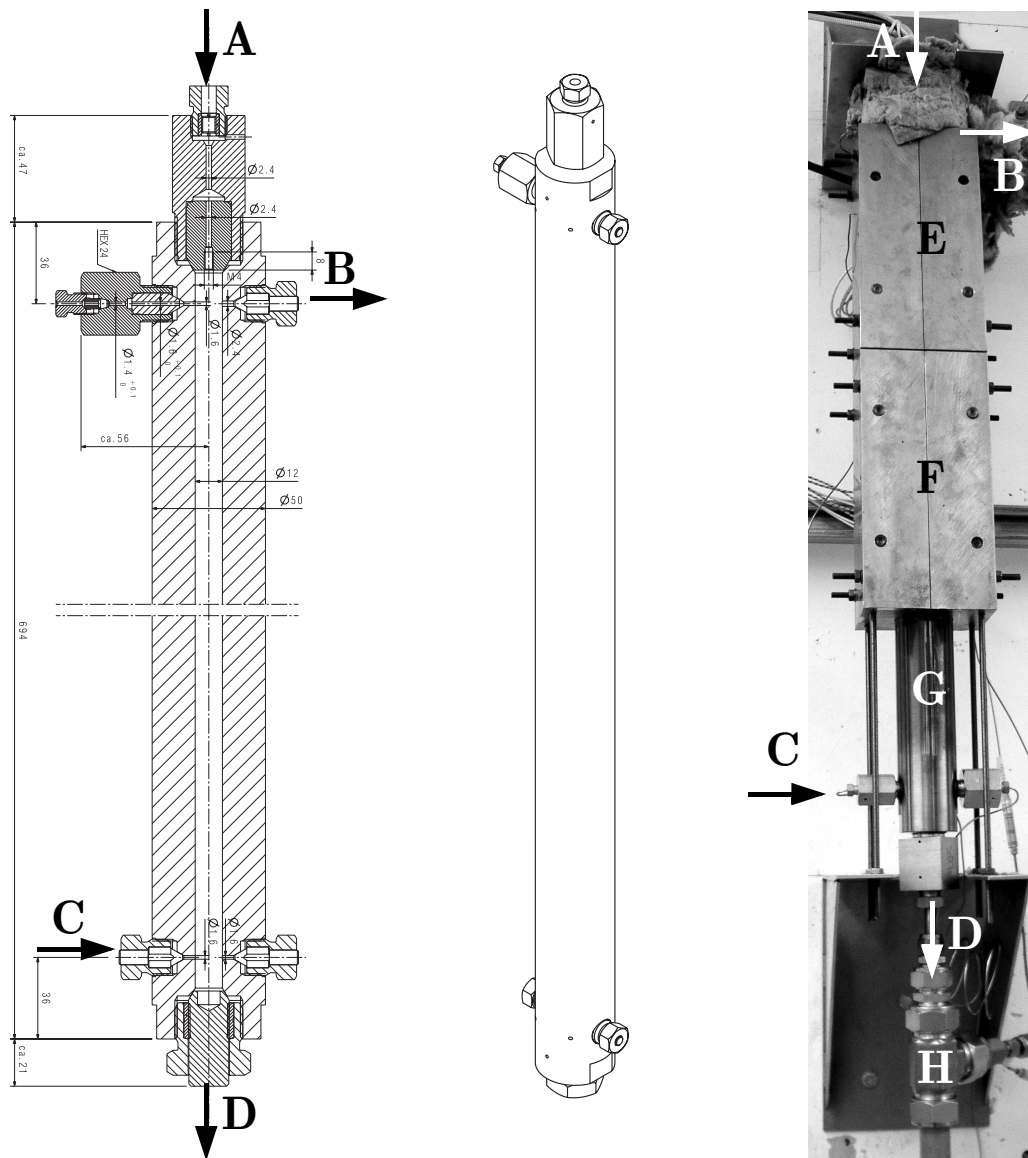


Figure 8.12: Left: Sketch of the salt separator vessel, made of titanium grade 5 (SITEC, Switzerland), middle: isometric view, right: Photograph of the non-insulated, mounted separator. A: biomass inlet, B: biomass outlet, C: optional brine dissolution water inlet. D: salt solution outlet, E: upper brass jacket, F: lower brass jacket, G: lowest section for re-dissolution of the salts, H: top of jacket cooler.

#### 8.6.4 Reactor

A tubular transfer line (i.d. = 1/8 ", o.d. = 1/4 ", L = 12 cm) connects the upper part of the salt separator via a cross (with a high-temperature pressure sensor PIR3, Dynisco MDT462F, Inconel 718, with optional NaK brine, type B171) to the fixed bed reactor tube (SITEC, i.d. = 12 mm, o.d. = 18 mm, L = 1350 mm, stainless steel 1.4435, L/i.d. > 100, thus plug flow can be assumed [74]). The tube is heated by heating bands (Hillesheim HBQ05) and insulated by mineral wool (thickness: 45 mm). In flow direction, the first 3 cm of the tube (top) and the last 14 cm (bottom) were filled with  $\alpha$ -Al<sub>2</sub>O<sub>3</sub> beads (Alfa Aesar, 99.8 % metal basis, d. = 1 mm), with the 2 wt % Ru/C (Engelhard) catalyst bed in between (L = 118 cm,  $m_{\text{cat.,dry}} = 61.2$  g). A titanium mesh (grid distance 500  $\mu\text{m}$ ) is inserted below the fixed bed to hold it. Downstream of the reactor tube is a cross, with a thermowell (i.d. = 1/16 ", o.d. = 1/8 ") protruding into the reactor tube from below, into which a type K thermocouple can be inserted to allow the measurement of temperature profiles.

#### 8.6.5 Cooling and Pressure Control + Letdown

The cross is connected to two helix type coolers in series (stainless steel, coiled tube length = 2 m each, manufactured in-house). A safety separator F3 (SITEC, stainless steel tube, i.d. = 12 mm, o.d. = 18 mm, L = 20 mm) with a ball valve (Swagelok) is attached after the coolers to trap possibly entrained particles (e.g. due to catalyst attrition), followed by an overflow spring relief valve V12 (Swagelok, preset to 45 MPa for the case of an overpressure situation), a pressure sensor PIR4 (WIKA LR110686-1), a filter F4 (Nupro, 7  $\mu\text{m}$ ), a manometer PI3 (WIKA EN837-1), and the pressure control valve V14 (Flowserve Kammer, type 80000, DN6, PN400,  $k_{\text{vs}} = 3.9 \times 10^{-4}$  m<sup>3</sup>/hr, actuated by Flowserve Kammer 3712IP using pressurized air), where an expansion of 5 MPa is achieved. The residual expansion to atmospheric pressure is then achieved over a spring relief valve V15 (SITEC, 1.4571 stainless steel, preset to 25 MPa). Samples of the liquid phase can be taken by redirecting the product phase over a three-way valve V16 (Swagelok) into a glass vial (the product gas



is rerouted to the phase separator). The section downstream of the reactor to the sampling station is depicted in Figure 8.13.

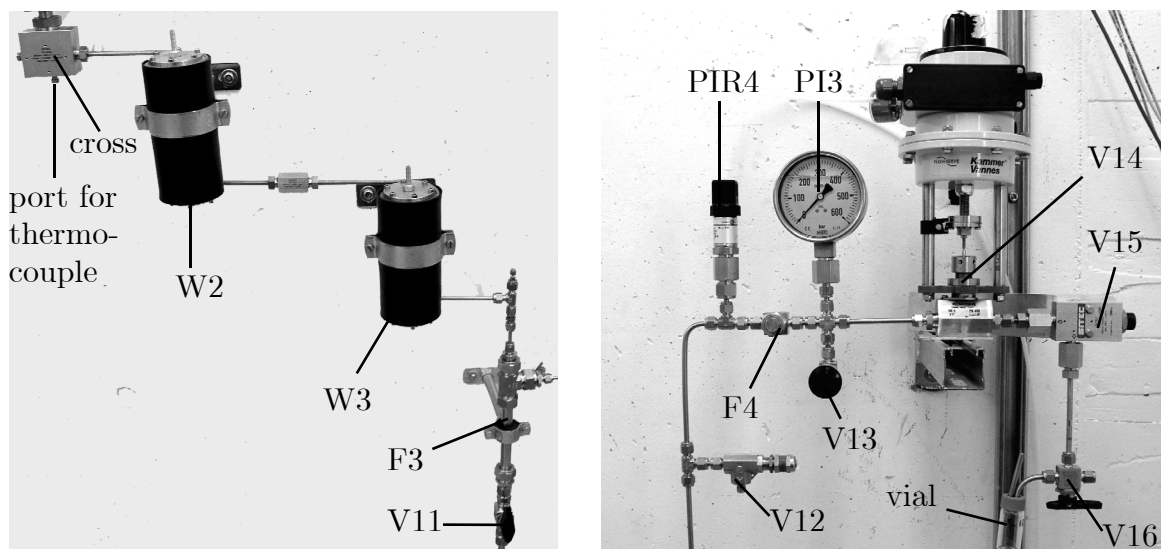


Figure 8.13: Cooling and pressure control + letdown. Left: cross downstream of the reactor tube, followed by two helix type coolers W2, W3 and a safety separator F3 (hatch) with ball valve V11. Right: overflow spring relief valve V12, pressure sensor PIR4, filter F4, manometer PI3 with flushing water valve V13, and pressure control valve V14, overflow valve V15, and three-way valve V16 with a sample vial.

### 8.6.6 Product Phase Separation (G/L Separator)

Gas/liquid phase separation is realized at atmospheric pressure (for reasons of constructional and operational simplicity). A high pressure separator was considered too elaborate and costly for a PDU of this size, as the pressure is then usually controlled via the gas phase and the incorporation of a level control for the liquid phase, integrated in a high-pressure vessel.

Here, the G/L phase separator consists of laboratory glassware: for the upper part, a bulb reduction adapter is used; for the middle part a multi neck adapter; and for the lower part a conical separating funnel ( $V = 0.5$  L, NS29/32 neck) with a PTFE stopcock (V17). At its lower end, the liquid flows through a PVC tube (i.d. = 6 mm, o.d. = 8 mm,  $L = 1$  m) into a collection tank, placed on a balance (Ohaus DP-60-XL-H). The liquid

flow rate out of the separator can be manually adjusted by the opening of the stopcock. In the top section of the G/L separator, the vapor is cooled in a high efficient condenser on top of the adapter. A cooling liquid (50 wt % ethylene glycol, 50 wt % water) of  $-20\text{ }^{\circ}\text{C}$  is used (Lauda RC25 CS edition 2000 cryostat, bath volume 27 L, coolant tubes insulated with Armaflex AF M-12A). Thereby, the gas is dried and flows through a PVC tube (i.d. = 12 mm, o.d. = 15 mm, L = 80 cm) over a test meter A1 (Wohlgroth, G4Type2.5) for the measurement of the accumulated gas volume. The G/L separator setup is depicted in Figure 8.14.

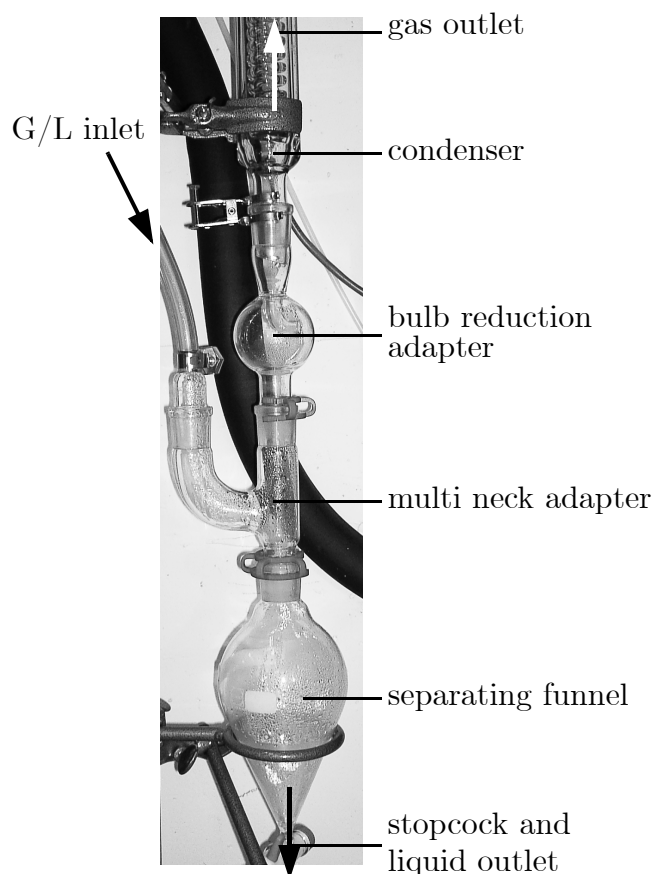


Figure 8.14: G/L separator consisting of laboratory glassware.

### 8.6.7 Product Gas Analysis and Treatment

A by-pass of the product gas stream was drawn by a gas pump P4 (KNF Laboport, model 1393-86) to a gas chromatograph (Agilent 6890) where it was analyzed for its constituents. The product gas is planned to be burnt in a torch, as depicted in the process flow sheet presented in Figure 8.9.

No experiences with this burner setup have been made yet, as it is just currently being implemented.

In an earlier version of the PDU which was used for the preliminary start-up tests of the plant, it had not yet been allowed (by the safety policy of PSI) to burn the product gas. Instead, it had to be totally oxidized to  $\text{CO}_2$  and  $\text{H}_2\text{O}$  over a  $\text{Pd}/\gamma\text{-Al}_2\text{O}_3$  catalyst in a fixed bed reactor, as shown in a cut-out of the process flow sheet (Figure 8.15).

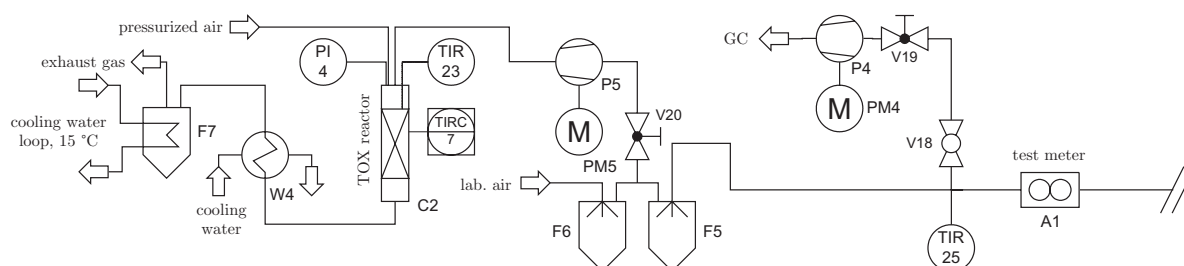


Figure 8.15: Catalytic total oxidation product gas treatment. This setup was only installed in a preliminary version of the PDU.

Unfortunately, when the product gas volume had increased to more than 300 L/hr in one of the starting experiments with EtOH as feed, the heat of reaction had led to a thermal runaway in the Pd-fixed bed (the temperature increased to 1100 °C), which destroyed the catalyst (transformation of  $\gamma$ - to  $\alpha$ - $\text{Al}_2\text{O}_3$ , for details see section 8.7). In addition, the pressure drop over the bed was too large (0.4 MPa). The TOX fixed bed reactor could have been replaced by a monolith reactor, but it turned out to be too costly if not synthesized in-house. Luckily, the option to burn the gas in a torch was finally approved by PSI safety officers, and the PDU is currently altered (February 2007).

### 8.6.8 Safety Considerations

The high pressure parts of the plant have an approximate total volume of 0.67 L. According to Swiss law, for pressure plants with volume  $V_{\text{plant}}$  at pressure  $p_{\text{plant}}$ , no technical approval by safety examiners is necessary as long as  $(p_{\text{plant}} \cdot V_{\text{plant}})$  is smaller than 100 MPa L. For the PDU,  $p_{\text{max.}}$  was set to 40 MPa, and this product is  $(p_{\text{PDU, max.}} \cdot V_{\text{PDU}}) = 27 \text{ MPa L}$ .

A HazOp (Hazards and Operability) study was carried out to identify possible hazards, and operational problems. They were grouped to scenarios, each of which was weighted with an impact factor and a probability to assess the risk of possible incidents. Countermeasures were then taken to eliminate all risks that can lead to substantial personal or material damage, to ensure the safety of the operators:

- Walls to protect from splinters are installed.
- An automatic emergency-stop if  $p > p_{\max}$ . or  $T > T_{\max}$ . is installed.
- A manual emergency-stop button is placed near the operator.
- Adequate ventilation is installed.
- A CO sensor (VarioGard CO, Dräger Safety) and an EX sensor (Polytron PEX 3000, Dräger Safety) are installed close to the test meter, in case of a release of burnable or toxic gas into the room (i.e. due to a leak).
- For redundancy, a portable CO/combustible gas/O<sub>2</sub> detection device (Crowcon TETRA 3) is always placed in the room when experiments are carried out.

## 8.7 Preliminary Gasification Experiments

After successful pressure tests with water up to 40 MPa, ethanol (conc. 5, 10, 20, 40 wt %) was gasified at a catalyst bed temperature of around 400 °C and 30 MPa<sup>2</sup>. Prior to switching to ethanol, deionized water was pumped into the plant, and the preheater, salt separator and reactor were heated to the preset temperature setpoints (360, 450 – 470, and 400 °C, respectively).

---

2. Experiments carried out by E. De Boni and M. Schubert, PSI.

Then the feed was switched to the previously mixed ethanol-water-solution. It was fed at a mass flow rate of  $\sim 0.85$  kg/hr. Samples of the liquid product phase were taken on a regular basis (every 30 minutes). A temperature profile of the preheater can be seen in Figure 8.16 (for pure water only; no data was recorded during ethanol gasification).

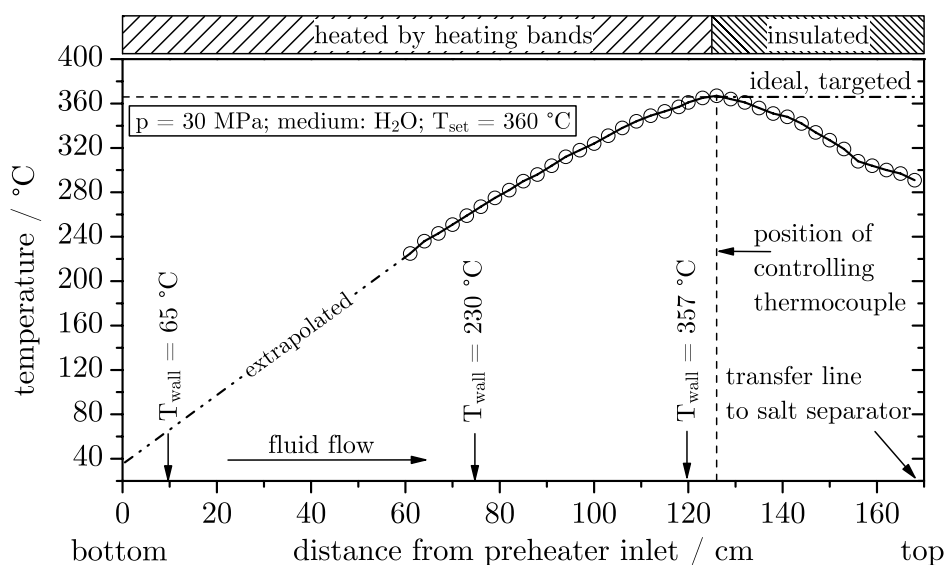


Figure 8.16: Temperature profile of the preheater when feeding water (1 kg/hr) at 30 MPa. The setpoint was 360 °C (controlled at position 125 cm). Three thermocouples measured the temperature  $T_{\text{wall}}$  on the outer side of the preheater. Fluid flow is from left to right (upward flow in reality).

The movable thermocouple was frequently jammed inside the thermowell; more so, the more it was inserted. Usually, the lowest position that could be reached was around 60 cm from the bottom. Hence, no measurements below that point could be obtained. But since the profile was almost linear, the values were graphically extrapolated from 60 cm to the inlet at 0 cm. After the ethanol gasification campaign, the preheater was dismantled and the thermowell replaced by a wider variant to ease the profiling (1/16 "  $\times$  1/32 " replaced by 1/8 "  $\times$  1/16 ").

The temperature profiles along the reactor during ethanol gasification are depicted in Figure 8.17 (here, data with pure water and 5 wt % EtOH were not recorded).

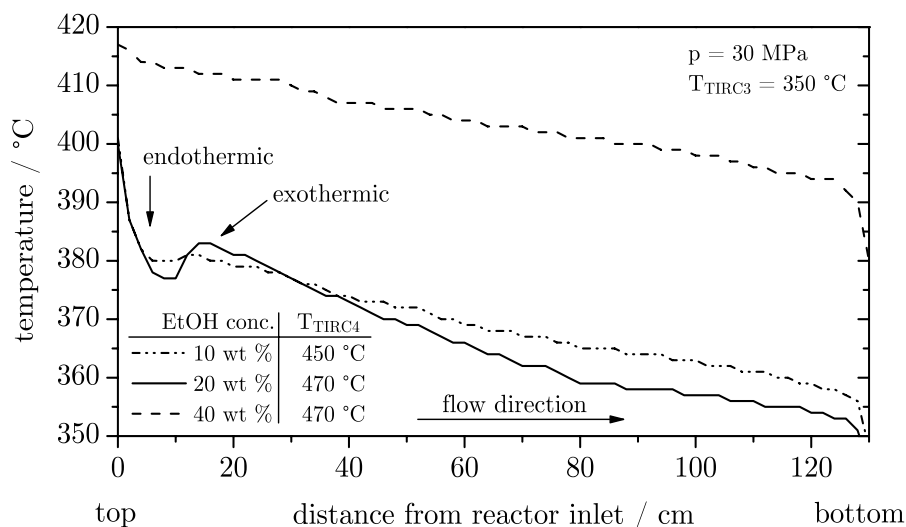


Figure 8.17: Temperature profile of the catalytic reactor during ethanol gasification at various concentrations (10, 20, and 40 wt %).

$T_{TIRC3}$  = controlled temperature at the bottom of the reactor;  
 $T_{TIRC4}$  = controlled temperature of the salt separator (upper part).

During the ethanol gasification experiment with 20 wt %, a zone of endothermic reactions, followed by an exothermic reaction is clearly visible in the temperature profile. This phenomenon was less distinct for 10 wt %, and not visible for 40 wt %. The temperature profiles were taken about 15 minutes after the formation of gas. It is interesting that for a concentration of 40 wt %, the reactor was about 30 °C hotter, despite identical heating setpoints. It is probable that the increased heat of reaction had caused an increased thermal conduction inside the tubular reactor, which led to higher temperatures. Nonetheless, the qualitative temperature profile was identical.

The gas production was linear with time and WHSV, as depicted in Figure 8.18. Since the test meter reported the values only every 10 liters to the computer, the graph shows a stepped curve. It can be seen that for typical mass flow rates around 0.8 kg/hr, the response lag time from switching between the feeds (from water to ethanol) until the detection of gas at the outlet of the plant is around 25 min. The lag time after switching from ethanol to water was shorter (20 min.) because of the shorter

feed line (water was fed out of a tank B2 right next to the pump, while the ethanol solution was fed from the stirred Dewar vessel B1, which was located further away).

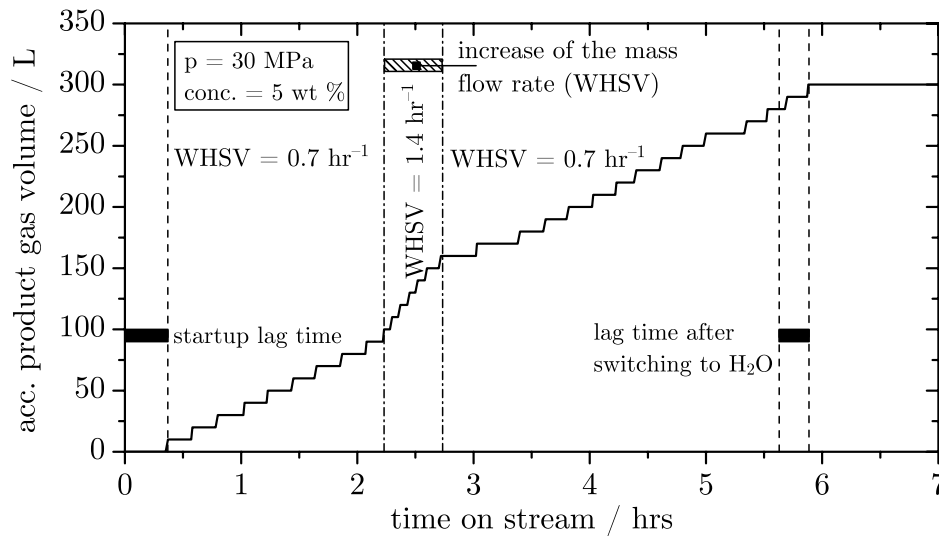


Figure 8.18: Product gas evolution during an ethanol gasification experiment (conc. 5 wt %).

In all experiments, the carbon conversion  $X_C$  was  $\geq 99.9\%$ , and the product gas corresponded to the chemical equilibrium composition (70 vol %  $\text{CH}_4$ , 28 vol %  $\text{CO}_2$ ,  $< 2$  vol %  $\text{H}_2$ , no detected  $\text{CO}$ ), independent of the feed concentration up to 20 wt %. For the highest concentration of 40 wt %, however, a thermal runaway in the catalytic total oxidation (TOX) reactor took place due to the exothermic reaction inside the bed, before a reliable measurement of the gas phase by GC could be obtained. The TOX reactor had not been specifically designed for this plant, but a reactor that had formerly been used for another application at PSI was re-installed instead (by T.-B. Truong, PSI). Apparently, the product gas flow rate at a feed concentration of 40 wt % (around  $12 \text{ mol}_{\text{CH}_4}/\text{hr}$ ) generated too much heat when oxidized to carbon dioxide. The heat could not be sufficiently extracted out of the TOX reactor anymore, despite the addition of pressurized air to dilute the gas and cool the reactor (at split ratio 1:20), and the catalytic bed reached temperatures exceeding  $1100^\circ\text{C}$ . At these temperatures, the  $\gamma\text{-Al}_2\text{O}_3$  support of the catalyst was

most probably transformed to  $\alpha\text{-Al}_2\text{O}_3$  (the catalyst beads had formed clumps). In addition, the oxidation was not complete, leading to carbon monoxide leaving the TOX reactor. Upon its detection, the plant was immediately stopped.

For further gasification experiments, the installation of a burner instead of a total oxidation reactor is currently under way.

## 8.8 Preliminary Salt Separation Experiments

### 8.8.1 Operating Conditions

The objective of the preliminary salt separation experiments<sup>3</sup> was to bracket operating conditions for the later implementation of a control feedback system to regulate the salt separator.

The setpoint temperature of the preheater was set to 300 °C, the one of the upper part of the salt separator to 470 °C, and the one of the lower part was switched off. The reactor was not heated either. A solution of sodium sulfate (conc. 1 wt %) was fed at a mass flow rate of 1.0 kg/hr. For this salt, solubility data (at 25 MPa) is available; in addition, this salt had already been added to synthetic liquefied wood for the catalyst deactivation studies presented in chapter 7. The electrical conductivity of the feed was 12 mS/cm. The pressure was set to 25 MPa, and the auxiliary HPLC pump P3 fed deionized water to the lower part of the salt separator at a flow rate of 0.12 kg/hr. The flow rate out of the salt separator was manually adjusted by the spring relief valve V11 (which turned out to be not ideal, as will be explained later), set to 0.3 L/hr (measured by filling a cylinder, i.e. volumetrically; no determination of the density was made).

---

3. Experiments carried out by E. De Boni and M. Schubert, PSI.



### 8.8.2 Results

The electrical conductivity at the salt separator outlet V11 and at the outlet of the PDU V17 as a function of sodium sulfate feed time for one of the experiments is depicted in Figure 8.19, together with the volumetric flow rates out of the salt separator and at the outlet of the PDU, respectively. Other experiments showed similar results.

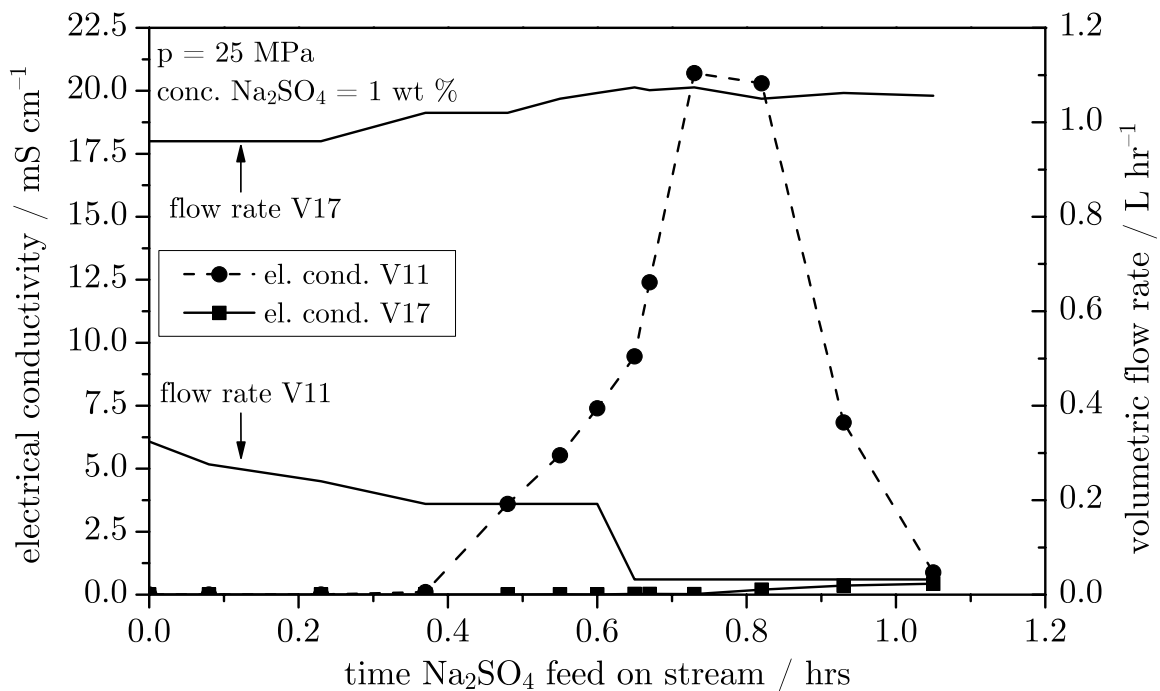


Figure 8.19: Volumetric flow rates and electrical conductivity of the leaving streams at the salt separator outlet V11 and the sample port V17 at the outlet of the PDU.

The electrical conductivity of the effluent out of the salt separator (V11) was around 20 mS/cm, thus almost twice as large as the conductivity of the feed stream. In contrast, the conductivity of the effluent leaving the PDU at the outlet of the plant (V17) increased only slightly over time, to around 0.3 mS/cm (less than tap water). Hence, this confirmed the functioning of the separator. However, as can be seen, the volumetric flow rate out of the salt separator decreased as soon as the electrical conductivity increased; possibly due to the increased viscosity of the brine leaving the system. When the spring relief valve V11 was reset at 0.9 hrs on stream,

the conductivity at V11 dropped, and the pressure of the system increased (not shown), indicating that the system was plugged. Hence, the plant had to be stopped. Plugging by salt crystal formation at the outlet valve V11 can be seen in Figure 8.20.

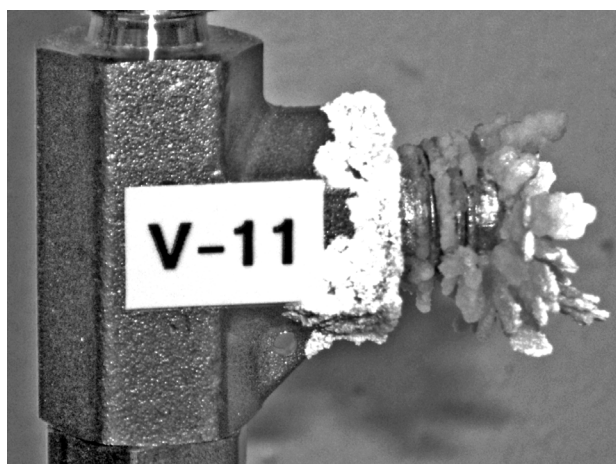


Figure 8.20: Salt crust and crystals of dried brine leaving spring relief valve V11.

While the reverse flow salt separation principle worked, it did so only over a short period of time (1 – 2 hrs for 1 wt %  $\text{Na}_2\text{SO}_4$ ). Minor improvements by extracting the brine over two spring relief valves in series instead of one led to a better controllability of the system. However, it still plugged after a certain time. When the separator was dismantled, a salt plug of 17 cm length was discovered inside the vessel. It is suspected that the entry region around the dip tube is not well dimensioned (i.e. too long, so that the salts can precipitate around the tube instead of further downstream inside the vessel).

## 8.9 Problems, Conclusions and Outlook

- The pump setup is only capable of conveying liquids, no slurries as planned originally.
- The preheater is adequately dimensioned.

- 
- Salt separation by reverse flow works. The co-feeding of brine dissolution water via an HPLC pump did not cause any problems. However, fine tunings on the salt separator design are necessary. First steps are the variation of the dip tube length and the arrangement of heating zones. The salt separator brine outflow should be implemented by a back-pressure regulator (e.g. as used in the continuously operating catalyst test rig) rather than by spring relief valves.
  - The reactor is well dimensioned for ethanol gasification up to 40 wt % (WHSV  $6.55 \text{ hr}^{-1}$  at 1 kg/hr mass flow rate). As soon as the salt separator is working satisfactorily, experiments with palm oil pyrolysis condensate can be carried out.
  - After minor revisions, the phase separator worked properly.
  - The TOX reactor for the exhaust gas treatment was not well dimensioned; this led to a thermal runaway. The installation of a monolith TOX reactor is too costly; hence it will be replaced by a torch. In addition, the evolution of SNG is thereby nicely visualized.



# Chapter 9: Summary, Conclusions and Recommendations

## 9.1 Summary and Conclusions

- The hydrothermal route to convert wet biomass to SNG is a feasible option. It can simultaneously solve the waste problem associated with certain types of biomass (e.g. manure or sewage sludge, world wide, or palm oil pyrolysis condensate, particularly in Malaysia).
- The distinction of organic and inorganic oxygen is crucial for the determination of the heating value of the feedstock. For this reason, a combination of several analytical tools (dry matter determination, elemental analysis, incineration residue, Soxhlet extraction, HPIEC and ICP analysis) was used to accurately determine the elemental composition of swine manure.
- A wood to SNG reaction network was proposed, based on experimental evidence and literature: lignin and celluloses are decomposed in hydrolysis reactions, and eventually converted to alcohols, carboxylic acids, aldehydes, and ketones, which are reformed to the primary gases  $\text{CO}_2$ ,  $\text{CO}$ ,  $\text{H}_2$ , and  $\text{CH}_4$  that equilibrate according to the thermodynamic equilibrium (assumption: active catalyst present).
- Knowledge about the gasification behavior of several types of biomass was gained in three different reactors: a batch system for biomass slurries (the need for active mixing became apparent), a continuously operating catalyst test rig for liquid model substances, and a heated quartz capillary micro-reactor setup for the visualization of the gasification process.

- Skeletal nickel catalysts exhibited high initial activity for the gasification of wood (methane yield acc. to the thermodynamic maximum yield,  $0.33 \text{ g}_{\text{CH}_4}/\text{g}_{\text{wood}}$ ), even at high feed concentrations (30 wt %). Manure slurries were also quite well gasified to a methane rich gas (at a gasification efficiency of 70 – 80 %). However, the skeletal nickel catalysts sintered rapidly in the hydrothermal environment (with crystallite growth factors around 5), and thereby deactivated. Stabilization by co-doping of Ru, Cu, or Mo, or by altering the Ni/Al ratio was not successful.
- The onset of catalytic wood gasification was determined to be at 250 to 290 °C:
  - 250 °C by pressure differential analysis in the batch reactor with a skeletal nickel catalyst.
  - 270 °C by gas sampling in the batch reactor with 2 wt % Ru/C as catalyst.
  - 290 °C, by visual observation in quartz microreactors with the same skeletal nickel catalyst (there: p was lower, lowering the hydrolytic power of the solvent).
- Supported ruthenium catalysts were evaluated for the biomass to SNG process. While 1 wt % Ru/TiO<sub>2</sub> exhibited a low activity in wood gasification experiments (possibly due to low dispersion, leading to a low surface area of active sites), a stable Ru/C catalyst was found (2 wt % Ru/C, Engelhard) that exhibited both high activity and high stability in the hydrothermal environment. No comparable catalyst has been presented in the literature so far.
- Despite its activity and stability, the tolerance towards sulfate of the promising 2 wt % Ru/C (Engelhard) was rather low. By elaborate long-term experiments it was discovered that the deactivation mechanism being consistent with all experimental results was a strong sulfate-ruthenium-interaction. The experiments corroborated a biomass gasification mechanism according to Mars-van-Krevelen, where the

active metal changes its oxidation state in a redox cycle (for Ru: IV to II to IV). The sulfate ligand masked the active sites, locking their oxidation state and thus deactivating the catalyst. The deactivation illustrated the importance of salt separation prior to reaction. A possible reactivation method by  $\text{H}_2\text{O}_2$  was found.

- Non-catalytic wood liquefaction experiments carried out in the batch reactor yielded good process conditions for the hydrolysis of wood to smaller, intermediate molecules at 30 MPa: a heat-up time of 5 min. to 330 – 350°C, with 0 – 2 min. holding time at these temperatures.
- A process demonstration unit was built with mass flow rates of around 1 kg/hr, where both salt separation and gasification can be demonstrated. For feed concentrations of 40 wt %, around 400 L/hr of gas were produced (corresponding to 200 L/hr methane or a thermal power of around 1 kW). Due to various problems with the feed system, no slurries could be conveyed at the scale of the PDU. Initial gasification tests with ethanol, and salt separation tests with sodium sulfate were successful. Next steps will be the gasification of palm oil pyrolysis condensate, which was identified as a suitable feedstock for the process demonstration as a substitute for wood or manure slurries.

## 9.2 Recommendations for Further Research

- Batch experiments with real biomass should be carried out in a stirred high-pressure vessel to ensure good mixing of the content. Catalysts in granular form could be introduced in a basket.
- The high initial cost of a supported noble metal catalyst such as 2 wt % Ru/C could limit the lowest economical size of a plant. Process simulation calculations, together with a cost assessment should be carried out to estimate the final price of the SNG for various plant

sizes. The price should always be compared to the ecological benefit of the associated waste destruction.

- Salt separation is crucial. The current design of the separator should be improved to decrease the salt concentration leaving the vessel with the biomass stream in order to prolong catalyst life-time.
- Further catalyst analyses (e.g. oxygen chemisorption at various pressures, and/or cooled to  $-78\text{ }^{\circ}\text{C}$ , and temperature programmed reduction with hydrogen, methane and higher hydrocarbons) should be carried out to find additional hints for the reasons of different performance of the various catalysts.
- The deactivation mechanism of Ru/C by sulfate should be verified by an *in-situ* EXAFS campaign.
- For process demonstration units of larger size (50 – 100 kg/hr), commercial pumps are available to convey slurries with high solids fractions. The liquefaction step should be carried out in a heat exchanger with mixing elements, protected against corrosion. The heat should be exchanged with the hot fluid stream leaving the catalytic reactor.
- The separation of the product phases should be carried out under pressure to take advantage of the high carbon dioxide solubility in water, which would then leave the process for the most part with the aqueous stream.



---

# References

- [1] Z. Grainger, Process: The potential for biomass in the energy mix. *Filtration & Separation*. 43(9), 2006: p. 28-30.
- [2] M. Balat, G. Ayar, Biomass energy in the world, use of biomass and potential trends. *Energy Sources*. 27(10), 2005: p. 931-940.
- [3] European Commission, EUR21350 - Biomass - Green energy for Europe. ISBN 97-894-8466-7, 2005.
- [4] H. Schmieder, J. Abeln, N. Boukis, E. Dinjus, A. Kruse, M. Kluth, G. Petrich, E. Sadri, M. Schacht, Hydrothermal gasification of biomass and organic wastes. *Journal of Supercritical Fluids*. 17(2), 2000: p. 145-153.
- [5] B. Oettli, J.-L. Hersener, U. Meier, K. Schleiss, J. Chételat, D. Bedniaguine, A. Dauriat, E. Gnansounou, M. Blum, M. Peter, O. Schwank, Potenziale zur energetischen Biomassenutzung in der Schweiz (Schlussbericht). Bundesamt für Energie BFE, 2004.
- [6] P. Mizsey, E. Newson, Comparison of different vehicle power trains. *Journal of Power Sources*. 102(1-2), 2001: p. 205-209.
- [7] M.C. Seemann, Methanation of biosyngas in a fluidized bed reactor – Development of a one-step synthesis process, featuring simultaneous methanation, Watergas shift and low temperature tar reforming, PhD thesis, Diss. ETH No. 16754, ETH Zurich, 2007.
- [8] A.V. Bridgwater, Renewable fuels and chemicals by thermal processing of biomass. *Chemical Engineering Journal*. 91(2-3), 2003: p. 87-102.

- 
- [9] A. Duret, C. Friedli, F. Maréchal, Process design of Synthetic Natural Gas (SNG) production using wood gasification. *Journal of Cleaner Production*. 13(15), 2005: p. 1434-1446.
- [10] M. Mozaffarian, R.W.R. Zwart, H. Boerrigter, E.P. Deurwaarder, S.R.A. Kersten, "Green Gas" as SNG (Synthetic Natural Gas) - A Renewable Fuel with Conventional Quality. ECN-RX--04-085, ECN Biomass, 2004.
- [11] P.C. Flynn, University of Alberta, CDN, personal communication, 2004.
- [12] E. Ghafoori, P.C. Flynn, J.J. Feddes, Pipeline vs. truck transport of beef cattle manure. *Biomass and Bioenergy*. 31(2-3), 2007: p. 168-175.
- [13] U. Meier, Meritec GmbH, personal communication, 2005.
- [14] Y. Yoshida, K. Dowaki, Y. Matsumura, R. Matsuhashi, D.Y. Li, H. Ishitani, H. Komiyama, Comprehensive comparison of efficiency and CO<sub>2</sub> emissions between biomass energy conversion technologies - position of supercritical water gasification in biomass technologies. *Biomass & Bioenergy*. 25(3), 2003: p. 257-272.
- [15] F. Vogel, F. Hildebrand. Catalytic Hydrothermal Gasification of Woody Biomass at High Feed Concentrations. in 4<sup>th</sup> International Symposium on High Pressure Process Technology and Chemical Engineering. Venice, Italy, 2002, September 22-25: Chemical Engineering Transactions.
- [16] F. Vogel, M.H. Waldner. Catalytic Hydrothermal Gasification of Woody Biomass at High Feed Concentrations. in Science in Thermal and Chemical Biomass Conversion STCBC. Victoria, Canada, 2004, August 30 - September 03.
- [17] M.H. Waldner, F. Vogel, Renewable production of methane from woody biomass by catalytic hydrothermal gasification. *Industrial & Engineering Chemistry Research*. 44(13), 2005: p. 4543-4551.

- 
- [18] Y. Matsumura, Evaluation of supercritical water gasification and biomethanation for wet biomass utilization in Japan. *Energy Conversion and Management*. 43(9-12), 2002: p. 1301-1310.
- [19] M. Modell, R.C. Reid, S.I. Amin, Gasification process, U.S. Patent 4,113,446, 1978, September 12.
- [20] Bundesgesetz über die Reduktion der CO<sub>2</sub>-Emissionen (CO<sub>2</sub>-Gesetz), SR 641.71, 1999, October, 8.
- [21] S.E. Ramesohl, Analyse und Bewertung der Nutzungsmöglichkeiten von Biomasse. Wuppertal Institut für Klima, Umwelt, Energie, 2006, January, 30.
- [22] A. Henni, P. Tontiwachwuthikul, A. Chakma, Solubility study of methane and ethane in promising physical solvents for natural gas sweetening operations. *Journal of Chemical and Engineering Data*. 51(1), 2006: p. 64-67.
- [23] H. Tretter, Neue Optionen für die Nutzung von Biogas - eine technoökonomische Analyse der Aufbereitung von Biogas zur Einspeisung ins österreichische Erdgasversorgungsnetz., Diploma Thesis, TU Wien, 2003.
- [24] R. Felder, R. Dones, Evaluation of ecological impacts of synthetic natural gas from wood used in current heating and car systems. *Biomass and Bioenergy*. In Press, Corrected Proof, doi:10.1016/j.biombioe.2006.08.005, 2007.
- [25] K.C. Park, H. Tomiyasu, Gasification reaction of organic compounds catalyzed by RuO<sub>2</sub> in supercritical water. *Chemical Communications*,(6), 2003: p. 694-695.
- [26] B.C. Wolverton, R.C. McDonald. Vascular Plants for Water Pollution Control and Renewable Sources of Energy. in *Proceedings, Bio-Energy '80*. Bioenergy Council: Washington, D.C., 1980.
- [27] Gewässerschutzverordnung, SR 814.201, 1998, October, 28.

- 
- [28] W. Habicht, N. Boukis, G. Franz, E. Dinjus, Investigation of nickel-based alloys exposed to supercritical water environments. *Microchimica Acta*. 145(1-4), 2004: p. 57-62.
- [29] H.C. Lee, J.H. In, S.Y. Lee, J.H. Kim, C.H. Lee, An anti-corrosive reactor for the decomposition of halogenated hydrocarbons with supercritical water oxidation. *Journal of Supercritical Fluids*. 36(1), 2005: p. 59-69.
- [30] A.A. Peterson, P. Vontobel, F. Vogel, J.W. Tester, In situ visualization of the performance of a supercritical-water salt separator using neutron radiography. *Journal of Supercritical Fluids*, 2007, submitted.
- [31] A. Baiker, R. Wandeler, *Supercritical Fluids; Opportunities in Heterogeneous Catalysis*. CATTECH. 4(1), 2000: p. 128-143.
- [32] W.L. Marshall, E.U. Franck, *Ion Product of Water Substance, 0°C-1000°C, 1-10,000 Bars - New International Formulation and Its Background*. *Journal of Physical and Chemical Reference Data*. 10(2), 1981: p. 295-304.
- [33] D.P. Fernandez, A.R.H. Goodwin, E.W. Lemmon, J. Sengers, R.C. Williams, A formulation for the static permittivity of water and steam at temperatures from 238 K to 873 K at pressures up to 1200 MPa, including derivatives and Debye-Huckel coefficients. *Journal of Physical and Chemical Reference Data*. 26(4), 1997: p. 1125-1166.
- [34] D.R. Lide, ed. *CRC Handbook of Chemistry and Physics*. 87 ed. Internet Version 2007, Taylor and Francis: Boca Raton, FL, USA.
- [35] NIST Chemistry Webbook, Internet Version, 2007, link: <http://webbook.nist.gov/chemistry/>.
- [36] J. Chrastil, *Solubility of Solids and Liquids in Supercritical Gases*. *Journal of Physical Chemistry*. 86(15), 1982: p. 3016-3021.

- 
- [37] P. Kritzer, Corrosion in high-temperature and supercritical water and aqueous solutions: a review. *Journal of Supercritical Fluids*. 29(1-2), 2004: p. 1-29.
- [38] B. Kuhlmann, E.M. Arnett, M. Siskin, Classical Organic-Reactions in Pure Superheated Water. *Journal of Organic Chemistry*. 59(11), 1994: p. 3098-3101.
- [39] P.E. Savage, S. Gopalan, T.I. Mizan, C.J. Martino, E.E. Brock, Reactions at Supercritical Conditions - Applications and Fundamentals. *Aiche Journal*. 41(7), 1995: p. 1723-1778.
- [40] P.E. Savage, Organic chemical reactions in supercritical water. *Chemical Reviews*. 99(2), 1999: p. 603-621.
- [41] D. Bröll, C. Kaul, A. Krämer, P. Krammer, T. Richter, M. Jung, H. Vogel, P. Zehner, Chemistry in supercritical water. *Angewandte Chemie-International Edition*. 38(20), 1999: p. 2999-3014.
- [42] A. Rabenau, The Role of Hydrothermal Synthesis in Preparative Chemistry. *Angewandte Chemie-International Edition in English*. 24(12), 1985: p. 1026-1040.
- [43] T. Miyazawa, T. Funazukuri, Hydrothermal production of mono(galacturonic acid) and the oligomers from poly(galacturonic acid) with water under pressures. *Industrial & Engineering Chemistry Research*. 43(10), 2004: p. 2310-2314.
- [44] H. Schmieder, J. Abeln, Supercritical water oxidation: State of the art. *Chemical Engineering & Technology*. 22(11), 1999: p. 903-908.
- [45] P. Kritzer, E. Dinjus, An assessment of supercritical water oxidation (SCWO) - Existing problems, possible solutions and new reactor concepts. *Chemical Engineering Journal*. 83(3), 2001: p. 207-214.
- [46] R.L. Smith, P. Atmaji, Y. Hakuta, M. Kawaguchi, T. Adschiri, K. Arai, Recovery of metals from simulated high-level liquid waste

- with hydrothermal crystallization. *Journal of Supercritical Fluids*. 11(1-2), 1997: p. 103-114.
- [47] W. Sugiyama, K.C. Park, T. Yamamura, H. Okada, Y. Sugita, H. Tomiyasu, Decomposition of radioactive organic wastes with supercritical water medium containing RuO<sub>2</sub>. *Journal of Nuclear Science and Technology*. 42(2), 2005: p. 256-258.
- [48] W. Sugiyama, T. Yamamura, K.C. Park, H. Tomiyasu, I. Satoh, Y. Shiokawa, H. Okada, Y. Sugita, Recovery of radioactivity as solids from nonflammable organic low-level radioactive wastes using supercritical water mixed with RuO<sub>2</sub>. *Journal of Supercritical Fluids*. 35(3), 2005: p. 240-246.
- [49] X.D. Xu, Y. Matsumura, J. Stenberg, M.J. Antal, Carbon-catalyzed gasification of organic feedstocks in supercritical water. *Industrial & Engineering Chemistry Research*. 35(8), 1996: p. 2522-2530.
- [50] T. Minowa, F. Zhen, T. Ogi, Cellulose decomposition in hot-compressed water with alkali or nickel catalyst. *Journal of Supercritical Fluids*. 13(1-3), 1998: p. 253-259.
- [51] T. Minowa, T. Ogi, Hydrogen production from cellulose using a reduced nickel catalyst. *Catalysis Today*. 45(1-4), 1998: p. 411-416.
- [52] T. Minowa, S. Inoue, Hydrogen production from biomass by catalytic gasification in hot compressed water. *Renewable Energy*. 16(1-4), 1999: p. 1114-1117.
- [53] I.G. Lee, M.S. Kim, S.K. Ihm, Gasification of glucose in Supercritical water. *Industrial & Engineering Chemistry Research*. 41(5), 2002: p. 1182-1188.
- [54] M. Sasaki, B. Kabyemela, R. Malaluan, S. Hirose, N. Takeda, T. Adschiri, K. Arai, Cellulose hydrolysis in subcritical and supercritical water. *Journal of Supercritical Fluids*. 13(1-3), 1998: p. 261-268.

- 
- [55] E. Tani, M. Yoshimura, S. Somiya, Formation of Ultrafine Tetragonal ZrO<sub>2</sub> Powder under Hydrothermal Conditions. *Journal of the American Ceramic Society*. 66(1), 1983: p. 11-14.
- [56] D.W. Matson, R.D. Smith, Supercritical Fluid Technologies for Ceramic-Processing Applications. *Journal of the American Ceramic Society*. 72(6), 1989: p. 871-881.
- [57] K. Sue, A. Suzuki, M. Suzuki, K. Arai, Y. Hakuta, H. Hayashi, T. Hiaki, One-pot synthesis of nickel particles in supercritical water. *Industrial & Engineering Chemistry Research*. 45(2), 2006: p. 623-626.
- [58] D.C. Elliott, L.J. Sealock, E.G. Baker, Chemical-Processing in High-Pressure Aqueous Environments. 2. Development of Catalysts for Gasification. *Industrial & Engineering Chemistry Research*. 32(8), 1993: p. 1542-1548.
- [59] L.J. Sealock Jr., D.C. Elliott, Method for the catalytic conversion of lignocellulosic materials, US Patent 5,019,135, 1991, May, 28.
- [60] X.D. Xu, M.J. Antal, Gasification of sewage sludge and other biomass for hydrogen production in supercritical water. *Environmental Progress*. 17(4), 1998: p. 215-220.
- [61] M.J. Antal Jr., S.G. Allen, D. Schulman, X.D. Xu, R.J. Divilio, Biomass gasification in supercritical water. *Industrial & Engineering Chemistry Research*. 39(11), 2000: p. 4040-4053.
- [62] G.T. Hong, M.H. Spritzer. Supercritical Water Partial Oxidation. in *Proceedings of the 2002 U.S. DOE Hydrogen Program Review2002: NREL/CP-610-32405*.
- [63] A. Kruse, A. Gawlik, Biomass conversion in water at 330-410 °C and 30-50 MPa. Identification of key compounds for indicating different chemical reaction pathways. *Industrial & Engineering Chemistry Research*. 42(2), 2003: p. 267-279.

- 
- [64] T. Yoshida, Y. Oshima, Y. Matsumura, Gasification of biomass model compounds and real biomass in supercritical water. *Biomass & Bioenergy*. 26(1), 2004: p. 71-78.
- [65] D.C. Elliott, G.G. Neuenschwander, T.R. Hart, R.S. Butner, A.H. Zacher, M.H. Engelhard, J.S. Young, D.E. McCready, Chemical processing in high-pressure aqueous environments. 7. Process development for catalytic gasification of wet biomass feedstocks. *Industrial & Engineering Chemistry Research*. 43(9), 2004: p. 1999-2004.
- [66] H. Nakagawa, A. Namba, M. Bohlmann, K. Miura, Hydrothermal dewatering of brown coal and catalytic hydrothermal gasification of the organic compounds dissolving in the water using a novel Ni/carbon catalyst. *Fuel*. 83(6), 2004: p. 719-725.
- [67] A. Sharma, H. Nakagawa, K. Miura, A novel nickel/carbon catalyst for CH<sub>4</sub> and H<sub>2</sub> production from organic compounds dissolved in wastewater by catalytic hydrothermal gasification. *Fuel*. 85(2), 2006: p. 179-184.
- [68] A. Sharma, H. Nakagawa, K. Miura, Uniform dispersion of Ni nano particles in a carbon based catalyst for increasing catalytic activity for CH<sub>4</sub> and H<sub>2</sub> production by hydrothermal gasification. *Fuel*. 85(17-18), 2006: p. 2396-2401.
- [69] A. Sharma, I. Saito, H. Nakagawa, K. Miura, Effect of carbonization temperature on the nickel crystallite size of a Ni/C catalyst for catalytic hydrothermal gasification of organic compounds. *Fuel*. 86(7-8), 2007: p. 915-920.
- [70] A. Kruse, A. Krupka, V. Schwarzkopf, C. Gamard, T. Henningsen, Influence of proteins on the hydrothermal gasification and liquefaction of biomass. 1. Comparison of different feedstocks. *Industrial & Engineering Chemistry Research*. 44(9), 2005: p. 3013-3020.
- [71] X.H. Hao, L.J. Guo, X.M. Zhang, Y. Guan, Hydrogen production



- from catalytic gasification of cellulose in supercritical water. *Chemical Engineering Journal*. 110(1-3), 2005: p. 57-65.
- [72] M.B. Valenzuela, C.W. Jones, P.K. Agrawal, Batch aqueous-phase reforming of woody biomass. *Energy & Fuels*. 20(4), 2006: p. 1744-1752.
- [73] P. D'Jesus, N. Boukis, B. Kraushaar-Czarnetzki, E. Dinjus, Influence of process variables on gasification of corn silage in supercritical water. *Industrial & Engineering Chemistry Research*. 45(5), 2006: p. 1622-1630.
- [74] P. D'Jesus, N. Boukis, B. Kraushaar-Czarnetzki, E. Dinjus, Gasification of corn and clover grass in supercritical water. *Fuel*. 85(7-8), 2006: p. 1032-1038.
- [75] P. D'Jesus, C. Artiel, N. Boukis, B. Kraushaar-Czarnetzki, E. Dinjus, Influence of educt preparation on gasification of corn silage in supercritical water. *Industrial & Engineering Chemistry Research*. 44(24), 2005: p. 9071-9077.
- [76] B. Potic, S.R.A. Kersten, M. Ye, M.A. van der Hoef, J.A.M. Kuipers, W.P.M. van Swaaij, Fluidization with hot compressed water in micro-reactors. *Chemical Engineering Science*. 60(22), 2005: p. 5982-5990.
- [77] B. Potic, S.R.A. Kersten, W. Prins, W.P.M. van Swaaij, A high-throughput screening technique for conversion in hot compressed water. *Industrial & Engineering Chemistry Research*. 43(16), 2004: p. 4580-4584.
- [78] M. Osada, T. Sato, M. Watanabe, M. Shirai, K. Arai, Catalytic gasification of wood biomass in subcritical and supercritical water. *Combustion Science and Technology*. 178(1-3), 2006: p. 537-552.
- [79] Y. Matsumura, T. Minowa, B. Potic, S.R.A. Kersten, W. Prins, W.P.M. van Swaaij, B. van de Beld, D.C. Elliott, G.G. Neuenchwander, A. Kruse, M.J. Antal, Biomass gasification in near-

- and super-critical water: Status and prospects. *Biomass & Bioenergy*. 29(4), 2005: p. 269-292.
- [80] W. Bühler, E. Dinjus, H.J. Ederer, A. Kruse, C. Mas, Ionic reactions and pyrolysis of glycerol as competing reaction pathways in near- and supercritical water. *Journal of Supercritical Fluids*. 22(1), 2002: p. 37-53.
- [81] Y.J. Lu, L.J. Guo, C.M. Ji, X.M. Zhang, X.H. Hao, Q.H. Yan, Hydrogen production by biomass gasification in supercritical water: A parametric study. *International Journal of Hydrogen Energy*. 31(7), 2006: p. 822-831.
- [82] J.B. Gadhe, R.B. Gupta, Hydrogen production by methanol reforming in supercritical water: Suppression of methane formation. *Industrial & Engineering Chemistry Research*. 44(13), 2005: p. 4577-4585.
- [83] J.T. Henrikson, P.E. Savage, Water-density effects on phenol oxidation in supercritical water. *Aiche Journal*. 49(3), 2003: p. 718-726.
- [84] W. Feng, H.J. van der Kooi, J. de Swaan Arons, Phase equilibria for biomass conversion processes in subcritical and supercritical water. *Chemical Engineering Journal*. 98(1-2), 2004: p. 105-113.
- [85] T. Sato, T. Furusawa, Y. Ishiyama, H. Sugito, Y. Miura, M. Sato, N. Suzuki, N. Itoh, Effect of water density on the gasification of lignin with magnesium oxide supported nickel catalysts in supercritical water. *Industrial & Engineering Chemistry Research*. 45(2), 2006: p. 615-622.
- [86] N. Akiya, P.E. Savage, Roles of water for chemical reactions in high-temperature water. *Chemical Reviews*. 102(8), 2002: p. 2725-2750.
- [87] W. Feng, H.J. van der Kooi, J.D.S. Arons, Biomass conversions in subcritical and supercritical water: driving force, phase equilibria,

- and thermodynamic analysis. *Chemical Engineering and Processing*. 43(12), 2004: p. 1459-1467.
- [88] T. Yoshida, Y. Oshima, Partial oxidative and catalytic biomass gasification in supercritical water: A promising flow reactor system. *Industrial & Engineering Chemistry Research*. 43(15), 2004: p. 4097-4104.
- [89] Y. Matsumura, M. Harada, K. Nagata, Y. Kikuchi, Effect of heating rate of biomass feedstock on carbon gasification efficiency in supercritical water gasification. *Chemical Engineering Communications*. 193(5), 2006: p. 649-659.
- [90] M. Saisu, T. Sato, M. Watanabe, T. Adschiri, K. Arai, Conversion of lignin with supercritical water-phenol mixtures. *Energy & Fuels*. 17(4), 2003: p. 922-928.
- [91] S. Karagöz, T. Bhaskar, A. Muto, Y. Sakata, T. Oshiki, T. Kishimoto, Low-temperature catalytic hydrothermal treatment of wood biomass: analysis of liquid products. *Chemical Engineering Journal*. 108(1-2), 2005: p. 127-137.
- [92] M. Yilgin, D. Pehlivan, Poplar wood-water slurry liquefaction in the presence of formic acid catalyst. *Energy Conversion and Management*. 45(17), 2004: p. 2687-2696.
- [93] F. Goudriaan, D.G.R. Peferoen, Liquid fuels from biomass via a hydrothermal process. *Chemical Engineering Science*. 45(8), 1990: p. 2729-2734.
- [94] S.D. Jackson, R.B. Moyes, P.B. Wells, R. Whyman, Chemisorption and Catalysis by Metal-Clusters - Hydrogenation of Carbon-Monoxide and Carbon-Dioxide Catalyzed by Supported Ruthenium Clusters Derived from  $Ru_3(CO)_{11}$  and from  $H_4Ru_4(CO)_{12}$ . *Journal of the Chemical Society-Faraday Transactions I*. 83, 1987: p. 905-911.
- [95] M.R. Prairie, A. Renken, J.G. Highfield, K.R. Thampi, M. Grat-

- zel, A Fourier-Transform Infrared Spectroscopic Study of CO<sub>2</sub> Methanation on Supported Ruthenium. *Journal of Catalysis*. 129(1), 1991: p. 130-144.
- [96] S. Aki, M.A. Abraham, Catalytic supercritical water oxidation of pyridine: Comparison of catalysts. *Industrial & Engineering Chemistry Research*. 38(2), 1999: p. 358-367.
- [97] K. Kudo, K. Komatsu, Selective formation of methane in reduction of CO<sub>2</sub> with water by Raney alloy catalyst. *Journal of Molecular Catalysis A - Chemical*. 145(1-2), 1999: p. 257-264.
- [98] Z. Kowalczyk, S. Jodzis, W. Rarog, J. Zielinski, J. Pielaszek, Effect of potassium and barium on the stability of a carbon-supported ruthenium catalyst for the synthesis of ammonia. *Applied Catalysis A - General*. 173(2), 1998: p. 153-160.
- [99] S. Scire, C. Crisafulli, R. Maggiore, S. Minico, S. Galvagno, Influence of the support on CO<sub>2</sub> methanation over Ru catalysts: an FT-IR study. *Catalysis Letters*. 51(1-2), 1998: p. 41-45.
- [100] M. Watanabe, M. Mochiduki, S. Sawamoto, T. Adschiri, K. Arai, Partial oxidation of n-hexadecane and polyethylene in supercritical water. *Journal of Supercritical Fluids*. 20(3), 2001: p. 257-266.
- [101] J.I. Kroschwitz, M. Howe-Grant, eds. *Kirk - Othmer Encyclopedia of Chemical Technology*, 4<sup>th</sup> Edition. 1991, Wiley-Interscience: New York.
- [102] T. Sato, S. Kurosawa, R.L. Smith, T. Adschiri, K. Arai, Water gas shift reaction kinetics under noncatalytic conditions in supercritical water. *Journal of Supercritical Fluids*. 29(1-2), 2004: p. 113-119.
- [103] X.H. Hao, L.J. Guo, X. Mao, X.M. Zhang, X.J. Chen, Hydrogen production from glucose used as a model compound of biomass gasified in supercritical water. *International Journal of Hydrogen Energy*. 28(1), 2003: p. 55-64.

- 
- [104] D.C. Elliott, R.T. Hallen, L.J. Sealock, Aqueous Catalyst Systems for the Water Gas Shift Reaction .2. Mechanism of Basic Catalysis. *Industrial & Engineering Chemistry Product Research and Development*. 22(3), 1983: p. 431-435.
- [105] Z. Fang, T. Minowa, R.L. Smith, T. Ogi, J.A. Kozinski, Liquefaction and gasification of cellulose with  $\text{Na}_2\text{CO}_3$  and Ni in subcritical water at 350 °C. *Industrial & Engineering Chemistry Research*. 43(10), 2004: p. 2454-2463.
- [106] M. Watanabe, T. Sato, H. Inomata, R.L. Smith, K. Arai, A. Kruse, E. Dinjus, Chemical reactions of C-1 compounds in near-critical and supercritical water. *Chemical Reviews*. 104(12), 2004: p. 5803-5821.
- [107] R.L. Keiski, T. Salmi, P. Niemisto, J. Ainassaari, V.J. Pohjola, Stationary and transient kinetics of the high temperature water-gas shift reaction. *Applied Catalysis A - General*. 137(2), 1996: p. 349-370.
- [108] T. Yagasaki, S. Saito, I. Ohmine, A theoretical study on decomposition of formic acid in sub- and supercritical water. *Journal of Chemical Physics*. 117(16), 2002: p. 7631-7639.
- [109] J.L. Yu, P.E. Savage, Decomposition of formic acid under hydrothermal conditions. *Industrial & Engineering Chemistry Research*. 37(1), 1998: p. 2-10.
- [110] Y. Izumizaki, K.C. Park, Y. Tachibana, H. Tomiyasu, Y. Fujii, Organic decomposition in supercritical water by an aid of ruthenium(IV) oxide as a catalyst - Exploitation of biomass resources for hydrogen production. *Progress in Nuclear Energy*. 47(1-4), 2005: p. 544-552.
- [111] J.H. Sinfelt, Materials Research in Catalysis, in *Advancing Materials Research*, P.A. Psaras and H. Dale, Editors. 1987, National Academy Press: Washington, D.C. p. 177-202.

- 
- [112] M. Krajnc, J. Levec, The role of catalyst in supercritical water oxidation of acetic acid. *Applied Catalysis B-Environmental*. 13(2), 1997: p. 93-103.
- [113] A. Baiker, Supercritical fluids in heterogeneous catalysis. *Chemical Reviews*. 99(2), 1999: p. 453-473.
- [114] Z.Y. Ding, M.A. Frisch, L.X. Li, E.F. Gloyna, Catalytic oxidation in supercritical water. *Industrial & Engineering Chemistry Research*. 35(10), 1996: p. 3257-3279.
- [115] M.G.E. Goemans, L. Li, E.F. Gloyna, Separation of Inorganic Salts from Supercritical Water by Cross-Flow Microfiltration. *Separation Science and Technology*. 30(7-9), 1995: p. 1491-1509.
- [116] M. Raney, Method of Preparing Catalytic Material, US Patent 1,563,587, 1925, December, 1.
- [117] P. Fouilloux, The Nature of Raney-Nickel, Its Adsorbed Hydrogen and Its Catalytic Activity for Hydrogenation Reactions - Review. *Applied Catalysis*. 8(1), 1983: p. 1-42.
- [118] K. Kudo, K. Komatsu, Reduction of alkali metal carbonate to methane with water in the presence of Raney alloy. *Journal of Molecular Catalysis A - Chemical*. 145(1-2), 1999: p. 159-167.
- [119] B.W. Hoffer, E. Crezee, P.R.M. Mooijman, A.D. van Lagneveld, F. Kapteijn, J.A. Moulijn, Carbon supported Ru catalysts as promising alternative for Raney-type Ni in the selective hydrogenation of D-glucose. *Catalysis Today*. 79(1-4), 2003: p. 35-41.
- [120] J.H. Sinfelt, Structure of Metal-Catalysts. *Reviews of Modern Physics*. 51(3), 1979: p. 569-589.
- [121] D. Bröll, A. Krämer, H. Vogel, I. Lappas, H. Fuess, Heterogeneously catalyzed partial oxidation in supercritical water. *Chemical Engineering & Technology*. 24(2), 2001: p. 142-146.
- [122] J.R. Rostrup-Nielsen, J.H. Bak Hansen, CO<sub>2</sub>-Reforming of Meth-

- ane over Transition Metals. *Journal of Catalysis*. 144(1), 1993: p. 38-49.
- [123] M.A. Vannice, The catalytic synthesis of hydrocarbons from H<sub>2</sub>/CO mixtures over the group VIII metals : I. The specific activities and product distributions of supported metals. *Journal of Catalysis*. 37(3), 1975: p. 449-461.
- [124] M. Osada, O. Sato, M. Watanabe, K. Arai, M. Shirai, Water density effect on lignin gasification over supported noble metal catalysts in supercritical water. *Energy & Fuels*. 20(3), 2006: p. 930-935.
- [125] C.V. Cavenaghi, Engelhard Italiana S.p.A., personal communication, 2005.
- [126] K. van Gorp, E. Boerman, C.V. Cavenaghi, P.H. Berben, Catalytic hydrogenation of fine chemicals: sorbitol production. *Catalysis Today*. 52(2-3), 1999: p. 349-361.
- [127] E.P. Maris, W.C. Ketchie, V. Oleshko, R.J. Davis, Metal particle growth during glucose hydrogenation over Ru/SiO<sub>2</sub> evaluated by X-ray absorption spectroscopy and electron microscopy. *Journal of Physical Chemistry B*. 110(15), 2006: p. 7869-7876.
- [128] M. Watanabe, H. Inomata, R.L. Smith, K. Arai, Catalytic decarboxylation of acetic acid with zirconia catalyst in supercritical water. *Applied Catalysis A - General*. 219(1-2), 2001: p. 149-156.
- [129] P. Gallezot, N. Nicolaus, G. Fleche, P. Fuertes, A. Perrard, Glucose Hydrogenation on Ruthenium Catalysts in a Trickle-Bed Reactor. *Journal of Catalysis*. 180(1), 1998: p. 51-55.
- [130] F.J. Long, K.W. Sykes, The Mechanism of the Steam-Carbon Reaction. *Proceedings of the Royal Society of London Series A-Mathematical and Physical Sciences*. 193(1034), 1948: p. 377-399.
- [131] Y. Matsumura, X. Xu, M.J. Antal, Gasification characteristics of

- an activated carbon in supercritical water. *Carbon*. 35(6), 1997: p. 819-824.
- [132] M. Sugiyama, M. Kataoka, H. Ohmura, H. Fujiwara, S. Koda, Oxidation of carbon particles in supercritical water: Rate and mechanism. *Industrial & Engineering Chemistry Research*. 43(3), 2004: p. 690-699.
- [133] I. Rossetti, N. Pernicone, L. Forni, Graphitised carbon as support for Ru/C ammonia synthesis catalyst. *Catalysis Today*. 102, 2005: p. 219-224.
- [134] M. Watanabe, M. Osada, H. Inomata, K. Arai, A. Kruse, Acidity and basicity of metal oxide catalysts for formaldehyde reaction in supercritical water at 673 K. *Applied Catalysis a-General*. 245(2), 2003: p. 333-341.
- [135] D. Fengel, G. Wegener, Wood. *Chemistry, Ultrastructure, Reactions*. 1984, Berlin, New York: Walter de Gruyter.
- [136] K. Ehara, S. Saka, H. Kawamoto, Characterization of the lignin-derived products from wood as treated in supercritical water. *Journal of Wood Science*. 48(4), 2002: p. 320-325.
- [137] B.M. Kabyemela, T. Adschiri, R.M. Malaluan, K. Arai, Kinetics of glucose epimerization and decomposition in subcritical and supercritical water. *Industrial & Engineering Chemistry Research*. 36(5), 1997: p. 1552-1558.
- [138] B.M. Kabyemela, T. Adschiri, R.M. Malaluan, K. Arai, Glucose and fructose decomposition in subcritical and supercritical water: Detailed reaction pathway, mechanisms, and kinetics. *Industrial & Engineering Chemistry Research*. 38(8), 1999: p. 2888-2895.
- [139] G.C.A. Luijkx, F. van Rantwijk, H. van Bekkum, Hydrothermal formation of 1,2,4-benzenetriol from 5-hydroxymethyl-2-furaldehyde and -fructose. *Carbohydrate Research*. 242, 1993: p. 131-139.



- 
- [140] T. Minowa, Z. Fang, Hydrogen production from biomass by low temperature catalytic gasification. *Progress in Thermochemical Biomass Conversion*. (Ed. by A. V. Bridgwater), 2003: p. 396.
- [141] A. Sinag, A. Kruse, V. Schwarzkopf, Key compounds of the hydro-pyrolysis of glucose in supercritical water in the presence of  $K_2CO_3$ . *Industrial & Engineering Chemistry Research*. 42(15), 2003: p. 3516-3521.
- [142] M. Osada, T. Sato, M. Watanabe, T. Adschiri, K. Arai, Low-temperature catalytic gasification of lignin and cellulose with a ruthenium catalyst in supercritical water. *Energy & Fuels*. 18(2), 2004: p. 327-333.
- [143] Y. Nagai, S. Morooka, N. Matubayasi, M. Nakahara, Mechanisms and kinetics of acetaldehyde reaction in supercritical water: Non-catalytic disproportionation, condensation, and decarbonylation. *Journal of Physical Chemistry A*. 108(52), 2004: p. 11635-11643.
- [144] M. Modell, Gasification and Liquefaction of Forest Products in Supercritical Water, in *Fundamentals of Thermochemical Biomass Conversion*, R.P. Overend, T.A. Milne, and L.K. Mudge Jr., Editors. 1985, Elsevier: Amsterdam. p. 95-119.
- [145] J.P.A. Neeft, H.A.M. Knoef, P. Onaji, Behavior of tar in biomass gasification systems. Tar related problems and their solutions. *Novem Report No. 9919, Energy from Waste and Biomass (EWAB)*, The Netherlands, 1999.
- [146] L. Devi, K.J. Ptasinski, F. Janssen, A review of the primary measures for tar elimination in biomass gasification processes. *Biomass & Bioenergy*. 24(2), 2003: p. 125-140.
- [147] NIST Chemistry WebBook, NIST Standard Reference Database Number 69, ed. P.J. Linstrom and W.G. Mallard. 2005, June, Gaithersburg MD, 20899: National Institute of Standards and Technology.

- 
- [148] J.C. de Hemptinne, A. Dhima, S. Shakir. The Henry constant for 20 hydrocarbons, CO<sub>2</sub> and H<sub>2</sub>S in water as a function of pressure and temperature. in 14<sup>th</sup> Symposium on Thermophysical Properties. Boulder, CO, USA, 2000, June 25 - 30.
- [149] A. Dhima, J.C. de Hemptinne, J. Jose, Solubility of hydrocarbons and CO<sub>2</sub> mixtures in water under high pressure. *Industrial & Engineering Chemistry Research*. 38(8), 1999: p. 3144-3161.
- [150] T. Aizawa, Y. Masuda, K. Minami, M. Kanakubo, H. Nanjo, R.L. Smith Jr. Direct observation of channel-T mixing of high-temperature high-pressure water. in 3<sup>rd</sup> International Meeting on High Pressure Chemical Engineering (HPCE-3). Erlangen, Germany, 2006, May 10-12.
- [151] J.L. Yu, P.E. Savage, Catalyst activity, stability, and transformations during oxidation in supercritical water. *Applied Catalysis B-Environmental*. 31(2), 2001: p. 123-132.
- [152] N. Boukis, V. Diem, W. Habicht, E. Dinjus, Methanol reforming in supercritical water. *Industrial & Engineering Chemistry Research*. 42(4), 2003: p. 728-735.
- [153] N. Boukis, W. Habicht, G. Franz, E. Dinjus, Behavior of Ni-base alloy 625 in methanol-supercritical water systems. *Materials and Corrosion-Werkstoffe Und Korrosion*. 54(5), 2003: p. 326-330.
- [154] S. Grunke, Main and side reactions in the Karl Fischer solution. *Food Control*. 12(7), 2001: p. 419-426.
- [155] S.K. Masthan, K.V.R. Chary, P.K. Rao, Measurement of Surface Dispersion of Ruthenium on Gamma-Al<sub>2</sub>O<sub>3</sub> Support by Low-Temperature Oxygen-Chemisorption (Ltoc) Technique. *Journal of Catalysis*. 124(1), 1990: p. 289-292.
- [156] G. Blanchard, H. Charcosset, Measurement of the Dispersity of Supported Ruthenium Catalysts by Oxygen-Chemisorption. *Reaction Kinetics and Catalysis Letters*. 15(2), 1980: p. 209-214.

- 
- [157] H. Kubicka, Hydrogen Adsorption and Hydrogen-Oxygen Titration on Ruthenium Powder. *Reaction Kinetics and Catalysis Letters*. 5(2), 1976: p. 223-228.
- [158] K.C. Taylor, Determination of Ruthenium Surface-Areas by Hydrogen and Oxygen Chemisorption. *Journal of Catalysis*. 38(1-3), 1975: p. 299-306.
- [159] J.H. Sinfelt, D.J.C. Yates, Catalytic Hydrogenolysis of Ethane over Noble Metals of Group 8. *Journal of Catalysis*. 8(1), 1967: p. 82-90.
- [160] H. Kubicka, Specific Activity of Technetium Rhenium Ruthenium Platinum and Palladium in Catalytic Reactions of Benzene with Hydrogen. *Journal of Catalysis*. 12(3), 1968: p. 223-237.
- [161] H.P. Klug, L.E. Alexander, *X-Ray Diffraction Procedures: For Polycrystalline and Amorphous Materials*. 1954, New York: John Wiley & Sons.
- [162] J.Y. Liu, Advanced electron microscopy characterization of nanostructured heterogeneous catalysts. *Microscopy and Microanalysis*. 10(1), 2004: p. 55-76.
- [163] S.A. Channiwala, P.P. Parikh, A unified correlation for estimating HHV of solid, liquid and gaseous fuels. *Fuel*. 81(8), 2002: p. 1051-1063.
- [164] L.C. Reichenbach de Sousa, Gasification of wood, urban waste-wood (Altholz) and other wastes in a fluidised bed reactor, PhD thesis, Diss. ETH No. 14207, ETH Zurich, 2001.
- [165] M.J. Antal Jr., S.G. Allen, X.F. Dai, B. Shimizu, M.S. Tam, M. Gronli, Attainment of the theoretical yield of carbon from biomass. *Industrial & Engineering Chemistry Research*. 39(11), 2000: p. 4024-4031.
- [166] J. Congleton, W. Zheng, H. Hua, The stress corrosion cracking

- behaviour of annealed 316 stainless steel in low oxygen 5 ppm chloride content water at 300°C. *Corrosion Science*. 30(6-7), 1990: p. 555-567.
- [167] J.E. Truman, The influence of chloride content, pH and temperature of test solution on the occurrence of stress corrosion cracking with austenitic stainless steel. *Corrosion Science*. 17(9), 1977: p. 737-746.
- [168] P.T. Williams, J. Onwudili, Subcritical and supercritical water gasification of cellulose, starch, glucose, and biomass waste. *Energy & Fuels*. 20(3), 2006: p. 1259-1265.
- [169] F. Vogel, Paul Scherrer Institut, personal communication, 2006.
- [170] R.H. Perry, D.W. Green, Heats Of Combustion, in Perry's Chemical Engineers' Handbook. 1997, McGraw-Hill. p. 2-195 ff, Table 2-221.
- [171] O. Bobleter, H. Binder, Dynamic Hydrothermal Degradation of Wood. *Holzforschung*. 34(2), 1980: p. 48-51.
- [172] G. Bonn, R. Concin, O. Bobleter, Hydrothermolysis - a New Process for the Utilization of Biomass. *Wood Science and Technology*. 17(3), 1983: p. 195-202.
- [173] T. Minowa, F. Zhen, T. Ogi, G. Varhegyi, Liquefaction of cellulose in hot compressed water using sodium carbonate: Products distribution at different reaction temperatures. *Journal of Chemical Engineering of Japan*. 30(1), 1997: p. 186-190.
- [174] H. Thunman, B. Leckner, Thermal conductivity of wood - models for different stages of combustion. *Biomass & Bioenergy*. 23(1), 2002: p. 47-54.
- [175] D.C. Elliott, T.R. Hart, Method for aqueous phase reactions, US Patent 6,152,975, 2000, November, 28.
- [176] D.C. Elliott, T.R. Hart, G.G. Neuenschwander, Chemical process-

- ing in high-pressure aqueous environments. 8. Improved catalysts for hydrothermal gasification. *Industrial & Engineering Chemistry Research*. 45(11), 2006: p. 3776-3781.
- [177] A. Ishihara, E.W. Qian, I.N. Finahari, I.P. Sutrisna, T. Kabe, Addition effect of ruthenium on nickel steam reforming catalysts. *Fuel*. 84(12-13), 2005: p. 1462-1468.
- [178] T. Sato, M. Osada, M. Watanabe, M. Shirai, K. Arai, Gasification of alkylphenols with supported noble metal catalysts in supercritical water. *Industrial & Engineering Chemistry Research*. 42(19), 2003: p. 4277-4282.
- [179] C.V. Cavenaghi, Engelhard Italiana S.p.A., personal communication, 2006.
- [180] Verein Deutscher Ingenieure, ed. *VDI Wärmeatlas*. 4<sup>th</sup> Edition, 1984. VDI-Verlag GmbH: Düsseldorf. Page Lb1.
- [181] F. Vogel, M.H. Waldner, A.A. Rouff, S. Rabe, Synthetic natural gas from biomass by catalytic conversion in supercritical water. *Green Chemistry*, 2007, in press, doi:10.1039/B614601E.
- [182] F.J. Armellini, Phase Equilibria and Precipitation Phenomena of Sodium Chloride and Sodium Sulfate in Sub- and Supercritical Water, PhD thesis, Massachusetts Institute of Technology, February 1993.
- [183] M. Osada, O. Sato, K. Arai, M. Shirai, Stability of Supported Ruthenium Catalysts for Lignin Gasification in Supercritical Water. *Energy & Fuels*. 20(6), 2006: p. 2337-2343.
- [184] Y. Yasaka, K. Yoshida, C. Wakai, N. Matubayasi, M. Nakahara, Kinetic and equilibrium study on formic acid decomposition in relation to the water-gas-shift reaction. *Journal of Physical Chemistry A*. 110(38), 2006: p. 11082-11090.
- [185] F.J. Armellini, J.W. Tester, Solubility of sodium chloride and sul-

- fate in sub- and supercritical water vapor from 450-550 °C and 100-250 bar. *Fluid Phase Equilibria*. 84, 1993: p. 123-142.
- [186] F.J. Armellini, J.W. Tester, G.T. Hong, Precipitation of sodium chloride and sodium sulfate in water from sub- to supercritical conditions: 150 to 550 °C, 100 to 300 bar. *The Journal of Supercritical Fluids*. 7(3), 1994: p. 147-158.
- [187] M.S. Khan, S.N. Rogak, Solubility of  $\text{Na}_2\text{SO}_4$ ,  $\text{Na}_2\text{CO}_3$  and their mixture in supercritical water. *Journal of Supercritical Fluids*. 30(3), 2004: p. 359-373.
- [188] O.C. Okorafor, Solubility and density isotherms for the sodium sulfate-water-methanol system. *Journal of Chemical and Engineering Data*. 44(3), 1999: p. 488-490.
- [189] H.A.D. Silva, B.R. McGarvey, R.H.D. Santos, M. Bertotti, V. Mori, D.W. Franco, Sulfate as a ligand in ruthenium(II) and (III) ammines. *Canadian Journal of Chemistry-Revue Canadienne De Chimie*. 79(5), 2001: p. 679-687.
- [190] J. Pecho, T.J. Schildhauer, M. Sturzenegger, S.M.A. Biollaz, A. Wokaun, Reactive bed materials for improved biomass gasification in a circulating fluidised bed reactor, *Chemical Engineering Science* (submitted).
- [191] D.C. Elliott, G.G. Neuenschwander, M.R. Phelps, T.R. Hart, A.H. Zacher, L.J. Silva, Chemical processing in high-pressure aqueous environments. 6. Demonstration of catalytic gasification for chemical manufacturing wastewater cleanup in industrial plants. *Industrial & Engineering Chemistry Research*. 38(3), 1999: p. 879-883.
- [192] G.T. Hong, W.R. Killilea, T.B. Thomasom, Method for solids separation in a wet oxidation type process, US Patent 4,822,497, 1989, April, 18.

- 
- [193] A. Demirbas, Mechanisms of liquefaction and pyrolysis reactions of biomass. *Energy Conversion and Management*. 41(6), 2000: p. 633-646.
- [194] A. Demirbas, Effect of lignin content on aqueous liquefaction products of biomass. *Energy Conversion and Management*. 41(15), 2000: p. 1601-1607.
- [195] M. Schüpfer, Hydrothermale Vergasung von Gülle, Semester Thesis, PSI / ETH Zurich, 2002.
- [196] P. Koller, apex koller trading GmbH, personal communication, 2004.





# Appendix A: Ru/C Catalyst Preparation and Analysis

## A.1 Impregnation of the Support with Ruthenate

Three different Ru/C catalysts (three types of supports, and active metal loadings of 7 or 2 wt %, respectively) were prepared by the dissolution-precipitation method, as described by Hoffer and co-workers [119]. This method is reported to usually result in a good dispersion of the active metal on the support.

Table A.1: Reagents and amounts used for the synthesis of Ru/C catalysts.

catalyst code <sup>a</sup>	Ru loading wt %	support type	$m(\text{K}_2\text{RuCl}_5 \cdot x\text{H}_2\text{O})$ g	$m(\text{support, dry})$ g
RG	7.06	graphite <sup>b</sup>	0.600	2.001
R18	7.08	act. carbon powder <sup>c</sup>	0.604	2.007
R19	1.96	act. carbon granules <sup>c</sup>	0.315	4.008

a. as used in the catalyst screening experiments described in section 6.3.2.

b. received from Timcal. BET = 500 m<sup>2</sup>/g.

c. activated carbon from coconut shell; received from Engelhard. BET = 850 – 1000 m<sup>2</sup>/g.

The individual amounts and reagents used for the synthesis are tabulated in Table A.1. The experimental procedure was as follows: The support was submitted to a 250 mL round-bottom flask. Potassiumpentachlororuthenate ( $\text{K}_2\text{RuCl}_5 \cdot x\text{H}_2\text{O}$ , Alfa Aesar,  $w_{\text{Ru}} \geq 25.4$  %) was dissolved in 50 mL HCl (conc. 0.01 M) in a volumetric flask. The solution was then transferred to the round-bottom flask, and a Dimroth condenser was

attached on top of it. The mixture was stirred and heated in a silicone oil bath at 250 °C under reflux for 18 hours. Then, the assembly was allowed to cool to room temperature. The content of the round-bottom flask was filtrated (0.45 µm regenerated cellulose filter, Schleicher & Schuell). The filtrate was collected for later visual determination of the amount of ruthenium on the support. To wash off any residual KCl, the filter cake was washed with water (approx. 40 times with 50 mL each, until the pH of the filtrate was 5.0), leaving Ru(III)Cl<sub>3</sub> on the support. The filter cake was then heated to 80 °C at 200 hPa of air for 12 hours.

To estimate the degree of ruthenium precipitation on the support, fresh K<sub>2</sub>RuCl<sub>5</sub>·xH<sub>2</sub>O was dissolved in an amount of HCl equal to the amount of filtrate received after the impregnation, until the color of the two solutions was identical; ruthenate solutions have a very distinct yellow color even at very dilute concentrations. Based on this visual comparison, 99.7 % of the ruthenate submitted to the flask must have been impregnated onto the support.

## A.2 Reduction of Ru(III) to Ru(0) with Hydrogen

The dried filter cake was filled into ceramic boats and put into a glass tube (i.d. = 30 mm, L = 300 mm), which was put into a tubular oven (Eurotherm). To reduce the Ru(III)Cl<sub>3</sub> to Ru(0), hydrogen was made to flow through the tube at 80 mL/min. The tube was heated at a rate of 1 °C/min. to 160 °C, and held for three hours (Hoffer et al. report a reduction temperature of 140 °C [119]; however, at a later stage of the project, the catalyst manufacturer recommended reduction temperatures of 150 – 200 °C for the surface and bulk reduction<sup>1</sup> of Ru(III) [179]).

---

1. The surface reduction of Ru with H<sub>2</sub> occurs around 120 – 140 °C, while the bulk reduction takes place at around 180 °C [179].

The hydrogen was switched off, and the sample was allowed to cool to room temperature under flowing nitrogen. For the catalysts RG and R18, slow passivation with 1 vol % O<sub>2</sub> in N<sub>2</sub> (60 mL/min., 2 hrs) was conducted at room temperature; R19 was tapped with water and stored moist.

### A.3 Catalyst Analysis

The catalysts were analyzed with respect to their BET surface area, and R18 and R19 were additionally visualized by HAADF-STEM, depicted in Figure A.1 and Figure A.2.

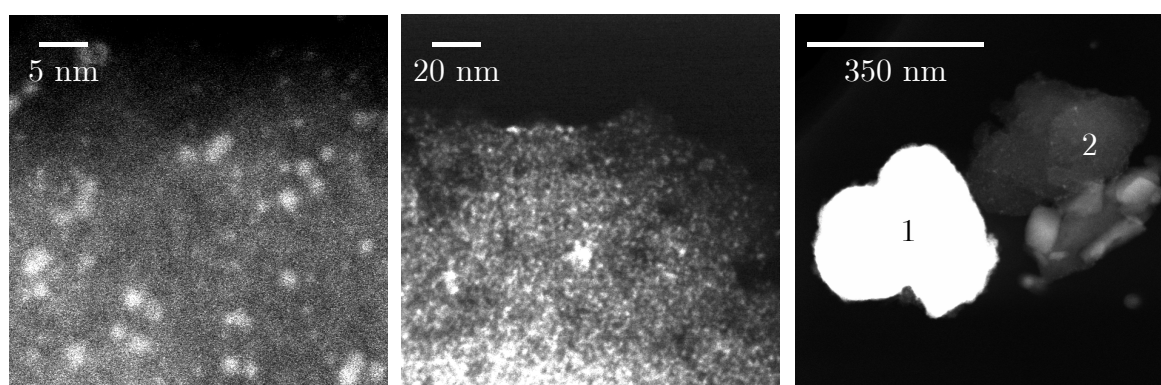


Figure A.1: HAADF-STEM images of catalyst R18 (7 wt % Ru/C<sub>pwd.</sub>, synthesized in-house). Wide particle size distribution, ranging from small crystallites of 1 – 2 nm to very few chunks of up to 350 nm. 1 and 2 on the right image refer to the measurement area of the EDXS analysis presented in Figure A.3.

Unlike on the commercially available 2 wt % Ru/C (Engelhard), the particle size distribution was not monodisperse. The majority of the crystallites were rather small, 1.5 – 2 nm, but a few chunks of up to 350 nm were detected. EDXS analysis confirmed that they consisted of ruthenium, see Figure A.3.

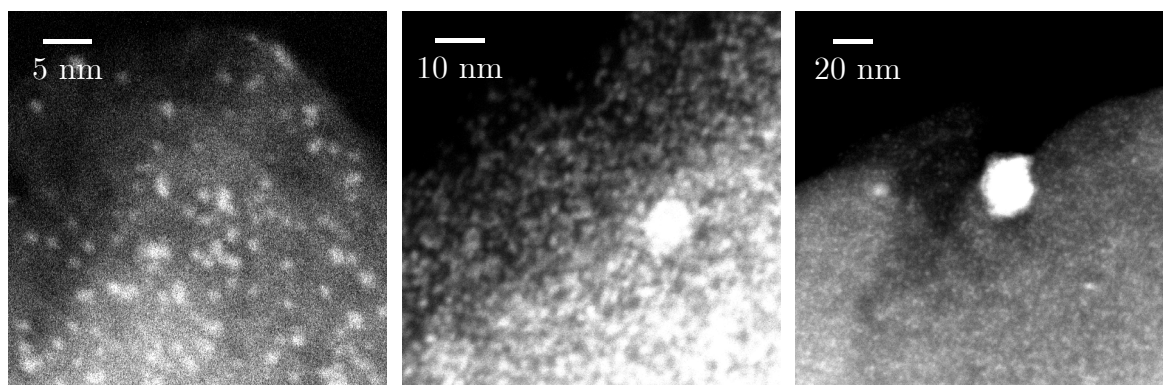


Figure A.2: HAADF-STEM images of catalyst R19 (2 wt % Ru/C<sub>gran.</sub>, synthesized in-house). Typical crystallite size is 1.5 – 2 nm, with a few larger crystallites from 10 to 30 nm.

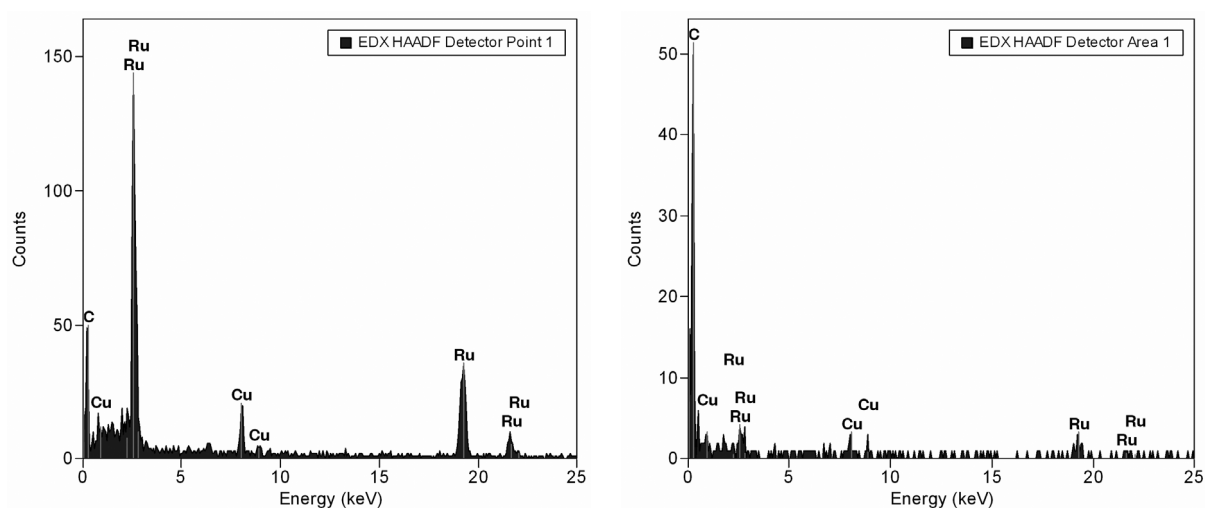


Figure A.3: EDXS analysis of the areas 1 and 2 of Figure A.1. The Cu signal originated from the sample holder (copper grid).

The dispersion was measured by the oxygen chemisorption method proposed in section 4.8; results are displayed in Table A.2. Typical sample masses were around 120 mg for the granular catalyst R19, and about 30 mg for the catalysts in powder form, as they could not be put into a mesh, but had to be filled into an alumina crucible, where the oxygen flow is slightly impaired. The ruthenium loading was calculated based on the average loading of the synthesis batch; inhomogeneity could have been checked with ICP analysis, but this was not considered necessary for these analyses. As can be seen, the dispersion of R18 was measured to

unity, which seems to be unlikely when crystallites up to 350 nm are present. On the one hand, the particles analyzed by HAADF-STEM might not have necessarily been representative; on the other hand, the catalyst performed fairly in wood gasification experiments, and thus the chemisorption method for catalysts in powder form might be carried out with a very fine Pt mesh instead of using an alumina crucible. In contrast, the dispersion obtained for R19 corresponds nicely to values reported by Hoffer et al., who synthesized their catalysts with the same anionic deposition method. They obtained a dispersion of 0.27 for their 5.6 wt % Ru/C catalyst [119].

Table A.2: Oxygen-chemisorption dispersion measurement and BET surface area of various Ru/C catalysts.

catalyst	$A_s$ $\text{m}^2_{\text{Ru}}/\text{g}_{\text{cat.}}$	$D$	$l$ nm	$S_{\text{BET}}$ $\text{m}^2/\text{g}_{\text{cat.}}$
RG (in-house, 7 wt % Ru)	N/A	N/A	N/A	474
R18 (in-house, 7 wt % Ru)	37.8	1.00	0.9	1020
R19 (in-house, 2 wt % Ru)	$2.9 \pm 1.2^{\text{a}}$	$0.28 \pm 0.11^{\text{a}}$	$3.6 \pm 1.5^{\text{a}}$	890
3 % Ru/C (AlfaAesar)	3.3	$0.20^{\text{b}}$	4.5	N/D
5 % Ru/C (Aldrich)				N/D

a. based on three measurements; 1 standard deviation. For  $l = 5.2$  nm of one of the measurements,  $\text{Ru}_s\text{-O}$  stoichiometry was applied.

b. based on  $\text{Ru}_s\text{-O}_2$  stoichiometry (valid for  $l$  up to  $4 \pm 1$  nm); border case.

In addition to the three catalysts synthesized in-house, two commercially available catalysts were also measured as a reference. All five catalysts were evaluated in wood gasification experiments, presented in section 6.3.2.



---

# List of Publications

## Patents

Patent application PCT 05021601.9 / EP05021601 (2005-10-04) “Verfahren zur Erzeugung von Methan und Methanhydrat aus Biomasse” (Process for the production of methane and methane hydrate from biomass), Paul Scherrer Institut, Inventors: F. Vogel, M.H. Waldner, T.-B. Truong, E. De Boni, S. Stucki, 2005.

## Peer-Reviewed Articles

M.H. Waldner, J. Sefcik, M. Soos, M. Morbidelli, *Initial Growth Kinetics and Structure of Colloidal Aggregates in a Turbulent Coagulator*. Powder Technology. 156(2-3), 2005: p. 226-234.

M.H. Waldner, F. Vogel, *Renewable Production of Methane from Woody Biomass by Catalytic Hydrothermal Gasification*. Ind. Eng. Chem. Res. 44(13), 2005: p. 4543-4551.

F. Vogel, M.H. Waldner, *Catalytic Hydrothermal Gasification of Woody Biomass at High Feed Concentrations*. Proceedings “Science in Thermal and Chemical Biomass Conversion STCBC”, A.V. Bridgwater, D.G.B. Boocock (Eds.), Vol. 2, 1001-1012, CPL Press, March 2006.

F. Vogel, M.H. Waldner, A.A. Rouff, S. Rabe, *Synthetic Natural Gas from Biomass by Catalytic Conversion in Supercritical Water*. Green Chemistry 9(6), 2007: p. 616-619.

M.H. Waldner, F. Krumeich, F. Vogel, *Synthetic Natural Gas by Hydrothermal Gasification of Biomass. Selection Procedure Towards a Stable Catalyst and its Sodium Sulfate Tolerance*. J. Supercritical Fluids (in press), doi:10.1016/j.supflu.2007.04.004.

## Articles

F. Vogel, M.H. Waldner, *Methan aus nasser Biomasse. Hydrothermale Vergasung forst- und landwirtschaftlicher Biomassen*. Gas Wasser Abwasser gwa, 5/2004, p. 327-335.

## Conference Proceedings (Posters and Talks)

M.H. Waldner, F. Vogel, *Catalytic Hydrothermal Gasification of Woody Biomass*. In: Proceedings 2<sup>nd</sup> World Conference and Technology Exhibition on Biomass for Energy, Industry and Climate Protection, Rome, Italy, May 10-14, 2004.

F. Vogel, M.H. Waldner, *Catalytic Hydrothermal Gasification of Woody Biomass and Manure at High Feed Concentrations*. Seminars at the National Renewable Energy Laboratory, Golden/CO, and the Pacific Northwest National Laboratory, Richland/WA, USA, August 25 & 27, 2004

F. Vogel, M.H. Waldner, *Hydrothermale Vergasung von nasser Biomasse zu Methan. 13. Symposium Energie aus Biomasse – Biogas, Flüssigkraftstoffe, Festbrennstoffe*, Poster Session, Kloster Banz, Bad Staffelstein, Germany, November 25-26, 2004.

A.A. Peterson, M.H. Waldner, F. Vogel, J.W. Tester, M. Fröling, *Fuels from Biomass: Use of Neutron Radiography to Improve the Design of a*



---

*Salt Separator in Supercritical Water Biomass Conversion.* AGS Annual Meeting, poster session, Massachusetts Institute of Technology, Cambridge/MA, USA, March 20-23, 2005.

A.A. Peterson, M.H. Waldner, F. Vogel, J.W. Tester, *Methane and Nutrient Salts from Waste Biomass: Development of a Catalytic Conversion Process in Supercritical Water.* Energy Technologies for a Sustainable Future ETSF 5, Energy and Large Research Facilities, Poster Session, Villigen PSI, Switzerland, June 9-10, 2005.

F. Vogel, M.H. Waldner, E. De Boni, *Efficient Production of Synthetic Natural Gas from Biomass by Hydrothermal Gasification.* In: Proceedings Joint 20<sup>th</sup> AIRAPT – 43<sup>rd</sup> EHPRG Conference on Science and Technology of High Pressure, ISBN 3-923704-49-6, Karlsruhe, Germany, June 27-July 1, 2005.

M.H. Waldner, F. Vogel, *Continuous Catalytic Hydrothermal Gasification of Synthetic Liquefied Wood to Synthetic Natural Gas at High Feed Concentrations,* In: Proceedings 14<sup>th</sup> European Biomass Conference and Exhibition, Paris, France, October 17-21, 2005.

F. Vogel, M.H. Waldner, *Scientific Challenges Towards an Efficient Hydrothermal Biomass Gasification Process,* 3<sup>rd</sup> International Meeting on High Pressure Chemical Engineering, Poster Session, Erlangen, Germany, May 10-12, 2006.

F. Vogel, M.H. Waldner, A.A. Rouff, S. Rabe, *Green Synthetic Natural Gas from Biomass by Catalytic Conversion in Supercritical Water.* Prepr. Pap.-Am. Chem. Soc., Div. Fuel Chem. 51(2), 2006.



---

# Curriculum Vitae

## Personal Details

name	Maurice Henri Waldner
date/place of birth	March 21, 1977, in Menziken (AG), Switzerland
nationality/citizenship	Swiss / Basel (BS) and Oberdorf (BL), Switzerland

## Education

1993 – 1997	Kantonsschule Beromünster, Switzerland Humanistic Matura Type A (Ancient Greek, Latin) graduated with highest distinction
1997 – 2003	Chemical Engineering studies at ETH Zurich graduated as Dipl. Chem.-Ing. ETH
2001	Exchange Semester at University of Illinois at Urbana-Champaign, IL, USA (senior class Chemical Engineering)
2003 – 2007	PhD Studies in Renewable Energy Technology at Paul Scherrer Institut (PSI), Switzerland graduated as Dr. Sc. ETH Zürich

## Awards

1996	Roche Youth Price for outstanding research in combinatorial chemistry within the framework of Schweizer Jugend Forscht
------	--